Cranfield University

Richard Gregory BULLER

Investigation of Helicopter Loading Spectra Variations on Fatigue Crack Growth in Titanium and Aluminium Alloys

School of Industrial and Manufacturing Science

Supervisor: Professor P.E. Irving

April 1999

This thesis is submitted to fulfil the requirement of the degree of Doctor of Philosophy

ABSTRACT

An investigation has been made into the effect of omitting small, vibratory load cycles from a helicopter load spectrum on the fatigue crack growth rates of high strength titanium (Ti-10V 2Fe 3Al) and aluminium (7010 T73651) alloys. The investigation is made in the light of new requirements for the damage tolerance design of transport helicopter structures that have normally been designed to safe life criteria. The work aims to improve the damage tolerance design of helicopter structures by understanding the contribution of the vibratory load cycles to fatigue crack growth damage. The experimental work consisted of two parts that considered fatigue crack growth under simple overload type loading and complex fatigue load sequences using compact tension specimens.

Simple overload and underload tests were run under near-threshold, plane strain crack growth rates typical of those experienced in helicopter components. These were supplemented by crack closure measurements made using a strain gauge adhered close to the crack tip. Fatigue crack growth rate retardation was observed after an overload and this was reduced if a tensile underload was subsequently applied. The experimental evidence suggested that observed crack growth transient behaviour could be explained by a residual stress field mechanism ahead of the crack tip with closure only serving in a secondary role to modify the applied external loading.

A fatigue load sequence was developed for a helicopter rotorhead component and included representations of manoeuvre loads superimposed with the high mean stress, vibratory load cycles. A technique of progressively omitting small load cycles of increasing range from this sequence was used to determine the effect of these cycles on the fatigue crack growth. It was found that the these cycles of 16% range caused up to 80% of the total crack length damage and that the observed crack growth rate of the cycles was three times greater than that predicted by a conservative fatigue crack growth model. These are significant observations because vibratory cycles are usually considered to be non-damaging under a safe life design to which most current transport helicopters have been certified to. It was proposed that the accelerated growth rate of these cycles was caused by frequent underloads in the rotorhead loading sequence. A residual stress field model was invoked to explain this behaviour. The results are used to provide guidance for damage tolerant design of helicopter structures.

ACKNOWLEDGEMENTS

I would like to express my sincere appreciation to my supervisor, Professor Phil Irving for his guidance and support throughout the duration of this thesis. I appreciated the patience he showed during the occasional testing mishaps and for the past year during my write-up.

I would like to acknowledge the Department of Trade and Industry who provided the funding to support the Link Project between Cranfield University and the project partners. A 'thank you' goes to the project participants Robin Cook from DERA, Pete Wood and Steve Jenkins from GKN Westland Helicopters Ltd., Ian Austen of nCode International and John Bristow of the CAA.

Much appreciation also goes to Tony Scott and Andy Baldwin in the SIMS workshops who gave me plenty of support on the test machines and equipment.

Finally, I would like to express my gratitude to my parents back in New Zealand for their immense support over the last few years.

The research work described in this thesis has also been presented at and published (or accepted for publishing) as papers in the proceedings of the following conferences:

(1) Irving, P.E., Buller, R.G., Wood, P., Rigden, S., Jenkins, S., Cook, R., Palmer, C., Austen, I., "Technologies for damage tolerance in rotorcraft metallic structures," 23rd European Helicopter Forum, Brighton, U.K., 1996.

(2) Buller, R.G., Irving, P.E., "Experimental investigation of small load cycle omission level in helicopter loading spectra," Proceedings of ICAF 97, Fatigue in New and Ageing Aircraft, Eds. R. Cook and P. Poole, 18-20 June 1997, Edinburgh, U.K., pp. 441-460.

(3) Irving, P.E., Buller, R.G., "Prediction of fatigue life under helicopter loading spectra for safe life and damage tolerant design," Fatigue and Fracture Mechanics, ASTM STP 1322, T.L. Panontin and S.D. Sheppard, Eds., American Society for Testing and Materials, 1998.

(4) Cook, R., Jenkins, S., Matthew, D., Irving, P.E., Buller, R.G., Wood, P., Austen, I., "The development of a robust crack growth model for rotorcraft metallic structures," Application of Damage Tolerance Principles for Improved Airworthiness of Rotorcraft, NATO Ageing Systems Specialists Meeting, Greece, 1999.

Investigation of Helicopter Loading Spectra Variations on Fatigue Crack Growth in Titanium and Aluminium Alloys

CONTENTS

Appendices

LIST OF FIGURES

LIST OF TABLES

NOMENCLATURE

Symbol/ Abbreviation	Description	Unit
a	Crack length	mm
a_i	Crack length at test start	mm
a_f	Crack length at test failure	mm
a_o	Intrinsic crack length in NASGRO equation	mm
a/W	Normalised crack length	
A_k	Fit parameter for NASGRO equation	
α	Constraint factor	
B_k	Fit parameter for NASGRO equation	
C	Crack growth law coefficient	
CAL	Constant amplitude loading	
CMOD	Crack mouth opening displacement	mm
CT	Compact tension specimen	
CVAL	Complex variable amplitude loading	
da/dN	Crack growth rate	mm/cycle
DCPD	Direct current potential drop	
D O/L	Double overload	
DVM	Digital voltmeter	
D_s	Delay distance for Stripy	mm
D_t	Delay distance for test	mm
G	Strain energy release rate	Joules
G_{IC}	Critical strain energy release rate	Joules
ΔK	Stress intensity factor range	$MPa.m^{½}$
ΔK_{eff}	Effective stress intensity factor range	$MPa.m^{½}$
$\Delta K_{eff,PR}$	Effective stress intensity factor range based on K_{PR}	$MPa.m^{½}$
$\Delta K_{eff,RCS}$	Lang model effective stress intensity factor range	$MPa.m^{½}$
ΔK_{th}	Threshold stress intensity factor range	$MPa.m^{½}$
ΔK_{tip}	Effective crack tip stress intensity range	$MPa.m^{½}$
ΔK_0	Threshold stress intensity factor at R=0	$MPa.m^{½}$
$f(a/W)$	Compact tension specimen geometry function	
K_{cl}	Crack closure stress intensity factor	$MPa.m^{½}$
K_I, K_{II}, K_{III}	Stress intensity factors in Mode I, II and III	$MPa.m^{½}$
K_{max}	Maximum stress intensity factor	$MPa.m^{½}$

K_{min}	Minimum stress intensity factor	MPa.m^{½}
K_{IC}	Fracture toughness stress intensity factor	MPa.m^{½}
K_C	Plane stress fracture toughness	MPa.m^{½}
K_{ol}	Overload stress intensity factor	MPa.m^{½}
K_{peak}	Peak stress intensity factor during CVAL	MPa.m^{½}
K_{PR}	Crack propagation stress intensity factor	MPa.m^{½}
K_{UL}	Underload stress intensity factor	MPa.m^{½}
KIAS	Indicated airspeed	knots
m	Crack growth law exponent	
N	Cycles	
N_f	Number of flights to failure	
N_s	Delay cycles for Stripy	
N_t	Delay cycles for test	
NTS	Near tip strain	
O/U	Overload-Underload	
OLR	Overload ratio (K_{ol}/K_{max})	
OLPZ	Overload plastic zone	mm
P	Applied load	kN
P_{peak}	Peak load during CVAL	kN
p	NASGRO equation exponent	
q	NASGRO equation exponent	
r	Radius from crack tip origin	mm
r_p	Plastic zone size	mm
r_{p_rev}	Reversed plastic zone size	mm
R	Stress ratio (K_{min}/K_{max})	
R_{cl}	R ratio above which ΔK_{th} becomes constant	
R_{tip}	Crack tip stress ratio (K_{cl}/K_{max})	
SAR	Search and rescue	
S_{cl}	Crack closure stress	MPa
S_{peak}	Peak stress during CVAL	MPa
SVAL	Simple variable amplitude loading	
S O/L	Single overload	
σ	Applied stress in tension	MPa
σ_D	Applied stress in compression	MPa
σ_f	Fracture stress	MPa
σ_x, σ_y	Normal stresses in crack tip stress field	MPa

σ_{YS}	Yield Stress	MPa
σ_{UTS}	Ultimate tensile strength	MPa
γ	Surface energy	Joules
t	Thickness	mm
τ_{xy}	Shear stress in crack tip stress field	MPa
VNE	Velocity never exceed	knots
V_x	Crack voltage	Volts
V_y	Reference voltage	Volts
$(V_x/V_y)_o$	Reference voltage ratio	Volts
W	Specimen width	mm
Y	Compliance function	

1. INTRODUCTION

1.1 Fatigue Evaluation Regulations

In 1989 the Federal Aviation Administration (FAA) issued a change in the requirements for the design and fatigue evaluation of structures of transport category helicopters [1]. The changes to FAA Airworthiness Regulations, Part 29, Section 29.571 stated that all critical components and structures now have to be of damage tolerance design where previously they have been designed to be safe life. Damage tolerance design enables a component or structure to retain sufficient strength in the presence of a flaw or defect throughout the service life of an aircraft but with detectable changes in this condition to avoid catastrophic failure [2].

These airworthiness regulations now require helicopters to be, as far as practically possible, designed with damage tolerance principles as a first priority. The safe life design approach is only permitted as a last resort with consideration of geometry, inspectability and good design practice [1]. Conservative assumptions and adequate safety factors have previously been used to account for the uncertainties associated with the use of the safe life design approach. The disadvantages of these uncertainties for fixed wing aircraft were realised back in the early 1970's by the United States Air Force (USAF). Since then they have introduced the damage tolerance philosophy and the success of this for fixed wing aircraft and engines has resulted in substantial cost reductions in addition to improved safety and reliability. The damage tolerance approach to helicopters is examined in more detail in Chapter 2.

To this date no civilian helicopters have been certified using the new damage tolerance regulations and manufacturers mostly still use the traditional safe life design approach. This is because helicopters operate in very different fatigue loading environments to fixed wing transport aircraft which makes it difficult to design components to meet the requirements. The changes in regulations have provided a requirement to investigate new methods and techniques for designing helicopters against fatigue. This thesis contains an account of an investigation into the fatigue loads experienced by helicopters and their effect on the damage tolerant properties of helicopter structural materials.

1.2 Investigation of Damage Tolerance Design for Helicopters

GKN Westland Helicopters Ltd. (GKN WHL) design and build transport category helicopters including the new Westland/Agusta EH101. Although the EH101 obtained civil certification using the safe life approach to fatigue evaluation there is a need for GKN WHL to demonstrate damage tolerance capabilities in line with the new regulations for current and future variants of the helicopter. Technologies relating to the damage tolerant design of helicopters were limited when the regulations were introduced so to comply with these will require the development of new methods. Hence, in 1994 GKN WHL initiated a project to investigate the issues related to the damage tolerance design of helicopters [3]. The project was set up as a Department of Trade and Industry (DTI) Link Project between the partners: GKN WHL, the Defense Evaluation and Research Agency (DERA), nCode International and Cranfield University. Within the bounds of the DTI project there was an opportunity to investigate the growth of fatigue cracks under typical helicopter loading conditions and to determine the effects of variations in helicopter loading sequences on crack growth rate behaviour. Some of the work performed in this investigation provided data for the DTI Project and where appropriate data from other members of the project group has been included in this work for analysis.

Past attempts to apply damage tolerance methodology (primarily developed for large fixed wing aircraft) to helicopter components have encountered two typical problems: (i) the application of damage tolerance methods to the life extension of previously safe life designed helicopters (ii) the application of damage tolerance methods to new design of transport helicopters.

Both issues include the problems of complex geometry, stress states and crack growth trajectories typical of helicopter components. Generally most helicopter structures have one main load path and so there is little opportunity of a redundant, fail-safe design. Helicopters also have a more complex load history due to the higher frequency and range of small vibratory loads. It is these vibratory loads which may contribute to rapid fatigue crack growth of existing flaws during flight.

Generally, there is a lack of comprehensive fatigue testing for helicopter airframe structures because most testing is done on rotor system components [5,6] or to support the safe life substantiation method [4]. As a result there is little information available on airframe stress and strain data for identification of critical stress areas or for the development of a stress-time loading spectrum. The identification of a critical location in a component by stress analysis is usually augmented with knowledge of service problems and full-scale fatigue tests which are also lacking. These are significant differences which exist between fixed wing and helicopter damage tolerance design but they are expected to change as rotorcraft manufacturers engage damage tolerance design for new helicopters.

1.3 Investigation of Helicopter Load Sequence Variations

The areas of fatigue crack growth that are relevant to helicopter structures are in the near-the-fatigue-threshold and high stress ratio (minimum stress/maximum stress) cycle regions. These are primarily driven by the type of loading which helicopter structures experience: Typical loading spectra are dominated by large numbers of high mean stress vibratory load cycles which are superimposed on the steady state and manoeuvre stresses. The effects of these on the near-threshold fatigue crack growth behaviour is relatively unknown. The vibratory cycles typically make-up 90% of the fatigue loads in a helicopter loading spectrum and so if they do not contribute to fatigue damage at operating or test stress levels then they can be removed and considerable time and cost savings can be made during analysis and component testing. Conversely, they may contribute to the growth of a flaw and so crack growth may be rapid and so compromising the structural integrity of the helicopter. Knowledge of the behaviour of these vibratory cycles would provide an accurate means to determine inspection periods and to ensure that the helicopter service life is achieved without premature failure due to fatigue.

The work described in this thesis had three main objectives:

(1) To develop a helicopter fatigue loading sequence for a primary load path component and to investigate fatigue crack growth under complex variable amplitude loading. This required definition of a method for representing the flight loading cycles in a component fatigue loading sequence.

(2) To investigate crack tip growth mechanisms through measurement of crack closure and growth rate transients under simple variable amplitude loading - particularly at high stress ratios and at near threshold crack growth rates. This includes an understanding of the load interaction effects which occur at a crack tip.

(3) To investigate omission of vibratory loads and the effect of this on fatigue crack growth using the helicopter fatigue loading sequence. Understanding the effects will contribute to development of more accurate models for helicopter damage tolerance design.

These points are summarised in the following sections as introductions to the chapters of this thesis.

1.3.1 Development of Helicopter Stress Loading Sequence

To determine the role of the vibratory loading cycles on fatigue crack growth damage, a standardised loading sequence was developed for a GKN WHL Lynx AH Mk9 helicopter main rotorhead. This is shown in Figure 1.1. The prototype rotorhead is manufactured from the titanium alloy Ti-10V-2Fe-3Al (Ti1023).

The development of the loading sequence is an adaptation of the procedure used in the development of the standardised loading sequences Helix and Felix [5,6]. Most aspects of the Helix/Felix method, such as the complicated mission and manoeuvre sequencing, were retained except for the original strain data taken from a location on the rotorhead during flight testing. This and other differences between Felix and the loading sequence are discussed in Chapter 5.

Figure 1.1 Lynx helicopter showing location of the rotorhead used in this investigation. (Courtesy of GKN Westland Helicopters Ltd.)

1.3.2 Development of Automated Crack Length Measurement System

The need to measure small changes in crack length due to testing of near-threshold growth rates meant that the design of a sensitive crack length measurement system was required. A high resolution, custom designed direct current potential drop (DCPD) crack length measurement system was designed for this purpose and is described in Chapter 6 and Appendix B.

1.3.3 Experimental Fatigue Investigation

A fatigue testing program was devised to address the previous objectives. All crack growth rate tests were performed on standard compact tension specimens manufactured from Ti1023 and the aluminium alloy 7010 T73651 (7010). Ti1023 was used because this is the material from which the main rotorhead mast is manufactured. The lower strength 7010 was used to compare the effect of yield strength differences on load interaction effects between the two alloys. 7010 is an alloy typically used in the manufacture of helicopter fuselage structures. The testing undertaken in this thesis is separated into two areas:

(i) Simple Variable Amplitude Loading
(ii) Complex Variable Amplitude Loading

The simple variable amplitude loading (SVAL) tests were designed to investigate the crack tip mechanisms occurring under simple overload events applied during constant amplitude loading. They are described in detail in Chapter 6.

The investigation of SVAL crack growth comprises of several overload types including single overloads, interacting overloads and overloads followed by underloads. The test loads were selected to approximate the near-threshold crack growth loading conditions found in helicopter components. Additionally, two techniques of fatigue crack closure measurement were used to investigate the changes in levels of closure occurring during the transient fatigue crack growth rates resulting from the overloads. The mechanisms proposed to be controlling transient fatigue crack growth rates under SVAL are discussed in Chapter 8.

The complex variable amplitude loading (CVAL) tests were designed to investigate the contribution to fatigue damage of the small vibratory cycles contained in the rotorhead fatigue loading sequence. Fatigue tests were performed at realistic stress levels and the results of these and the consequences on fatigue crack growth modelling for helicopter damage tolerance design are discussed in Chapter 8.

2. FATIGUE EVALUATION OF HELICOPTER STRUCTURES

2.1 Background

The structural integrity of helicopter components under dynamic loading has usually been maintained by the initiation based, safe life approach which requires that a component is free of fatigue cracks and is safe to fly until retirement time is reached [7]. However, in reality operational experience indicates that some failures are caused by the growth of cracks originating at flaws from either existing manufacturing defects such as scratches and tool marks, or from in-service damage sites such as corrosion pits or maintenance damage. The main failure of the safe life design approach for fixed wing aircraft is that it did not properly account for the possibility of these "rogue" defects in the structure [4].

To overcome the deficiencies in the safe life method the United States Air Force (USAF) developed the damage tolerance approach in the early 1970's to ensure increased levels of structural integrity in their fixed wing aircraft [8]. Since then, the USAF has had some success in applying the damage tolerance philosophy to fixed wing aircraft which is now a firmly established process for maintaining safety in their aircraft as military specification MIL-A-83444 Aeroplane Damage Tolerance Requirements [9]. The damage tolerance approach is based on component inspection at pre-determined intervals derived from a fracture mechanics assessment of the component. The approach maintains the overall safety and reliability of a component by a combination of the inspection intervals and prescribed replacement times which are longer than the current safe life replacement times [4].

2.2 Design Against Fatigue Damage

Over the last decade there has be a shift in favour of the damage tolerance approach to helicopter fatigue evaluation by the military and civilian regulatory authorities. Subsequent to the experiences of the USAF, the Federal Aviation Authority (FAA) and Joint Airworthiness Authority (JAA) substantially revised their regulations in 1989 for the fatigue design of helicopter structures [1]. These now state that the structure must be designed in compliance with a flaw tolerant design unless this cannot be achieved within the limitations of geometry, inspectablity or good design practice [1]. If this is the case then a fatigue evaluation using a safe life design can still be used.

There are several routes which can be taken: These fatigue design methods are termed safe-life, flaw tolerant safe-life (enhanced safe life) and fail-safe design considering flaw growth as described in FAA Advisory Circular (AC) 29.571 [2].

The safe life design method is based on the Palmgren-Miner linear damage accumulation method where no initial flaw is assumed to exist in the structure. The flaw tolerant safe life design method is based upon the capability of a flawed structure to sustain, without measurable flaw growth, the spectrum of operating loads expected during the lifetime of the aircraft or within a prescribed replacement time. The fail safe design method is based upon the capability of a flawed structure with an initial crack or a detectable crack to sustain the spectrum of loads expected during an inspection interval whether it be an inspection threshold or inspection period.

For purposes of this thesis, the term "damage tolerance" is defined as the fatigue evaluation method which uses fracture mechanics for the prediction of slow flaw growth as defined in AC 29.571 [2]. This method is generally applicable to a fail-safe design considering flaw growth methods such as multi-load path design, flaw arrest features and slow flaw growth. The fail-safe design method does not always imply analysis using slow flaw growth but explicitly requires consideration of fatigue damage from flaws until cracks are detected during an appropriate inspection of the part. The crack growth curve and terminology for a single load path structure is given in Figure 2.1.

An essential requirement of damage tolerance design is the ability to predict the growth of a flaw and to provide guidance for inspection, so as to ensure that initial damage will grow at a stable, slow rate under service environment and not achieve a size large enough to cause rapid unstable propagation [9]. See Figure 2.1. The airframe structure, with flaws present, has to maintain satisfactory strength, deformation and stiffness during slow crack growth [10].

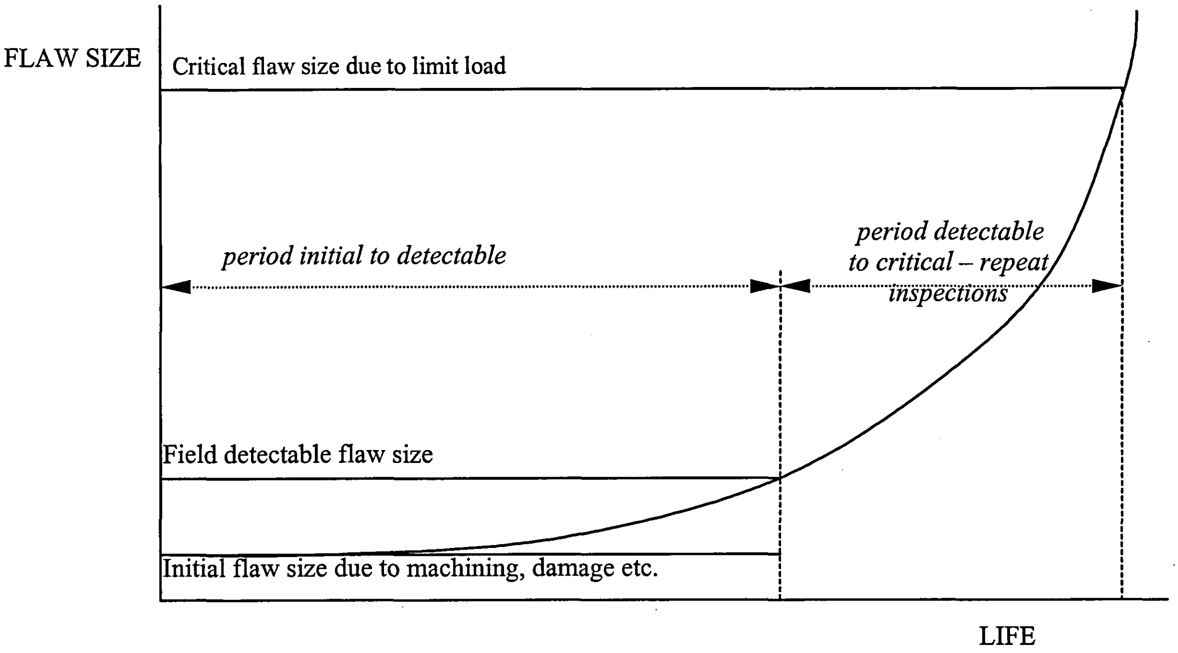

Figure 2.1 Crack growth curve and inspection periods for single load path structure.

2.3 Deficiencies of the Safe Life Method

Despite the successes of damage tolerance applied to fixed wing aircraft, all current designs of transport helicopter (military and their civilian derivatives) have mostly been substantiated against fatigue using the safe life method. The damage tolerance design method is considered to be generally superior to the safe life design method for the following reasons:

1. The stress-life (S-N) curve used by the Palmgren-Miner linear damage accumulation method is based on component or specimen tests which are usually constant amplitude in nature, whereas the operational loads of a helicopter are quite complex [11].

2. The Palmgren-Miner rule does not account for load interaction effects of cycles and as a result is not unconditionally valid. This is especially important for ground-air-ground (GAG) cycles and manoeuvre loads [7]. Where the Palmgren-Miner rule has given unconservative results the damage summation is not always carried out to unity and as a result a service life or replacement time is prescribed much lower than the calculated fatigue life.

The load spectrum used in a safe life analysis is based on an assumed mission profile and measured flight loads. The uncertainties of each are of an entirely different nature:

3. The mission profile is based on the expected future use of the helicopter usually defined by the procurement agency. The calculated fatigue life is always related to the assumed mission profile which is usually conservative in the first instance and different to that experienced in reality [7].

The calculation of a fatigue life varies significantly between helicopter manufacturers as demonstrated by the American Helicopter Society (AHS) round robin predictions on a helicopter pitch link [12] in which life predictions varied by as much as ten times. Most of the variations were attributed to the method by which each manufacturer treated the S-N curves.

2.4 Damage Tolerance Methods for Helicopters

The application of the fail-safe design considering flaw growth procedure to the damage tolerance analysis of helicopter components can not simply be translated from the well established methods of damage tolerance design used in fixed wing aircraft. There are several important differences between the fixed wing and helicopters which impact on the design process [13]:

1. Highly variable nature of the loading experienced by a component due to a wide variety of manoeuvre loads and ground-air-ground cycles.

2. Large numbers of vibratory load cycles due to revolution of the main rotorblades.

3. Complex components usually manufactured from high strength materials. This is usually advantageous for a safe life design but might have undesirable fatigue crack growth properties. The complex geometries usually result in complex stress states and crack path trajectories.

Various helicopter manufacturers have attempted to apply damage tolerance design to current and new helicopters. The approaches and experiences of some helicopter manufacturers with damage tolerance design are summarised below:

A retrospective damage tolerance analysis performed by Schneider of Sikorsky [14,15] on an existing safe life designed transport helicopter highlighted several problems due to the uneconomical inspection periods they predicted. This was due to the very small critical crack sizes, particularly in rotor and transmission components. Sikorsky believe that Non-

Destructive Inspection (NDI) of 0.005-0.010 inch cracks may be required for some rotor components and that some airframe parts may require reliable inspections for 0.030 inch cracks. This could be achieved by using NDI technologies borrowed from the jet engine industry but could be very expensive if required for airframe inspections [15].

The Sikorsky study also showed that there were extreme inconsistencies for a component that was originally safe lifed and subsequently analysed using crack propagation predictions. For example a tail rotor component had a ten hour crack propagation period from a 0.127 mm flaw to a critical crack size even though it had a recommended component replacement time of 11,000 hours [4]. This crack size has been attributed to the high operating stresses of some safe life designed components and the detrimental affect of these on crack growth thresholds and propagation.

Van Etten and Keary of Kaman [16] applied an enhanced safe life type approach to the design of engine mount fittings on a naval helicopter. This requires that the applied stress intensities for existing flaws are always below the fatigue threshold, ΔK_{th} during the service life so the flaw will not grow and no special inspection is required. Kaman successfully demonstrated that a 0.010 inch initial flaw could exist in the structure, without propagation, under conservatively estimated service loads. The design had a 10% weight increase over the fail safe designed fittings but this was offset by there being no need for special inspections as was found in other investigations [17,18].

Marquet and Struzik of Eurocopter [19] provide a good summary of the deficiencies in the technologies required for achieving a damage tolerant design for helicopter structures. Two of these important points are addressed in this thesis are:

- Lack of understanding of fatigue crack growth in the near-threshold region.
- Lack of understanding of load interaction effects in helicopter load sequences and in particular the effect of the ground-air-ground (compressive loading) cycle on fatigue crack growth.

3. MECHANISMS OF FATIGUE CRACK GROWTH

3.1 The Energy Approach

Theories of fracture analysis are based on the work of Griffith who formulated a criteria for the static fracture of a crack in a brittle solid in terms of a balance between changes in mechanical and surface energies. Griffith postulated that for unit crack extension to occur under the influence of the applied stress, the decrease in potential energy of the system must be equal to the increase in surface energy (γ) due to the crack extension. This concept was later modified by Orowan and Irwin by including plastic work in the surface energy term, calling the resultant G. The strain energy release rate, G is equivalent to the rate of decrease of the total potential energy with respect to unit crack length per unit thickness [20]. The fracture stress, σ_f can be expressed as:

$$\sigma_f = \left(\frac{EG_{IC}}{\pi(1-\nu^2)a} \right)^{1/2} \qquad \textbf{\textit{Eqn. 3.1}}$$

Where, E is the elastic modulus, a is the crack length and ν is Poisson's ratio. G_{IC} is the critical strain energy release rate for unstable fracture.

The Griffith concept provided the basis for the physics of fracture but its energy balance considerations cannot be directly applied to most engineering components because it usually requires an experimental determination of G. Although the Griffith fracture theory regards fracture from an energy viewpoint, the conditions for the growth of flaws can also be formulated in more precise terms by means of linear elastic stress analysis.

3.2 Linear Elastic Fracture Mechanics (LEFM)

3.2.1 Crack Tip Stress Field

Linear elastic fracture mechanics (LEFM) is the stress analysis of cracked bodies which relies on the concepts of elastic theory. The two main principles on which the theory of elasticity is founded are that (i) the stresses should be in equilibrium and (ii) the deformations produced by these stresses must be such that elastic and plastic continuity is maintained throughout the body. The deformations should not cause discontinuities in the continuum and the material obeys Hooke's Law.

To describe the conditions of stress and strain in an elastic body containing a crack, a solution must be found that satisfies the elasticity conditions and also the boundary conditions (applied loads) appropriate to the problem being considered. Airy first demonstrated that a stress function could exist for a two-dimensional deformation and showed that equilibrium equations are satisfied [20]. Westergaard then defined a stress function that satisfied the equilibrium and elastic continuity conditions for bodies containing a sharp crack by examining the properties of a particular type of complex function and determined which boundary conditions would be suitable for these properties [20]. The solution only holds in the close proximity of the crack and gives an infinite stress at the crack tip.

3.2.2 The Stress Intensity Factor

By considering the analysis of Westergaard, the stresses in the vicinity of the two-dimensional crack tip under a bi-axial tension stress σ_g, can be expressed in the following form [20]:

$$\sigma_x = \sigma_g\left(\frac{a}{2r}\right)^{1/2} \cos(\theta/2)(1-\sin(\theta/2)\sin(3\theta/2)) + \text{non-singular terms} \qquad \textbf{\textit{Eqn. 3.2}}$$

$$\sigma_y = \sigma_g\left(\frac{a}{2r}\right)^{1/2} \cos(\theta/2)(1+\sin(\theta/2)\sin(3\theta/2)) + \text{non-singular terms} \qquad \textbf{\textit{Eqn. 3.3}}$$

$$\tau_{xy} = \sigma_g\left(\frac{a}{2r}\right)^{1/2} \cos(\theta/2)\sin(\theta/2)\sin(3\theta/2) + \text{non-singular terms} \qquad \textbf{\textit{Eqn. 3.4}}$$

where r and θ are the radius from the crack tip and polar angle respectively for a polar co-ordinate system as given in Figure 3.1. and a is the crack length. Near to the crack tip the first term in the series dominates giving for instance:

$$\sigma_y = \sigma_g\left(\frac{a}{2r}\right)^{1/2} \qquad \textbf{\textit{Eqn. 3.5}}$$

As r tends to zero near the crack tip, σ_y will tend to infinity for purely elastic materials. For real materials, plastic yielding will occur, and a plastic enclave or zone will be formed at the crack tip. Outside the plastic zone, elastic stress fields will prevail, and providing small scale plasticity exists, Equation 3.5 predicts the near tip stress fields. If Equation 3.5 is written:

$$\sigma_y = K(2\pi r)^{-1/2} \qquad \textit{Eqn. 3.6}$$

where $K = \sigma_g (\pi a)^{1/2}$

K is termed the stress intensity factor and under small scale plasticity (linear elasticity) characterises the rate of approach to the crack tip singularity. K is a function of the remote stress field and crack length, as well as geometry of the component.

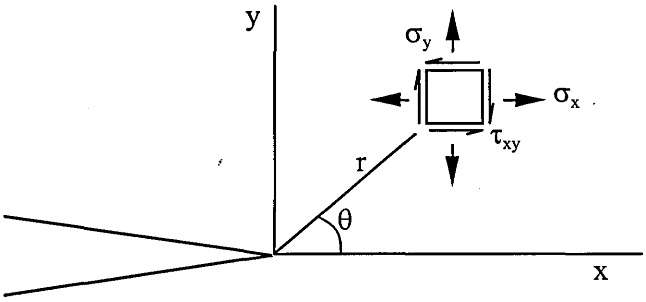

Figure 3.1 Crack tip stresses for polar co-ordinate system

The stress intensity factor approach to fracture analysis has the advantage over the energy approach because it is possible to determine the conditions for static fracture by calculating K through knowledge of loading and geometry. However, substitution of the expression for K into the Orowan /Irwin expression leads to the equations:

$$G = K^2/E \quad \text{for plane stress} \qquad \textit{Eqn. 3.7}$$

$$G = \frac{K^2(1-\nu^2)}{E} \quad \text{for plane strain} \qquad \textit{Eqn. 3.8}$$

where E is the elastic modulus and ν is Poisson's ratio.

This equivalence implies that the LEFM approach to the analysis of fatigue crack growth is able to be related to the Griffith energy approach using the above equations. The relationship between fatigue crack growth and K is introduced in Section 3.5.

Equations similar to Equations 3.2 to 3.4 can be written for the crack tip region stress field corresponding to the displacements induced along the crack surface in tension (Mode I), in-plane shear (Mode II) and anti-plane shearing (Mode III) respectively as shown in Figure 3.2. Hence, K_I, K_{II} and K_{III} are the stress intensity factors pertaining to the three modes of crack tip deformation. The work undertaken in this thesis is mostly concerned with the Mode I tension loading.

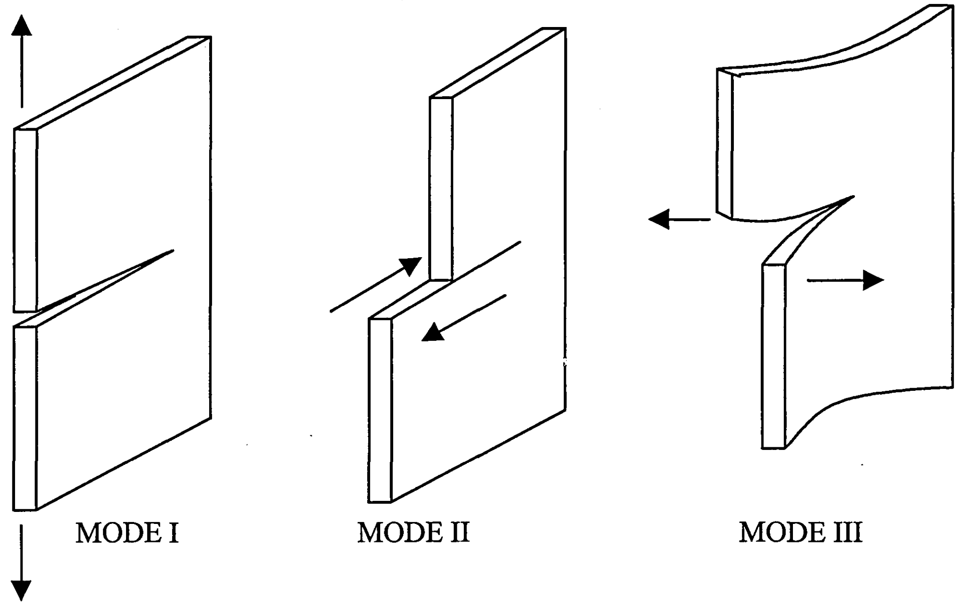

Figure 3.2 The three modes of crack tip deformation: Mode I - tensile, Mode II - in-plane shear, Mode III - anti-plane shearing.

An important feature of the stress intensity factor is that cracks in different bodies with the same K have the same stress distribution as described by Equations 3.2, 3.3 and 3.4. If material properties of two different bodies containing cracks are identical then the stress and deformation distributions in elastic regions are presumably identical. This is not usually the case because stress and strain distributions in separation prone material require plasticity treatments for reasonable accuracy [21].

In general, stress intensity factors for most engineering applications are usually expressed as:

$$K = Y(a/W)\sigma\sqrt{\pi a} \qquad \textbf{\textit{Eqn. 3.9}}$$

where *Y(a/W)* is a dimensionless geometrical scaling factor that is given a value or is a function of the characterising crack length, *a* and characterising dimension, *W* for a particular geometry. The stress intensity factor can be readily determined from known values of the remotely applied stress, σ and the crack length, *a*.

3.3 Crack Tip Plastic Zone

The stress field described by the stress intensity function Equation 3.6 gives an infinite stress as *r* tends to zero which is known as the crack tip singularity. The stresses near the crack tip are limited by the local yielding of the material over a region of the crack tip known as the crack tip plastic zone. The plastic zone size establishes a boundary indicating the region over within which deviations from elastic behaviour occurs [21]. Figure 3.3 shows the distribution of the stress field, under monotonic loading, described by LEFM up to the plastic boundary at which point the stress level is limited by the local yield stress of the material.

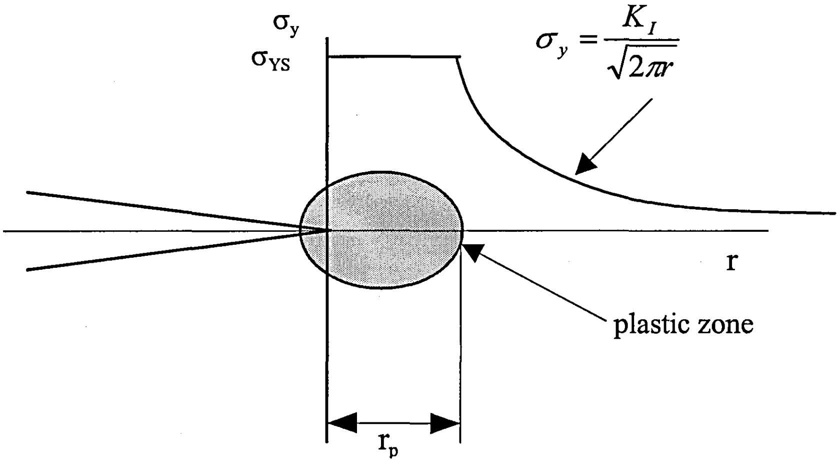

Figure 3.3 Crack tip plastic zone size showing stress field limited by the material yield stress σ_{YS}

3.3.1 Size of the Crack Tip Plastic Zone

The influence of yielding is to effectively extend the crack some distance ahead of the crack tip, with yield stresses σ_{YS} acting to restrain the extended crack surfaces. The computation is then elastic and the plastic zone size is determined as the length r_p which defines the extent of the plastic yielding. For the Mode I the small scale yielding solution for the crack tip elastic singularity leads to the plastic zone size given by Dugdale [22]:

$$r_p = \frac{\pi}{8}\frac{K_I^2}{\sigma_{YS}^2} \approx 0.392\frac{K_I^2}{\sigma_{YS}^2} \qquad \textit{Eqn. 3.10}$$

Equation 3.10 refers to the plane stress plastic zone size. For conditions of plane strain the triaxial stress field constrains the size of the plastic zone because of strain restraints in the through-thickness direction. The result is that the effective yield stress in plane strain can be up to three times as high as the uniaxial yield stress [20]. The general plastic zone size is given by:

$$r_p = \frac{\pi}{8}\frac{K_I^2}{(\alpha\sigma_{YS})^2} \qquad \textit{Eqn. 3.11}$$

Where α is termed the constraint factor and can have values from 1 for plane stress to 3.0 for plane strain using the definition by Newman [23]. For a thick body the plastic zone size will be larger at the free surface, where plane stress condition prevail, than in the centre where plane strain conditions occur.

3.3.2 Shape of the Crack Tip Plastic Zone

Dugdale assumed that the crack tip yield zone is limited to an infinitesimally thin strip of material along the crack front [22]. Other treatments of the plastic zone size along the *x*-direction give the plastic zone shape as circular. In reality the plastic zone shape is somewhat more complex and can be obtained by the yield condition for θ-angles different than zero. The boundary of the plastic zone can be estimated by imposing the Tresca or Von Mises criterion for yielding at different values of angle θ in Equation 3.3 and solving for the r at which yield occurs [20].

3.4 Elastic-Plastic Response to Cyclic Loading

The monotonic residual stress distribution ahead of the crack changes character under the influence of cyclic fatigue loading. During cyclic unloading from a maximum stress intensity factor, K_{max} to a lower level, say K_{min}, there is a compressive or reversed plastic zone embedded in the plastic zone [21]: The material ahead of the crack tip at K_{max} is plastically deformed but after unloading to K_{min} it still has to fit into the surrounding elastic material. The elastic material resumes its original size but the material in the plastic zone does not. The elastic compressive stresses build up until the compressive yield stress in the plastic zone is reached and a zone of reversed, plastically flowed material is formed with compressive residual stresses.

The changes in stresses due to the load reduction are then given by a solution identical to that for original monotonic loading (Equation 3.9) but with the loading parameter replaced by the stress intensity reduction, ΔK and the yield replaced by $2\sigma_y$. Hence the stresses have the correct magnitude and direction in the reversed zone when the changes due to load reduction are subtracted from the distributions corresponding to the original monotonic loading [21].

For unloadings K to K-ΔK and reloadings K-ΔK to K, the reversed plastic zone size and cyclic variations in stress, strain and displacements depend only on the load fluctuation ΔK [21]. The size of the plane stress reversed plastic zone is given by Equation 3.12 and shown in Figure 3.4.

$$r_{p\_rev} = \frac{\pi}{8}\frac{\Delta K_I^2}{(2\sigma_{YS})^2} \qquad \textbf{\textit{Eqn. 3.12}}$$

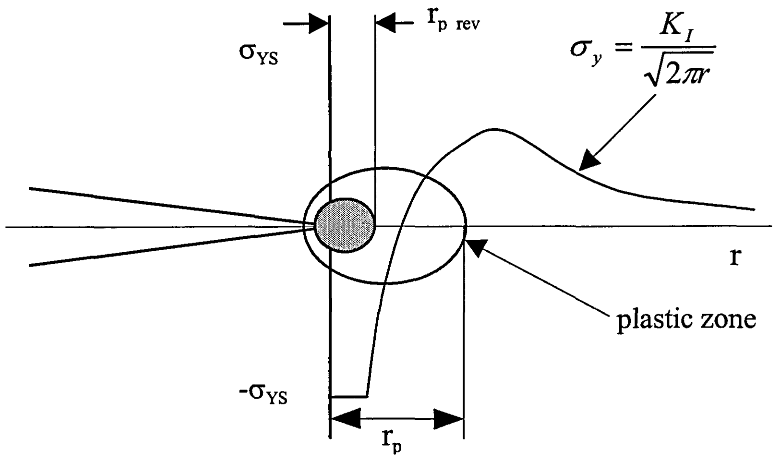

Figure 3.4 Reversed plastic zone with residual stress distribution at minimum load

3.5 Constant Amplitude Loading Fatigue Crack Growth

The types of crack growth considered in this thesis are long cracks with growth rates ranging from near-threshold to fast fracture. Such macrocracks can be analysed using LEFM and so the K concept can be applied to correlate fatigue crack growth with externally applied cyclic loading. The LEFM treatment of fatigue crack growth was proposed by Paris and Erdogan [24] who gave the following equation for fatigue crack growth rates under constant amplitude loading (CAL):

$$\frac{da}{dN} = C\Delta K^m \qquad \textit{Eqn. 3.13}$$

Where m and C are considered to be fitting parameters and ΔK is the stress intensity factor range defined as:

$$\Delta K = K_{\max} - K_{\min} \qquad \textit{Eqn. 3.14}$$

where K_{max} and K_{min} are the maximum and minimum stress intensity factors respectively given by Equation 3.9.

The Paris Law is a power law relationship which implies the growth rate, da/dN is a linear function in a log da/dN versus log ΔK sense. See Figure 3.5. However, the power law relationship usually only occurs over a narrow band of ΔK and other material properties tend to cause the da/dN versus ΔK relationship to have a sigmoidal shape as shown in Figure 3.4. These material properties are the fatigue threshold and fracture toughness (which is also geometry dependent).

The fatigue threshold (ΔK_{th}) is defined as the material property which is the largest excursion of the stress intensity factor range which does not produce fatigue crack growth under any loading condition [6]. At the other extreme is the very rapid increase in growth rates as K_{max} approaches a critical stress intensify factor called the material fracture toughness (K_{IC}).

Several other factors negate the use of the Paris Law to correlate da/dN with ΔK as a linear relationship beside ΔK_{th} and K_{IC}. For example change in the mean load level result in a shift in the growth rate curves. Hence da/dN is not only a function of ΔK but also the stress ratio, R ($R=K_{max}/K_{min}$). However, the most significant diversion of da/dN from the Paris Law is caused by abrupt changes in applied load level as discussed in the following section.

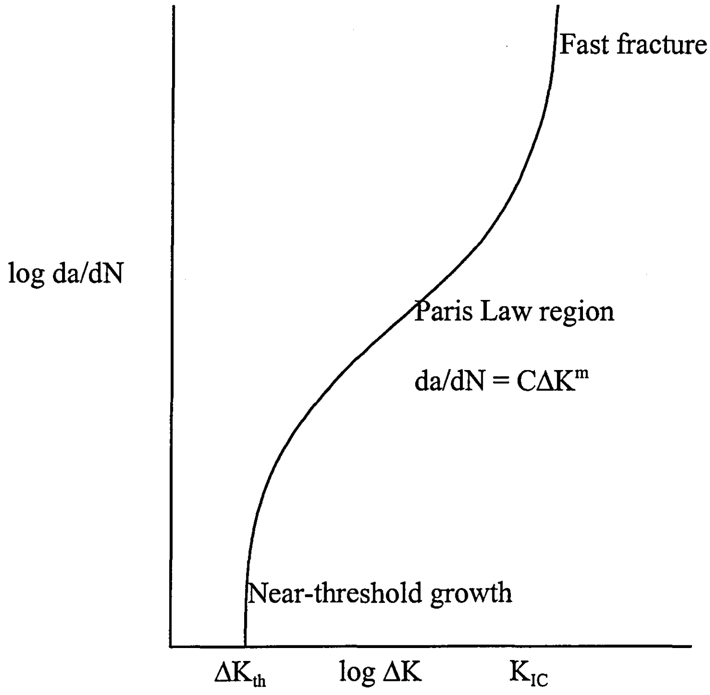

Figure 3.5 Variation of fatigue crack growth rates with ΔK

3.6 Fatigue Crack Growth under Simple Variable Amplitude Loading

Generally, most engineering components are subject to loading that is variable in nature rather than steady constant amplitude loading. Variable amplitude loading can range from simple overloads applied during constant amplitude loading to complex variable amplitude loading such as that experienced by a component in an aircraft. It has been well experimentally documented that a simple tensile overload results in a typical transient response in fatigue crack growth rates as described below and illustrated in Figure 3.6:

(1) Steady state crack growth rate at constant amplitude load levels before overload.
(2) Crack growth during overload cycle - increment of crack growth by ductile tearing during overload.
(3) Initial accelerated crack growth.
(4) Delayed retardation of crack growth or immediate retardation if acceleration at (2) is absent.
(5) Crack arrest or gradual return to steady-state, pre-overload growth conditions.

Although the transient responses to fatigue crack growth following load level changes are well known and occur under most simple variable amplitude loading conditions, the actual mechanisms that cause the response are not yet clearly understood. An understanding of the mechanisms is important so as to provide accurate calculation of fatigue crack growth in aircraft components.

Many researchers [23,25-30] have examined crack growth responses due to single or multiple tensile overloads and various concepts have been proposed to account for mechanisms of crack growth including: (a) crack closure due to plastic deformations in the wake of the crack [23,31], (b) residual stresses ahead of the crack tip resulting in an increase in the size of the compressive residual stress zone by the overload [27,28,32], (c) crack tip blunting of the crack tip due to the overload [25], (d) crack deflection where the overload event causes a change in crack path and results in mixed mode loading at the crack tip [25,26], and (e) strain hardening from either monotonic hardening of material in the overload plastic zone following tensile overloads or cyclic hardening following block loading [33].

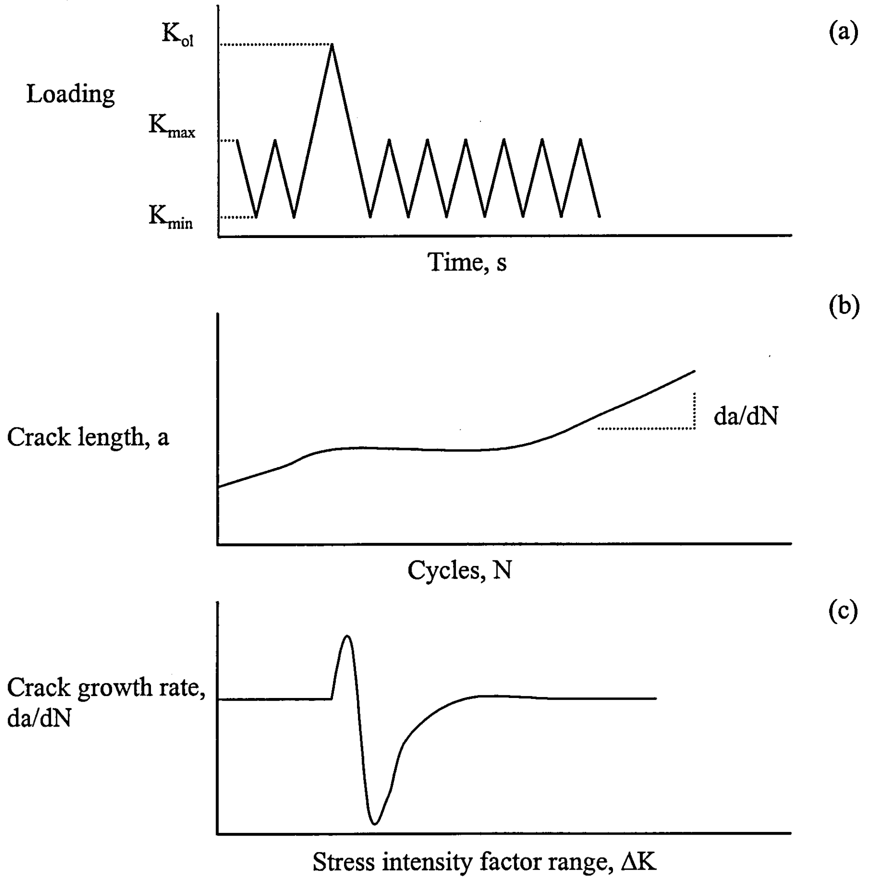

Figure 3.6 Typical response to tensile overload (a) during constant amplitude loading. Crack growth rate affected after application of overload (b) and crack growth rate response showing delayed retardation (c).

Of the proposed mechanisms, the role of the residual stress field ahead of the crack tip and the effect of crack closure in the wake of the crack are generally accepted as providing a good basis for rationalising many of the effects. For example, advanced residual stress models and crack closure models can predict delayed retardation observations [23,34,35]. Most of the evidence for these mechanisms have been gathered at medium to high growth rates, under predominantly plane stress conditions and at low stress ratios, R (R=minimum cycle stress/maximum cycle stress). Contrasting the research in general literature is the behaviour of transient growth rates in the near-threshold crack growth region, underloading in the tensile region and crack growth at high R ratios typical of the loading which helicopter components experience.

Characterising fatigue crack growth processes requires an understanding of fatigue crack tip stress-strain fields including residual stress fields. Closure studies have placed attention on residual stresses behind the crack tip. However, residual stresses still develop within the forward plastic zone when crack closure does not occur. Both the residual stresses and those arising from plasticity induced crack closure are a deciding factor in fatigue crack growth rates [36].

3.7 Fatigue Crack Closure

On the supposition that a crack cannot propagate when it is closed, because there are no changes in stresses ahead of the crack, Elber [31] proposed the effective stress intensity range, ΔK_{eff} is given by:

$$\Delta K_{eff} = K_{\max} - K_{cl} \qquad \textit{Eqn. 3.15}$$

where K_{max} and K_{cl} are the maximum and closure stress intensity factors respectively. Refer to Figure 3.7.

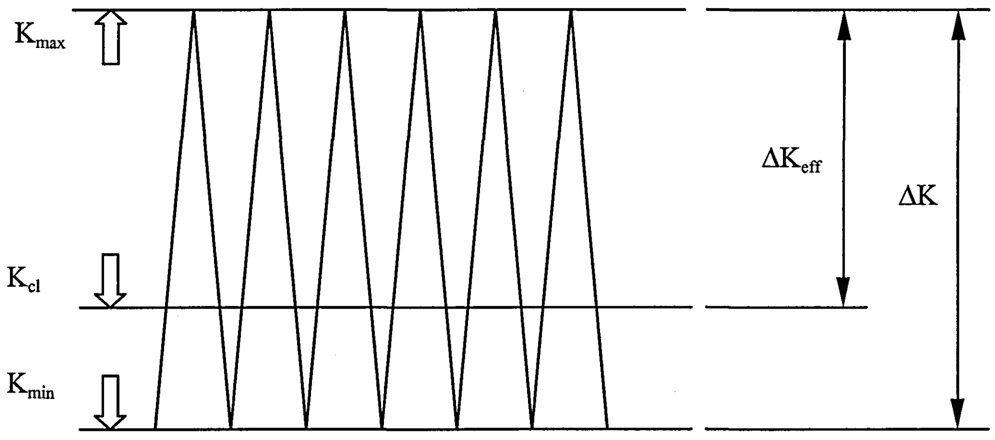

Figure 3.7 Definition of crack closure and the effective stress intensity factor range

Elber [31] suggested that the permanent residual tensile displacements perpendicular to the crack surface due to plastic deformation at the crack tip could result in contact between the fracture surfaces in the wake of the crack, even under tensile externally applied loads. This form of closure is generally referred to as *plasticity induced closure* and forms the basis of many fatigue crack growth prediction models [23,35]. However, crack closure can generally result from any phenomena that causes premature closure of the fracture surfaces such as oxide layers [26], roughness induced closure [25,26] resulting from mis-matching of the mating surfaces or stress-induced phase transformation closure.

With the introduction of the crack closure concept many fatigue crack growth phenomena were able to be explained (qualitatively at least) such as: mean stress (R ratio) variations during constant amplitude loading, transient fatigue crack growth following an overload and fatigue thresholds [37].

3.7.1 Observations of Crack Closure

3.7.1.1 High Stress Ratio Loading

A large majority of research conducted into variable amplitude loading concentrate efforts on observing or determining crack closure at low to medium R ratios. This is either due to the difficulty of observing crack closure at high R ratios ($R \geq 0.5$) [28] or that very few engineering applications need closure descriptions at high R ratios. The loading environment of helicopter structures necessitates an understanding of crack growth mechanisms at high R ratio. However, current closure based models [23,35] do not provide for the existence of crack closure at high R ratio. Additionally the closure models do not adequately explain observations of transient fatigue crack growth behaviour at high R ratios [28,30,32,36,38].

An example of this is where closure was not observed using near crack tip or global measurement methods at an R ratio of 0.5, although there was evidence of crack growth retardation [40]. Previous papers assumed that if closure was not measured during overload events at high R ratio, even though transient effects were observed, then it must be attributed to other mechanisms such as crack tip blunting branching or the formation of residual stresses ahead of the crack tip [39]. Marci and Lang [32] state that observed load interaction effects at high R ratio need an explanation other than crack closure which is only negligible at high R ratios and a combination of plasticity induced closure and crack tip residual stresses is responsible.

Tsukuda et. al. [38] through numerical analysis have shown that closure is present at high R ratios. Finite elements (FE) analysis of cracked specimens at $R \geq 0.5$ has shown that plasticity induced closure can exist. They compared experimental levels of K_{cl} with observed crack growth rates and did not find a good correlation. However, a good correlation was observed between crack growth rates and ΔK_{eff} obtained from FE analysis for $R \geq 0.5$. The difference is due to plasticity induced closure being confined to an area close to the crack tip such that measurement is very difficult using conventional compliance methods.

3.7.1.2 Compressive Loading and Underloading

The effect of tensile overloads on fatigue crack growth rates has received much attention although very little has been paid to the effect of compressive loading and tensile underload excursions. Usually, it is common to ignore the contribution to crack growth from compressive loading and so for a negative stress ratio, R cycle the stress intensity factor range, ΔK is set equal to the maximum stress intensity factor, K_{max}. A review of papers on compressive loading and compressive load excursion by Carlson and Kardomateas [41] found that several recent investigations have concluded that is it incorrect to ignore compressive load excursions (by setting them to zero) as compressive load cycles do contribute to crack growth.

Topper and Yu [42] found that intermittent compressive underloading caused the 'squeezed' crack tip to have a decreased compressive residual stress and a decreased crack closure stress. This significantly decreased the threshold stress intensity and increased the crack propagation rate. Zuidema et. al. [43] found that if a tensile overload is followed immediately by an underload then the retardation transient of the overload is significantly reduced or removed altogether.

Carlson and Kardomateas [41] attribute compressive excursion behaviour to a closure obstruction mechanisms. The crushing deformation of asperities or plastic deformation due to negative load excursions in the wake of the crack which reduces the subsequent closure level giving a corresponding increase in the effective stress intensity factor range. Observations of underload tests showed that even under maximum compression complete closure did not occur due to asperities in the crack wake. A large compressive stress could then produce localised compressive yielding near the crack tip. Upon reloading there would be a larger tensile residual stress in front of the crack promoting accelerated growth rates.

A residual stress field explanation was offered by Zhang et. al. [33] who performed a numerical simulation (FE) to determine crack closure levels for an overload followed by an underload combination. A single overload-underload cycle caused reductions in the overload induced compressive residual stress and this reduces the retardation effect although the overload effect is not completely cancelled.

3.7.1.3 Loading Near the Fatigue Threshold

Near-threshold crack closure is important in two areas: (i) where cyclic loading gives ΔK values that approach the fatigue threshold values of the particular material and (ii) where crack growth transients give retarded growth rates which approach the fatigue threshold value. At near-threshold levels there are several factors such as microstructure, environment, loading conditions and crack length which significantly affect crack propagation rates [46].

It is well documented that microstructure influences fatigue crack growth and it effect is most significant at near-threshold growth rates when the crack tip plastic zone size approaches that of the local microstructure [26,44,45]. At low ΔK levels fatigue crack growth processes now change from a continuum mechanism to one which is dependent on local microstructure and LEFM is not always conditionally valid.

Near-threshold crack closure behaviour has been observed to be different to that at higher K levels. At near-threshold crack growth, normalised crack closure levels tend to decrease with increasing stress intensity factor whereas at higher grow rates the is generally no crack closure dependency on K [44].

Crack closure at low values of K may be driven not by crack wake plasticity but by crack surface roughness or oxidation [44]. At near-threshold growth rates the increasing grain size to crack increment proportion generally increases the resistance to crack propagation. As the R ratio of the near-threshold loading increases, the influence of grain size decreases [26].

Ritchie et al. [46] state that the existence of ΔK_{th} for long cracks is associated with the high level of crack closure, due to mechanisms involving wedging of oxides and fracture surface asperities in addition to plasticity induced closure, with values of $\Delta K_{eff}/\Delta K$ approaching 0.7. They found that by accounting for such closure by experimentally determining ΔK_{eff}, the influence of load ratio in affecting near-threshold growth rates was minimal. These observations all suggest a strong relationship between the microstructure and crack growth characteristics.

3.7.2 What Form of Fatigue Crack Closure?

Crack closure is now widely accepted as a real phenomenon with changes in crack closure levels being associated with the many variable amplitude loading fatigue crack growth effects. However, there is still no general agreement on the concepts of crack closure and the determination of the crack closure load [32].

The author believes there are three main reasons behind the disagreements of the crack closure levels:

(i) Determination of the location of closure in relation to the crack tip front and how this affects ΔK_{eff} is unclear. Crack closure is a three-dimensional phenomena which is affected by through-thickness stress states (plane stress and plane strain) which can significantly affect the level of closure measured [40] and the location of the measurement device does not give a unique indication of closure levels [47].

(ii) One form of crack closure is not always acting solely on its own and other forms may be occurring simultaneously in a synergistic manner.

(iii) Interaction of crack closure with the crack front residual stress field. Closure does not *cause* fatigue crack growth itself but modifies the stress-strain conditions at the crack tip which do cause fatigue damage.

A good discussion is given by McClung [44] where a large amount of experimental and analytical evidence is critically compared and evaluated. This work states that no single relationship between crack closure levels and the parameters of stress, crack length and K is found to hold universally because of the wide range of mechanisms which cause or influence closure [44]. It would be prudent to suggest that a unique level of crack closure will only exist for a specific combination of stress state, material and loading condition and that a fatigue crack growth model using the closure concept will only have limited applicability.

3.7.2.1 Three-dimensional Nature of Crack Closure

The thickness and states of stress under which a crack grows significantly influences the effective stress intensity factor at the crack tip. This section reviews the influence of specimen thickness on the material response to simple variable amplitude loading and the mechanisms which cause this.

Experimental evidence from Shuter and Geary [40] shows that delay effects due to a single overload are dependent on the specimen thickness with delay cycles and distances increasing with decrease in specimen width. Crack closure measurements made near the crack tip and remote from the tip during the overload tests showed that measured crack closure levels are different between each technique for thick specimens but become similar as the thickness decreases below 10mm [40]. These observations, supported by others [48,49], show that crack closure is predominantly a near-surface, plane stress phenomenon.

Mechanical methods such as machining away the specimen surfaces following an overload show that removal of the surfaces can significantly reduce the retardation effect of the overload [30,50]. Experiments designed to examine the form of closure obstruction following a tensile overload by machining surface areas close to the crack tip showed that upon resumption of loading no retardation transient was observed. McEvily and Yang [30] reasoned that most of the closure controlling the transient growth was located in the plane stress, surface region of the specimens.

Fleck [48] has shown from measurements of fatigue crack growth rates made in thick specimens, after an applied overload, that the response differs at the surface and interior. These differences in post-overload growth rate are related to the difference in plane strain state ahead of the crack tip in the specimen interior and the plane stress state at the surface. The effect of the growth rates was attributed to crack closure being greater in the plane stress region so that thin specimens displayed more retardation than thick specimens. Similar influences of constraint having a strong influence on fatigue crack growth and closure behaviour of metallic materials were observed by Newman using his FASTRAN model [51,52].

Three dimensional nature will also affect the measurement of closure as most closure measurement techniques employ displacement measurements taken from the surface of a test specimen. This is discussed later.

3.7.2.2 Plasticity Induced Crack Closure

The conventional effective stress intensity range approach uses the idea of plasticity induced crack closure which has been incorporated in many fatigue crack growth models [23,35]. As the crack propagates it is continually creating (and then growing through) a zone of plastically deformed material parallel to the loading direction. See Figure 3.8. This material is permanently deformed and will come into contact in the wake of the crack tip which is the crack closure point.

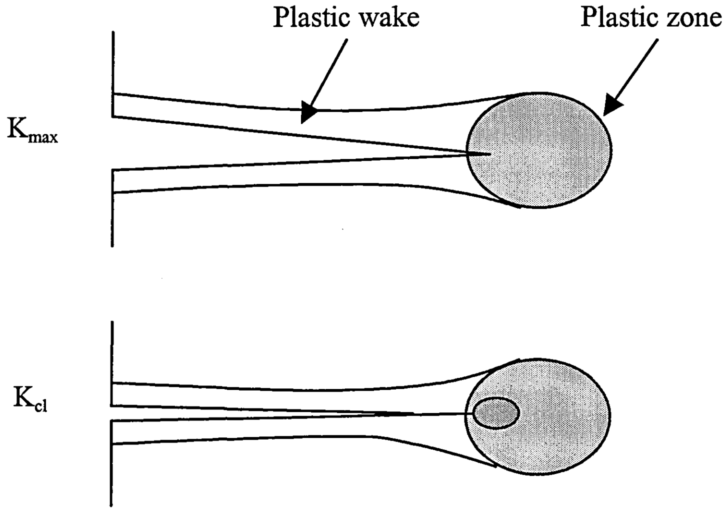

Figure 3.8 Plasticity induced fatigue crack closure

Plasticity induced closure offers an explanation for increased retardation effects on the surfaces of thick specimens [40]: crack tip plasticity generated by an overload results in additional material being transferred to the crack face from the specimen surface due to Poisson contraction effects. This increases the closure at the surface areas but not in the centre, plane strain region of the specimen where no strains in the z-direction can be generated. This suggests that plasticity induced closure is important only in plane stress situations.

Finite element investigations of plasticity induced crack closure by Sun and Sehitoglu [36] showed that closure occurred under plane strain conditions but the resulting residual displacements were confined to a short distance behind the crack tip. Other numerical simulations [28,38] have also shown that the extent of plasticity induced closure under plane strain occurs over a very short distance. Reduced crack closure in plane strain was also explained by reduced contribution of residual material in crack wake. Under plane strain the contraction of material in the transverse direction is small compared to plane stress near the free surface [36].

Shin and Fleck [53] state that plasticity induced closure is responsible for crack growth retardation under plane stress and high stress intensity values but that under plane strain, near-threshold conditions the retardation is due to strain hardening and residual stresses ahead of the crack. Where crack growth occurs over a range of stress states (through thickness) and stress intensity factors it is likely that several forms of closure will act to obstruct the cyclic load conditions at the crack tip.

3.7.2.3 Influence of Microstructure - Roughness Induced Closure

Suresh states that plasticity induced crack closure does not play a major role in some crack growth retardation transients, particularly under plane strain conditions [26]. Therefore, there are some mechanistic processes in addition to plasticity effects that contribute to crack growth retardation. Experimental evidence [26] indicate that during Stage I propagation mechanisms result in faceted fracture features and an irregular surface morphology which is accompanied by a Mode II displacement even under nominally Mode I external loading. The occurrence of Mode II displacements during the post-overload growth region provide a mechanism for further reduction in ΔK_{eff} due to premature contact and sliding of the fracture surfaces. This is termed 'roughness induced closure'.

During transient crack growth following an overload, it is important to note that the micro-roughness mechanism does not initiate the process of retardation but only prolongs crack growth attenuation once Stage I fatigue mechanisms are activated in the post-overload zone by residual compressive stresses, crack branching and possibly closure in the crack wake of the advancing crack front [25]. While residual compressive stresses are known to play an important role in reducing effective stress intensity values over distances of the order of the reversed plastic zone due to the overload, the retarded crack growth distance could be up to an order of magnitude larger than the extent of the reversed plastic zone directly ahead of the crack tip [26], especially under plane strain conditions.

Post-overload crack advance is strongly influenced by the micromechanisms of near-threshold fatigue crack growth. The microstructure of an alloy is known to affect the transient growth rates following an overload event through the process of roughness induced closure [29]. A larger effective grain size structure results in some crack deflection and crack-path meandering which in turn promotes roughness induced crack closure. It is most effective where the size of the wedges is comparable to crack-tip-opening displacements such as at low ΔK levels or ΔK_{th} [25]. In coarse grained polycrystals cracks may propagate perpendicular to the loading axis in a macroscopic scale, but microscopically they propagate along crystallographic planes [52]. The corresponding crack path depends on the orientation of each grain in front of the crack tip. Generally Mode II and partially Mode III, in addition to Mode I, contribute to K and it is difficult to use the ΔK_{eff} concept based on plasticity induced closure alone [52].

3.7.3 Role of Crack Tip Residual Stress Fields

While most crack closure studies concentrate on residual stresses in the wake of the crack, residual stresses ahead of the crack tip develop due to the plastic zones undergoing monotonic and cyclic loading which have an important consequence on transient fatigue crack growth.

Damri and Knott [30] performed single tensile overloads on a low carbon steel, with subsequent stress relieving through heat treatment. They found that at both high and low R ratios (0.2 and 0.6) the residual compressive stress field ahead of the crack tip appears to be the primary mechanism for crack growth retardation. At R=0.6 the retardation effect was absent following the stress relieving process and this was attributed to the removal of the residual stresses.

Davidson [27] states that transient growth rates result from a combination of the residual stress surrounding the crack tip and the elongation of the material in the crack wake caused by irreversible deformation as the crack tip passes through the residual stress field during growth. Recently, this approach has been refined by numerous numerical FE analyses [28,36,38]. Sun and Sehitoglu [36] maintain that the residual stresses evolve from two contributions:

(1) Residual stresses due to reversed deformation in the absence of crack closure,

(2) Residual stresses due to the crack closure phenomena.

For an ideal 'closure free' crack the residual stress originates from the reversed plasticity at the crack tip whereas a fatigue crack will have added residual stresses due to plasticity induced crack closure in the wake of the crack. The study of the influence of residual stresses on transient fatigue crack growth rates is based on determining the stress intensity factor at which the crack tip first becomes tensile, denoted K_{PR} which is the 'crack propagation stress intensity factor' [54]. This is not necessarily the same point at which K_{cl} occurs. Hence the effective stress intensity factor can now be defined as:

$$\Delta K_{eff,PR} = K_{\max} - K_{PR} \qquad \textit{Eqn. 3.16}$$

This concept was used by Tsukuda et. al. [38] who found that a good correlation with crack growth rate and $\Delta K_{eff,PR}$ was obtained between test and FE analysis for high R ratio constant amplitude loading. It seems reasonable that the crack growth rates can be characterised by $\Delta K_{eff,PR}$ because it provides a basis for determining load interaction effects at high R ratios where closure measurement is deficient. Further work by Tsukuda et. al. [28] employed the concept under overload simple variable amplitude loading. The transient behaviour of K_{PR} was explained by changes in stress distribution at the minimum applied stress which is closely associated with the development of the plastic zone formed ahead of the crack tip as it grows through the overload plastic zone. They also found that transient crack growth behaviour following single tensile overloads at high R ratios was substantially different from that at low R ratio. The differences were well correlated by analysing the results with $\Delta K_{eff,PR}$.

The study by Sun and Sehitoglu [36] demonstrated differences in the crack closure and residual stress contribution to K_{PR} between plane stress and plane strain. They found from FE analysis that the residual stress contribution to K_{PR} was more significant in plane strain than in plane stress. On the other hand the crack closure contribution to K_{PR} was more significant in plane stress compared to plane strain which coincides with previous observations in Section 3.6.2.1.

The contribution of residual stresses to ΔK_{eff} as a primarily mechanism rather than crack closure provides the ability to rationalise observed load interaction effects at high R ratios: Marci and Lang [32] presented a model for crack tip residual stress fields which is divided into the plastic wake zone behind the crack tip and the plastic zone ahead of it. Although the processes behind the crack are separated from those in front of it the model is still based on the ΔK_{eff} concept. Instead of using the Elber concept of closure (contact in the wake), the point above which the active plastic zone is free of compressive stresses, K_{PR} is used in place of K_{cl}.

The model is based on the premise that a crack can only propagate if the stresses in front of the crack tip change from compression to tension. Hence the effective stress intensity factor range due to compressive residual stresses, $\Delta K_{eff, RCS}$ is given by:

$$\Delta K_{eff, RCS} = (K_{max} - K_{PR}) - \Delta K_{th} \qquad \textit{Eqn. 3.17}$$

The ΔK_{th} term is used here because there is a loading range which must be applied before the intrinsic threshold of the material is overcome [32]. The concept of crack closure is still used and is assumed to only be a reduction in the applied stress intensity factor ranged experienced by the crack:

$$\Delta K_{tip} = K_{max} - K_{cl} \qquad \textit{Eqn. 3.18}$$

The stress intensity ratio experienced by the crack tip is then:

$$R_{tip} = K_{cl}/K_{max} \qquad \textit{Eqn. 3.19}$$

The amplitude ΔK_{tip} is not the effective amplitude which drives the crack but only the applied amplitude ‘seen’ by the crack tip due to consideration of crack closure. The terminology of the concept is shown in Figure 3.9.

Experimental determination of K_{PR} by Lang and Huang [54] on centre cracked tension (CCT) 7475-T7351 aluminium alloy specimens found that a relationship exists for K_{PR} under constant and simple variable amplitude loading in terms of R_{tip} and K_{max}:

$$K_{PR} = f(R_{tip}) \cdot K_{max} \qquad \textit{Eqn. 3.20}$$

If no crack closure occurs then R_{tip} is the applied R ratio. The relationship should extend to materials other than 7475-T7351 aluminium alloy because similar residual stress fields occur if they exhibit typical elasticity and plasticity.

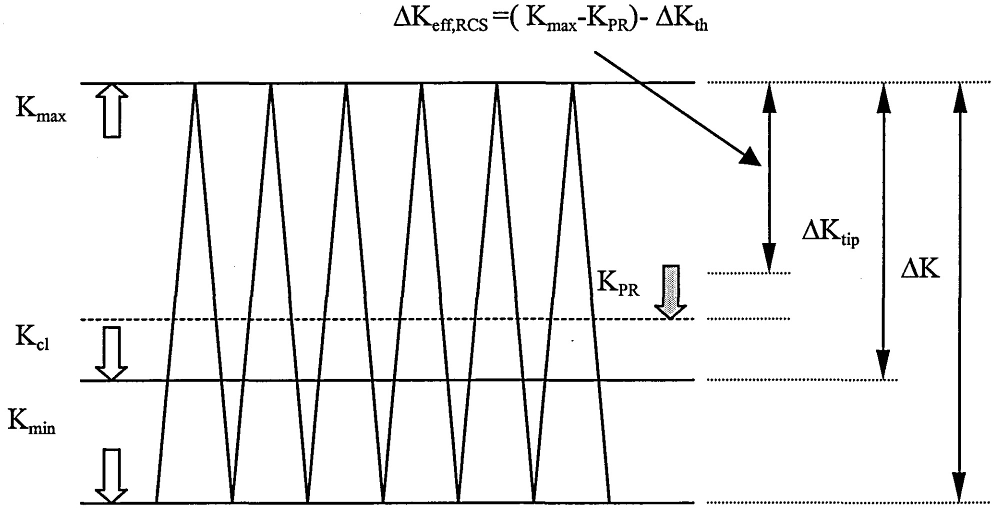

Figure 3.9 Crack propagation model proposed by Marci and Huang [54]

Marci and Lang [32] applied the method to constant amplitude loading in tension and in tension-compression for various R ratios and produced the following relationships:

$K_{PR} = (0.455+0.321R_{tip}+0.208R^2_{tip}) \cdot K_{max}$ ***Eqn. 3.21***

for tension-tension loading and

$K_{PR} = (0.448+0.367\cdot (\sigma_D/\sigma_{YS}) \cdot K_{max}$ ***Eqn. 3.22***

for tension-compression loading where the gross compressive stress (σ_D) to yield stress ratio is used instead of R_{tip}. As shown in Figure 3.10 the curves coincide reasonably well.

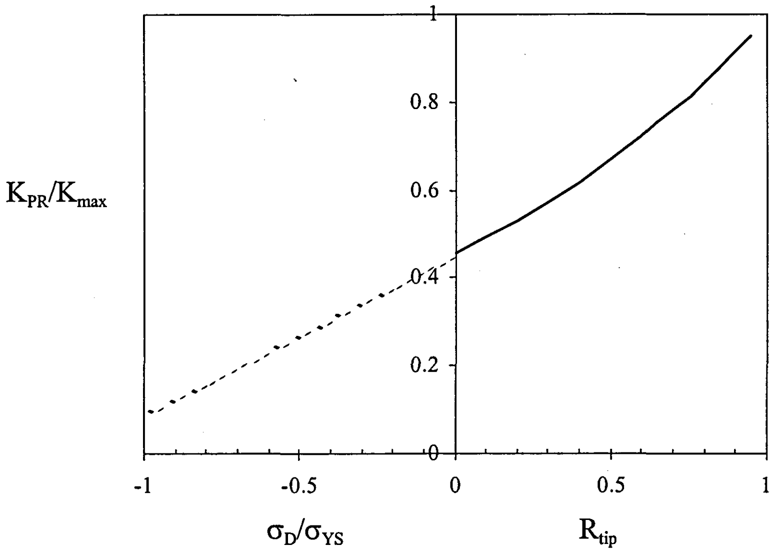

Figure 3.10 K_{PR} under constant amplitude loading for positive and negative R ratios using Marci and Lang [32] model

A relationship for single tensile underloads following a period of constant amplitude loading was also established, where the underloading ratio, UR ($UR=K_{UL}/K_{max}$) replaces both R_{tip} for the tension range and σ_D/σ_Y for the compression range [32]:

$$K_{PR} = (0.453+0.34\cdot UR+0.134\cdot UR^2+0.07\cdot UR^3)) \cdot K_{max} \qquad \textbf{\textit{Eqn. 3.23}}$$

The equation gives a curve which is almost exactly the same as both Equations 3.21 and 3.22. Hence the K_{PR} data after unloading following constant amplitude loading coincides very well with the curves shown in Figure 3.10. This is a significant observation which implies that K_{PR} depends only on UR and K_{max} and that the prior R ratio of the constant amplitude loading has no influence on K_{PR}. This is demonstrated in Figure 3.11.

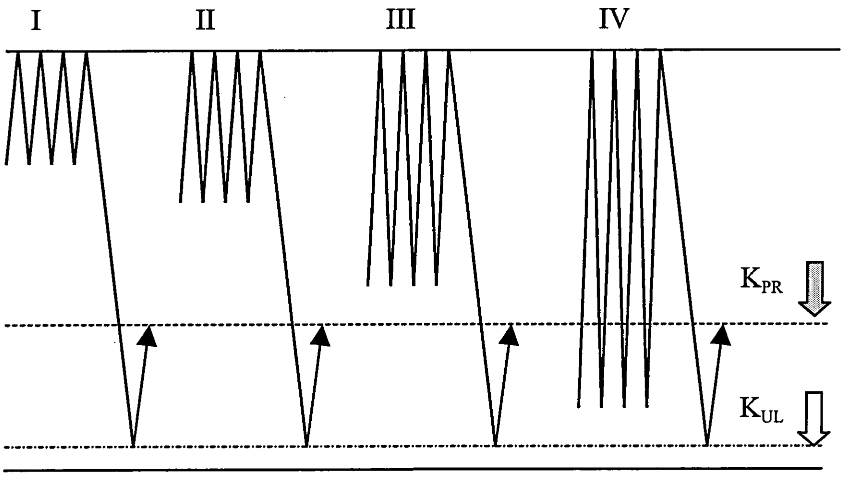

Figure 3.11 Marci and Lang model which implies that only the unloading ratio and K_{max} determines K_{PR} after constant amplitude loading.

The influence on K_{PR} of overloads to K_{ol} during CAL followed immediately by an underload to K_{UL} was also established for different unloading ratios, UR [32]. It was found that K_{PR} depends only on K_{ol} and the subsequent unloading ratio, UR and takes the following form:

$$K_{PR,ol} = (0.322+0.58\cdot UR+0.241\cdot UR^2-0.18\cdot UR^3)\cdot K_{ol} \qquad \textit{Eqn. 3.24}$$

Where $K_{PR,ol}$ is the crack propagation stress intensity factor after the application of the overload. This is shown in Figure 3.12 together with the underloading curve given by Equation 3.23.

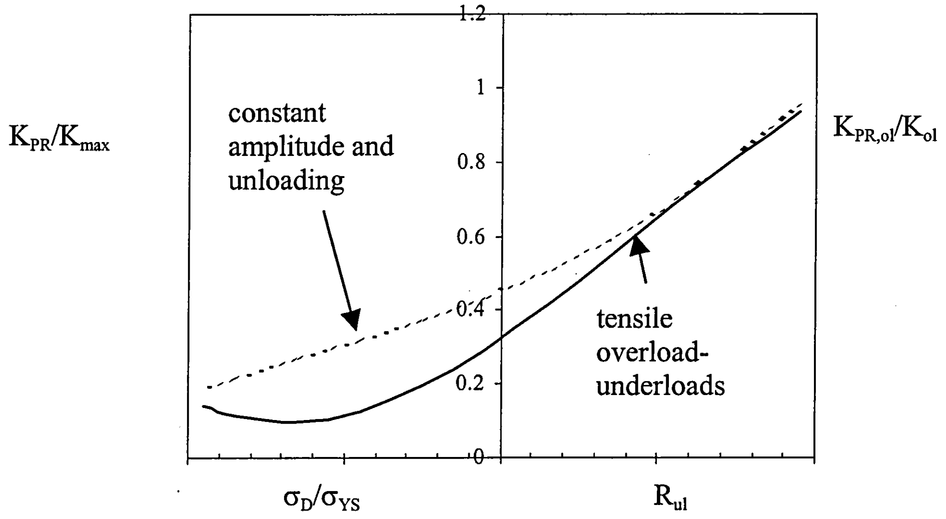

Figure 3.12 K_{PR} for constant amplitude loading with applied underloads and overload-underloads [32].

The model proposed, implies that a crack closure concept can not explain the instantaneous change in K_{PR} following loading events. Marci and Lang [32] suggest that a residual compressive stress mechanism is responsible where the stress level in front of the crack tip changes simultaneously with the remote loading. The model requires that closure is the mechanism which only controls applied remote loading and does not control the fatigue crack growth behaviour due to changes in load levels. This model is used in Chapter 8 to explain some experimental observations.

3.7.4 Measurement of Fatigue Crack Closure

A somewhat contentious issue in literature of fatigue crack closure is the measurement of crack closure. Many transient crack growth behaviours have been attributed to crack closure yet the definition and accuracy of what is 'crack closure' is still in doubt.

Studies examining the stress/strain distribution around the crack tip for a closure affected crack indicate that progressive contact of the crack faces means that the compliance characteristics below the first point of crack wake contact during unloading are non-linear [55]. Refer to Figure 3.13. This should give a convenient way of determining the crack closure level using compliance measurement techniques. However, the region of non-linearity is not always unambiguously associated with K_{cl}.

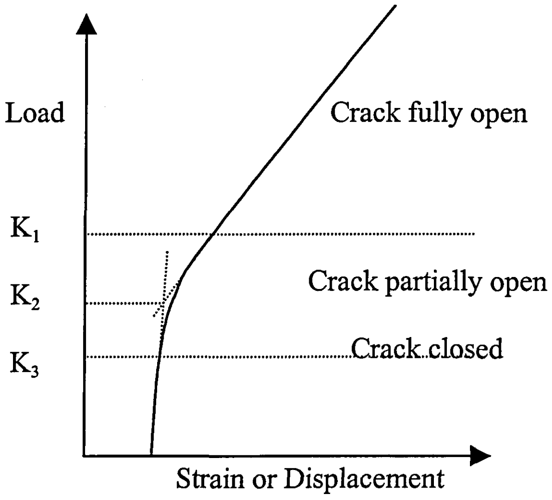

Figure 3.13 Typical compliance curve for loaded crack exhibiting crack closure

Some researchers consider the first point of non-linearity, K_1 as the closure load. Allison et. al. [56] assume the intersection of the tangential lines at K_2 to be the closure load so that a increasing level of crack tip obstruction is occurring as K_3 is approached. Other variations on the definition of the crack closure load include consideration of curve tangents [57] and slopes [58]. A comparison of two different closure measurements was made by Allison et. al. [56] where measurements of closure made using 'remote' compliance techniques (back face strain and crack mouth opening displacement gauges) gave equivalent measurements. However, they found that the level of closure determined through analysis depended strongly on the numerical procedure used.

Apart from inconsistencies in numerical methods used to determine closure the main problem which exists is the correlation of crack closure from different locations. A remotely positioned gauge is likely to measure a 'global' or averaged closure level. A gauge located close to the crack tip on the specimen surface where plasticity induced closure may predominate will measure 'local' closure levels which may only be an indication of the closure in the immediate vicinity. This raises the question on how to unambiguously determine a closure level to define ΔK_{eff}.

Most measurements of crack closure are based on mechanical compliance measurement of a cracked specimen and most methods suffer from accurate determination because of the location of measurement. Crack closure measurements have been made using a multitude of techniques and position. In compact tension specimen crack mouth opening displacement gauges or back face strain gauges [59] are commonly used. Small gauge length strain gauges may be placed close to the crack tip to increase measurement sensitivity [52]. A survey of different techniques and analysis techniques has shown that different values of closure can be determined depending on the method used [44].

Abdel Mageed et. al. [47] state that the value of K_{cl} depends on the measurement location and crack length. K_{cl} was found to decrease with increasing distance behind the crack tip. As the crack grows away from a fixed gauge its effectiveness will decrease. Through measurements of closure using a clip gauge close to the crack tip they also found that K_{cl} was a sensitive function of K_{max}, thickness and yield strength. Clerivet and Bathias [60] using aluminium 2024 T3 correlated crack growth retardation with variation in closure levels using a near tip gauge but were not able to observe a corresponding variation of closure with a centre-crack clip gauge.

Usually crack closure is not detected during fatigue loading at R ratios above R=0.5 when using conventional compliance techniques. This is due small compliance changes confined only near the crack tip and so mechanical compliance measurement have reduced sensitivity [38]

4. FATIGUE CRACK GROWTH UNDER COMPLEX LOADING

4.1 Loading Spectrum Variations and Effects on Fatigue Crack Growth

Observations of spectrum variations from fixed wing aircraft are reviewed here in light of the unique requirements for design of helicopter loading spectra. Variations in loading sequences for testing and modelling, such as small vibratory cycle omission, truncation of high peak loads and removal of compressive loads, can give indications on how these types of loads can effect crack growth rates. There is currently little information available on how these loading types effect crack growth under helicopter loading conditions but there exist similarities with investigations from fixed wing aircraft. For instance the work on cycle omission is mostly based on omission of cycles due to gust loading on transport aircraft wings [61] whereas the requirement for helicopters is the omission of vibratory cycles due to main rotor revolution. Studying fatigue spectrum variables gives an improved understanding of fatigue crack growth behaviour under flight simulation loading and the feasibility of sequence simplification.

4.1.1 Omission of low range cycles

Large reductions in testing time can be achieved by omitting low amplitude cycles below a certain stress cycle range from the loading spectrum. To do this safely without altering the fatigue damage, the stress range below which cycles are not damaging needs to be established. By conducting tests with various levels of omission of low amplitude cycles, the contribution of these cycles to fatigue crack growth can be determined.

Schijve [62] states that valid arguments about which small cycles can be omitted are not readily available and that omission criteria are more or less arbitrary. However, Sunder [63] states that omission criteria can be related to crack opening and threshold stress intensity factor, ΔK_{th} values. That is, a fatigue cycle range can be omitted provided it is below ΔK_{th} for the entire test. The criteria can be different for various specimen geometries and components because they are material thickness and yield stress dependent and changes in crack closure level can affect ΔK_{th}. The problem of deciding which small cycles to omit is further complicated by the variations in loading spectra for different structural components in a helicopter so a single omission criteria may not always be applicable.

Several other workers [61,64-66] have investigated the effect of small range cycle omission from fixed wing aircraft loading spectra. Schra and Wanhill [65] showed that the omission of small range cycles from miniTWIST gave varying effects for different aluminium alloys, but in general an increase in flights to failure was observed. This was due to damaging cycles being removed from the loading sequence and so an increase in life resulted. The observation of smaller omission level effects in an aluminium-lithium alloy, compared to a conventional aluminium alloy, was attributed to a higher level of crack closure occurring in this material when compared with a conventional aluminium alloy as the small cycles omitted are affected by crack closure levels [65].

The contribution of small range cycles in a truncated spectrum, where the high loads are reduced to a lower level, was significantly greater than in an un-truncated spectrum. This is due to the lower crack closure stresses in the small cycles for the clipped spectrum, which are attributed to the smaller peak load plastic zones [65]. No measurement of crack closure levels were attempted during these tests to confirm that the changes in omission levels effects could be attributed to closure.

Abelkis [66] found that where a cycle stress range is used as a cycle omission criterion for transport aircraft wing loading spectra, the optimum omission range for no effect on life was 9% of the peak stress for high strength aluminium alloys. By increasing the omission range to 16% of peak stress, a fivefold increase in the number of cycles to failure resulted.

Omission effects can also be different for plane strain and plane stress crack growth. Schijve et al. [64] found that an increase in crack growth life was not observed in thin sheet material (2mm, 2024-T3) loaded under FALSTAFF and short-FALSTAFF whereas longer lives were observed for 10 mm compact tension specimens subjected to the same sequences. In the latter case crack growth was occurring under predominantly plane strain conditions at the crack tip. Under these conditions plasticity induced crack closure is reduced, which suggests that small load cycles can be more damaging under plane strain conditions [64]. This is of significance to helicopter fatigue design as their construction usually gives thick cross-sections resulting in mainly plane strain stress states and the loading sequences are usually dominated by small vibratory load cycles.

4.1.2 Truncation of High Loads

Truncation is the removal or reduction of extreme or high tensile loads from a flight loading sequence. In stress spectrum testing, very high peak loads should be avoided in view of their beneficial effect on fatigue crack growth which could lead to unconservative results. An increase in the magnitude or frequency or both of high peak loads in a transport wing loading spectrum can produce retardation effects that result in crack propagation lives up to 3.5 time longer [66]. Reducing the extreme loads may result in reduced crack tip plasticity and so reduces crack closure levels.

Truncation effects are dependent on the relative number of high cycles in a fatigue sequence such as the difference between a transport wing (gust spectrum loading) and a fighter wing (manoeuvre spectrum loading) spectrum which have different effects on fatigue crack growth under truncation [62]. Truncation of test spectra should only be conducted if a real indication of maximum loads experienced during flight has been quantified by flight testing.

4.1.3 Clipping of Compressive Loads

Clipping of compressive loads in a flight loading spectrum is the removal of the compressive part of a load cycle so that the minimum load is increased to zero. As explained in Section 3.6.1.2 compressive load cycles can result in an increase in crack growth rates. If a component experiences significant compressive loading during its lifetime then these should be included in the test load spectrum. Clipping of compressive loads below zero from a transport aircraft wing spectrum can result in a 37% increase in component test life [66]. Removal of these loads by clipping could result in unconservative crack growth test results if used to verify damage tolerance design methods. Compressive load cycle clipping should be done carefully, with consideration of the crack growth rate accelerations that compressive loads can cause.

4.2 Crack Closure under Complex loading

The above observations of crack growth rate changes under complex loading can be explained by variations in the level of crack closure. Although crack closure is a real phenomenon, there exist difficulties in modelling it under spectrum loading because of the complexity of the three-dimensional nature of the crack front in real components and the continual variation in the plastic-zone size among other factors. Nevertheless observations of closure have been used to approximate crack closure and subsequently used to obtain a ΔK_{eff} for crack growth rate calculations.

Various researchers have investigated how crack closure varies during a complex loading sequence. Newman [23] investigated crack closure behaviour during flight simulation loading using a strip yield model and found that closure levels follow an irregular pattern while cyclic loads are applied and these tend to oscillate about a mean value. This justified the use of an "equivalent" crack closure stress over a small crack increment which greatly reduces the computational time of the FASTRAN model.

Kim and Song [67] performed experimental crack closure measurements using a random loading sequence and found that the crack closure load fluctuates only slightly during a random loading block. The fluctuation was so small that they assumed the closure levels to be constant under random loading. The crack closure level was found to be dependent on the largest load cycle in the loading sequence because the growth increment per loading block is smaller than the monotonic plastic zone size due to the largest load cycle [67]. This was supported by Sundar [68] who states that spectrum loading crack closure is controlled by the extreme peak loads if the peaks are applied sufficiently frequently.

Specimen thickness can have an important effect on crack growth rate properties under flight simulation loading. Wanhill [69] observed increases in crack growth rates under miniTWIST with increasing specimen thickness. These observations are attributed to the state of stress surrounding the crack tip due to different specimen thicknesses which affect the level of crack closure. In thinner, plane stress specimens the crack tip plastic zones due to peak loads are considerably larger, implying increased plasticity induced crack closure, which produces increased crack growth retardation. The effect of retardation due to peak loads is lesser in thick plane strain stress state specimens [69]. Where the peak loads occur frequently and the crack is quasi-stationary[†], crack closure levels due to changes in load levels may remain relatively constant, agreeing with previous observations. Where the high peak loads occur infrequently in the a loading sequence there may be discrete retardations of crack growth rates so the crack closure level may change significantly throughout the test.

[†] The loading sequence repeats within the maximum plastic zone or the repeated major peak loads occur within the previous peak load plastic zone size.

Observations of crack closure under complex loading generally agree that crack closure levels remain relatively constant for most complex loading conditions. Where measurements of closure are made, they are a function of the measurement position and crack length as explained in the previous chapter. The subjectivity of closure measurements and the extension of observations to fatigue crack growth predictions brings into question the applicability of ΔK_{eff} as a suitable parameter to describe loading conditions at a crack tip in a real structure. Nevertheless, the ΔK_{eff} approach is seen as the best estimate and many models use this method for crack growth rate calculations as explained below.

4.3 Prediction of Fatigue Crack Growth under Complex Loading

4.3.1 Types of Fatigue Crack Growth Prediction Models

The prediction of fatigue crack growth under complex variable amplitude loading (CVAL) is a very complex procedure. Numerous models, mostly developed for aeronautical applications, have been presented over the last twenty-five years. Some provide accurate results under specific material and load conditions but a model with general applicability does not yet exist. Although simple load interaction effects are reasonably well understood the task of quantitative predictions of growth under CVAL with complex load interaction effects is still a difficult task.

Most prediction models calculate fatigue crack growth under complex loading on a cycle-by-cycle basis using a crack growth equation, so that the total predicted life is a summation of all the crack growth increments of each load cycle. Crack growth models require three basic inputs: (1) Loading data in the form of a cycle-by-cycle stress loading sequence (2) material data usually in the form of da/dN versus ΔK over various R ratios, fatigue thresholds and fracture toughness and (3) geometry data which relates the loading and geometry to the stress intensity factor at the crack tip in the form of a compliance solution (Equation 3.6).

How a model uses these inputs to predict fatigue crack growth increments depends on the concept of model used. Generally, models can be divided in two groups, namely the yield zone models, such as the Wheeler [70] and Willenborg [71] models, and the more complex analytical crack closure models such as STRIPY [35] and FASTRAN by Newman [23].

The yield zone models predict the acceleration and retardation of crack growth under CVAL by reducing the crack growth rate or stress intensity factor range by analysis of the extent of the residual stress zone created by previous overloads [70,71]. The amount of retardation depends on the ratio of the current crack tip plasticity to the previous plasticity. These semi-empirical models are usually based on fitting parameters for material and maximum spectrum stress so they do not have general applicability. Recent models, such as Kraken [34], have modified the Willenborg model so that it is generally applicable to all loading sequences and materials and can analyse crack tip plastic zone interactions for complex loading sequences.

The crack closure models are based on the Elber [31] concept of closure which employs an effective stress intensity factor at the crack tip. These models are based in the premise that crack growth is not only controlled by the residual stress fields ahead of the crack tip but also the residual plastic deformations left on the crack faces as the crack grows. Hence the models calculate the level of crack closure at the applied minimum load and the resulting ΔK_{eff} is used by the crack growth equation to calculate the crack growth increment on a cycle-by-cycle basis. The ΔK_{eff} is considered the similitude parameter which assumes a correlation between crack growth under constant amplitude loading and variable amplitude loading.

Some crack closure models are based on the concept of plasticity induced crack closure where a Dugdale [22] type analysis of the residual stress fields ahead of the crack tip is used to define the elastic-perfectly plastic deformations occurring at the crack tip. These 'strip yield' models were first developed by Dill and Saff [72] and later by Newman [23] and de Koning [73]. As the crack tip advances under external loading the crack tip deformations are left in the wake of the crack as permanent residual deformations, which preserve the previous loading history (modelling load interaction effects). These are used to calculate the minimum load at which crack face contact occurs for ΔK_{eff} calculation. Crack closure and crack opening are assumed to be equal and are defined by the load at which the region immediately behind the crack tip is last to open. Strip yield models have proved to be the most reliable crack growth prediction method in a comparison of various CVAL predictions models by Lazzeri et al. [74].

Crack closure models should be able to calculate a unique crack closure load for a given geometry, material and applied load. In addition, the generation of a crack length dependent plastic wake would results in a crack opening load that would vary with crack length. Various researchers [23,36,37,44] have shown that crack closure levels are dependent on crack length and K_{max} so the models should be able to accurately predict these effects in a quantitative way. A modified plasticity induced crack closure model [75] showed crack opening loads as a function of crack length with crack closure loads reducing with increasing crack length.

The crack tip plastic wake involves a geometry dependent interaction between the extent of crack tip plastic deformation at the maximum load and the degree of reversed plasticity associated with the unloading process which provides for a prediction of stress ratio effects. Crack closure models have been shown to adequately predict stress ratio effects and can predict the effects of additional overloads in a periodic spectrum [35,76].

Crack closure models are usually computationally intensive so they are often simplified to efficiently predict spectrum loading crack growth lives although recent advances in computing speed no longer holds this as a disadvantage. For instance the Esacrack model described below simplifies the crack closure under block loading to a set of analytical equations derived from analysis of crack growth in a centre cracked panel [77] based on the analytical observations of Newman [23].

4.3.2 European Space Agency Crack Growth Model - Esacrack

The Esacrack crack growth model was originally developed by the European Space Agency (ESA) to analyse damage tolerance properties of space structures. This program was based on the NASA/FLAGRO (NASGRO) software for predicting fatigue crack growth but without the ability to predict load interaction effects. The model is essentially a linear summation of the fatigue crack growth increments due to cyclic loading blocks of N cycles.

4.3.2.1 Crack Growth Relationship

The Esacrack model performs fatigue crack growth rate equations using the NASGRO 2.0 equation [77]:

$$\frac{da}{dN}=\frac{C(1-f)^n\,\Delta K^n\,(1-\frac{\Delta K_{th}}{\Delta K})^p}{(1-R)^n\,(1-\frac{\Delta K}{(1-R)K_c})^q} \qquad \textbf{\textit{Eqn. 4.1}}$$

Where *da/dN* is the crack growth rate

R is the stress ratio

ΔK is the applied stress intensity factor range

C, n, p and q are empirical constants

f is the crack opening function described below

K_{IC} is the material fracture toughness

ΔK_{th} is the fatigue threshold stress intensity factor range given below.

There are options in the software for the method of describing the constant amplitude crack growth rate input data, including the full Forman equation, the variables in which could be considered as fitting parameters for model optimisation.

4.3.2.2 Fatigue Crack Closure

The Esacrack program incorporates plasticity induced fatigue crack closure by using an equation which calculates the effect of the stress ratio on fatigue crack growth rates under constant amplitude loading. The crack closure function f describes plasticity induced crack closure under constant amplitude loading and has been defined by Newman [23] as:

$$f = \frac{K_{cl}}{K_{\max}} \qquad \textbf{\textit{Eqn. 4.2}}$$

and is an empirical function of the stress ratio, R and the material yield stress. Details of these functions are given in Ref. [77]. The closure function is not used to calculate fatigue crack closure changes due to load interaction effects nor does it model other closure effects such as oxide or roughness induce crack closure.

4.3.2.3 Fatigue Threshold

The fatigue threshold stress intensity factor range is approximated as a function of the stress ratio, R and the threshold stress intensity factor range at R=0, ΔK_O, the crack length a and the intrinsic crack length a_o, given by the following empirical equation:

$$\Delta K_{th} = \Delta K_O \left[\frac{4}{\pi} \tan^{-1}(1 - R) \right] \left(\frac{a}{a + a_O} \right)^{-\frac{1}{2}} \qquad \textit{Eqn 4.3}$$

where a_o accounts for the short crack effect and is given a default value of 0.102 mm. The end part of Equation 4.3 becomes unity at long crack lengths and is sometimes omitted.

4.3.3 European Space Agency Strip-Yield Model – Stripy

4.3.3.1 General Description

To improve the predictions of the Esacrack software, the Strip-Yield model (Stripy) of de Koning and ten Hoeve [78] was incorporated into it by NLR, Netherlands in 1993. This model is based on plasticity induced crack closure and allows load interaction effects to be accounted for by modelling the plastic deformation near the crack tip [78]. Since the original version was incorporated, several modifications have been made to the Strip-Yield model including plane strain to plane stress transitions during crack growth and variable constraint factor behaviour near the crack tip which have improved the accuracy of the model. [79].

4.3.3.2 The Crack Growth Laws

The description of crack growth under constant amplitude loading is given by the ΔK_{eff} concept and uses the NASGRO 2 (Equation 4.1) crack growth law to predict the crack growth increment per block [79]. The crack closure function f in Equation 4.1 for the constant amplitude load cycles in a block of a spectrum is calculated from K_{cl} using the Strip-Yield model as described below. When using the original non-retardation crack growth model option in Stripy is selected the empirically based Newman equation for the crack closure is used [79]. Failure usually occurs when K_{max} exceeds the fracture toughness, K_c of the material. The stress intensity range at threshold, ΔK_{th} is given by Equation 4.3.

4.3.3.3 The Crack Closure Model

The strip yield model calculates plasticity induced crack closure by employing a method first proposed by Dugdale [22] which calculates the stress and plastic deformation around a loaded crack. It considers the material to act as a series of elements behaving in a rigid plastic manner within an infinitely thin strip located along the crack line. This crack tip strip is divided into a number of discrete bar elements which are used to represent the plastic deformation ahead and behind the crack tip. As the fatigue crack progresses through the material, the elements which were ahead of the crack tip become surface contact elements and can only carry compressive loads as shown in Figure 4.1. Crack growth is assumed to proceed along the crack line and is obtained by disconnecting the strip over a distance corresponding with the amount of calculated growth. When the crack has grown, a plastically deformed layer is left in the wake of the crack to simulate plasticity induced crack closure [35].

The crack closure stress S_{cl} is determined from the element stresses along the crack surface following a minimum load using the method developed by Newman for the FASTRAN strip yield model [23]. The underlying equations and explanations of the calculation of closure in Stripy are given in more depth in Ref. [73]. Using the stress intensity solution for the component, the value of σ_{cl} is converted into the crack closure stress intensity factor K_{cl} and substituted into Equation 4.1 to calculate the crack growth rate.

The size of the plastic zone is defined by the Dugdale model and is an important factor when modelling the extent of load interaction effects:

$$r_p = \frac{\pi}{8}\left(\frac{K}{\alpha\sigma_0}\right)^2 \qquad \textit{Eqn. 4.4}$$

Where α is the constraint factor which is supposed to simulate three dimensional effects of uniaxial tensile strength variations through the thickness but it is mostly considered to be a material fitting parameter to the crack growth law. The value for α varies from 1.15 for plane stress to 3.0 for plane strain stress states.

4.4 Data Fitting to the ESA Models

The material parameters for the NASGRO 2.0 equation used by the Stripy model are taken from Ref. [80]. The equation parameters have been optimised by choosing an arbitrary value for the constraint factor α and comparing the NASGRO 2.0 equation with constant amplitude loading experimental data. The value for α is chosen in an iterative manner until the user is satisfied that a good agreement is made between predicted and experimental crack growth results [79].

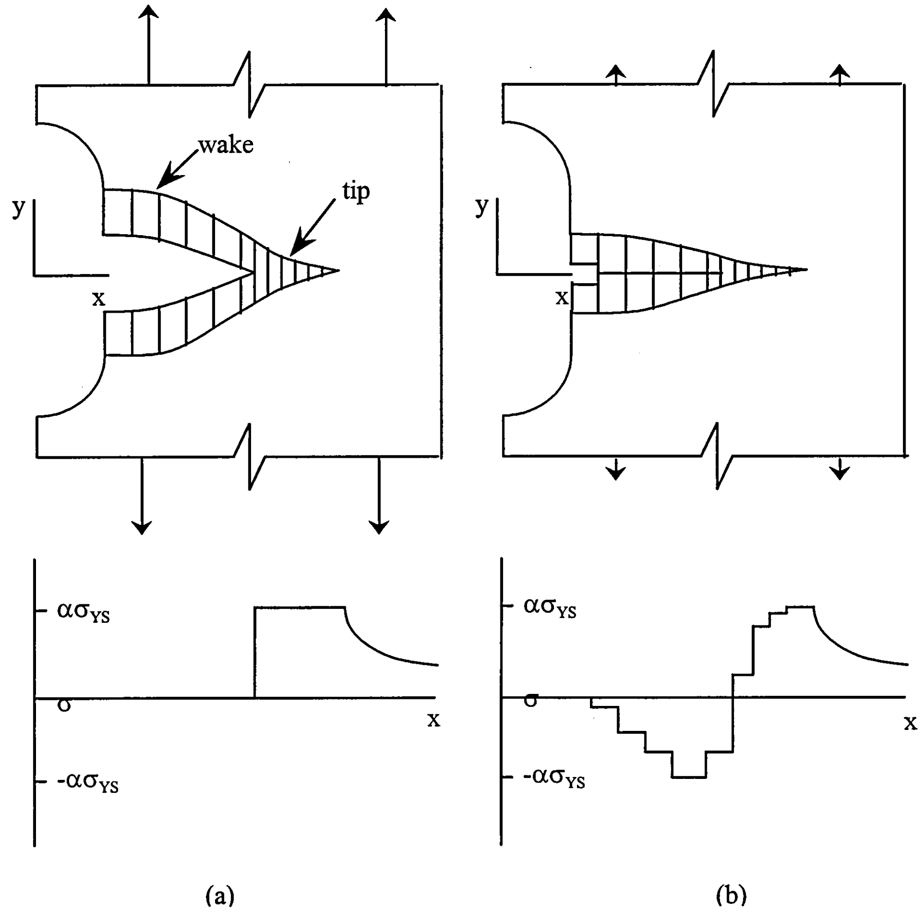

Figure 4.1 Schematic of stress and deformation distributions calculated by STRIPY along the crack line at (a) maximum stress and (b) minimum stress.

4.5 Application of ESA models

As Esacrack and Stripy were originally developed for damage tolerance analysis of space structures they calculate crack growth on a block-by-block basis (each block containing *N* load cycles) as this is the typical type of analysis performed in this industry. Blocks containing single cycles can be used to simulate simple overload events during constant amplitude loading or blocks containing multiple cycles can be used to simulate aircraft type loading as will be used later in this thesis.

An evaluation of the Stripy model was performed by Lazzeri et al [74] for simplified overload sequences on aluminium alloy 2024 T3. The results were fairly accurate with N_{model}/N_{test} between about 0.8 and 0.9, which are conservative results. The limited application of Stripy to constant and simple variable amplitude loading restricted the evaluation of the model. However, against the other models considered, the strip yield models evaluated proved to be the most reliable methods for these types of loading.

5. DEVELOPMENT OF STANDARDISED ROTORHEAD LOADING SEQUENCE

5.1 Development of Helicopter Stress Sequence

The main problem associated with developing a helicopter variable amplitude loading sequence for test and analysis is accounting for the wide variety of manoeuvre and vibratory load cycles that a component can experience. An example of a flight loading strain gauge trace from a typical helicopter component which shows manoeuvre loads superimposed with main rotor vibratory loads is shown in Figure 5.1. The source of these vibratory loads is the main rotor system where the once per revolution and *n*-blades per revolution vibratory forces acting on the rotor blades result from lift, drag and centrifugal forces [13]. Typical sources and the frequency of the load cycles are as follows:

• Cycles at blade passing frequency	~20 Hz
• Cycles at rotor frequency	~5-6 Hz
• Manoeuvre cycles	~0.1-0.5 Hz
• Ground-air-ground (GAG) cycles	~0.01-0.001 Hz

These high frequency cycles are very significant when considering the rate of accumulation - up to 40,000 cycles per hour compared to a typical rate of accumulation of a few hundreds of cycles per hour for a fixed wing aircraft. The high accumulation rate of rotor vibratory cycles is an important consideration in the damage tolerance design process as cracks can grow at stress ranges below those required to initiate them under a safe life design [81].

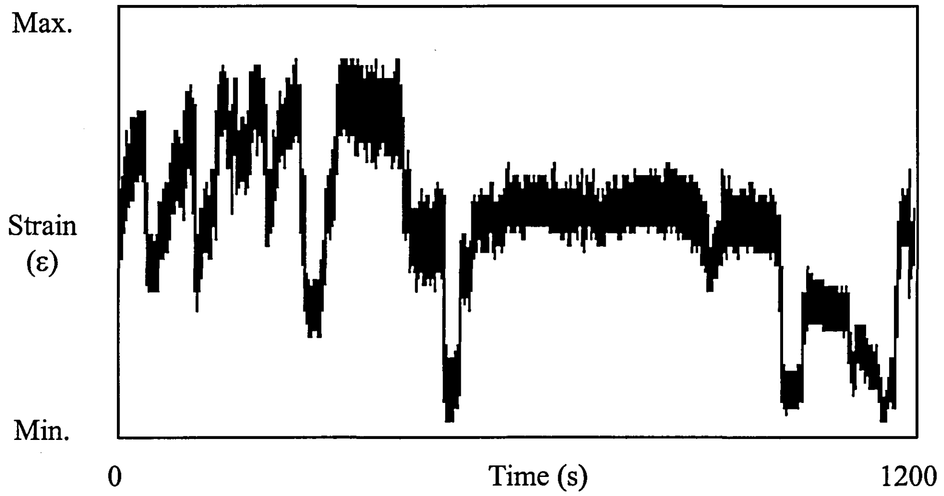

Figure 5.1 Highly variable strain gauge data from helicopter rotorhead component showing vibratory loads superimposed on manoeuvre loads.

5.2 Previous Helicopter Load Spectra Development

Very little information exists in literature which provides standardised procedures for helicopter loading sequences. Several investigations have used the 'standardised' loading sequences for helicopter rotorblades, Felix and Helix [5,6] for testing and modelling of fatigue crack growth in various components [12,14,82]. These loading sequences were developed by the DERA for the fatigue evaluation of helicopter rotorblades.

Felix is based on measurement of loads taken at the position of maximum flap-wise bending moment on a semi-rigid or fixed rotorblade of the Lynx helicopter. They each consist of a sequence of 140 sorties representing 190.5 hours of flight. Each sortie in the sequence represents either training, transport, anti-submarine warfare (ASW) or search and rescue (SAR) flight. Each of these sorties are in turn described by a defined sequence of twenty two manoeuvre types and are given in three flight lengths of 0.75, 2.25 and 3.75 hours [5,6].

5.3 The Helicopter Lynx Bolted Rotorhead

The GKN Westland Lynx helicopter bolted main rotorhead was chosen as the main component on which to base the investigation of helicopter load spectra influences on fatigue crack growth. This is shown in Figure 5.2. This is a flight critical component and would be subject to in-depth damage tolerance analysis if the Lynx helicopter were to be designed as a damage tolerant aircraft. Currently, this component has been design using the safe life approach. A critical, high stress location from which fatigue cracks are likely to propagate from was selected and a standardised load sequence occurring at this location was developed for fatigue crack growth testing.

The Lynx helicopter main bolted rotorhead is a new design which is manufactured from two Ti-1023 forgings. The upper forging is termed the hub disc and this is bolted to the rotorhead mast. The rotorhead from which all the loading sequence information for this thesis originated is a prototype rotorhead on GKN WHL Lynx AH Mk9 helicopter [83].

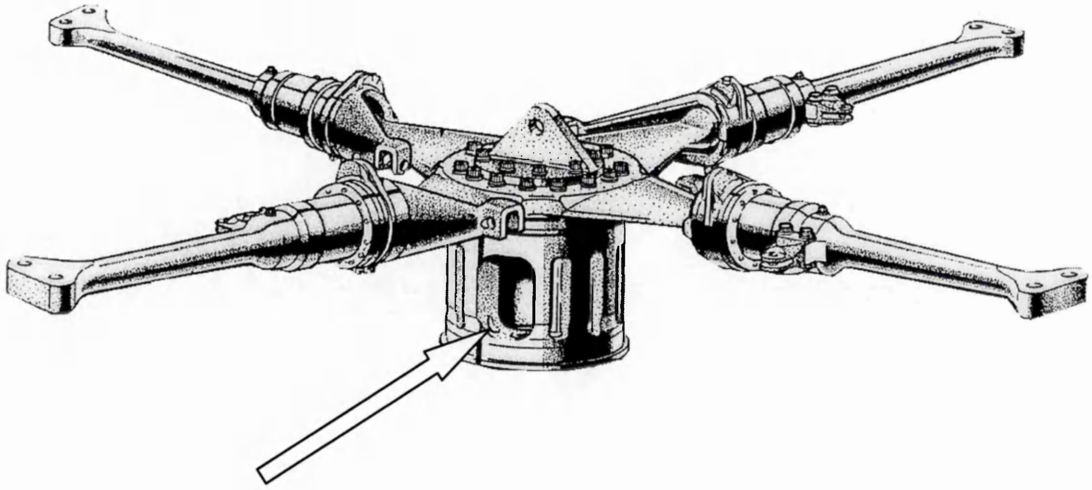

Figure 5.2 GKN Westland Lynx helicopter bolted main rotorhead and location of high stress region. (Courtesy of GKN Westland Helicopters Ltd.)

The rotorhead experiences very complex combinations of external loads during flight, which include: the steady torque from the transmission gearbox, the lift loads and the once per revolution head moment load, which changes with manoeuvre type. The helicopter is controlled by in-flight changes in the pitch of the rotor blades, which control the lift load vector at the rotorhead. The pitch angle on the blades is changed by pitch-link rods which are connected to the pitch control mechanism inside the rotorhead mast. The pitch control mechanism arms protrude through the 'control windows' on the mast.

The rotorhead mast was analysed under a dominant design load cases by engineers at GKN WHL using a NASTRAN finite element model [83]. The results of the analyses showed that the highest stress location was at the lower corners of each control window for most flight conditions due to the nature of the loading. This is indicated in Figure 5.2. The analyses showed that the maximum flight stress is typically around 400 MPa.

5.4 Stress Sequence Development

The approach used to generate the loading sequence Felix [5,6] was adapted to best represent the loading experienced at the location of maximum stress on the Lynx rotorhead. Felix is used here instead of Helix because it was originally based on the Lynx helicopter. This approach has the capability of retaining, to a certain extent, the definition of the small vibratory loads which the structure experiences due to rotor rotation. Most aspects of the Felix method, such as the complicated mission and manoeuvre combinations, were retained except for the original strain data from which the loading spectra were defined.

The strain data used in this thesis to develop the loading sequence were taken from the high stress location at the rotorhead control window. This location was strain gauged and data were recorded during several test flights [83]. Several binary files containing the raw strain gauge data were provided by GKN WHL from the test flights. An example of a section of flight strain gauge data is shown in Figure 5.1.

The rotorhead loading sequence has been called 'Rotorix' to signify the rotorhead and to give a family resemblance to Felix from which it is adapted. Where the Rotorix method is mentioned this also implies the adaptation of the Felix method.

5.4.1 Definition of Manoeuvres

Rotorix has a set of 22 standard manoeuvres given in Table 5.1. These are the same manoeuvres described by Felix but with one significant difference: Manoeuvre 17 - Auto-rotation with large amplitudes - was not undertaken during flight testing of the bolted main rotorhead so this was substituted with 'auto-rotation with bank turn starboard at 80 KIAS (Knots Indicated Airspeed)'.

5.4.2 Non-Dimensionalising Flight Strain Gauge Data

Sections of strain gauge data representing the 22 standard manoeuvres were identified and extracted from raw data files using the test flight log and event descriptions. The strain gauge data for each manoeuvre were then normalised on a scale up to 100 with respect to the maximum strain value of all the manoeuvre data. This maximum strain occurred during the longitudinal control reversal manoeuvre at 0.7 VNE (Velocity Never Exceed). The cycle loads were then assigned or 'binned' into integer levels of 4 (4,8,12 and so on) in accordance with the procedure given in Table 5.2. This is the procedure used in Rotorix as a means of simplifying the generation of the final sequence [6]. Each normalised manoeuvre was then rainflow cycle counted and processed as described below.

Table 5.1 Types, definition and duration of rotorhead loading sequence manoeuvres.

No.	Description	Steady State (S)/ Transient(T)	Time (sec)	Number of cycles	Manoeuvre applications
1	Take off	S	16.7	19	6
2	Forward flight 0.2 VNE	S	4.1	15	2
3	Forward flight 0.4 VNE	S	7.8	26	1
4	Forward flight 0.6 VNE	S	4.5	14	2
5	Forward flight 0.8 VNE	S	2.1	15	1
6	Forward flight 0.9-1.1VNE	S	7.5	29	4
7	Max power climb	S	4.6	21	1
8	Transition to hover	T	3.3	8	1
9	Hover	S	6.4	34	1
10	Cruise turns 0.4-0.8 VNE	S	5.2	19	3
11	Cruise turns 0.8-1.0 VNE	S	3.9	26	2
12	Sideways flight port	S	5.7	12	2
13	Sideways flight starboard	S	4.0	19	1
14	Rearward flight	S	3.6	23	1
15	Spot turns	S	15.5	19	9
16	Auto-rotation	S	14.3	18	3
17	Auto-including banked turn	S	12.7	17	4
18	Recovery from auto-rotation	S	6.7	21	2
19	Control reversal 0.4 VNE	S	17.1	14	7
20	Control reversal 0.7 VNE	S	15.3	34	4
21	Descent	S	6.2	31	1
22	Landing	S	17.1	19	7

A simplified example of a rainflowed manoeuvre is given in Figure 5.3. Cycles of range 4 were omitted from the data at this stage because there were too many to warrant realistic test times. From the results of the rainflow count the cycle mean with the most number of cycles is designated as the 'dominant' mean load for that manoeuvre.

Table 5.2 Procedure for assigning normalised strain gauge data to integer levels.

Non-dimensionalised strain range	Rotorix load range 'bin'	Rotorix load amplitude 'bin'
4.0 – 11.9	8	4
12.0 – 19.9	16	8
20.0 – 27.9	24	12
etc.	etc.	etc.

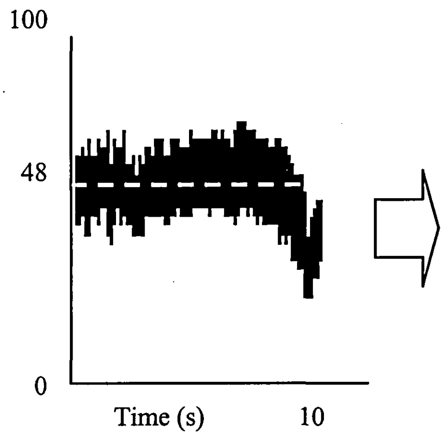

	Mean						
Range	…	44	48	52	56	60	etc
…							
4	3	10	15	7	3	1	
8	2	5	9	5	1		
16		1	5	2			
24			2	1			
32			3				
Etc.							

Figure 5.3 Procedure for converting steady state manoeuvre strain gauge data into Rotorix format. Extracted strain gauge data were normalised (0 to 100) and then rainflow cycle counted. Dominant cycle mean assigned (48 in this example) and cycles with range 4 are omitted.

The next step used the assigned 'dominant' load as the manoeuvre mean load and the vibratory loads are taken from a summation of the rainflow counted ranges. Hence the example in Figure 5.3 is now given by:

		Vibratory loads:	8	16	24	32	40	48
No.	Manoeuvre	Mean	No. of cycles					
1	Example	48	22	8	3	3		

The mean load and vibratory load values derived from the rainflow analysis of each manoeuvre are given in Table 5.4. The final mean load and sequence of vibratory loads for the Rotorix manoeuvres are given in Table 5.5. The number of cycles in each manoeuvre is also given in Table 5.1.

This normalisation, integer binning and rainflow cycle count procedure tends to over-simplify the load cycles which define each manoeuvre. This procedure was originally adopted by DERA because of storage limitations on earlier computers [5,6]. Current computers can easily deal with large numbers of cycles in a loading sequence so there is no need to over-simplify the manoeuvre loads. However, for the sake of conforming to the Felix procedure no modifications are made. A comparison of 'real' strain gauge data and processed data is given in Section 5.5.

5.4.3 Steady State Manoeuvres

Each manoeuvre was designated as either a steady state or a transient manoeuvre. Manoeuvres which contain significant variation in the load cycle mean level during their performance are termed 'transient' manoeuvres. Steady state manoeuvres have one obvious or dominant mean load for the entire manoeuvre. The steady state and transient manoeuvres are dealt with in different ways as described below.

In most instances the duration of the Rotorix manoeuvres selected from strain gauge data did not correspond each Felix manoeuvre duration. To achieve the correct duration of manoeuvres in the generation of the Rotorix loading sequence, the number of 'manoeuvre applications' of each flight case is determined. For example the 'Take off' manoeuvre has a duration of 16.7 seconds as defined by Felix. The sample time used for the rainflow count was 2.8 seconds so that to equate this to the equivalent Felix time it needs at be applied six times. This is the 'manoeuvre application' number given in Table 5.1. This number is used by the generation program to determine how many times that manoeuvre should be repeated to give the correct time in the final generation of Rotorix. The time in manoeuvre, number of vibratory loads and manoeuvre applications for Rotorix are all given in Table 5.1 above.

5.4.4 Transient Manoeuvres

Only one transient manoeuvre was identified from the strain gauge data - the transition to hover manoeuvre. The mean level of the manoeuvre loads changed from 40 to 28 to 68 during the manoeuvre. Although the Felix procedure only allows one mean level for each manoeuvre, the transient nature of the manoeuvre can be simulated in the loading sequence by changes in mean levels between different manoeuvres: This transition to hover manoeuvre (mano. #8, mean load 28) is always preceded by the forward flight 0.2 VNE (mano. #2, mean load 40) manoeuvre and itself always precedes the hover manoeuvre (mano. #9, mean load 68). Therefore the transition between three sequential manoeuvres will provide for a transient type manoeuvre - albeit simplified.

No attempt has been made to equate the transient manoeuvre duration with its Felix equivalent. Instead, when a transient manoeuvre is called up within the flight generation algorithm, the number of matrix applications is always 1. Applying this methodology gives Rotorix sortie lengths which are not exactly equal to the 1.75, 2.25 and 3.75 hour Felix durations. To equate the sortie lengths the number of matrix applications of the high speed forward flight manoeuvre, forward flight 0.9-1.1VNE, were adjusted so that the 3.75 hour sortie lengths of the four mission types were the same.

5.4.5 Sortie Duration and Sequence

The sortie manoeuvre mix, number of sorties and their sequence are identical to those defined by Felix. However the sortie times are slightly different to the 3.75 hour (13,500 seconds) duration and this is due to the inclusion of transient manoeuvres. The times for each sortie are given in Table 5.3.

Table 5.3 Duration for the Rotorix sorties

Sortie	Time for 3.75 hour sortie (secs.)
ASW	13,495
SAR	13,500
Transport	13,498
Training	13,504

5.4.6 Ground Load

Between each of the 140 flights in the Rotorix sequence the generation algorithm inserts a 'ground load' to simulate the ground-air-ground cycle. The ground load for all Rotorix versions is load level 4 which is the minimum load in the Rotorix sequence.

Table 5.4 Mean load and vibratory load sequences for the Rotorix manoeuvres

Vibratory loads:			8	16	24	32	40	48
No.	Manoeuvre	Mean	No. of cycles					
1	Take off	56	17	2				
2	Forward flight 0.2 VNE	40	14	1				
3	Forward flight 0.4 VNE	36	3	23				
4	Forward flight 0.6 VNE	44	12	2				
5	Forward flight 0.8 VNE	60	15					
6	Forward flight 0.9-1.1VNE	88	23	6				
7	Max power climb	80	11	10				
8	Transition to hover	28	8					
9	Hover	68	20	14				
10	Cruise turns 0.4-0.8 VNE	76	16	3				
11	Cruise turns 0.8-1.0 VNE	84	21	5				
12	Sideways flight port	56	10	1	1			
13	Sideways flight starboard	60		19				
14	Rearward flight	52	5	17	1			
15	Spot turns	60	14	3	2			
16	Auto-rotation	-4	18					
17	Auto-including banked turn	-4	12	5				
18	Recovery from auto-rotation	52		21				
19	Control reversal 0.4 VNE	44	5	3	3	3		
20	Control reversal 0.7 VNE	76	15	8	5	4	1	1
21	Descent	52	29	2				
22	Landing	44	18	1				

*Table 5.5 Sequence of loads in a manoeuvre for Rotorix**

No.	Manoeuvre	Mean	Load **amplitude** sequence
1	Take off	56	4 4 4 4 4 4 8 4 4 4 4 4 8 4 4 4 4 4 4
2	Forward flight 0.2 VNE	40	4 4 4 4 8 4 4 4 4 4 4 4 4 4 4
3	Forward flight 0.4 VNE	36	4 4 8 8 8 8 8 4 8 8 8 8 8 8 8 8 8 8 8 8 8 8 8 8 8 8
4	Forward flight 0.6 VNE	44	4 4 8 8 4 4 4 4 4 4 4 4 4 4
5	Forward flight 0.8 VNE	60	4 4 4 4 4 4 4 4 4 4 4 4 4 4 4
6	Forward flight 0.9-1.1VNE	88	4 4 4 8 8 4 4 4 8 4 4 8 8 4 8 4 4 4 4 4 4 4 4 4 4 4 4 4 4
7	Max power climb	80	4 4 4 8 8 8 8 4 8 8 8 4 4 8 4 8 8 4 4 4 4
8	Transition to hover	28	4 4 4 4 4 4 4 4
9	Hover	68	4 4 4 4 4 8 8 8 8 4 4 8 8 4 8 4 8 4 4 4 4 4 8 8 4 4 8 8 8 8 4 4 4 4
10	Cruise turns 0.4-0.8 VNE	76	4 4 4 8 4 8 8 4 4 4 4 4 4 4 4 4 4 4 4
11	Cruise turns 0.8-1.0 VNE	84	4 4 4 4 4 8 4 8 8 4 8 4 8 4 4 4 4 4 4 4 4 4 4 4 4 4
12	Sideways flight port	56	8 12 4 4 4 4 4 4 4 4 4 4
13	Sideways flight starboard	60	8 8 8 8 8 8 8 8 8 8 8 8 8 8 8 8 8 8 8 8
14	Rearward flight	52	4 12 8 8 8 8 4 4 8 8 4 4 8 8 8 8 8 8 8 8 8 8 8
15	Spot turns	60	4 4 4 12 8 12 8 8 4 4 4 4 4 4 4 4 4 4 4
16	Auto-rotation	8	4 4 4 4 4 4 4 4 4 4 4 4 4 4 4 4 4 4
17	Auto-including banked turn	8	4 4 8 8 4 8 4 4 4 4 4 8 8 4 4 4 4
18	Recovery from auto-rotation	52	8 8 8 8 8 8 8 8 8 8 8 8 8 8 8 8 8 8 8 8 8
19	Control reversal 0.4 VNE	44	4 8 12 16 16 12 16 4 4 8 12 8 4 4
20	Control reversal 0.7 VNE	76	4 4 4 4 4 8 8 8 8 8 12 12 12 16 16 20 24 16 16 12 12 4 4 4 8 8 8 4 4 4 4 4 4 4
21	Descent	52	4 4 4 4 4 4 4 4 4 8 4 4 4 4 4 4 8 4 4 4 4 4 4 4 4 4 4 4 4 4 4
22	Landing	44	8 4 4 4 4 4 4 4 4 4 4 4 4 4 4 4 4 4 4

** Notes:*

(1) The version used for testing was the Rotorix 16 sequence has all the above 4's removed.

(2) The vibratory loads are expressed here as amplitudes which is used by the generation algorithm.

5.5 Comparison with Original Strain Gauge Data

The accuracy of the Rotorix loading sequence was evaluated by comparing the representation of a single flight with the same flight taken from the original strain gauge data. The comparison was accomplished by taking strain gauge data files, from which the Rotorix manoeuvres were originally extracted and concatenating them (in a correct sequence) into a single file which represented the 'Flight 23' sortie ('23' means transport flight - '2' of 3.75 hour duration - '3'). This was then gated at range level 8 to compare directly with Rotorix. Similarly, the computer generation program was altered so that only Flight 23 was generated for Rotorix.

Figures 5.4 and 5.5 compare the two methods of generating Flight 23. Mean levels defined in Rotorix for each manoeuvre type reflect the mean level changes in the strain gauge data reasonably well.

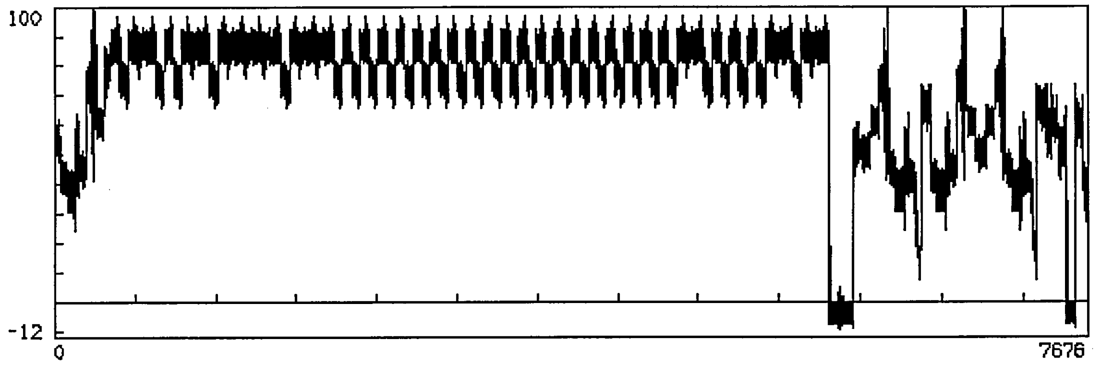

Figure 5.4 Three hour transport flight generated using original strain gauge data

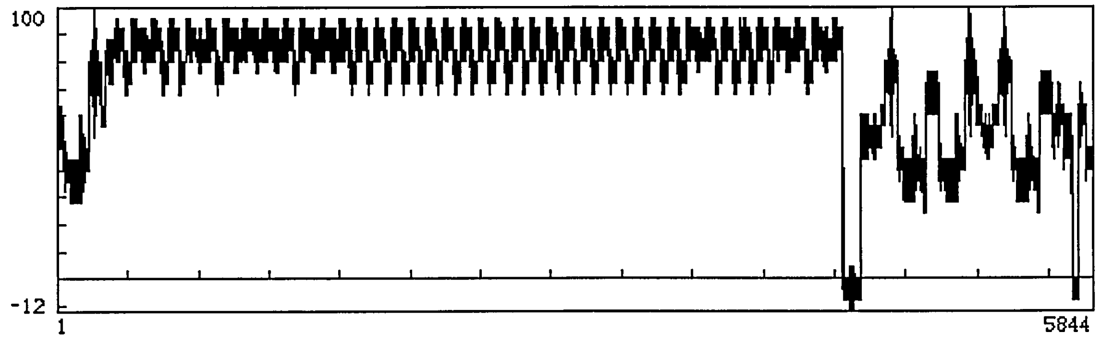

Figure 5.5 Three hour transport flight generated using the Rotorix procedure

The lengths of the two Flight 23's are 7676 and 5844 turning points for strain gauge data and Rotorix respectively. The difference implies that some cycles have been lost in the generation mostly due to omission of cycles below level 4.

A cumulative exceedence plot of the cycle ranges in each flight representation is given in Figure 5.6. The distinct steps in Figure 5.6 for the Rotorix flight is a result of binning manoeuvre load matrices into distinct integer levels of 4. The Rotorix Flight 23 compares well with the strain gauge data in the range 12 to 105 exceedences. Below this range (1 –11 exceedences) the range levels are lower for Rotorix implying unconservatism in the way the loads are assigned. This is of little significance as the requirement to accurately represent flight data is not as stringent for loading sequences used for comparative testing and modelling which is the case here. However, to alleviate this problem it is suggested that integer levels of 1 could be used without compromising the efficiency of generating Rotorix. This is strongly recommended for future improvements to Rotorix. Additionally the allocation of only one load cycle mean to the entire manoeuvre produces inaccuracies compared with the original strain gauge data. It should be possible to develop a procedure whereby each load cycle in a manoeuvre maintains its original mean from the strain gauge data. See discussion.

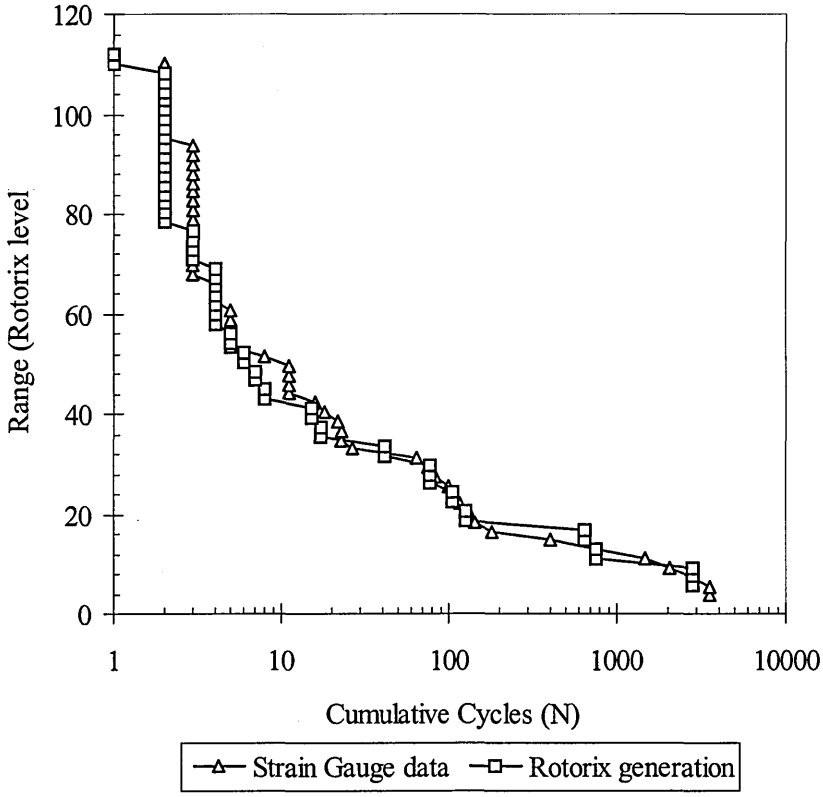

Figure 5.6 Cumulative exceedance plot for three hour transport flight. Comparison of strain gauge data and Rotorix method.

5.6 Sequence Modification for Compact Tension Specimen Testing

The rotorhead loading sequence has compressive loads experienced during the autorotation manoeuvres. The compact tension specimen is unsuitable for loading under compression because there is a small amount of fit clearance between the pins and the specimen at zero load. The servo-hydraulic machine is not able to adequately control compressive loads near the zero point because of this. To overcome this it was decided to modify the loading sequence to eliminate compressive load cycles for all compact tension tests. The modification involved shifting all the mean loads of the compressive load cycles so that the minimum turning points were positive. The mean load levels of autorotation manoeuvres (manoeuvres 16 and 17) were shifted from -4 to +8.

A computer program was written from Ref. [6] which generates the loading sequence from data files that define the sequence of manoeuvres, sequence of flight and sorties, and the mean and vibratory loads. A file containing each turning point in the sequence was made available for post-processing procedures, such as rainflow counting, and preparation for installation into the fatigue loading machine.

The number of turning points given for the entire Rotorix 8 loading sequence was 8,893,687. This size of loading spectrum is not practical for general analysis and testing purposes so the minimum cycle range was defined as level 16 and cycles below this were removed or omitted. This gave a workable loading sequence length of 1989925 cycles. Hence, a new version of the loading sequence called Rotorix 16 was used for testing and analysis in this thesis. It is likely that such a significant omission of small cycles will result in changes in crack growth life of the specimens if these cycles are above the fatigue threshold during the test. See discussion.

The loading sequence provides a good simulation of the types of loads that the critical location in the rotorhead mast control window might experience during flight. This was demonstrated by the comparison with the original loading data. It must be stressed that the manoeuvre load levels in this loading sequence are specific to this location and might not be applicable to other areas on the rotorhead or other power transmission components. Similarly, the Felix loading sequence is only applicable to helicopter rotor blades.

5.7 Loading Sequence Characteristics

5.7.1 Small Range Cycles in Loading Sequence

A rainflow cycle count of the rotorhead loading sequence reveals that it is dominated by a large number of high mean stress cycles with ranges of level 16 as shown in Figure 5.7. This is the most significant feature of the rotorhead loading sequence because these small level 16 cycles constitute nearly 94% of the sequence. The importance of these cycles is realised when considering their origin: Examination of the original strain gauge data showed that these cycles mostly originated from the once-per-revolution (1R) vibratory loads at 17.5 Hz of the rotorhead and hence are accumulated quickly during flight.

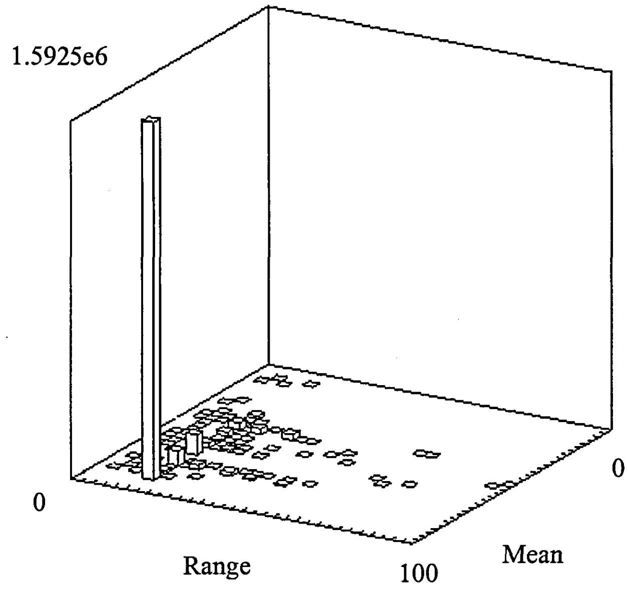

Figure 5.7 Rainflow cycle count histogram of rotorhead loading sequence. The cycles at level 16 dominate the number of counted cycles.

5.7.2 Progressive Omission of Small Range Cycles

A novel method has been devised to determine the fatigue damage contribution of the different small range cycles by progressively omitting small range cycles of increasing range from the rotorhead loading sequence. The method uses the Rotorix 16 loading sequence, with all small range cycles retained, to perform a CVAL test under realistic stress conditions.

Subsequently, the level 16 cycles are omitted so that the smallest cycles range is now level 20 and another test is performed. The difference in crack growth rates between the two omission level tests will be due to the contribution of the level 16 cycles. The procedure is repeated at progressively higher range omission levels. The 'peak-valley filtering' method was used to omit the cycles at each step where trough-peak pairs are retained or omitted according to the desired load range. It maintains the correct ordering of the sequence as is shown in Figure 5.8.

Four omission range levels were defined for the current series of tests with the results given in Table 5.6. The changes in the loading spectrum due to the omission procedure are shown in Figure 5.9. The method assumes that the contribution of the small range cycles to crack length damage is the same for each omission test sequence.

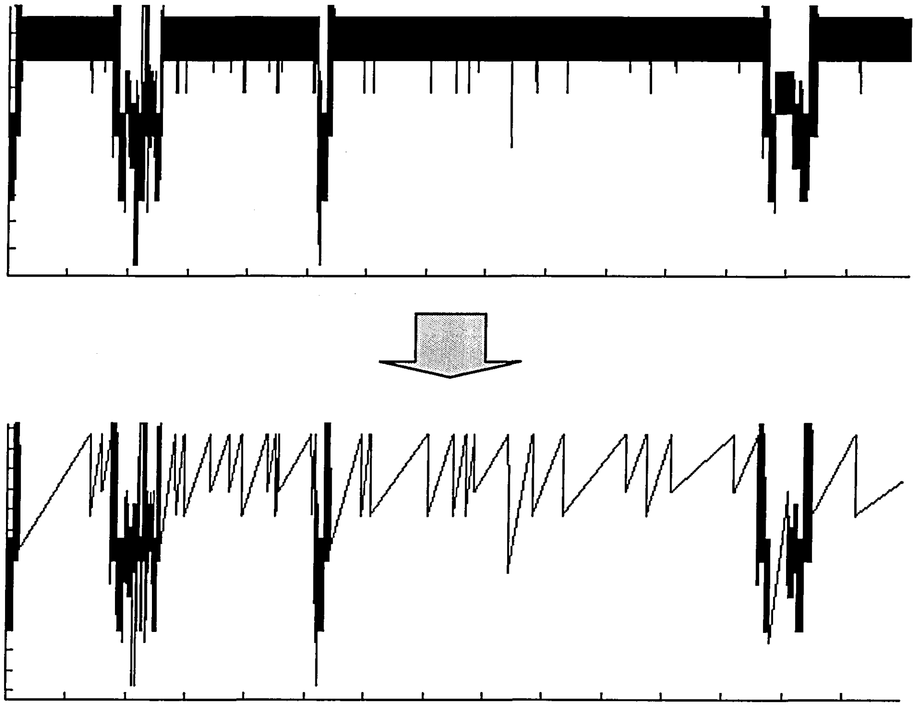

Figure 5.8 Retention of ordering in loading sequence during omission process. Load cycles of range 16 have been omitted from the bottom sequence.

Table 5.6 Progressive small range cycle omission in rotorhead loading sequence

Omission range level*	Points in sequence	Rainflow cycle count	Reduction in length (%) from original	Test Designation
Rotorix 16	3979850	1989925	-	L16
20	226129	113063	94.3	L20
24	221817	110907	94.4	L24
32	102811	51404	97.4	L32

* Omission range level is the maximum cycle range *retained.*

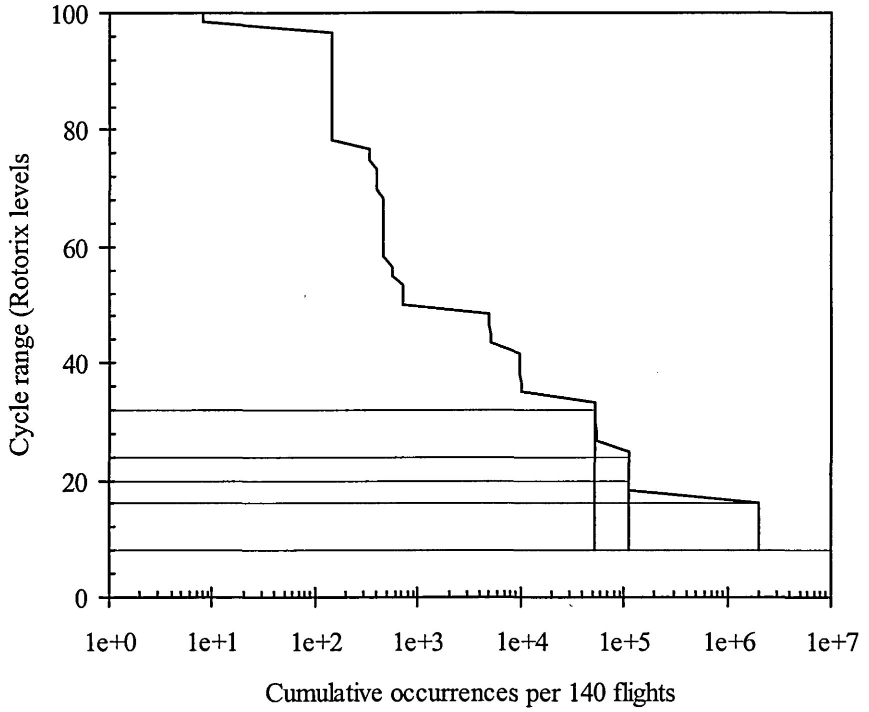

Figure 5.9 Rotorhead loading sequence and change in spectrum for different omission levels (at 16,20,24 and 32).

Another stress spectrum variation that could be tested is the truncation of the infrequently occurring high loads due to either gusts or rare severe loads. However, insufficient data were made available during the short flight test period to quantify the extent of gust loads and severe manoeuvres that may result in high peak loads during helicopter service. Therefore, the rarely occurring high loads have been ignored in this stress spectrum. Hence the loading sequence does not have any peak overloads which may affect the crack growth rates during the tests. This is because the overloads tend to promote retardation of crack growth rates.

5.7.3 Mean Stress Distribution of Loading Sequence Cycles

The rainflow cycle count can also be used to determine the distribution of cycle R ratios in the loading sequence. Figure 5.10 shows that the large number of small range cycles that dominate the loading sequence have very high mean stress values of between R=0.8 and 0.9.

Analysis of the R ratio distribution of the sequences resulting from the progressive omission of the small range cycles reveals that the high R ratio cycles are almost completely removed from the spectrum as the omission level increases. At an omission level of 32 the dominating cycles have R ratios of R = 0.5 to 0.65. This is important when considering the effect of crack closure and load interaction effects, which may have a significant effect at high R ratio cycles.

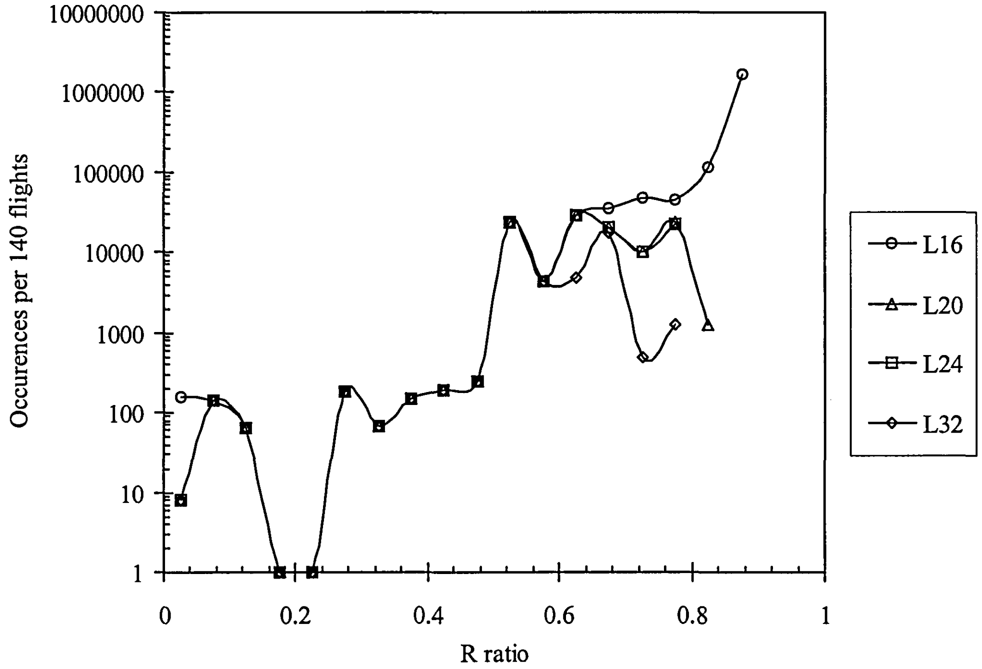

Figure 5.10 Effect of different level of omission on stress ratio R distribution for rotorhead loading sequence.

6. EXPERIMENTAL PROCEDURES

All fatigue tests were carried out, using standard compact tension specimens, on two Instron 8500 digitally controlled 30 kN and 250 kN hydraulic fatigue machines. Loading was performed under load control, at 10Hz and under ambient laboratory conditions. The tests were carried out in accordance with the procedures defined in ASTM E 647-93 "Standard Test Method for Measurement of Fatigue Crack Growth Rates" [84].

6.1 Specimen Design

Compact tension (CT) specimens, manufactured in accordance with ASTM E 647-93 [84], were used for all fatigue crack growth testing. The CT specimens were t=17.5 mm thick giving predominantly plane strain stress states throughout all the tests. Ten Ti-10V-2Fe-3Al (Ti-1023) CT specimens were provided by GKN WHL. Ten 7010 T73651 (7010) CT specimens were machined from a 50mm thick billet. The 7010 CT specimens were machined from positions at 5mm below the surface of the billet. The specimens were machined so that the crack would propagate in the L-T orientation from a chevron type notch of length a=14 mm to aid uniform initiation of the pre-cracks. A photograph of the *in situ* test specimen is given in Figure 6.1. The dimensions for manufacture are given in Appendix A.

All specimens were pre-cracked to a pre-test crack length of a=15.5 mm in accordance with the load step-down procedures given in ASTM E 647 [84]. The loads were then maintained at the same maximum load level as the test up to 16 mm to preclude any load interaction effects before each test.

The stress intensity factor, K solution for the CT specimen in terms of the applied load is given by [85]:

$$K = \frac{P}{tW^{1/2}} . f(a/W) \qquad \textbf{\textit{Eqn 6.1}}$$

where

$$f(a/W) = \frac{(2 + a/W)(0.886 + 4.64a/W - 13.32(a/W)^2 + 14.72(a/W)^3 - 5.6(a/W)^4}{(1 - a/W)^{3/2}}$$

Eqn 6.2

and a = crack length

W = specimen width = 70 mm

t = specimen thickness = 17.5 mm

P = applied load

Equations 6.1 and 6.2 are valid for $0.24 < a/W < 0.7$.

6.2 Measurement of Fatigue Crack Growth

A high resolution, custom designed direct current potential drop (DCPD) crack length measurement system was designed to provide measurement of fatigue crack growth rates for all the fatigue tests. This fatigue crack growth measurement technique has been widely used and is reviewed by Sutton [86]. This method was developed to overcome three main problems associated with measuring voltage changes in a metallic fatigue crack growth specimen:

1. Drifts in the measured voltage due to changes in resistivity of the test specimen, measurement device and current supply caused by changes in temperature.
2. Thermoelectric electromotive forces (emfs) generated between the measurement probes and the test specimen.
3. Crack closure causing electrical shorting across the fracture surfaces.

These problems are solved by mounting two pairs of probes (V_x and V_y) on the specimen and normalising the voltages (V_x/V_y) measured at each probe pair. V_x is the changing voltage measured across the crack mouth and V_y is the reference voltage on a dummy specimen. The resulting ratio is independent of temperature changes. The method for eliminating the thermoelectric electromotive forces (emf) involved taking voltage measurements with the current off (V_{emf}) and subtracting it from the voltage measured with the current on (V_{on}) to give a voltage without emf's (i.e. $V_x = V_{onx}$.- V_{emfx} and $V_y = V_{ony}$.- V_{emfy}). To eliminate problems of electrical shorting the current is pulsed so that the voltage measurement is taken at maximum tensile load when the fracture faces should be fully separated.

The combination of these enhancements for crack length measurement greatly increases the ability to measure small increments of crack growth and this method was adopted for crack length measurement in this thesis. The system described in Appendix B was developed under the guidelines provided in ASTM E 647, Annex A3 [84].

6.3 Grip Design

When using the DCPD technique it is necessary to ensure that the specimen is fully electrically insulated from the test machine frame by means of electrically insulating the grips. This is to prevent the high current entering the load machine and to prevent earth loop voltages occurring around the test machine and measurement equipment which can contribute to electrical noise. This was achieved by using a clevis and pin arrangement shown in Figure 6.1. The EN24T steel grips were separated into two parts by non-conducting 'Tufnol' spacers between the flanges and bolt heads. Assembly drawing of the grips are given in Appendix A.

The pins used to transfer load to the CT specimens were EN24T steel with polished surfaces. The pins used for the titanium CT specimens were coated with an aluminium-oxide (Al_3O_2) ceramic to prevent current flow into the pins themselves and effecting the calibration of the specimen. No special consideration for pin friction was given, such as using roller bearings, except that the pins were coated with a graphite based lubricant before each test.

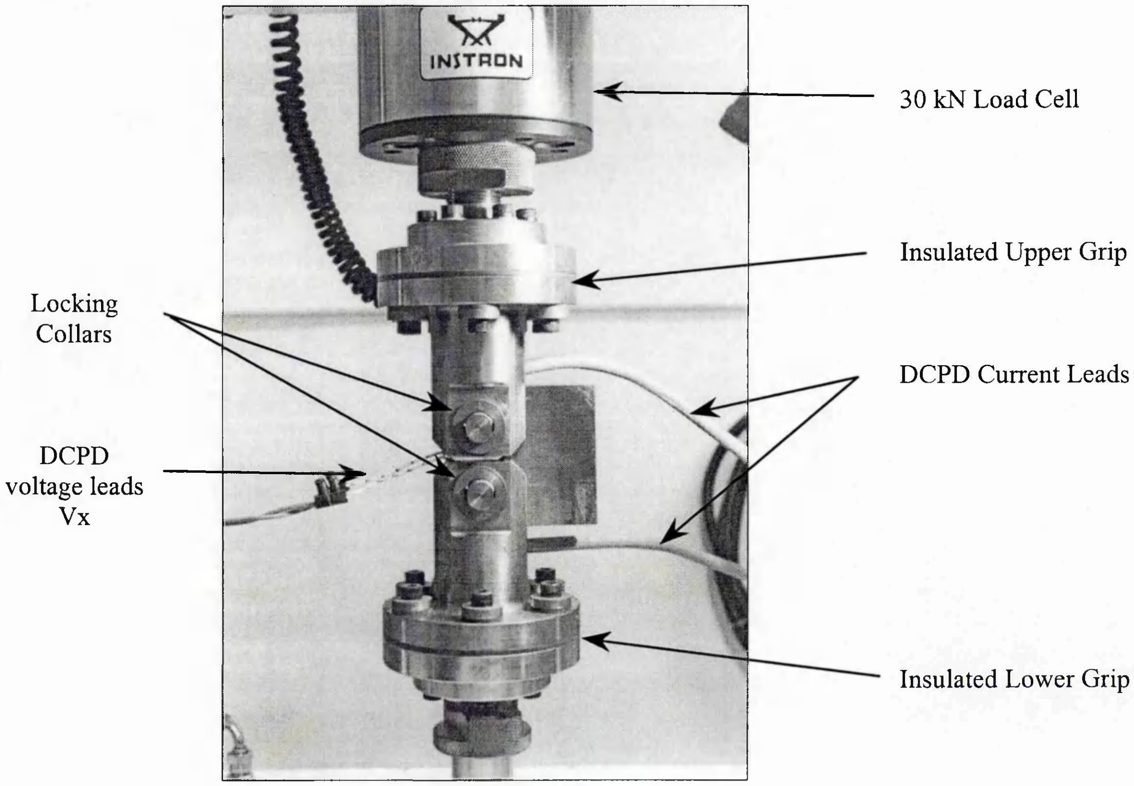

Figure 6.1 Compact tension specimen test set-up showing DCPD current and voltage leads and grips. The pins were prevented from rotating by locking collars.

6.4 Crack Length Calibration for Compact Tension Specimen

The calibration method employed here establishes a relationship between the voltage potential drop ratio $(V_x/V_y)/(V_x/V_y)_o$ and the normalised crack length (*a/W*) of the specimen. The ratio $(V_x/V_y)_o$ is the voltage ratio of the V_x and V_y probes at the start of the test when the crack length is at 14mm. This further normalisation of the test voltage potential ratio helps to reduce errors associated with the differences in positioning of the probes between specimens.

To determine the calibration relationship a test was run under CAL conditions with a travelling microscope of 10 μm resolution which was used to make measurements of the crack length on both surfaces together with corresponding test voltage ratio $(V_x/V_y)/(V_x/V_y)_o$ from the DCPD system. An average of the two surface crack lengths and the mid-section length (measured after test) was used in the calibration because the crack front is usually curved. The crack length calibration curve is plotted in Figure 6.2.

A third order polynomial of the following form was fitted to the calibration points using a least squares curve fitting procedure:

$$a/W = A_0 + A_1((V_x/V_y)/(V_x/V_y)_o) + A_2((V_x/V_y)/(V_x/V_y)_o)^2 + A_1((V_x/V_y)/((V_x/V_y)_o)^3$$

- ***Eqn. 6.3***

where *a/W* is the normalised crack length and the coefficients are:

$A_0 = 0.03057$
$A_1 = -0.4020$
$A_2 = 0.77384$
$A_3 = -0.2037$

$R^2 = 0.9995$ (the least squares fit residual)

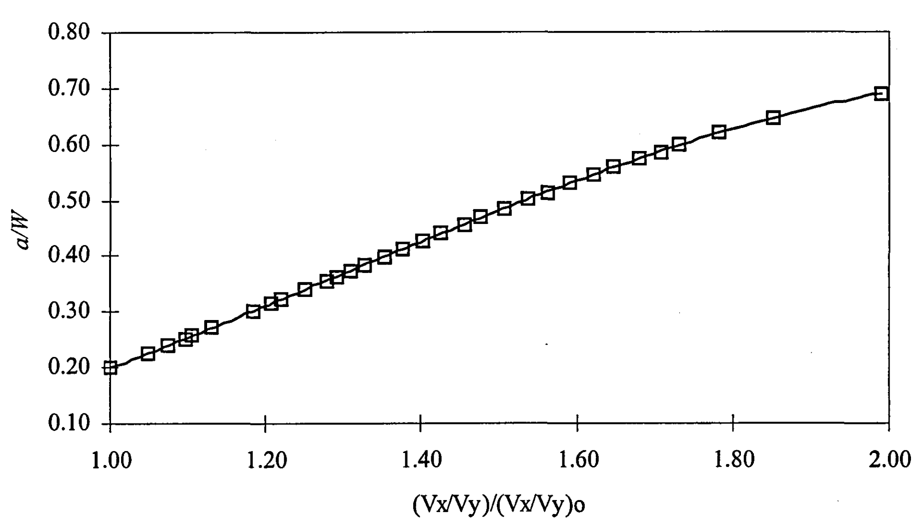

Figure 6.2 DCPD calibration measurements and calibration curve for the compact tension specimen

6.5 DCPD Crack Length Measurement System Specifications

6.5.1 Resolution

The resolution of the DCPD system is defined as smallest measurable *change* in crack length per voltage increment of 100 nV (resolution of DVM). The resolution depends on a number of factors including digital voltage meter (DVM) resolution, current magnitude, specimen geometry (calibration equation), current input and voltage measurement probe locations and electrical conductivity of the specimen material. The resolution of the DCPD was determined and given as 3 μm and 10.5 μm for titanium and aluminium respectively. The difference between materials is due to the greater resistively of titanium and so higher voltages are generated for a fixed current.

However, the resolution only represents an ideal smallest measurable change in crack length. This is effected by the stability of the DCPD system over long periods of time and the measurement of electrical noise which determines the accuracy.

6.5.2 Accuracy

To evaluate the accuracy of the equipment when measuring changes in crack length, a static 'bench test' was set up with test and reference specimens for the two materials used in the experimental work. The system was left to gather voltage data over certain periods of time and this was then analysed to determine the long term accuracy characteristics. The results of the 'bench tests' are summarised in Table 6.1.

Table 6.1 Testing for evaluation of DCPD system accuracy

Material	**Duration (hours)**	**Sample Count**	**Mean (mm)**	**Standard Deviation (mm)**	**Min. (mm)**	**Max. (mm)**
Titanium	10	500	14.039	0.008	14.019	14.072
Aluminium	14	600	16.222	0.067	16.082	16.374

The accuracy of the system is defined as the first standard deviation of the data. Hence the accuracy of the DCPD system is:

± 0.008 mm for Titanium
± 0.067 mm for Aluminium

Again the large difference between the materials is due to the low relative resistivity of aluminium which results in a higher noise to signal ratio than for titanium.

6.5.3 Absolute Crack Length

The accuracy represents the certainty to which changes in crack length, *da* can be measured by the DCPD system. However, the absolute measurement of the crack length, *a* is affected by crack front curvature. Typical fatigue cracks form a 'bow' shape with the crack length longer in the specimen interior than at the edges. The calibration equation (Eqn. 6.3) accounts for this but only gives an average of the edge and interior lengths. The absolute crack length can vary by up to approximately 1mm through-the-thickness and this will affect the stress intensity factor, K which is dependent on absolute *a*.

6.6 Measurement of Fatigue Crack Closure

Two compliance techniques were used to measure crack closure during the SVAL and CVAL tests: (1) A near (crack) tip strain (NTS) gauge and (2) a crack mouth opening displacement (CMOD) clip gauge mounted across the mouth of the compact tension specimen.

Measurement of 'local' or near tip crack closure was made using the NTS gauges. They were cemented to the specimens by the Measurement Group UK Ltd. using their strain gauges CEA-06-032-UW-120 and CEA-13-032-UW-120 for titanium and aluminium respectively. These gauges have a gauge length of 0.81mm and were located 0.5mm behind and 0.6mm below each crack tip and orientated to measure transverse strain which gives better sensitivity to closure [52]. Measurements within 1mm behind the crack tip have been demonstrated to have greater sensitivity to closure [47]. An *in-situ* NTS gauge is shown in Figure 6.3.

There were some errors in the positioning of the NTS gauges relative to the crack tip. These were attributed to position errors during the cementing process - typically in the order of ±0.2 mm in both directions. Additionally the NTS gauges were placed ahead of the crack to allow 1mm of growth before the crack tip was 0.5 mm in front of and 0.6mm above the gauge. The cementing positions were therefore based on the proposition that the crack would grow straight but inevitably some cracks deflected upon resumption of testing. Any significant deflections were noted and discussed in the results.

Measurements of 'global' crack closure levels were made using the CMOD gauge. The knife-edges of an Instron 10mm gauge-length clip gauge were mounted on to grooved, fibreglass tabs adhered to each side of the crack mouth and secured in place with rubber bands. The fibreglass tabs were required to prevent electrical shorting of the DCPD current through the clip gauge during the tests.

An analogue to digital (A-D) convertor was used to record load and strain/displacement data from each gauge simultaneously during cyclic loading and unloading of the specimen under both SVAL (before and after overload event) and CVAL. The system is described in Appendix B. The load-strain/displacement or compliance curves were used to determine the point of non-linearity which can be used as an indication of the level of crack closure that is occurring in the specimen. Automatic measurements were made by digitally recording the complete cyclic load-NTS/CMOD curves at a frequency of 0.1 Hz at various crack lengths before, during and after particular loading events. Two hundred data points per cycle were collected for analysis at each crack length.

The analysis of the load-strain/displacement or compliance curves is based on a method used by Donald [58]. A line straight is fitted through the data points of the upper 25% of the load range. The 'reduced' or 'differential' strain is found by subtracting the data points from this line. A computer program was written to perform the data averaging, fitting of the line and calculating the differential strain curve. The actual point on the curve which defines crack closure is rather subjective. Recent interpretations of compliance curves by Donald et. al. [87] and Marci and Lang [32] state that the crack closure contribution to ΔK_{eff} is not necessarily the point of the first non-linearity. However, the differential strain curve is still useful for amplifying the non-linearity of the load-strain/displacement curves and interpretation of closure levels.

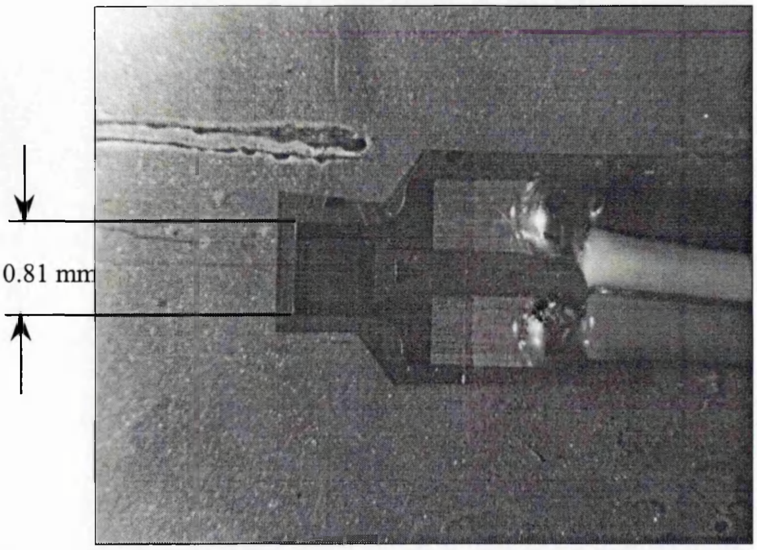

Figure 6.3 Photograph showing Near Tip Strain (NTS) gauge and location of crack tip (Distorted by protective layer of gel).

6.7 Material Characterisation

6.7.1 Titanium Alloy Ti-10V-2Fe-3Al

6.7.1.1 Mechanical and Fatigue Crack Growth Properties

Ti-1023 belongs to the near beta (β) or solute-lean beta alloy class where the body centred cubic (bcc) β phase is predominant [88]. When compared with alpha (α) and α/β titanium alloys, the near-β titanium alloys have a good combination of strength and toughness, increased strength-to-density ratio, improved formability and deeper hardenability which is essential in obtaining uniform properties through relatively thick sections [89]. The chemical composition of the alloy is given in Table 6.2.

The static tensile strength, fracture toughness and constant amplitude fatigue crack growth rate properties for a forged billet, utilised as the source of the CT specimens, used in this investigation were obtained from Ref. [90]. The static tensile strength and fracture toughness properties are shown in Table 6.5. The alloy has a high ultimate tensile strength (σ_{UTS}) of 1146 MPa and a 0.2% proof stress (σ_{YS}) of 1048 MPa. The constant amplitude loading fatigue crack growth data parameters used for the Esacrack NASGRO 2.0 equation (Equation 4.1) were taken from Ref. [90]. Theses are given in Table 6.5 and are used for modelling of the subsequent Ti-1023 tests given in Section 7.1.7. The constant amplitude loading fatigue crack growth rates for a range of R ratios are shown in Figure 6.4. The threshold stress intensity factors for a range of R ratios are shown in Figure 6.5. This curve displays a characteristic 'knee' at R=0.7 above which the ΔK_{th} value remains constant.

Table 6.2 Chemical composition of titanium alloy Ti-1023 [91]

Element	**Al**	**C**	**Fe**	**H**	**N**	**O**	**V**	**Y**	**Balance**
Composition %wt	2.6-3.4	0.05	1.6-2.2	0.015	0.05	0.13	9-11	0.005	Ti

6.7.1.2 Metallography

Metallographical sections in three planes (L-T, T-S and L-S) were taken from a Ti-1023 compact tension specimen and etched using Kroll's reagent. The microstructure of the Ti-1023 alloy is shown in Figures 6.8 to 6.8.

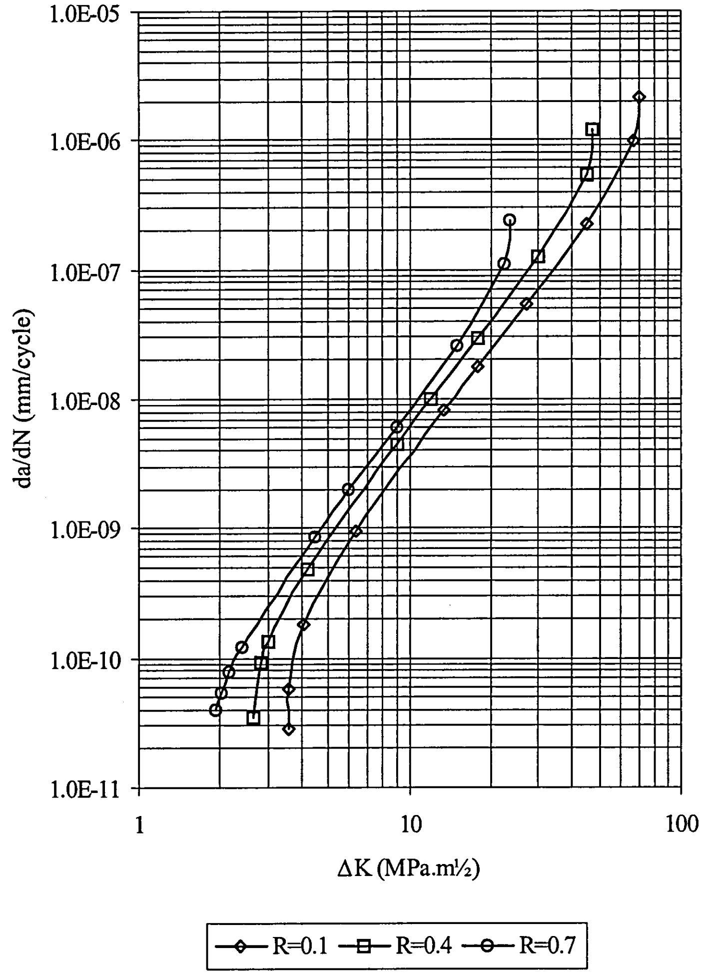

Figure 6.4 Crack growth rate curves for Ti1023 using Esacrack model with parameters taken from Ref. [90].

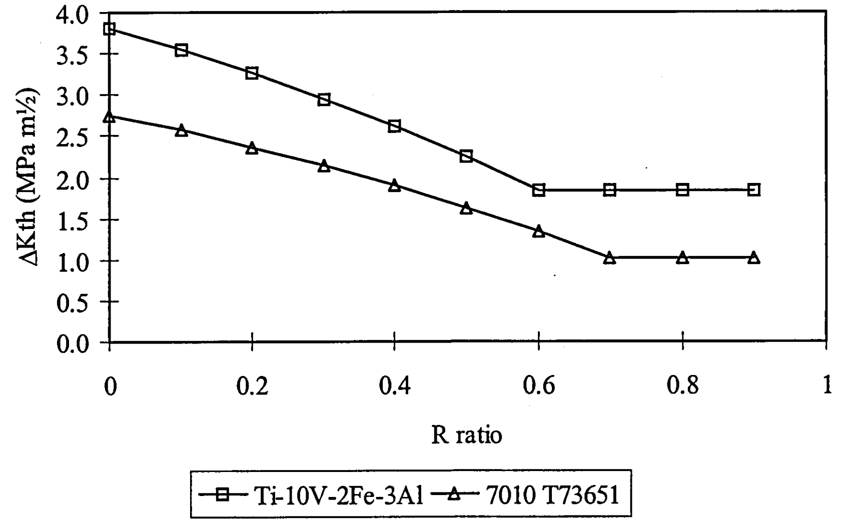

Figure 6.5 Relationship between R ratio and ΔK_{th} for Ti1023 [90] and 7010 [77] using Equation 4.3.

Figure 6.6 Microstructure of Ti-1023 in L-T plane (Mag. ×30)

Figure 6.7 Microstructure of Ti-1023 in L-S plane (Mag. ×60)

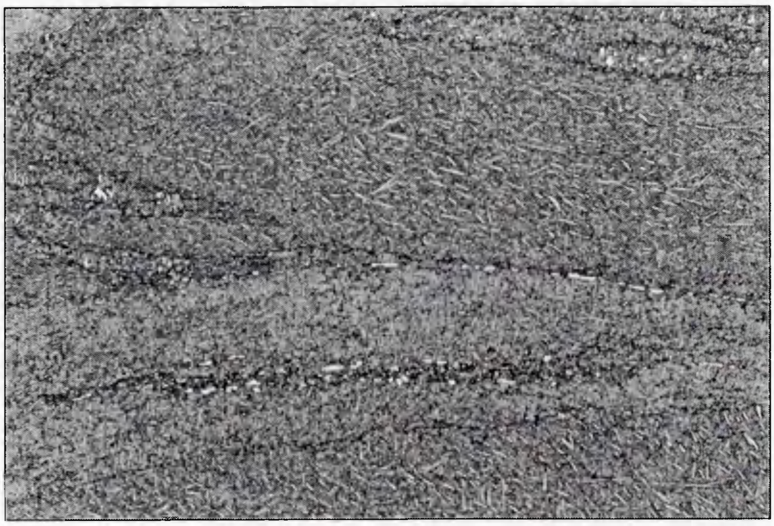

Figure 6.8 Microstructure of Ti-1023 in T-S plane (Mag. ×30)

The micrographs show normal elongation of the grain structure with respect to the rolling direction. A significant feature of the alloy microstructure is the large β grains. These are elongated with the forging direction as shown in Figure 6.6. α phase particulates are visible along the β phase grain boundaries and high aspect ratio primary α are evenly dispersed within the large β grains as shown in Figure 6.7. The primary α particulates are equi-axed or slightly elongated and form a Widmanstatten basketweave type structure. The microstructural features are consistent with observations in Ref.s [91] and [92].

6.7.2 Aluminium Alloy 7010 T73651

6.7.2.1 Mechanical and Fatigue Crack Growth Properties

The aluminium alloy 7010 was developed to have higher static strength, improved stress corrosion and fracture toughness properties in comparison with the widely used 7075 aluminium alloy. 7010 has good corrosion properties which are a result of reduced quench sensitivity in thick section because of added zirconium [93]. The chemical composition of the alloy is given in Table 6.3.

Table 6.3 Chemical composition of aluminium alloy 7010

Element	**Si**	**Fe**	**Cu**	**Mn**	**Mg**	**Cr**	**Zn**	**Zr**	**Balance**
Composition %wt	0.05	0.07	1.6	0.01	2.3	0.01	5.9	0.11	Al

The mechanical properties of 7010 were determined in accordance with ASTM B577M. The resulting strength properties are shown in Table 6.4 and are within the required limits given by the DTD 5130A specification [94].

Table 6.4 Tensile strength properties of 7010 T73651

Property	**Test (MPa)**	**DTD 5130A [94] (MPa)**
Ultimate Tensile Strength σ_{UTS}	529	> 500
0.2% Proof Stress σ_{YS}	465	> 420
Young's Modulus	69,300	-

The constant amplitude fatigue crack growth properties for 7010 were taken from the existing materials database in the Esacrack model [77] which are summarised in Table 6.5. To verify and to gain confidence in these properties, two 7010 CT specimens were tested under CAL at R=0.1 and R=0.7 using the test machine and crack length measurement techniques described in this chapter.

The test results were analysed using the ASTM polynomial curve fit approach [84] and are shown in Figure 6.9 along with the curves from the Esacrack model. The test results show good agreement with the model curves within an acceptable crack growth rate scatter factor of two [95].

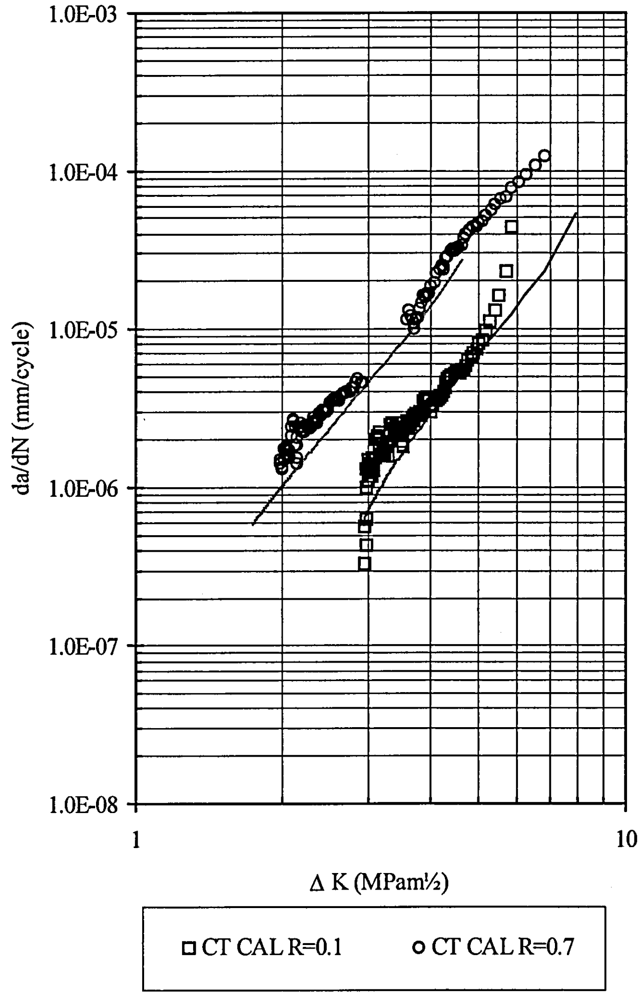

Figure 6.9 Compact tension CAL results for R=0.1 and R=0.7 with Esacrack curves for same R ratios.

Table 6.5 Ti-1023 and 7010 material strength and fracture parameters for ESA Esacrack and Stripy models

Parameter	**Description**	**Ti-1023 [90]**	**7010 [77]**
σ_{UTS}	Ultimate Tensile Strength	1146 MPa	529MPa
σ_{YS}	Yield Strength	1048 MPa	465 MPa
K_{IC}	Fracture Toughness	63.9 MPa.m^{½}	34.1 MPa.m^{½}
A_k	Fit parameter to Equation 4.1	1	1
B_k	Fit parameter to Equation 4.1	1	1
t	Thickness	17.5 mm	17.5 mm
K_C	Plane stress fracture toughness	64.8 MPa.m^{½}	42.6 MPa.m^{½}
C	Crack growth coefficient	0.222 x 10^{-10}	0.362 x 10^{-11}
n	Crack growth exponent	2.545	3.122
p	Exponent to Equation 4.1	0.4	0.5
q	Exponent to Equation 4.1	0.2	1.0
ΔK_0	Threshold at R=0	3.8 MPa.m^{½}	2.75 MPa.m^{½}
R_{cl}	R ratio above which ΔK_{th} becomes constant	0.6	0.7
α	Constraint factor	2.5	1.75
$\sigma_{max} / \sigma_{YS}$	Yield stress ratio	0.30	0.30

6.7.2.2 Metallography

Metallographic sections in three planes (L-T, T-S and L-S) were taken from a 7010 compact tension specimen and etched using Keller's reagent. The microstructure of the 7010 alloy are shown in Figures 6.10 to 6.12. The micrographs show normal elongation of the grain structure with respect to the rolling direction. The grain boundaries are clearly visible and the inclusions are evenly distributed.

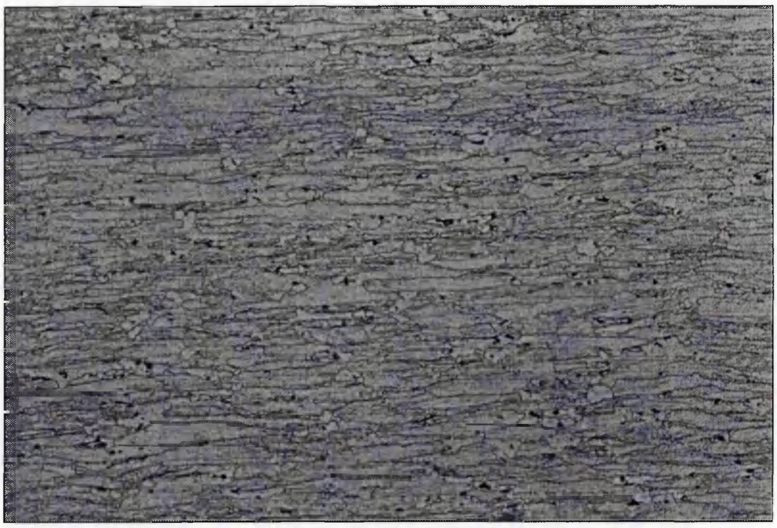

Figure 6.10 Microstructure of 7010 in L-T plane (Mag. ×30)

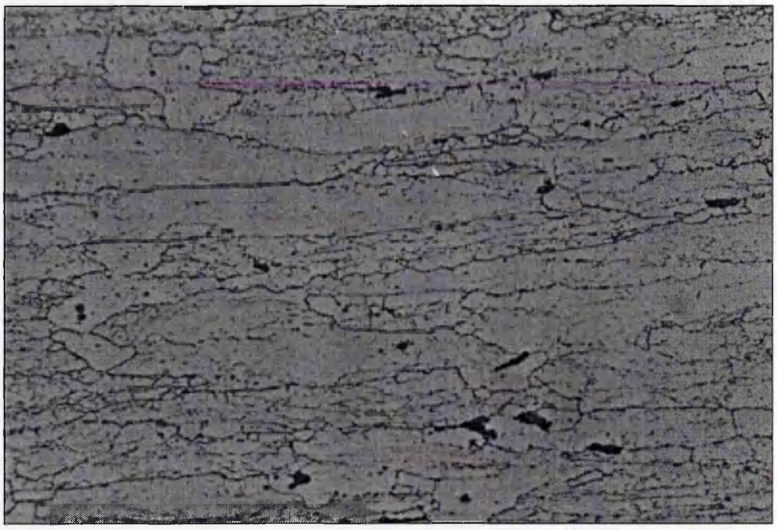

Figure 6.11 Microstructure of 7010 in T-S plane (Mag. ×30)

Figure 6.12 Microstructure of 7010 in L-S plane (Mag. ×30)

6.8 Test Matrices for Variable Amplitude Loading Tests

6.8.1 Simple Variable Amplitude Loading

SVAL sequences usually consist of CAL preceding a single overload (or underload) cycle, followed by the resumption of the CAL cycles. The overload was applied using a ramp sequence from mean CAL load to the overload load and returning to the mean CAL load or underload at an arbitrary ramp rate of 2.1 kN/second. The SVAL tests for the CT titanium Ti-1023 and aluminium 7010 were divided in two parts:

(i) Test set investigating the effect of various overload magnitudes on the transient fatigue crack growth behaviour of Ti-1023 during constant amplitude loading at three R ratios.
(ii) Test set on two Ti-1023 and 7010 compact tension specimens each, with NTS gauges adhered near the crack tip and a CMOD clip gauge, to measure 'local' and 'global' crack closure respectively during overload events.

6.8.1.1 Fatigue Crack Growth following Simple Overload Events

The SVAL tests were defined with tensile overloads of various overload ratios (OLR = overload load/maximum CAL load)) were applied during CAL of R=0.1, 0.4 and 0.7. Three types of overloads were investigated:

a) Single tensile overload (S O/L)
b) Double tensile overloads with overload spaced 3000 cycles apart (D O/L)
c) Overload followed by immediately by an underload (O/U)

The applied loads were defined such that the maximum stress intensity factor (K_{max}) at each overload was the same. The maximum stress intensity factor of the CAL was fixed at 8.0 MPam$^{1/2}$ for all tests. This was to approximate near-threshold loading conditions for the R=0.7 loading: The stress intensity factor range for the R=0.7 CAL was chosen to be ΔK = 2.4 MPam$^{1/2}$ which is just above the threshold value of ΔK_{th} = 1.84 MPam$^{1/2}$ for Ti1023. Additionally the form of the rotorhead spectrum (Refer to Figure 5.8) is such that most cycles have a similar maximum load level and only the R ratio changes. The loads and crack lengths at each overload event type are summarised in Tables 6.6 to 6.11.

Table 6.6 SVAL loads and crack lengths for single overload during R=0.4

Test No.	R Ratio	Type	Overload ratio	o/l 1 @ (mm)	K_{max} (MPa.m^{½})	K_{min} (MPa.m^{½})	ΔK (MPa.m^{½})	$K_{o/l}$ 1 (MPa.m^{½})
1	0.4	S O/L	1.75	20.26	8.099	3.240	4.859	14.175
2	0.4	S O/L	2.00	24.00	8.021	3.209	4.812	16.050

Table 6.7 SVAL loads and crack lengths for single overloads during R=0.1

Test No.	R Ratio	Type	Overload ratio	o/l 1 @ (mm)	K_{max} (MPa.m^{½})	K_{min} (MPa.m^{½})	ΔK (MPa.m^{½})	$K_{o/l}$ 1 (MPa.m^{½})
3	0.1	S O/L	1.47	20.32	9.469	0.947	8.522	13.919
4	0.1	S O/L	1.47	24.02	10.851	1.085	9.766	15.937

Table 6.8 SVAL loads and crack lengths for overloads during R=0.7

Test	R ratio	Type	Overload ratio	o/l 1 @ (mm)	o/l 2 @ (mm)	K_{max} (MPa.m^{½})	K_{min} (MPa.m^{½})	ΔK (MPa.m^{½})	$K_{o/l}$ 1 (MPa.m^{½})	$K_{o/l}$ 2 (MPa.m^{½})
5	0.7	S O/L	1.24	23.94	-	8.032	5.602	2.430	9.995	-
6	0.7	D O/L	1.47	16.00	17.01	8.021	5.613	2.408	11.786	11.790
7	0.7	S O/L	1.75	20.98	-	8.014	5.610	2.404	14.037	-

Table 6.9 SVAL loads and crack lengths for double overloads during R=0.1

Test	R ratio	Type	Overload ratio	o/l 1 @ (mm)	o/l 2 @ (mm)	K_{max} (MPa.m^{½})	K_{min} (MPa.m^{½})	ΔK (MPa.m^{½})	$K_{o/l}$ 1 (MPa.m^{½})	$K_{o/l}$ 2 (MPa.m^{½})
8	0.1	D O/L	1.47	16.50	16.83	8.183	0.818	7.365	12.029	12.184
9	0.1	D O/L	1.47	16.21	16.24	8.087	0.809	7.278	11.857	11.891
10	0.1	D O/L	1.75	20.00	20.03	8.019	0.802	7.217	14.025	14.029
11	0.1	D O/L	2.00	24.00	24.04	8.021	0.803	7.218	16.037	16.047

Table 6.10 SVAL loads and crack lengths for double overloads during R=0.4

Test	R ratio	Type	Overload ratio	o/l 1 @ (mm)	o/l 2 @ (mm)	K_{max} (MPa.m^{½})	K_{min} (MPa.m^{½})	ΔK (MPa.m^{½})	$K_{o/l}$ 1 (MPa.m^{½})	$K_{o/l}$ 2 (MPa.m^{½})
12	0.4	D O/L	1.47	16.30	16.32	8.117	3.247	4.870	11.912	11.931
13	0.4	D O/L	1.47	16.21	16.23	8.027	3.211	4.816	11.787	11.795
14	0.4	D O/L	1.75	21.00	21.03	8.025	3.210	4.815	14.035	14.037
15	0.4	D O/L	2.00	24.00	24.07	8.022	3.209	4.813	16.025	16.074

Table 6.11 SVAL measured loads and crack lengths for overload-underload during R=0.7

Test	R Ratio	Type	Overload ratio	o/l 1 @ (mm)	K_{max} (MPa.m^{½})	K_{min} (MPa.m^{½})	ΔK (MPa.m^{½})	$K_{o/l}$ (MPa.m^{½})	K_{UL} (MPa.m^{½})
16	0.7	O/L - U/L	1.47	16.02	8.026	5.618	2.408	11.789	0.302
17	0.7	O/L - U/L	1.75	20.26	8.096	5.668	2.428	14.171	0.305
18	0.7	O/L - U/L	2.00	24.80	8.014	5.614	2.400	16.037	0.209

6.8.1.2 Crack Closure Measurements following Overload Events

Two baseline CAL R ratios of R=0.1 and 0.7 with single tensile overloads tests were defined to make crack closure measurements on CT specimens with two closure measurement techniques. The same stress intensity ranges as the previous Ti1023 SVAL tests were maintained and the OLR's selected to give reasonable transient crack growth rate responses. The details of the loading are given in Table 6.12.

Table 6.12 Details of global and local crack closure measurement tests

Test	CAL R ratio	Material	OLR	ol @ (mm)	K_{max} (MPa.m^{½})	K_{min} (MPa.m^{½})	K_{ol} (MPa.m^{½})
19	0.1	7010	2.01	29.13	8.37	0.837	16.86
20	0.7	7010	1.33	29.47	8.48	5.93	11.29
22	0.1	Ti1023	2.00	27.51	7.87	0.787	15.74
23	0.7	Ti1023	1.35	30.74	8.02	5.61	10.86

6.8.2 Complex Variable Amplitude Loading

6.8.2.1 Omission Level Investigation in Ti-1023 and 7010

Four tests on each of the Ti-1023 and 7010 CT specimens were conducted using the progressive omission of small cycles from the Rotorix 16 loading sequence as described in Table 5.6 (sequences L16, L20, L24 and L32). The loads chosen for the tests are defined in terms of the peak or maximum load experienced by the sequence which is level 100 in Rotorix. Hence the peak stresses and stress intensity factors are referenced to this level and are termed S_{peak} and K_{peak} respectively.

The test load, P_{peak} for all the tests was selected so that the small range 16 cycles ΔK would be just below ΔK_{th} for Ti-1023 (1.8 MPa.m^{½}) at the start of the Rotorix 16 test. The P_{peak} value was found by considering the 'dominant' R ratio for the level 16 load range (R_{dom}=0.875) in the loading sequence. Using the stress intensity solution (Eqn. 6.1) the load which gives ΔK =

1.66 MPam^{½} for Ti-1023 at the start crack length of 16 mm was solved for. This gave P_{peak} = 10 kN which was used for all the omission level tests.

The specimens were fatigue pre-cracked to 16 mm in accordance with the load step down procedures defined in ASTM E 647 to avoid transient crack growth effects. The test matrices are summarised in Tables 6.13 and 6.14.

Table 6.13 Test matrix for Ti-1023 CT progressive omission level tests

Test	P_{peak} (kN)	Omission level	Start length (mm)	End length (mm)	Start K_{peak} (MPa.m^{½})	End K_{peak} (MPa.m^{½})
24	10	L16	16.9	49.77	10.4	49.41
25	10	L20	16.74	49.15	10.3	47.08
26	10	L24	17.43	49.47	10.6	48.26
27	10	L32	16.76	48.63	10.3	45.27

Table 6.14 Test matrix for 7010 CT progressive omission level tests

Test	P_{peak} (kN)	Omission level	Start length (mm)	End length (mm)	Start K_{peak} (MPa.m^{½})	End K_{peak} (MPa.m^{½})
28	10	L16	16.39	41.54	10.2	28.75
29	8	L16	17.60	48.47	8.54	35.78
30	10	L20	16.39	41.45	10.2	28.61
31	10	L24	16.37	42.18	10.2	29.79
32	10	L32	16.38	41.45	10.2	28.61

6.8.2.2 Crack Closure Levels During Rotorhead Sequence

To investigate the level of closure occurring during the CVAL sequences, crack closure measurements were made on one Ti1023 and one 7010 CT specimen for a selected sequence of 12,000 cycles from the Rotorix 16 loading sequence. The selected section was taken from points 538,000 to 562,000 (cycles 269,000 to 281,000) and is shown in Figure 6.14. The selection contained representative load features such as high R ratio cruise manoeuvre dispersed with low R ratio low speed manoeuvres. The tests were conducted with a peak stress intensity levels of K_{peak} = 20.1 MPa.m^{½} and 21.8 MPa.m^{½} as given in Table 6.15.

Table 6.15 Test matrix for Ti-1023 and 7010 CT CVAL closure measurement tests

Test	**Material**	**Omission level**	**Selected L16 Sequence (turning point no.)**	**P_{peak} (kN)**	**Start crack (mm)**	**K_{peak} (MPa.m^{½})**
33	Ti-1023	L16	538,000-562,000	13.0	27.59	20.1
34	7010	L16	538,000-562,000	13.0	29.70	21.8

The NTS gauges were adhered near the crack tip in the same relative position as for the SVAL NTS tests. The closure measurements were made by digitally recording the complete cyclic load-NTS/CMOD curves at a frequency of 0.1 Hz in a similar manner to the SVAL closure measurement tests. The loading sequence test was paused at pre-determined cycles to take closure measurements for the load range of that particular cycle. This is shown in Figure 6.13. This was done to avoid introducing artificial load cycles whilst taking closure measurements. To achieve this, the selected loading sequence was divided up into fragmented files which were then run on the machine and closure measurements taken at the end of each.

The CAL loads before the selected sequenced commenced were 11.19 ± 1.25 kN (R=0.8) to simulate a long period of growth from high R ratio range 16 cycles over 0.7 mm. Therefore the residual stress zone at the crack tip would approximate that experienced during actual CVAL and the loading sequence would not be influenced by previous pre-cracking loads.

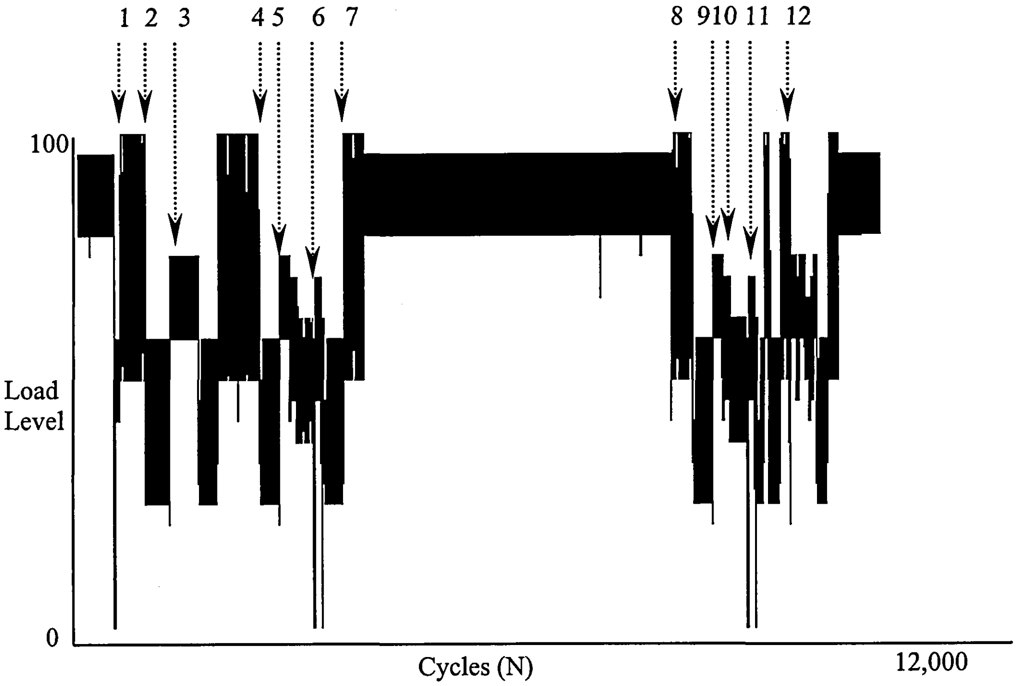

Figure 6.13 Selected loading sequence for CVAL crack closure measurements showing points of NTS gauge and CMOD gauge closure measurements.

7. RESULTS

7.1 Simple Variable Amplitude Loading on Ti1023

The results of crack growth responses to different overload types for the SVAL tests on Ti1023 are presented below. The results are divided into different baseline CAL R ratios with varying OLR or overload type (single, double or overload-underload). Tables 7.1 to 7.6 summarise the loading parameters for each test.

For each SVAL test, the overall delay distances (or affected distance) and cycles were taken from da/dN versus ΔK plots. These are useful for describing the extent of the crack growth transient following an overload event. The delay distances and cycles were given by a standardised procedure for interpreting crack growth retardation as follows: Using the da/dN versus ΔK plot, the delay distance (from first overload event for double overloads) was found when the post-overload growth rate reaches 90% of the pre-overload growth rate as illustrated in Figure 7.3. The pre-overload crack growth rate was taken as the average of the five data points before the overload is applied. The corresponding delay distances and cycles were determined through reading the *a* versus N data file. If there was a large amount of scatter on the crack growth rate data then this method could not be rigorously applied. In these cases, personal judgement was used and this is noted. The results of all the SVAL tests are presented in Tables 7.7 to 7.11.

7.1.1 Tensile Overloads During R=0.4 CAL

Single overloads were applied to two specimens at two different overload ratios.

Table 7.1 Single tensile overloads during R=0.4 CAL

Test No.	**Type**	**Overload ratio**	**K_{max} (MPa.m^{½})**	**K_{min} (MPa.m^{½})**	**$K_{o/l}$ (MPa.m^{½})**
1	S O/L	1.75	8.10	3.24	14.18
2	S O/L	2.0	8.02	3.21	16.05

For the single overload of OLR = 1.75 applied during R=0.4 CAL there was distinct fatigue crack growth transient measured following the overload as shown as a small perturbation in the crack growth curve of Figure 7.1. Referring to Figure 7.2, there is a delayed retardation of crack growth rate following the overload with a reduction in crack growth rate from 6.6 x 10^{-6} mm/cycle (pre-overload) to 3.3 x 10^{-6} mm/cycle. The point of maximum retardation occurred 0.04 mm after the point of the overload. The point at which the growth rate returns to pre-overload rates occurred after 0.12 mm which is the delay distance.

The single overload of OLR = 2.0 gave significantly more delayed retardation following an initial acceleration after the overload event as indicated by Figure 7.1. Referring to Figure 7.3, the initial acceleration appears to occur before the overload is applied because the growth rates are averaged over five points using a least squares fit method. The ΔK applied during the overload cycle was 12.8 $\text{MPa}\sqrt{\text{m}}$ and would correspond to a crack growth increment of approximately 1×10^{-4} mm (from CAL growth rates) which is much less than the growth increment of 0.066 mm measured 2500 cycles after the overload. The pre-overload growth rate of 6.5×10^{-6} mm/cycle would give a crack growth increment of just 0.016 mm over 2500 cycles so the overload caused some increase growth rates. Therefore, the initial acceleration took place sometime after the overload event and before the first measurement at 2500 cycles. The point of maximum retardation occurred 0.08 mm after the overload. The point at which the growth rate returns to pre-overload rates occurred 0.29 mm after the overload which is the delay distance.

7.1.2 Tensile Overloads During R=0.1 CAL

Two single overloads at OLR = 1.47 were applied during R=0.1 CAL.

Table 7.2 Single tensile overloads during R=0.1 CAL

Test No.	**Type**	**Overload ratio**	**K_{max} ($\text{MPa.m}^{1/2}$)**	**K_{min} ($\text{MPa.m}^{1/2}$)**	**$K_{o/l}$ ($\text{MPa.m}^{1/2}$)**
3	S O/L	1.47	9.47	0.947	13.92
4	S O/L	1.47	10.85	1.085	15.94

There were no distinct transient effects distinguishable from the scatter in fatigue crack growth rates. It may be concluded that this magnitude of overload does not produce significant transient effects.

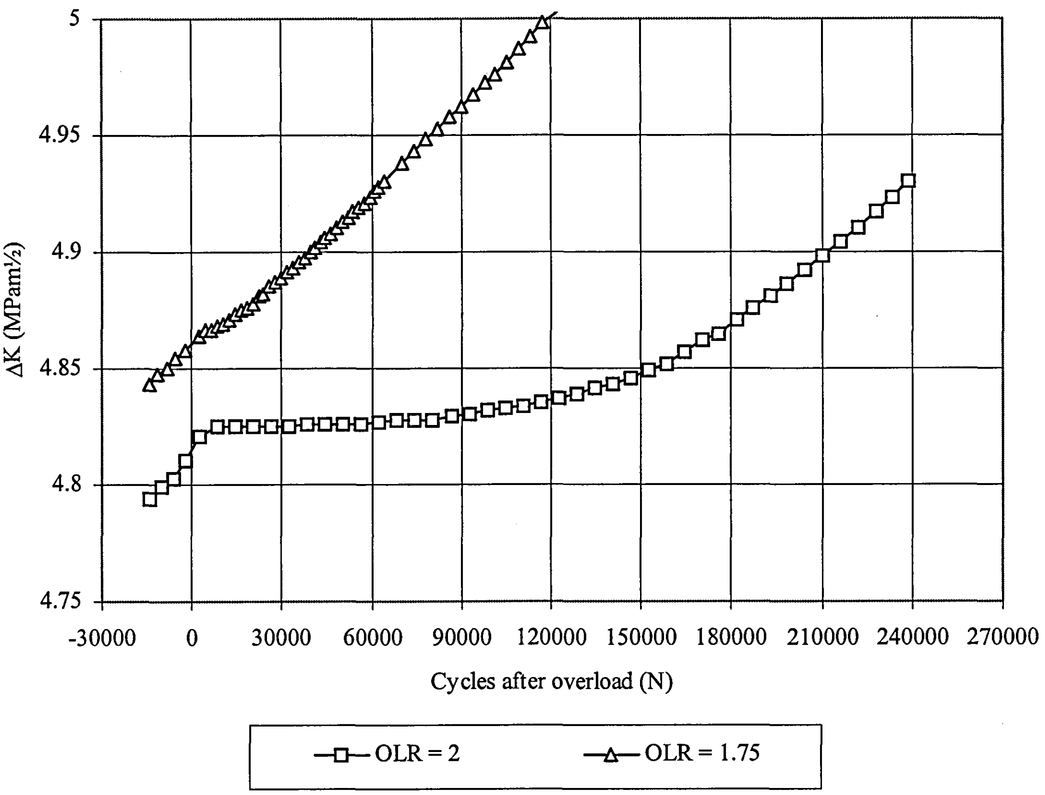

Figure 7.1 Crack growth results for various overloads on R=0.4 CAL Ti-1023, K_{max}=8.02 MPa.$m^{½}$

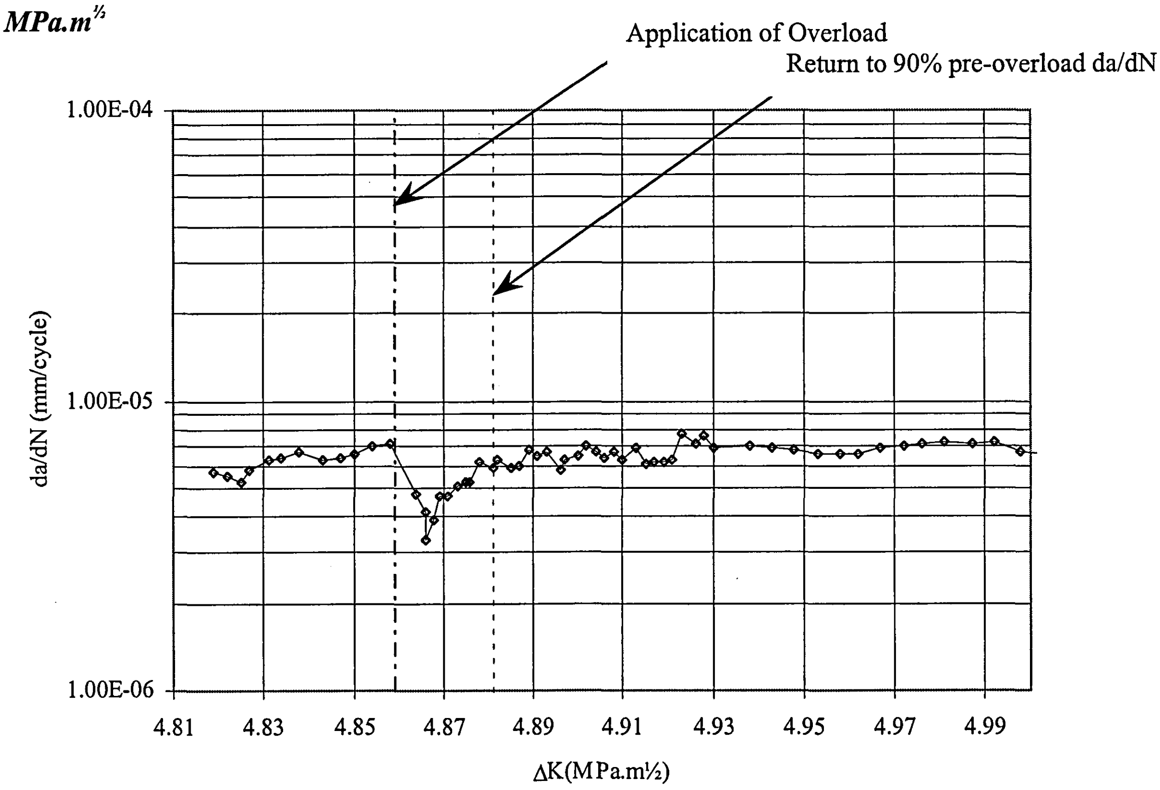

Figure 7.2 Crack growth transient for overload ratio of 1.75 on R=0.4 CAL, Ti-1023 K_{ol}=14.2 MPa.$m^{½}$ showing application point of overload and return to 90% pre-OL growth rates

7.1.3 Tensile Overloads During R=0.7 CAL

Overloads were applied to three specimens at three different overload ratios. The last two overloads resulted in delayed crack arrest. The OLR of 1.24 in the first test did not give crack arrest.

Table 7.3 Tensile overloads during R=0.7 CAL

Test No.	Type	Overload ratio	K_{max} (MPa.m^{½})	K_{min} (MPa.m^{½})	$K_{o/l}$ 1 (MPa.m^{½})	$K_{o/l}$ 2 (MPa.m^{½})
5	S O/L	1.24	8.03	5.60	10.00	-
6	D O/L	1.47	8.18	5.61	11.79	11.79
7	S O/L	1.75	8.01	5.61	14.04	-

For the single overload, OLR = 1.24, there was only a small crack growth transient after the overload event. This was a small delayed retardation following the overload, with a reduction in crack growth rate from 1.5x 10^{-6} mm/cycle (pre-overload) to 9.6 x 10^{-7} mm/cycle. The point at which the growth rate returned to pre-overload rates gave a delay distance of 0.02 mm. Interestingly, for the double overloads, OLR = 1.47 there was a small amount of measurable crack growth of 0.01 mm (measured from the point of the first overload) until complete crack arrest occurred. This period was approximately 34,000 cycles. Likewise, for the single overload, OLR = 1.75 there was an increment of growth of 0.04 mm and 45,000 cycles before complete crack arrest as shown in Figure 7.4.

For the high R ratio, R=0.7 CAL tests there was a significant change in delay responses with change in OLR. That is, an OLR=1.24 will give a small transient effect whereas an OLR=1.47 will cause crack arrest.

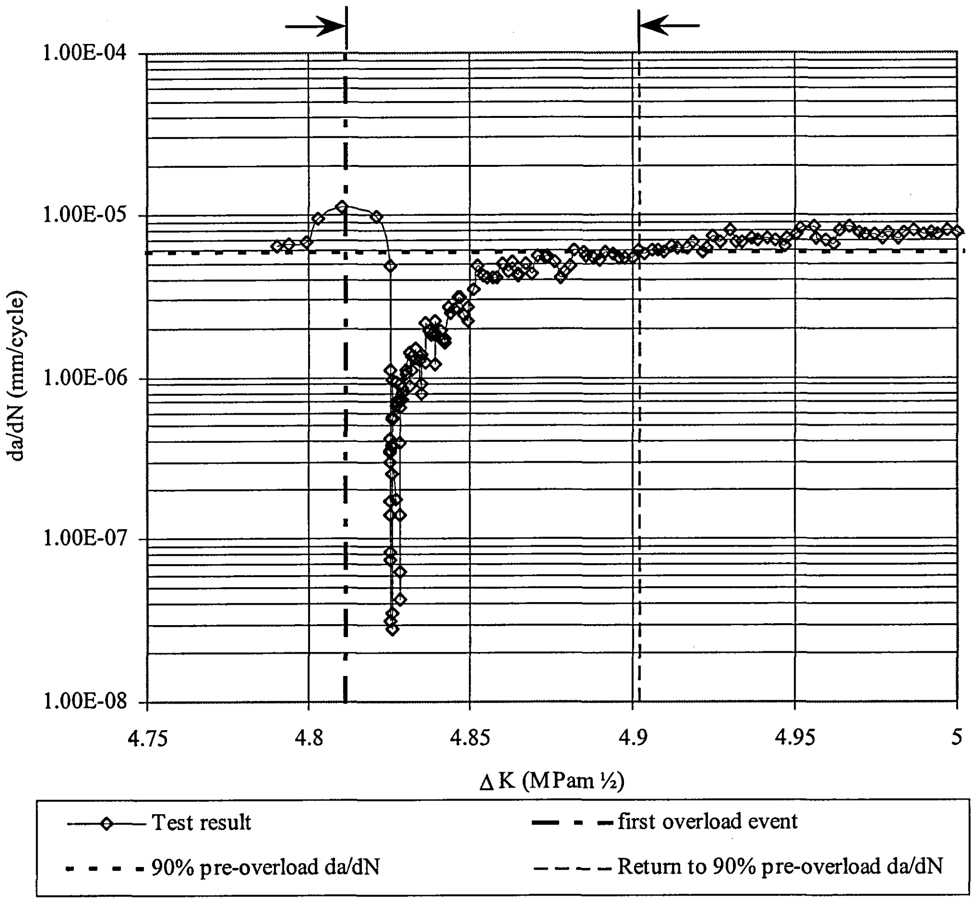

Figure 7.3 Crack growth transient for overload of 2.0 on R=0.4 CAL Ti-1023. Also shown is method for deriving crack growth rate transient information and overload affected zone.

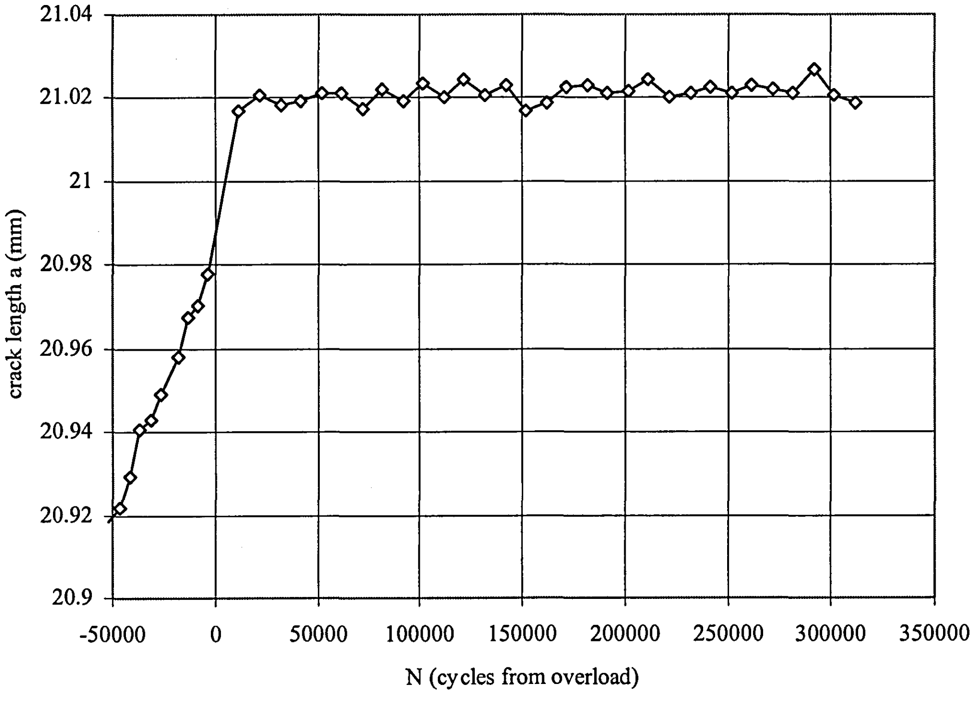

Figure 7.4 Crack arrest after overload of 1.75 on R=0.7 CAL, Ti-1023, K_{ol}=14.04 MPa.m$^{1/2}$. Note increment of growth (0.04mm) before arrest occurred.

7.1.4 Double Tensile Overloads During R=0.1 CAL

Double overloads spaced 3000 cycles apart were applied to four specimens at three different overload ratios.

Table 7.4 Double tensile overloads during R=0.1 CAL

Test No.	Type	Overload ratio	K_{max} (MPa.m^{½})	K_{min} (MPa.m^{½})	$K_{o/l}$ 1 (MPa.m^{½})	$K_{o/l}$ 2 (MPa.m^{½})
8	D O/L	1.47	8.18	0.818	12.03	12.18
9	D O/L	1.47	8.09	0.809	11.86	11.89
10	D O/L	1.75	8.02	0.802	14.03	14.03
11	D O/L	2.00	8.02	0.802	16.04	16.05

For the double overload, OLR = 1.47 there was a small amount of retardation measured. There was a brief return to pre-overload growth rates before the second overload was applied. The crack growth between overloads was 0.03 mm. The second overload produced a similar transient response as the first.

For the double overload, OLR = 1.75 there was a delayed retardation, during which the second overload was applied. Upon application of the second overload the crack rate increased rapidly, then delayed again. The extent of delay was slightly less for the second overload. The overall delay distance was 0.10 mm.

Similarly, for the double overload, OLR = 2.0 there was an initial acceleration, followed by delayed retardation during which point the second overload was applied as shown in Figure 7.5. The growth rate increased slightly due to the second overload, then delayed retardation occurred again, in a similar manner, before slowly returning to pre-overload growth rates giving a significant delay distance of 0.29 mm.

For the overloads applied at OLR = 1.75 and 2.0 the application of the first overload generally produced a crack growth transient which was interrupted by the application of the second overload. In each case the response after the second overload was similar to a single overload transient tending to 'wipe-out' the effect of the first overload.

7.1.5 Double Tensile Overloads During R=0.4 CAL

Double overloads spaced 3000 cycles apart were applied to four specimens at three different overload ratios.

Table 7.5 Double tensile overloads during R=0.4 CAL

Test No.	Type	Overload ratio	K_{max} (MPa.m^{½})	K_{min} (MPa.m^{½})	$K_{o/l}$ 1 (MPa.m^{½})	$K_{o/l}$ 2 (MPa.m^{½})
12	D O/L	1.47	8.12	3.25	12.03	12.18
13	D O/L	1.47	8.03	3.21	11.79	11.80
14	D O/L	1.75	8.03	3.21	14.04	14.04
15	D O/L	2.0	8.02	3.21	16.03	16.07

The double overload, OLR = 1.47, gave a negligible amount of growth rate transient measured even though there was an increment of 0.02 mm of growth measured between each overload. The measured changes in growth rates were within the bounds of the DCPD system accuracy.

For the double overload, OLR = 1.75 there was an initial acceleration followed by a delayed retardation during which the second overload was applied as shown in Figure 7.6. The second overload resulted in a brief increase in growth rates followed by another delayed retardation. The overall delay distance was 0.14 mm which was larger than the 0.12 mm given by the equivalent single overload test. The distance to the point of the second overload was only 0.03 mm. Therefore the delay distance of a second overload is approximately 0.14 - 0.03 = 0.11 mm which is similar to that of the single overload test. The second overload tends to behave as if the previous event did not occur or alternatively it tends to override the effect of the first overload as found in the R=0.1 double overloads.

For the double overload, OLR = 2.0 there was an initial acceleration of crack growth rate followed by a delayed retardation. During this retardation the second overload was applied 0.061 mm later and this briefly increased growth rates but was followed by complete crack arrest.

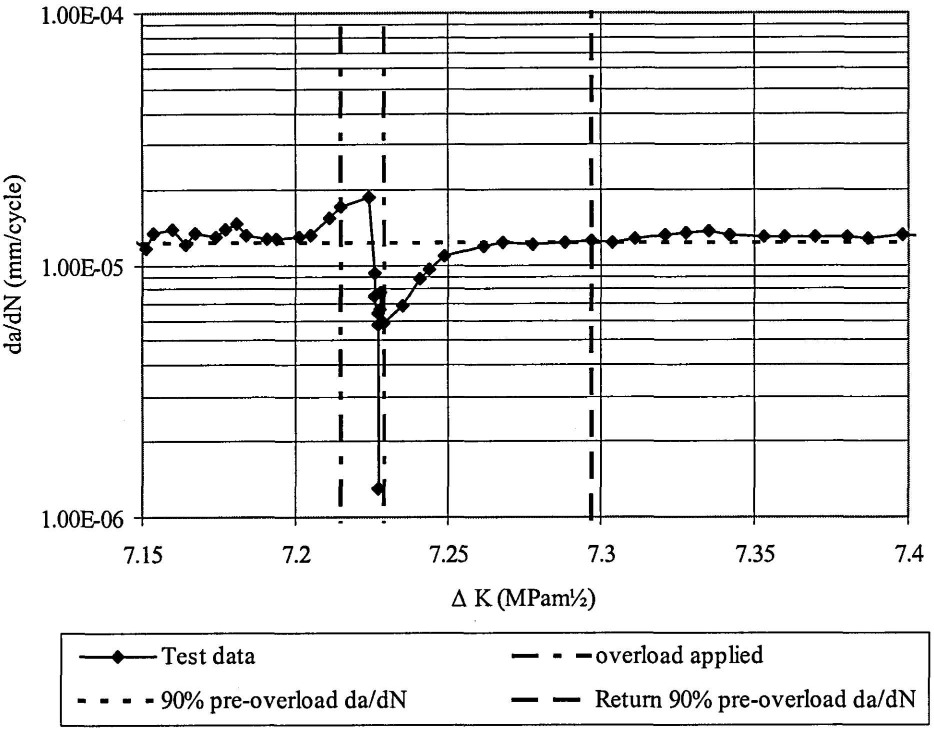

Figure 7.5 Crack growth rate transient for double overload 2.0 applied 3000 cycles apart during R=0.1 CAL, Ti-1023, K_{ol}=16.05 MPa.m^{½}.

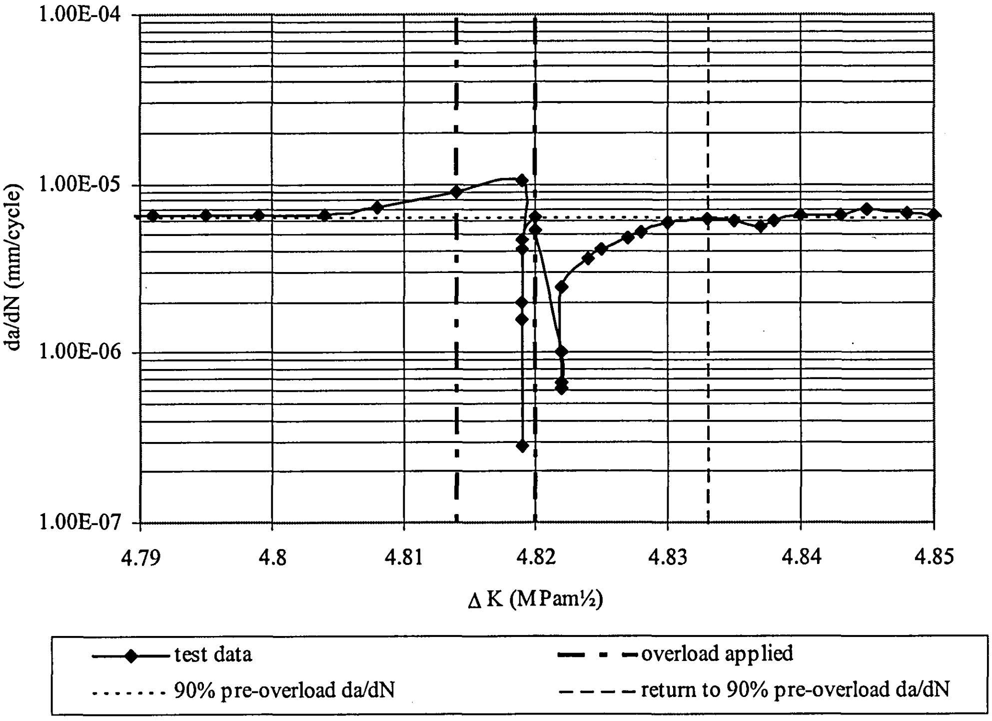

Figure 7.6 Crack growth curve following double overload of 1.75 during R=0.4 CAL Ti-1023, K_{ol}=14.04 MPa.m^{½}. Note immediate acceleration upon application of second overload then subsequent retardation.

7.1.6 Tensile Overload-Underloads During R=0.7 CAL

Three overloads at OLR = 1.47, 1.75 and 1.24 all followed immediately by a tensile underloads were applied during R = 0.7 CAL.

Table 7.6 Tensile overload followed by underload during R=0.7 CAL

Test No.	Type	Overload ratio	K_{max} (MPa.m^{½})	K_{min} (MPa.m^{½})	$K_{o/l}$ (MPa.m^{½})	K_{ul} (MPa.m^{½})
16	O/U	1.47	8.03	5.62	11.79	0.302
17	O/U	1.75	8.10	5.27	14.17	0.305
18	O/U	2.00	8.01	5.61	16.04	0.209

For the single overload-underload at OLR = 1.47 there was no measurable transient effect even though the equivalent single overload test (Section 7.1.3) gave complete crack arrest. For the single overload-underload OLR=1.75 there was an initial acceleration of crack growth rate but no significant retardation, whereas the single overload test gave complete crack arrest. For the single overload-underload OLR=2.0 there was an initial acceleration followed by delayed retardation, then complete crack arrest. The effect of an immediate underload is to reduce the extent of transient behaviour resulting from a tensile overload. See discussion.

7.1.7 SVAL Delay Distances and Cycles

The delay distances and cycles resulting from each SVAL overload test are summarised in Tables 7.7 to 7.11 along with the results from the Stripy predictions. The ratios between measured and predicted delay distances are also given. All Stripy tests were performed with a plane strain constraint factor of α= 2.5. This factor controls the size of the crack tip plastic zone. The numbers in brackets for each 'test delay distance' is the plane strain overload plastic zone (OLPZ) size for that overload given by Equation 3.8. It is significant to note that in most cases the measured delay distance is up to an order of magnitude *greater* than the analytical OLPZ size. See discussion

Table 7.7 Delay results for single tensile overloads during R=0.4 CAL

Test No.	Type	Overload ratio	Test delay distance D_t (mm)	Test delay cycles N_t	Stripy delay distance D_S (mm)	Stripy delay cycles N_S	D_t/D_S	N_t/N_S
1	S O/L	1.75	0.12 (0.010)	22500	0.006	2005	20	11.2
2	S O/L	2.0	0.40 (0.013)	195000	0.011	4413	36	44

These two single over load tests produced the most dramatic transient responses following each overload. The delay distances were significantly greater than the plane strain OLPZ by up to 30 times for the OLR=2.0. The Stripy results were similar to the OLPZ size indicating the delay distance in the model is controlled by this. Comparing the delay distances with the plane stress OLPZ (OLR=1.75 gives 0.062 mm, OLR=2.0 gives 0.080mm) on the specimen surfaces the test still gives prolonged delay effects. The model also underestimates the number of cycles to delay end.

Table 7.8 Delay results for tensile overloads during R=0.7 CAL

Test No.	Type	Overload ratio	Test delay distance D_t (mm)	Test delay cycles N_t	Stripy delay distance D_S (mm)	Stripy delay cycles N_S	D_t/D_S	N_t/N_S
5	S O/L	1.24	0.02 (0.013)	24147	0.001	1203	20	20
6	D O/L	1.47	0.01 (0.007)	arrest	0.005	9026	-	-
7	S O/L	1.75	0.04 (0.010)	arrest	0.004	1265	-	-

For these test with overloads applied during R=0.7 CAL the delay distances are of a similar order to the OLPZ size. Note that the latter two cases are measured up to the point of crack arrest. The case of delay measured for OLR=1.24 and crack arrest for the other two, is an interesting result because most models do not predict significant closure effects at high R ratio yet the crack arrest suggests a significant load interaction effect. The results also demonstrate a dramatic response to overloads for high R ratio loading: A small overload of 1.24 gives a small delay effect and increasing this to 1.47 gives complete crack arrest whereas at lower R ratios the responses are more 'gentle'.

Stripy does not predict the crack arrest cases and only gives a small delay cycle for the OLR=1.24 case. Stripy is a model based on crack closure in the wake of the crack so it might be suggested that there is another mechanism in addition to closure that is contributing to the observed delay effects.

Table 7.9 Delay results for double tensile overloads during R=0.1 CAL

Test No.	Type	Overload ratio	Test delay distanceD_t (mm)	Test delay cycles N_t	Stripy delay distance D_S (mm)	Stripy delay cycles N_S	D_t/D_S	N_t/N_S
8	D O/L	1.47	No delay	-	0.053	4602	-	-
9	D O/L	1.47	0.06 (0.007)	5564	0.053	4602	1.1	1.2
10	D O/L	1.75	0.10 (0.010)	10567	0.052	5003	1.9	2.1
11	D O/L	2.00	0.294(0.013)	28261	0.054	5802	5.4	4.9

These double overload tests showed a general increase in delay distances and cycles with increase in OLR. The comparison with the OLPZ size only provides a guide as there were two overload applied with crack growth between them. Stripy predicted the delay effects reasonably well at OLR=1.47 but became less accurate for higher OLR's.

Table 7.10 Delay results for double tensile overloads during R=0.4 CAL

Test No.	Type	Overload ratio	Test delay distanceD_t (mm)	Test delay cycles N_t	Stripy delay distance D_S (mm)	Stripy delay cycles N_S	D_t/D_S	N_t/N_S
12	D O/L	1.47	0.04 (0.007)	7571	0.021	4102	1.9	1.8
13	D O/L	1.47	0.04 (0.007)	7559	0.021	4102	1.9	1.8
14	D O/L	1.75	0.14 (0.010)	33276	0.018	4907	7.8	6.8
15	D O/L	2.0	0.08 (0.013)	arrest	0.013	4814	-	-

These double overload tests for R=0.4 CAL showed a general increase in overload effects as the OLR was increased. Again the comparison with the OLPZ size only provides a guide as there were two overloads applied with crack growth between them. The two repeated tests at OLR=1.47 gave similar results which gave some confidence to the results. The double OL at OLR=2.0 gave complete crack arrest with the distance to arrest point measured. This is significantly less than the delay distance measured for the equivalent single overload test which was 0.40 (see Table 7.7).

Table 7.11 Delay results for tensile overload followed by underload during R=0.7 CAL

Test No.	Type	Overload ratio	Test delay distance D_t (mm)	Test delay cycles N_t
16	OL-UL	1.47	0.03 (0.007)	45500
17	OL-UL	1.75	0.05 (0.010)	33276
18	OL-UL	2.00	0.02 (0.013)	arrest

The delay effects were significantly reduced by the addition of an underload following the overload for R=0.7 CAL. OLR's of 1.47 and 1.75 now gave measurable delay effects where previously with just a single overload they gave crack arrest.

The overload-underload tests at R=0.7 was not modelled because Stripy cannot represent the underload correctly: Stripy is given load information which represents the rising part of a fatigue cycle and it assumes that a complete fatigue cycle results. This is satisfactory for CAL and overloads. However, the first part of the underload half cycle is falling and the cycle completes when the load rises again. Stripy would model this as a rising half cycle followed by a falling half cycle which effectively adds an extra half cycle as shown in the figure below:

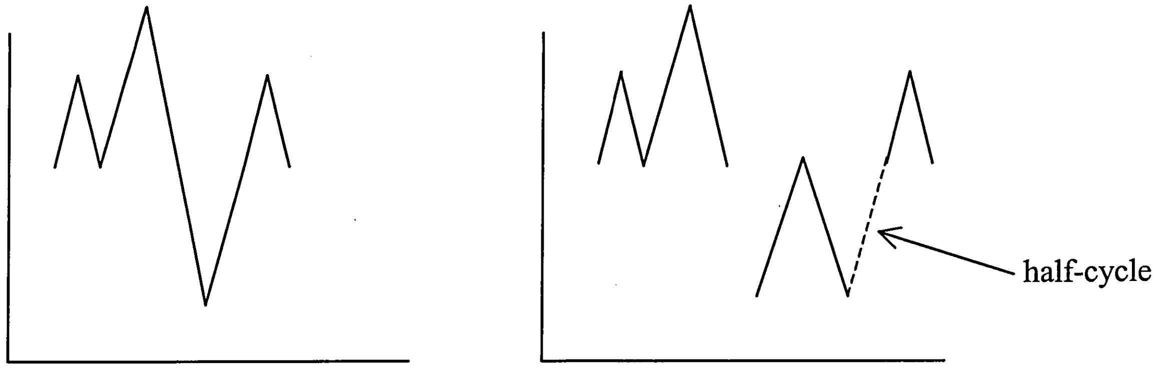

(i) Overload-underload sequence (ii) Stripy representation of overload-underload

Figure 7.7 Additional half cycle due to Stripy representation of overload-underload test

In general, the effect of increasing OLR for the tests increases the extent of the delay distance and the delay cycles. The effect of increasing OLR on delay is more significant with increasing R ratio. There is a dramatic increase in delay effects for overloads during R=0.7 CAL which conflicts with the model which does not predict this. The cases of crack arrest demonstrated that growth rates can be reduced to nearly zero by an overload and occur at a point just greater than the OLPZ. The Stripy results show similar trends compared with the test delay distance and cycles results but consistently under-predicted the effects. Crack arrest was not predicted by the model.

7.2 Fatigue Crack Closure Measurements During SVAL

7.2.1 Fatigue Crack Closure in Ti1023

Figure 7.8 shows the transient growth rate for the OLR of 2 on R=0.1 CAL for which NTG and CMOD crack closure measurements were made. The delay effect was relatively small but there was a reduction in growth rate by a factor of ten at the point of maximum retardation. There was no crack growth acceleration observed after the application of the overload. The delay length was 0.06 mm which is larger than the plane strain OLPZ size of 0.02 mm.

Figures 7.9 and 7.10 show the differential NTG strain and differential CMOD versus K_{app} for three selected points before (a = -0.005 mm), immediately after (a = 0.002 mm) and at the point of maximum retardation (a = 0.006 mm) of the crack growth transient. Two significant observations are evident: Firstly the changes in linearity which are indications of closure levels give different values for each measurement technique: The NTG gave K_{cl} = 4.0 MPa.m^{½} whereas the CMOD gauge gave K_{cl} = 2.3 MPa.m^{½}. Secondly, there were no detectable *changes* in closure level during the overload transient from either gauge. Other closure measurements that were made during the test gave similar results to the three curves shown here - only three curves are shown for clarity.

The overload of 1.35 on R=0.7 CAL gave crack arrest after a small increment of crack growth following the overload and no further crack growth was observed after $2x10^6$ cycles. The NTG strain-load curves shown in Figure 7.11 show no indication of crack closure at this high R ratio because the curves have no change in linearity. Additionally there were no indications from further analysis using the differential displacement method which might suggest a change in curvature of the strain/CMOD versus load curves from the point of overload to crack arrest. Although there were distinct observations of a crack growth arrest there were no detectable changes in compliance of the specimen. This suggests that the techniques used here to measure crack closure are not sensitive enough or another crack tip damage mechanism is responsible. See discussion.

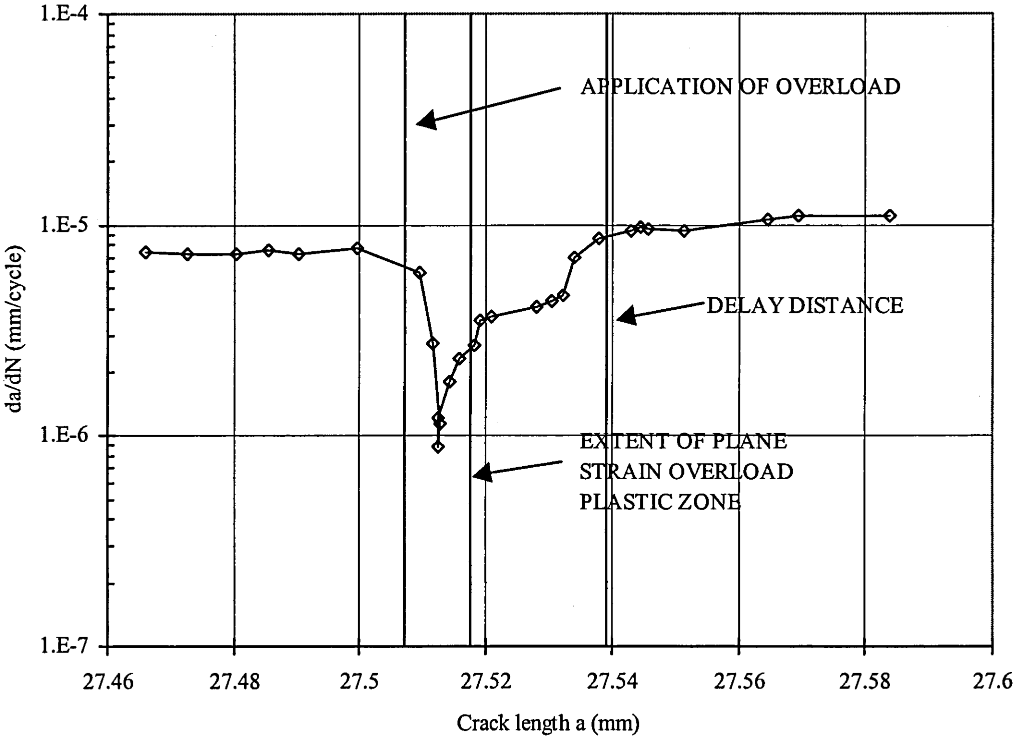

Figure 7.8 Crack growth rate transient for overload of 2 on R=0.1 CAL Ti-1023, K_{ol}=15.74 MPa.m½ showing extent of OLPZ and delay length caused by the overload.

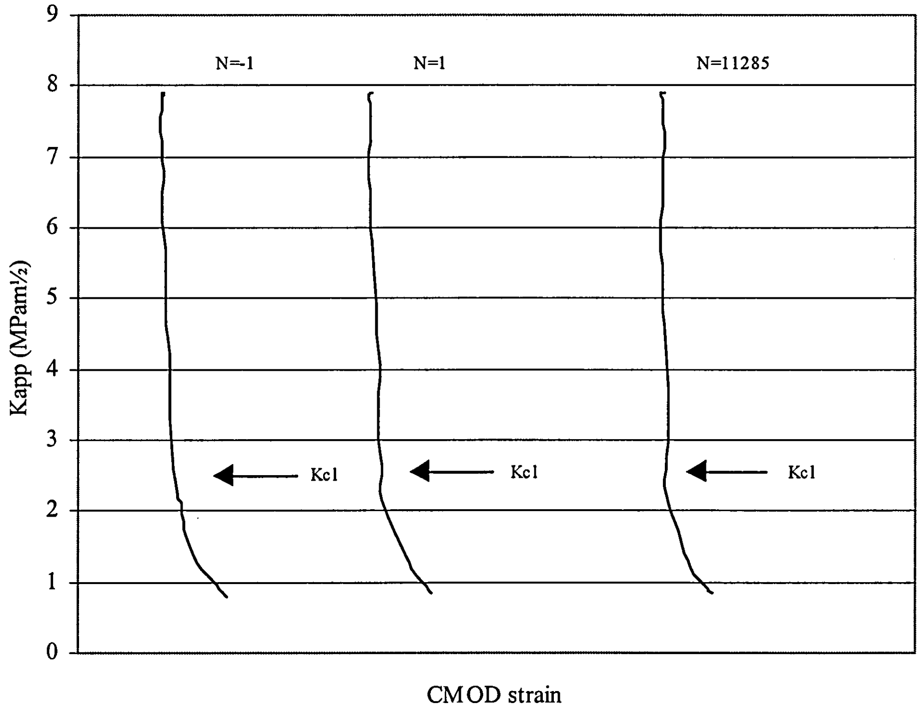

Figure 7.9 Differential strain versus applied stress intensity factor for crack closure measurements using a CMOD gauge during overload of 2 on R=0.1 CAL.

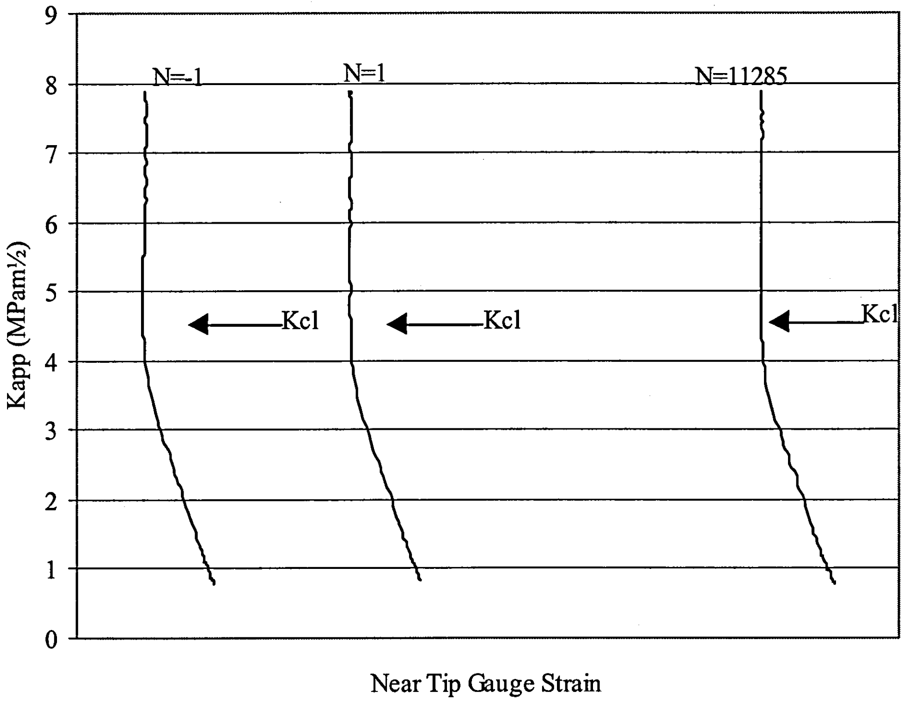

Figure 7.10 Differential strain versus applied stress intensity factor for crack closure measurements using a near-tip strain gauge during overload of 2 on R=0.1 CAL.

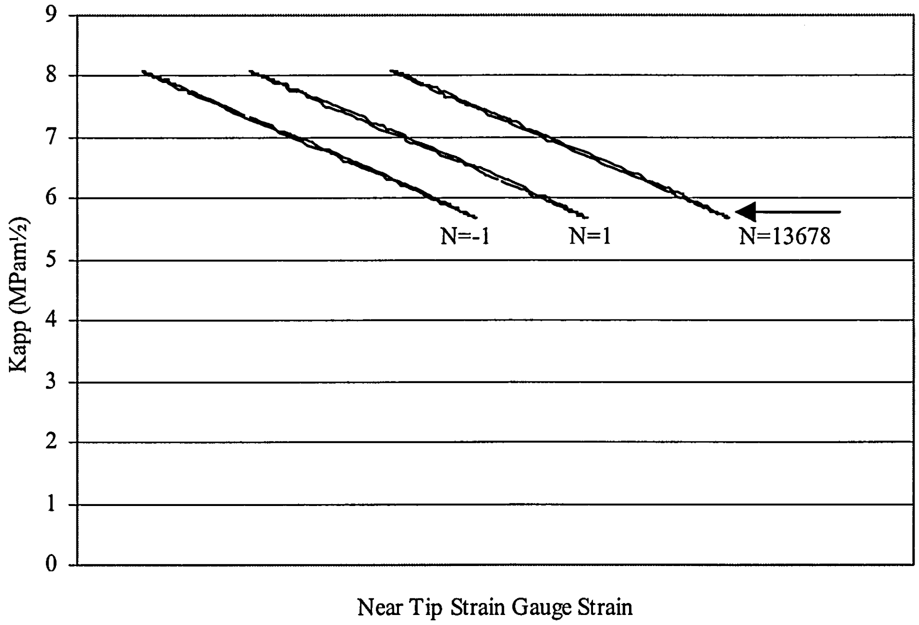

Figure 7.11 NTS strain versus applied stress intensity factor for crack closure measurements using a near-tip strain gauge during overload of 1.35 on R=0.7 CAL.

7.2.2 Fatigue Crack Closure in 7010

Figure 7.12 shows the transient growth rates for the OLR of 2 on R=0.1 CAL for which NTG and CMOD crack closure measurements were made on the 7010 CT specimen. As with the Ti1023 test, the delay effect was relatively small but there was a reduction in growth rate by a factor of twenty at the point of maximum retardation. Measurements of delay distances and cycles are not clear due to DCPD noise.

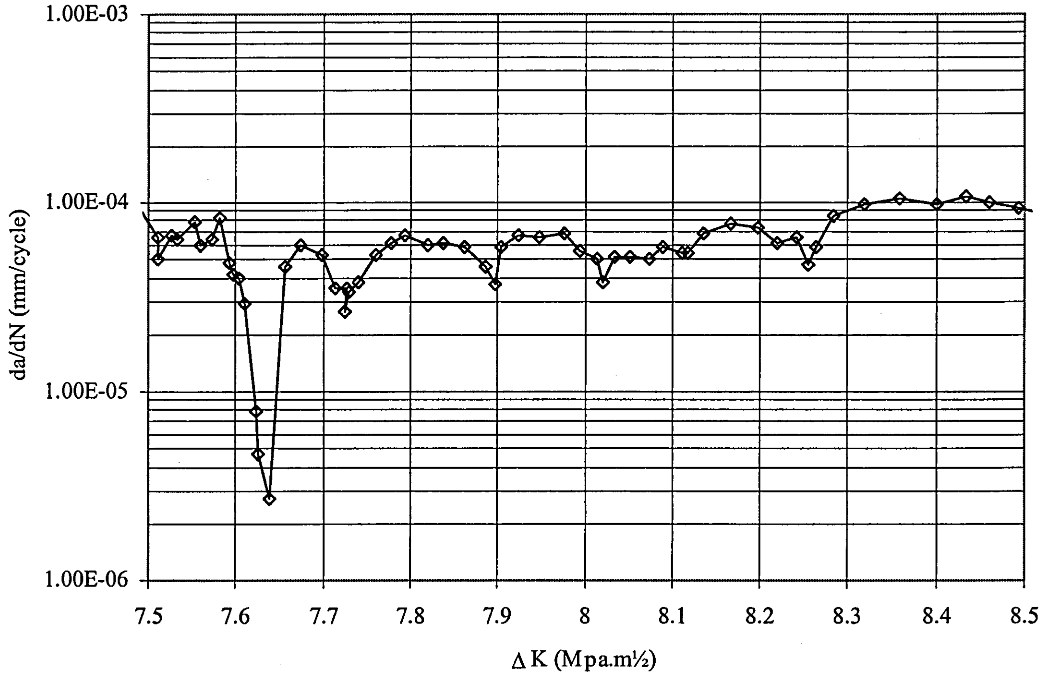

Figure 7.12 Crack growth rate transient for overload of 2 on R=0.1 CAL for 7010, K_{ol}=16.86 MPa.m^{½}.

Figures 7.13 and 7.14 show the differential NTG strain and differential CMOD versus applied K curves respectively for cycle positions before, immediately after and at maximum retardation for the overload test. Again, only three curves are shown here for clarity. The differential NTG strain curves gave a distinct point of non-linearity which might suggest a crack closure level around K_{cl} = 3.0 MPam$^{1/2}$. There were only very small detectable *changes* in closure level during the overload transient from either gauge. The CMOD gauge did not give any significant non-linearity that could be interpreted as a crack closure point as shown in Figure 7.14. This was due to the crack growing close to the strain gauge matrix.

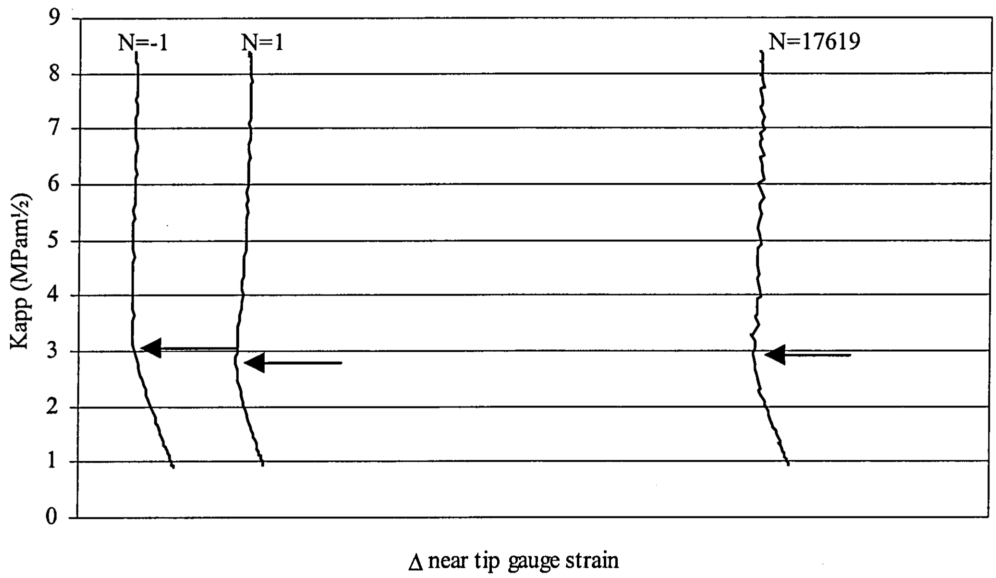

Figure 7.13 ***Differential strain versus applied stress intensity factor for crack closure measurements using a CMOD gauge during overload of 2 on R=0.1 CAL on 7010.***

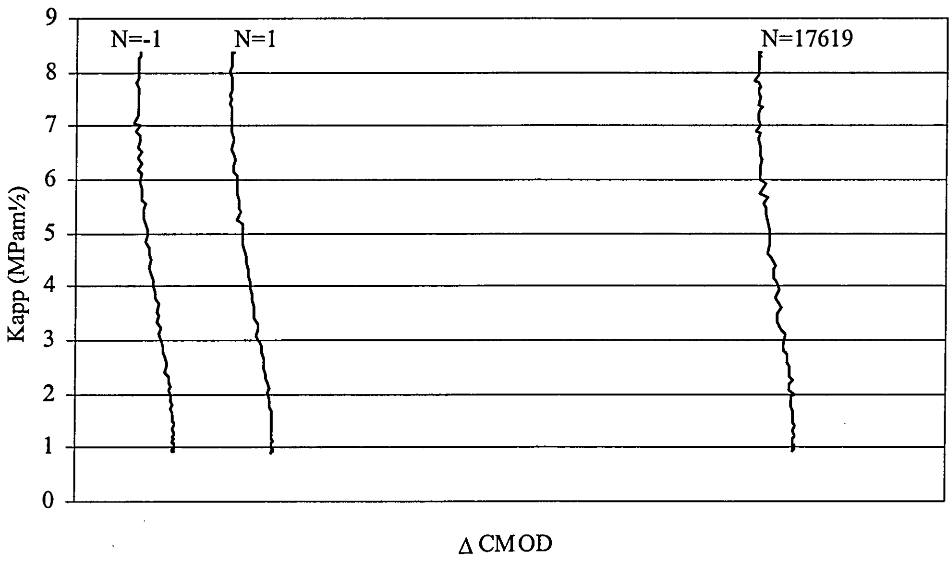

Figure 7.14 ***Differential strain versus applied stress intensity factor for crack closure measurements using a near-tip strain gauge during overload of 2 on R=0.1 CAL 7010.***

The overload of 1.35 on R=0.7 CAL did not give a significant load interaction effect that was detectable within the noise level of the DCPD system. This is in contrast to the Ti1023 test which gave crack arrest. The strain-load and CMOD-load curves were virtually linear giving no points of non-linearity on the differential strain/CMOD-load curves and hence no indication of crack closure levels.

7.2.3 SVAL Fractography

A selection of Ti1023 specimens from the SVAL tests were broken open after the test to reveal the fracture surfaces under scanning electron microscope (SEM) examination. The fractographs presented in this section are representative of the fracture surfaces and features examined. Pre- and post-overload fracture surfaces were examined to observe and correlate fracture surface feature with observations from DCPD measurements. All fractographs are shown with growth direction from top to bottom.

The fracture surfaces formed under CAL at R=0.1, 0.4 and 0.7 were examined to determine the typical fracture mechanisms in the Ti1023 alloy. The R=0.1 loading at $\Delta K = 7.2$ MPa.m$^{1/2}$ is typically transgranular with the prior beta grains visible on the fracture surfaces. See Figure 7.15. The R=0.4 loading at $\Delta K = 4.8$ MPa.m$^{1/2}$ has by comparison, flatter surfaces with the Widmanstatten structure of the Ti1023 grains clearly visible. See Figure 7.16. The near-threshold R=0.7 loading at $\Delta K = 2.4$ MPa.m$^{1/2}$ is very flat, no distinguishable microstructural features of the Ti1023 are clearly visible. See Figure 7.17.

The contrasting appearance of the fracture surfaces under CAL are shown in Figure 7.18 which shows the NTG test for OLR=1.33 during R=0.7 CAL, $\Delta K = 2.55$ MPa.m$^{1/2}$. The top part of the fractograph shows the flat transgranular R=0.7 CAL prior to the overload. The point at which the overload was applied and crack arrest occurred is clearly shown. After the crack arrest, R=0.1 loading at $\Delta K = 7.22$ MPa.m$^{1/2}$ was applied to propagate the crack so that the specimen could be broken open for examination. On resumption of the R=0.1 loading the microstructural features of the material (mainly prior beta grains) become clearly visible again.

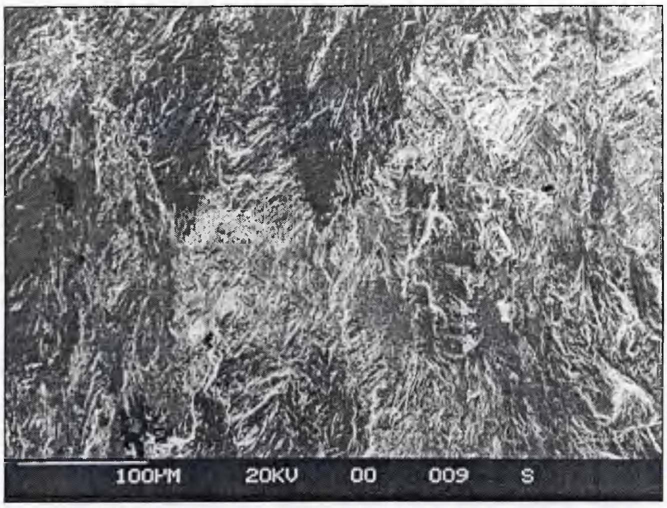

Figure 7.15 Fractograph of R=0.1 CAL at $\Delta K = 7.2$ MPa.m$^{1/2}$ on Ti1023

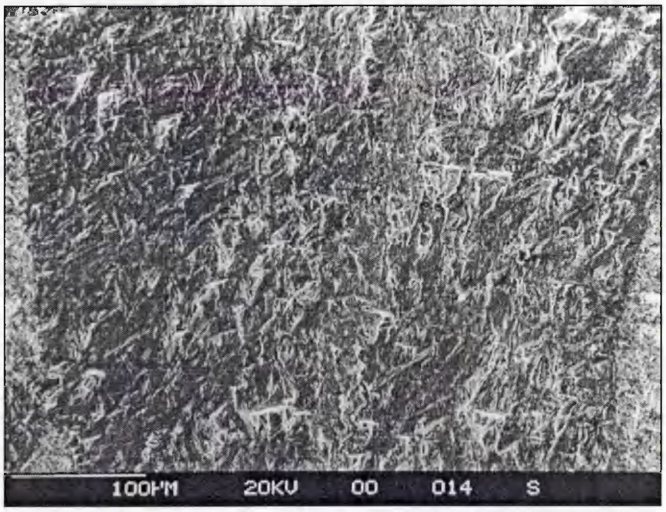

Figure 7.16 Fractograph of R=0.4 CAL at $\Delta K = 4.8$ MPa.m$^{1/2}$ on Ti1023

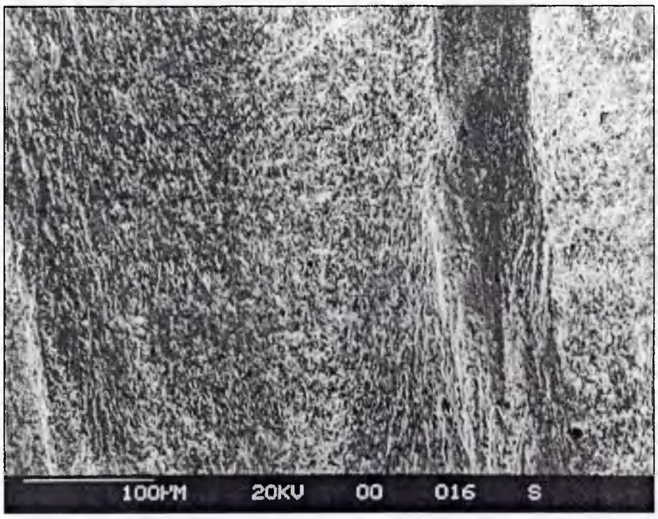

Figure 7.17 Fractograph of R=0.7 CAL at $\Delta K = 2.4$ MPa.m$^{1/2}$ on Ti1023

Figure 7.19 shows the fracture surface of an OLR of 1.75 during R=0.4 CAL, ΔK = 4.86 MPa.m^{½} which gave an average delay distance of 0.12 mm which far exceeded the overload plastic zone size. The Widmanstatten structure of the Ti1023 grains is clearly visible on the fracture face with the overload event indicated by a distinct striation across the fracture surface. There is no evidence of change in fracture surface characteristics before or after the overload and in subsequent growth under CAL which might suggest that closure levels did not change during the overload event .

Figure 7.20 shows the fracture surface of an OLR of 2.0 during R=0.4 CAL, ΔK = 4.8 MPa.m^{½}. The average delay distance given by DCPD measurements for this overload was 0.29 mm which was greater than the OLPZ size. Again, there are no changes in the appearance of the fracture surface before and after the overload event which is clearly shown by the large striation.

Figure 7.21 shows the fracture surface of a double OLR of 2.0 during R=0.1 CAL, ΔK = 7.2 MPa.m^{½}. The fractograph shows the two striations from each overload with a growth of about 40 μm between each applied overload. There is a change in the coloration of the fracture surface after the first overload but the fracture surface topography remains unchanged during the overload events.

In general, the fracture surfaces did not elucidate any evidence that might suggest crack growth rate transients have occurred following the applied overloads through change in surface topography. The DCPD results consistently gave delay distances that were greater than the OLPZ yet there was no obvious fractographic evidence of this. In most cases the point of overload was clearly visible only as a single striation.

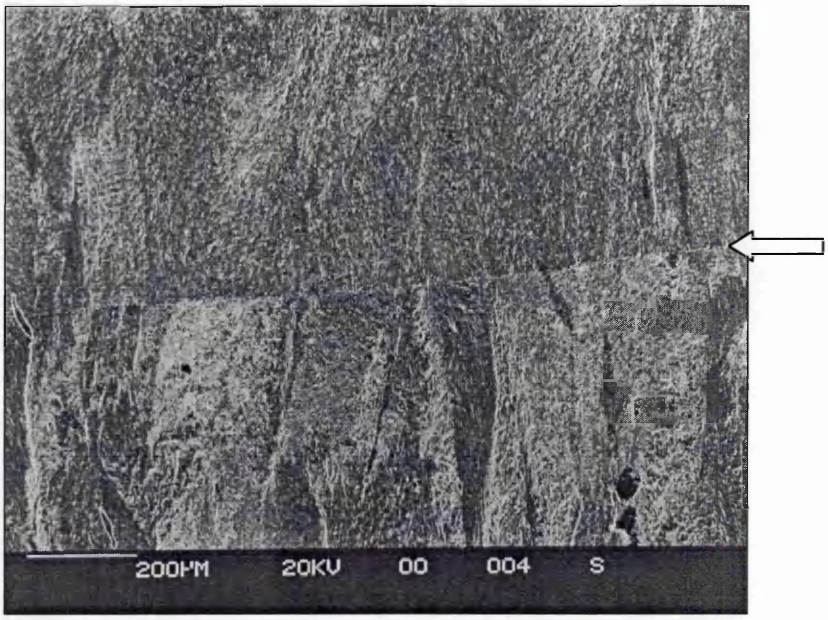

Figure 7.18 Fractograph of overload of 1.33 during $R=0.7$ CAL at $\Delta K = 2.4$ MPa.m$^{1/2}$ on Ti1023 and $R=0.1$ loading applied after crack arrest had occurred.

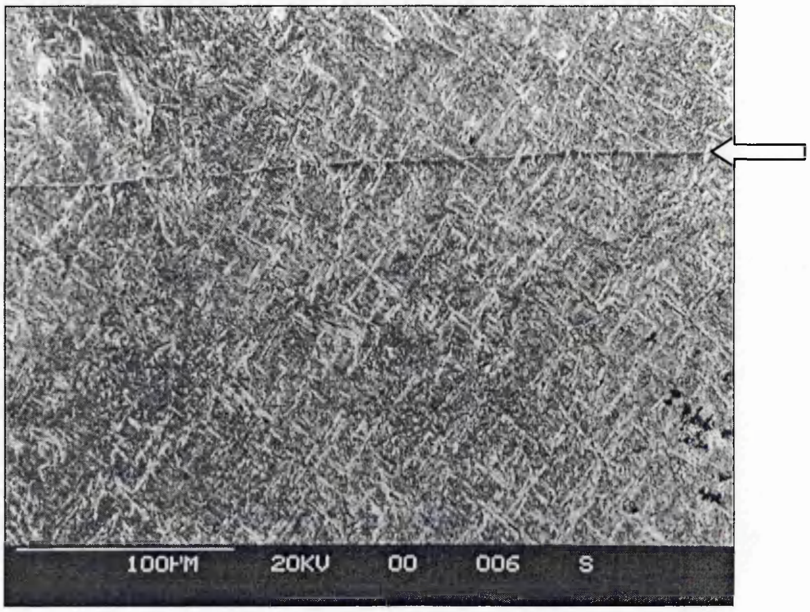

Figure 7.19 Fractograph of overload of 1.75 during $R=0.4$ CAL $\Delta K = 4.8$ MPa.m$^{1/2}$ on Ti1023. Clearly shows application of overload.

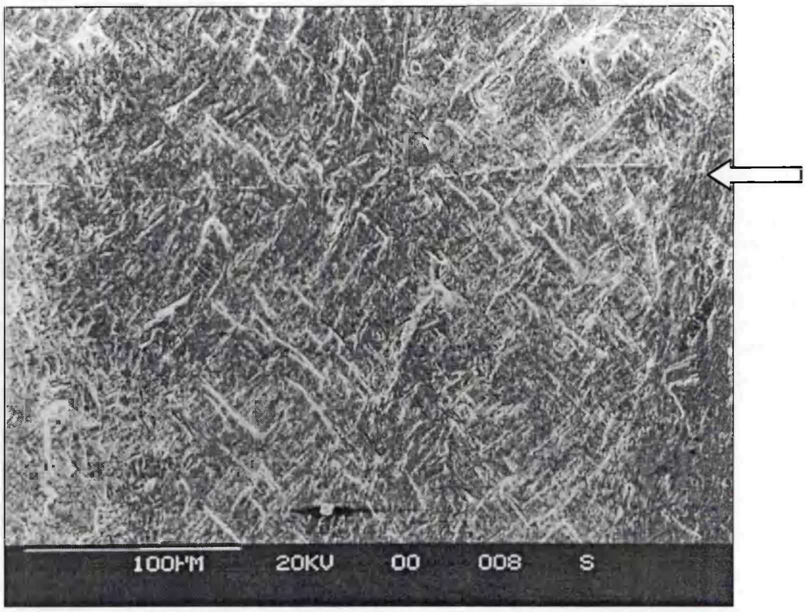

Figure 7.20 Fractograph of overload of 2.0 during R=0.4 CAL ΔK = 4.8 MPa.m$^{1/2}$ on Ti1023. Clearly shows application of overload.

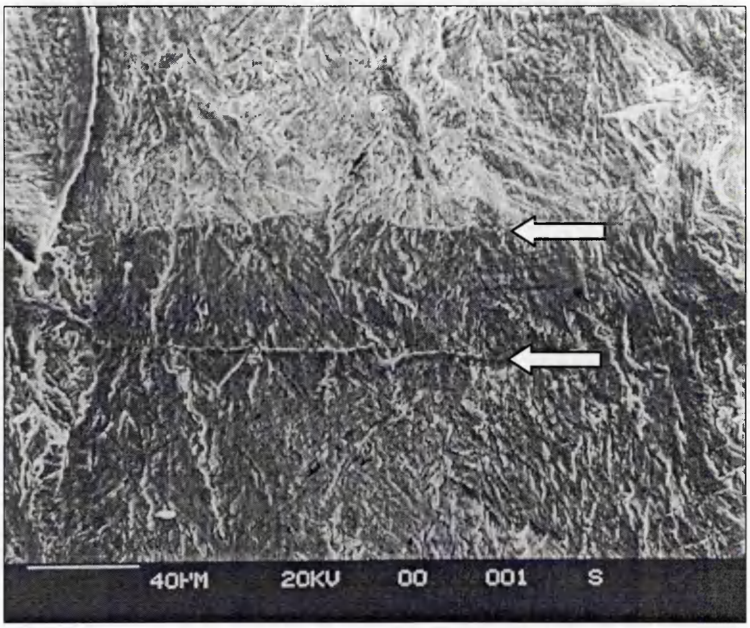

Figure 7.21 Fractograph of double overload of 2.0 during R=0.1 CAL at 7.22 MPa.m$^{1/2}$ on Ti1023. Clearly shows application of both overloads.

7.3 Complex Variable Amplitude Loading

7.3.1 Effect of Omission Range Levels on Flights to Failure

The fatigue crack growth curves plotted in terms of flights are shown in Figures 7.22 and 7.23 for Ti1023 and 7010 respectively for the $P_{peak} = 10$ kN tests. For both materials the effect of progressively omitting small range cycles is to increase the flights to failure for the specimens. Removal of the level 16 cycles from the L16 sequence gave an increase in life of 3.6 and 5.2 times for 7010 and Ti1023 respectively. In each material the number of flights to failure were almost identical for the L20 and L24 tests as expected because both of these spectra are very similar in cycle content. There are only 2156 cycles of range level 20 per sequence and these caused little fatigue damage.

Figure 7.24 shows the results of the flights to failure for each material as a function of omission range level. The main difference between the materials is that the effect of omission is less marked in 7010 when considering the relative increase of flights to failure of levels L20, L24 and L32 compared with the L16 spectrum test. This is significant because it implies that the small range cycles cause a smaller amount of fatigue crack damage in 7010 when compared with those in the same Ti1023 test.

7.3.2 Effect of Omission Range Levels on Fatigue Crack Growth Rates

Figures 7.25 and 7.26 show the crack growth rates per sequence for each material against the peak stress intensity factor, K_{peak}. The 7010 fatigue crack growth rates were approximately four to five times that of the Ti1023 for each of the four omission level tests. The effect of omitting small range cycles is clearly shown for each material as the growth per sequence is reduced for all the L20, L24 and L32 spectra indicating the omitted cycles from each were causing fatigue crack damage in the previous test.

7.3.3 Esacrack CVAL Test Modelling

The omission level tests on both materials were modelled using Esacrack. The modelling was performed without load interaction affects accounted for. To obtain load sequence input data for the modelling the Rotorix loading sequence was rainflow cycle counted and the cycles were processed into blocks containing the same minimum and maximum values. The results

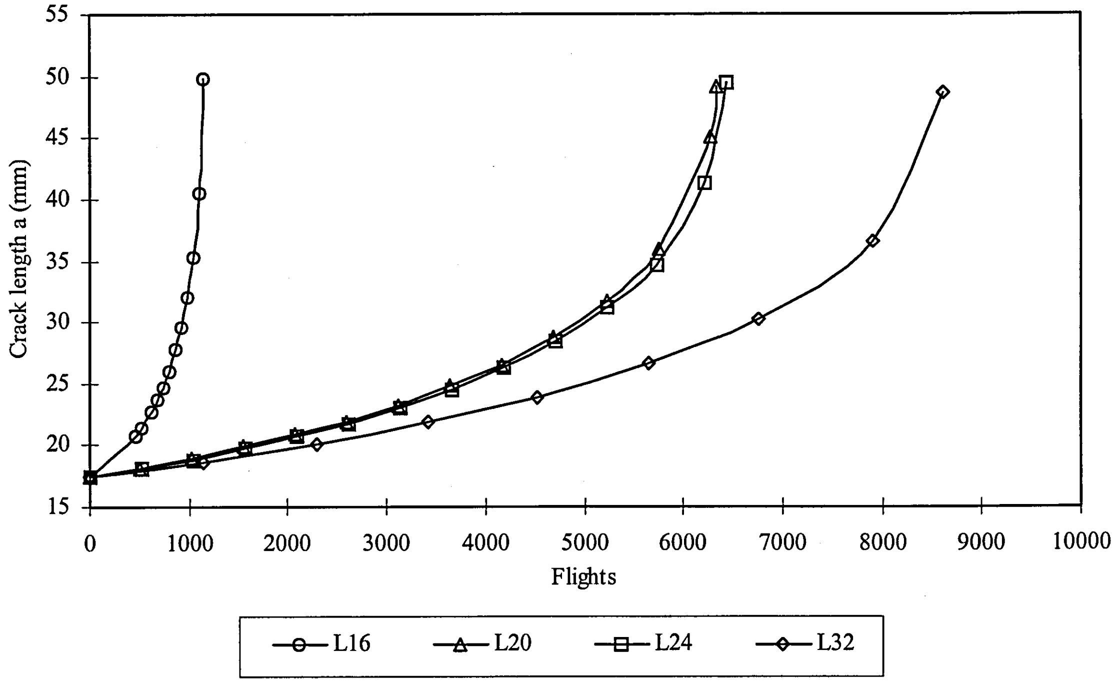

Figure 7.22 Crack growth curves for rotorhead loading sequence omission level tests in Ti1023.

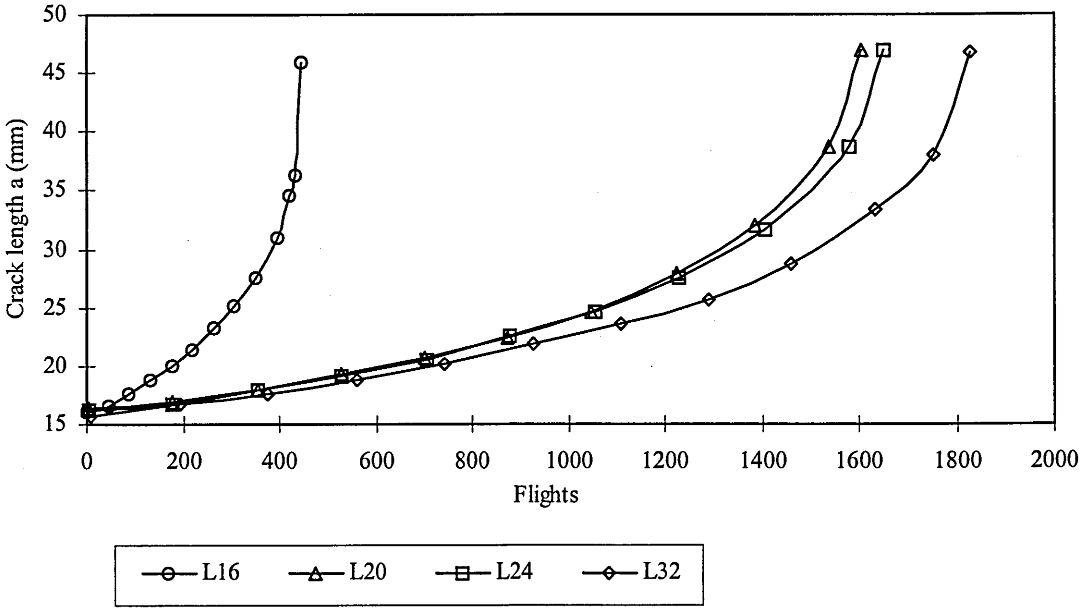

Figure 7.23 Crack growth curves for rotorhead loading sequence omission level tests in 7010.

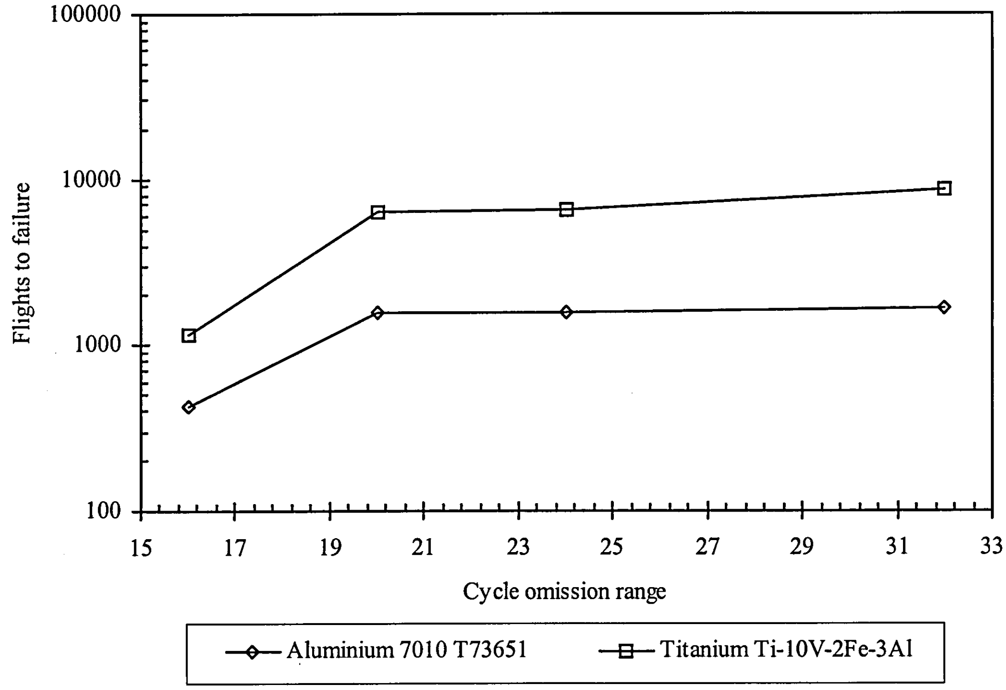

Figure 7.24 Flights to failure as a function of omission level.

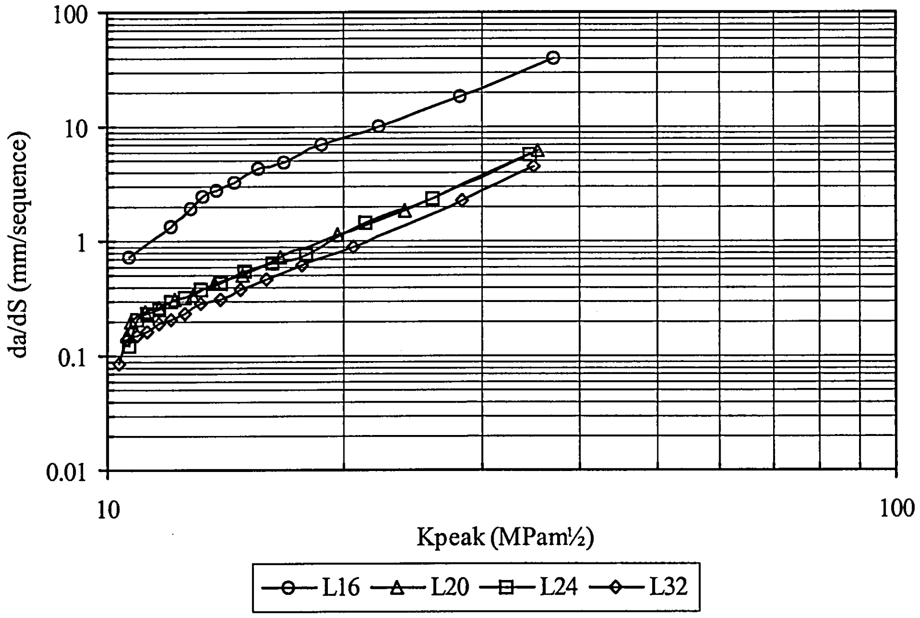

Figure 7.25 Crack growth rate per sequence (da/dS) for rotorhead loading sequence on Ti1023.

are given in Table 7.12 and are compared with the test results.

Table 7.12 Esacrack modelling of omission level tests on Ti-1023 and 7010

Test	a_i (mm)	Test N_f	Test a_f (mm)	Model N_f	Model a_f (mm)	Test N_f /Model N_f
Ti-L16	17.43	1145	49.8	3629	53.6	0.32
Ti-L20	17.43	6341	49.2	6107	57.9	1.04
Ti-L24	17.43	6440	49.5	6129	53.9	1.05
Ti-L32	17.43	8612	48.6	8496	54.0	1.01
Al-L16	16.2	447	41.5	756.6	48.7	0.59
Al-L20	16.2	1604	41.5	2328	54.1	0.69
Al-L24	16.2	1650	42.2	2345	53.9	0.70
Al-L32	16.2	1827	41.5	3068	48.1	0.60

The results for Ti-1023 indicate that the model predictions without any load interaction effects gave non-conservative predictions for the Ti-L16 test and were very good for the other sequences. The parameters used for the modelling were carefully validated in Ref. [21] so the non-conservatism for the L16 test indicates that the crack growth rates of these small L16 cycles under sequence loading are *higher* than under equivalent CAL. The Esacrack model does not account for load interaction effects which suggests that the high R ratio L16 cycles are influenced by load interaction effects generated by the CVAL.

The modelling of the 7010 tests gave consistently non-conservative results although the 7010 L16 test did not show the same non-conservatism as the equivalent Ti1023 L16 test. However, the initial stage (early crack lengths) of this test was influenced in some way because a repeat test at a lower P_{peak} (8 kN) indicated that there were actually higher growth rates than in the 10kN test. If the L16 test had behaved normally then the growth rates would have be higher and the flights to failure would have been less. Therefore, it is assumed that the Esacrack prediction would have been more non-conservative giving consistency with the Ti1023 result.

7.3.4 Fatigue Crack Closure Measurements During Rotorhead Sequence

7.3.4.1 CVAL Fatigue Crack Closure in Ti1023

Figure 7.27 shows the crack growth recorded during the selected loading sequence during which crack closure measurements were made for the Ti-1023 CT specimen. The average crack growth rate over the test sequence was $4.1\text{x}10^{-6}$ mm/cycle. Figures 7.28 and 7.29 show selected differential CMOD-load and NTG strain-load curves for the rotorhead loading sequence test. The differences in ranges of applied K over which the data were recorded match the load cycle at which the measurement was taken. The nominal crack closure levels are indicated by linearity changes on the graph and remained constant at K_{cl} = 5.1 MPa.m^{½} during the sequence. The same procedure was applied to the CMOD-load data but a lower crack closure level was recorded at K_{cl} = 4.2 MPa.m^{½}. Again the closure level remained constant during the sequence. Two points are evident: Firstly, the closure levels were different for both measurement techniques. Secondly, there are no detectable changes in closure levels measured by either gauge during the sequence.

7.3.4.2 CVAL Fatigue Crack Closure in 7010

Figure 7.30 shows the crack growth recorded during the selected loading sequence during which crack closure measurements were made for the 7010 CT specimen. Figure 7.31 shows selected differential NTG strain-load curves for the rotorhead loading sequence. In contrast to the above Ti1023 test the change in linearity of each differential NTG strain-load curve varies during the test sequence. The changes can be correlated to major variations in the loading sequence: At the start of the sequence the loading is mostly lower R ratios (see Figure 7.31) and the change of linearity level measured is about 7.0 MPa.m^{½}. After the middle section of sustained high R loading (R=0.83) the change of linearity level rises to 13.5 MPa.m^{½}. The latter part of the loading sequence contains more cycles of lower R ratio and here change of linearity level drops off again to around 11.0 MPa.m^{½} and then to 7.0 MPa.m^{½} again. These detectable changes are in contrast to the Ti1023 test where the change of linearity levels remained constant. This may be due to the greater level of plasticity in 7010 (lower yield strength) and the subsequent improved detectability of a strain gauge close to the crack tip plastic zone. It is unsure at this stage if the changes measured in the 7010 test are due to closure or load level changes or both. See discussion.

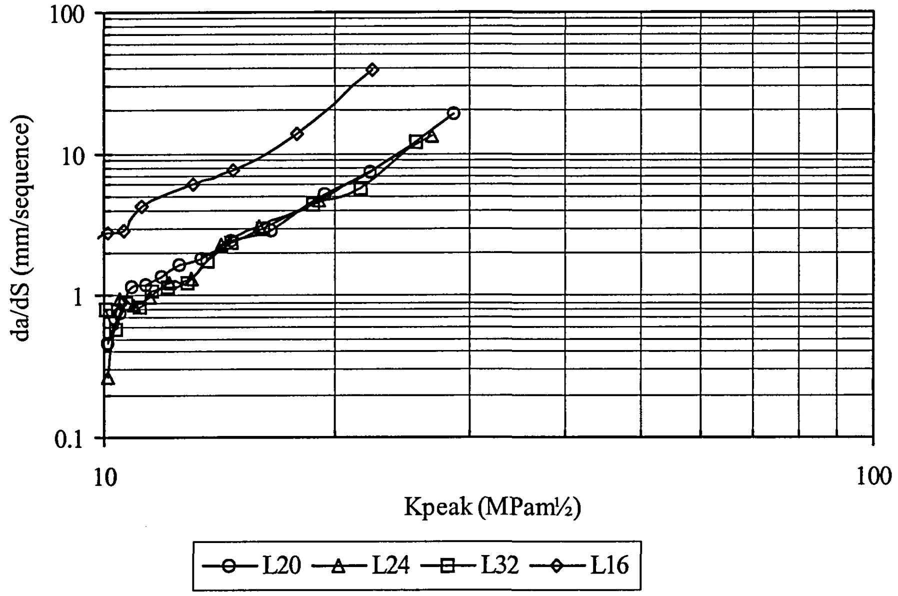

Figure 7.26 Crack growth rate per sequence (da/dS) for rotorhead loading sequence in 7010. Curve for L16 test taken from P_{peak} = 8kN test.

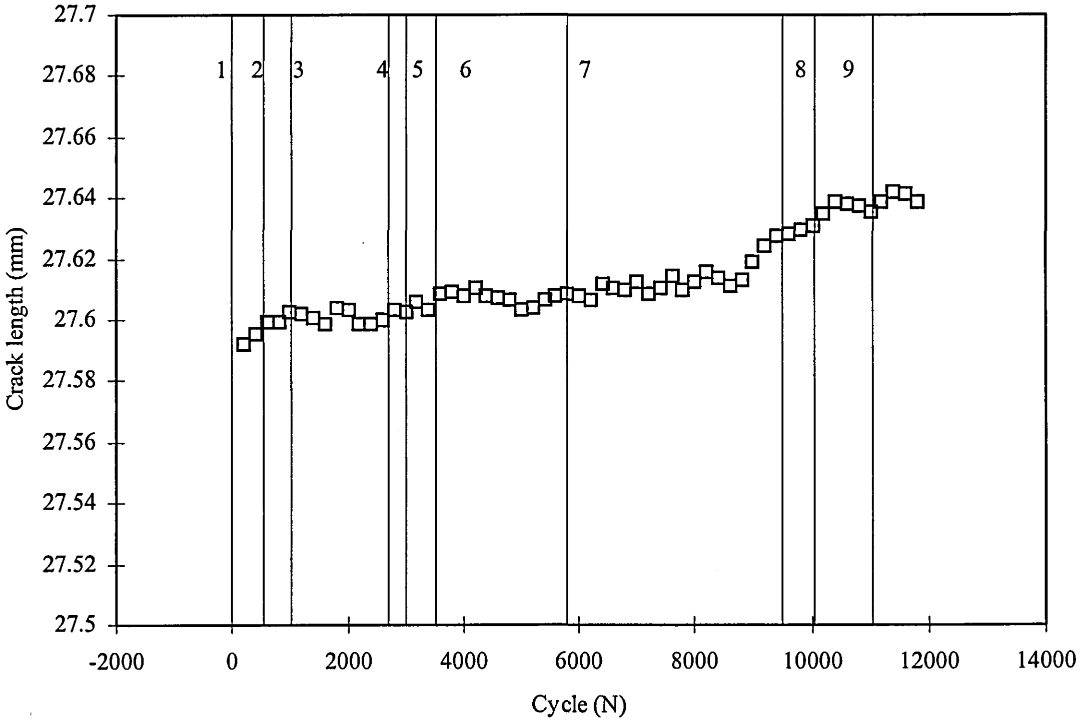

Figure 7.27 Crack growth during selected rotorhead loading sequence showing positions at which closure measurements were taken on Ti-1023

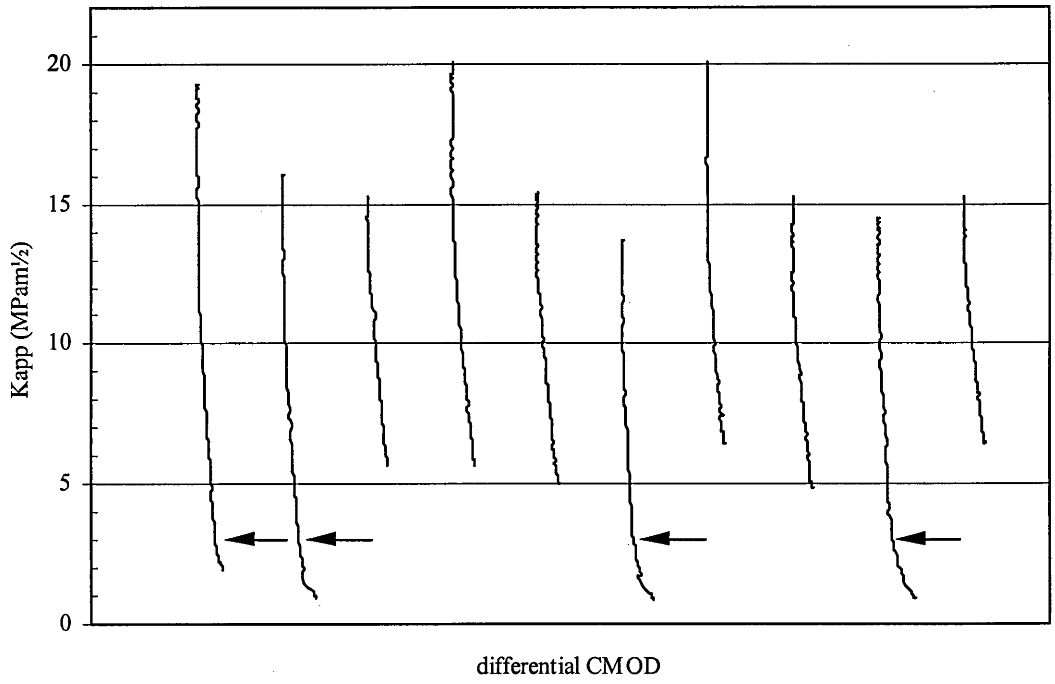

Figure 7.28 Crack opening values (K_{op} = 5.1 MPa√m) from differential CMOD – load curves during selected loading sequence on Ti-1023

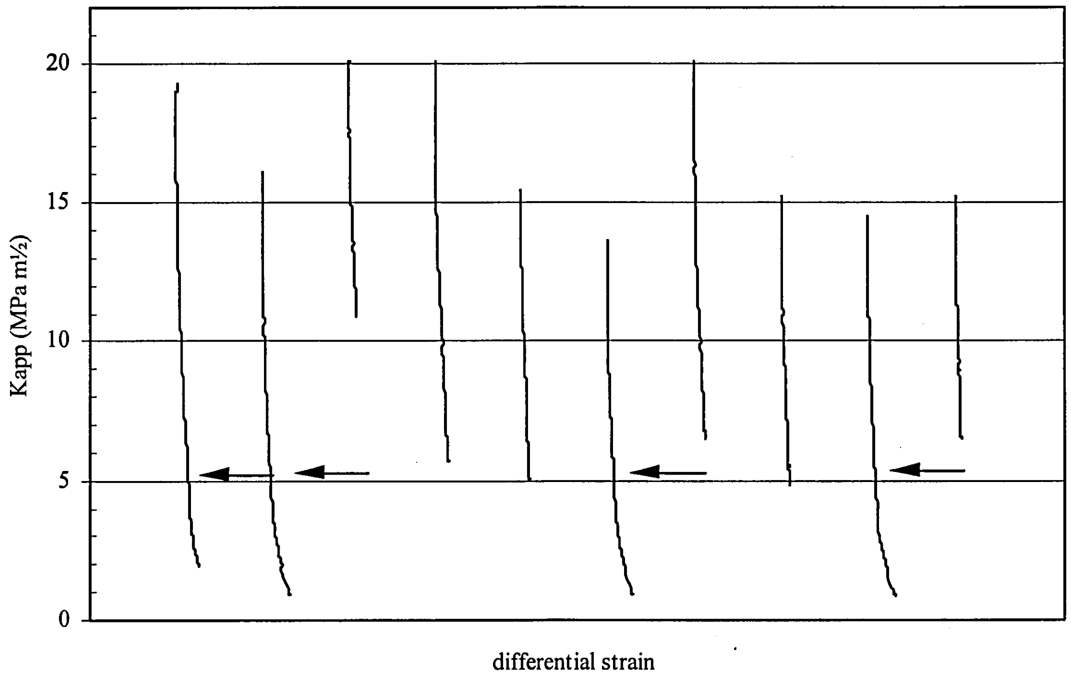

Figure 7.29 Crack opening values (K_{op} = 4.2 MPa.m^{½}) from differential CMOD – load curves during selected loading sequence on Ti-1023.

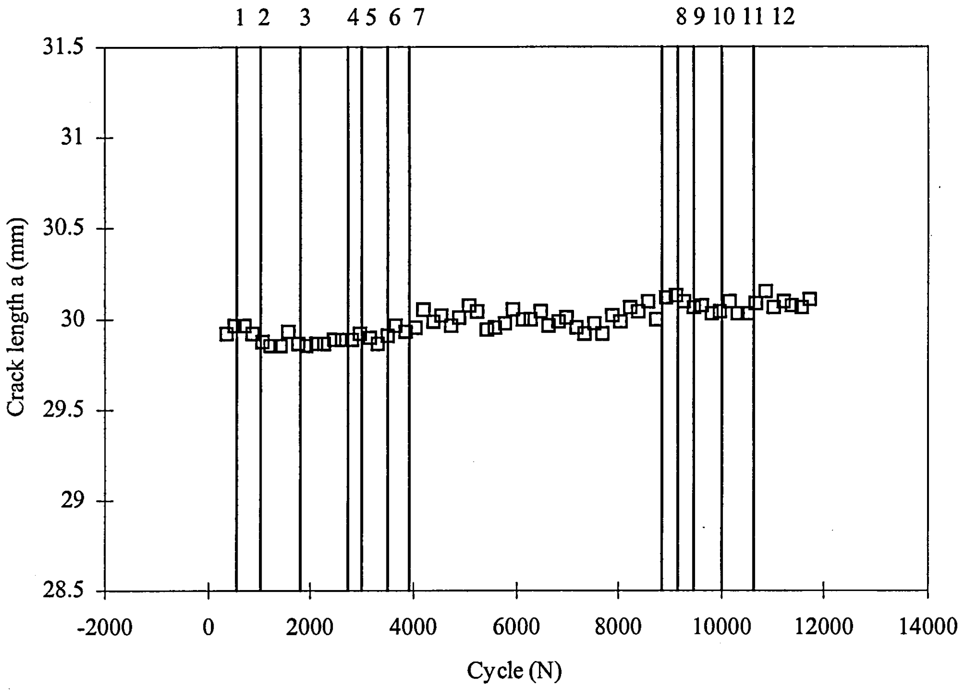

Figure 7.30 Crack growth during selected rotorhead loading sequence showing positions at which closure measurements were taken on 7010.

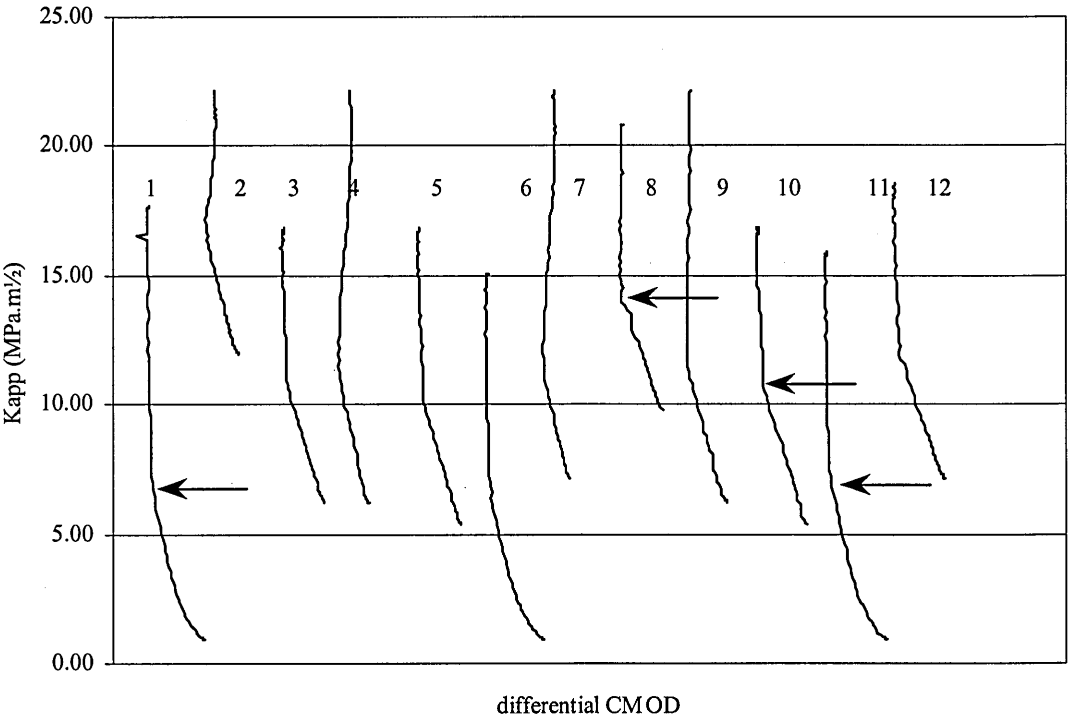

Figure 7.31 Crack opening values from differential NTG – load curves during selected loading sequence on 7010.

7.3.5 CVAL Fractography

Two Ti1023 specimens representing the L16 and L32 tests from the CVAL tests were broken open after the test to reveal the fracture surfaces under scanning electron microscope (SEM) examination. All fractographs are shown with growth direction from top to bottom.

Figure 7.32 shows the fracture surface of the Ti1023 L16 test at low K_{peak} (17 MPa.m^{½}). The fractograph shows the large prior β grains and oxides along the grain boundaries are visible. There is slight evidence of beach-marking visible at this low magnification. At a higher magnification shown in Figure 7.33, there is clear evidence of change in load levels due to manoeuvres and ground-air-ground loading indicated by striation marking. The larger gaps are due to the high R ratio, low range L16 cycles during the long periods of steady state flight and the narrow bands are due to the lower R ratio, L32 range and higher manoeuvre loads as explained later.

Figure 7.34 shows the fracture surface of the Ti1023 L16 test at high K_{peak} (36 MPa.m^{½}) near the edge of the specimen. Again the prior β grains are visible but the grain boundaries are not emphasised by oxides which occur at lower K_{peak}. A higher magnification given in Figure 7.35 shows fatigue striations on the fracture surface. The elongated Widmanstatten structure is not as clearly evident when compared with the low K_{peak} example.

Figure 7.36 shows the fracture surface of the L32 test (all L16, 20 and 24 cycles removed) at low K_{peak} (17 MPa.m^{½}) which has an overall 'rougher' appearance compared to the L16 CVAL test fracture surface at similar K_{peak}. The prior β grains are not as distinctive as before. A higher magnification of the fracture surface shown in Figure 7.37 shows a distinct absence of load cycle change markings or striations.

At the higher K_{peak} (36 MPa.m^{½}) the Ti1023 L32 fracture surface shows no obvious beach-marking as shown in Figure 7.38. This is in contrast to the L16 test which has visible load level change markings which are separated by periods of growth under L16 cycles. Fatigue striations are shown at a higher magnification in Figure 7.39. These are probably due to individual medium to low R ratio L32 and higher range loading cycles.

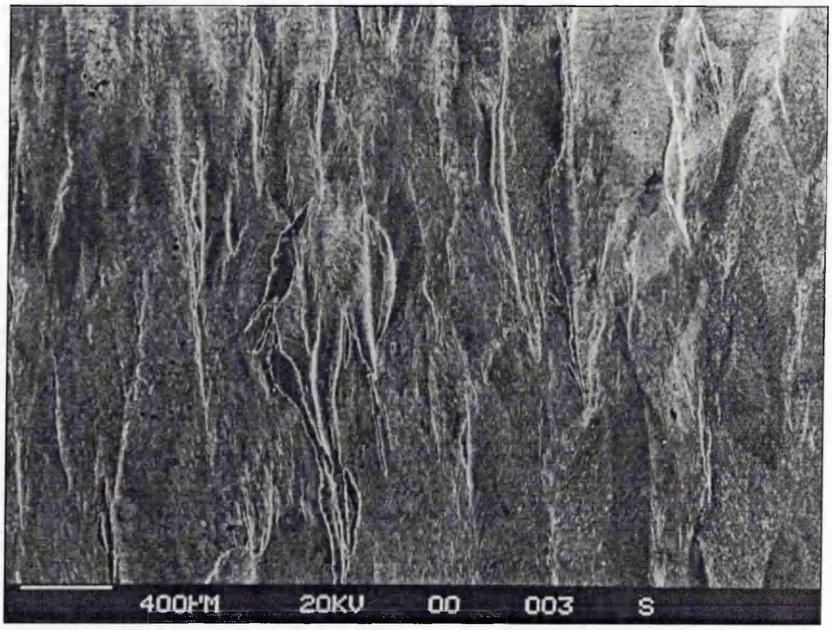

Figure 7.32 Fractograph of Ti1023 L16 CVAL test at low K_{peak} = 17 MPa.m$^{1/2}$. Large beta grains evident.

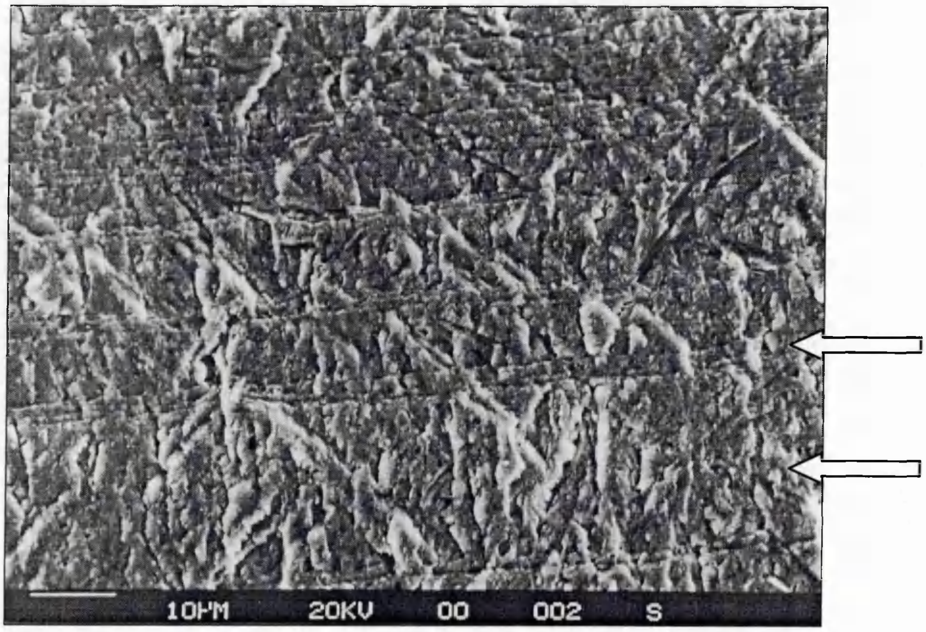

Striation features due to low R ratio manoeuvres

Larger 'bands' due to growth under L16 cycles

Figure 7.33 Fractograph of Ti1023 L16 CVAL test at low K_{peak} = 17 MPa.m$^{1/2}$. Bands of crack growth damage caused by different types of load cycles in CVAL sequence.

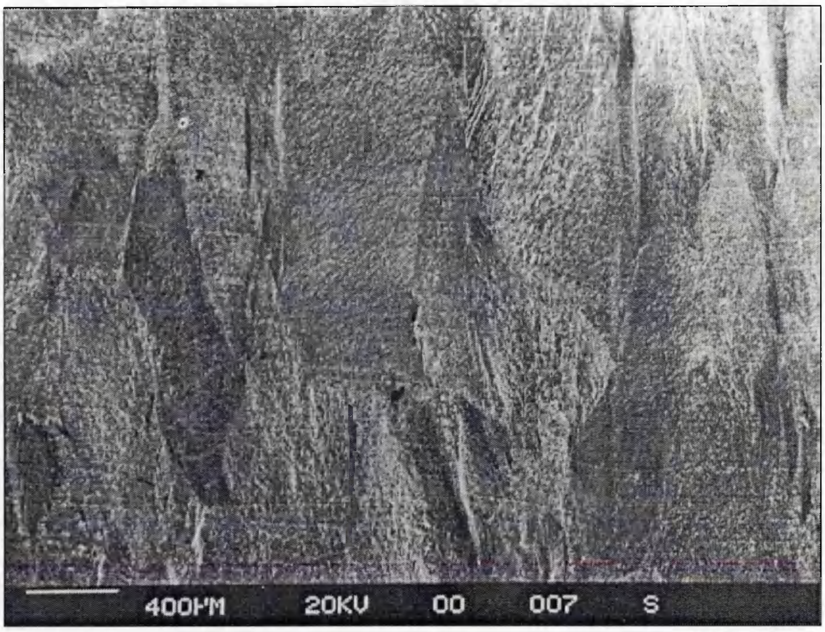

Figure 7.34 Fractograph of Ti1023 L16 CVAL test at high K_{peak} = 36 MPa.m$^{1/2}$. Some beachmarking by cycles evident.

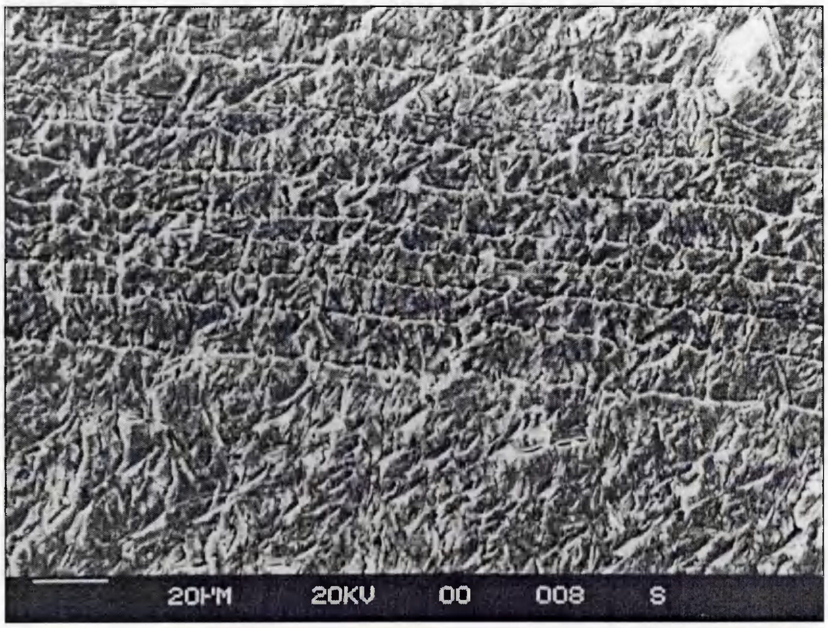

Figure 7.35 Fractograph of Ti1023 L16 CVAL test at high K_{peak} = 36 MPa.m$^{1/2}$. Bands of crack growth damage caused by different types of load cycles in CVAL sequence.

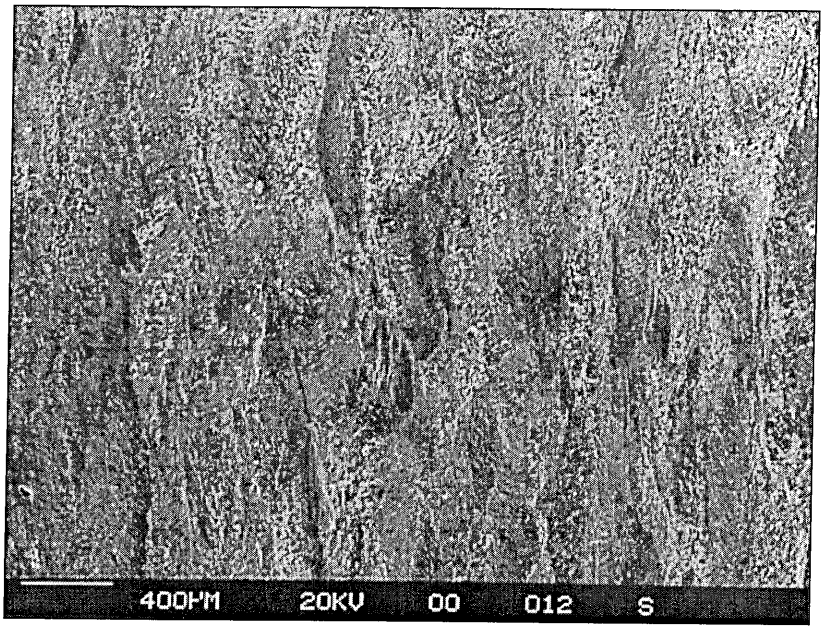

Figure 7.36 Fractograph of Ti1023 L32 CVAL test at low K_{peak} = 17 MPa.m^{½}. Less evidence of large beta grains.

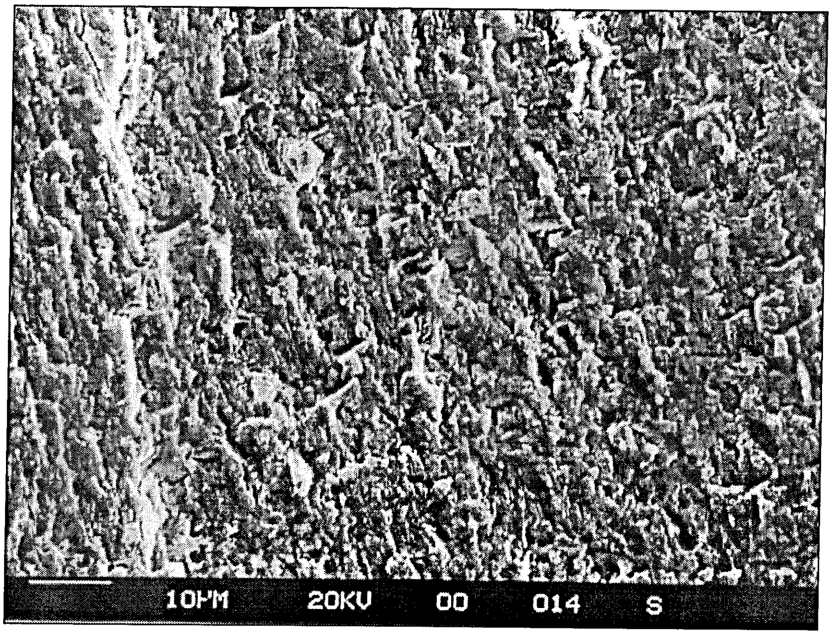

Figure 7.37 Fractograph of Ti1023 L32 CVAL test at low K_{peak} = 17 MPa.m^{½}. No presence of bands of crack growth damage caused by different types of load cycles in CVAL sequence.

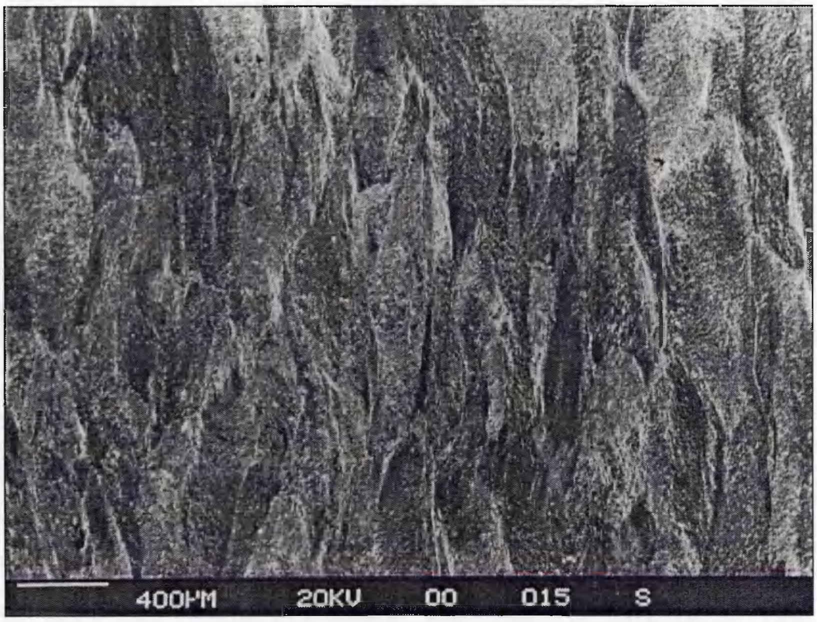

Figure 7.38 Fractograph of Ti1023 L32 CVAL test at high K_{peak} = 36 MPa.m$^{1/2}$. No distinctive beachmarking evidence.

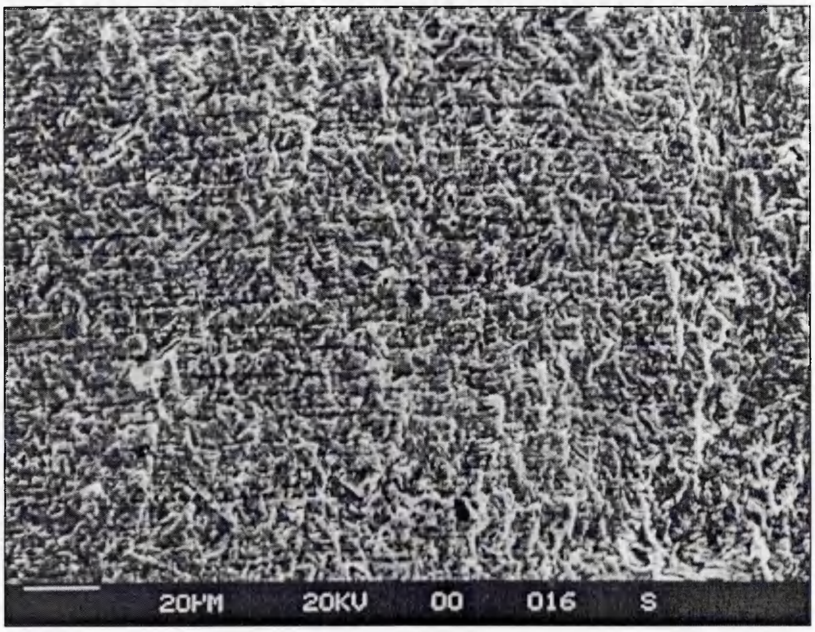

Figure 7.39 Fractograph of Ti1023 L32 CVAL test at high K_{peak} = 36 MPa.m$^{1/2}$. Striations due to individual load cycles shown.

The distinct absence of beach-markings in the L32 test fracture surface at low K_{peak}, suggests that the main reason for their appearance in the L16 test is due to the high R ratio, low range L16 cycles (the L20 and L24 cycles are considered to be negligible). If the gaps between beach-markings are due to the L16 cycles then these cycles constitute 70-80% of the fracture surface area which means they contribute to a significant amount of fatigue crack growth even though they have small cycle ranges.

Figure 7.40 shows the fracture surface from the NTS gauge CVAL crack closure test on Ti1023 using the selected CVAL sequence (Details in Section 6.8.2.2). The striation markings have been correlated with major changes in load levels in the sequence (Figure 6.13). The main striations are due to near-zero load excursions as marked on the figure and the centre band is due to the long period of steady state flight simulated by high R, low range L16 cycles.

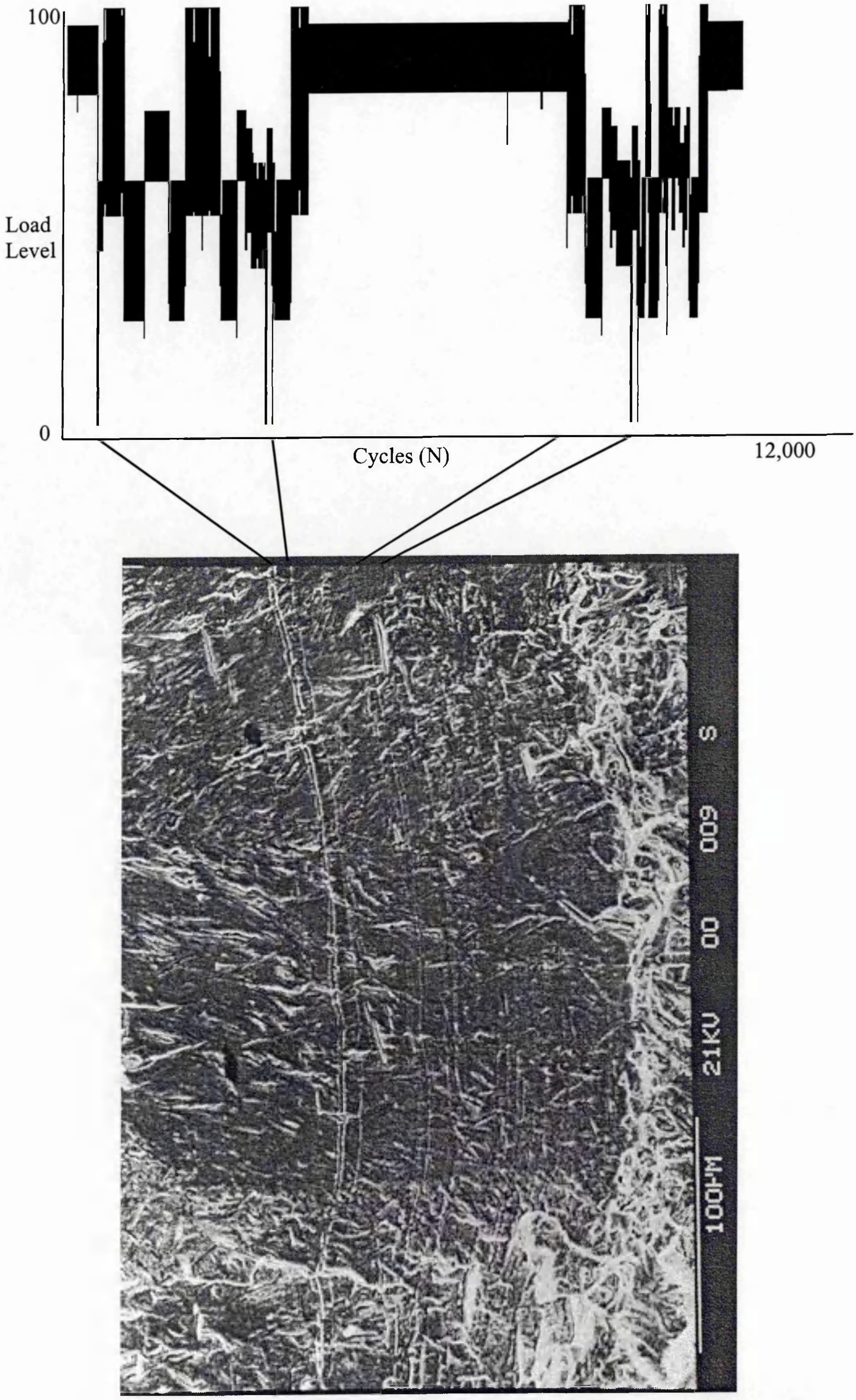

Figure 7.40 Fractograph of Ti1023 L16 CVAL selected loading sequence crack closure NTG test showing correlation between fatigue surface banding and loading during the sequence.

8. DISCUSSION

The results of the research work are discussed in this chapter and interpreted in relation to other similar research. The discussion will be presented in three sections: The first part covers the simple variable amplitude loading tests on Ti1023. The second part contains discussion on the complex variable amplitude loading tests on Ti1023 and 7010 for which the results revealed unexpected crack growth rate behaviour for the small high frequency vibratory cycles. A model drawn from residual stress field analysis is invoked to explain this behaviour. Finally, the third section contains discussion on the implications of the results on the damage tolerant design of helicopter structures.

8.1 Simple Variable Amplitude Loading

Load interaction effects on fatigue crack growth rates were observed for different CAL R ratios subjected to various overloads, interacting overload and overload-underload combinations. In particular, load interaction effects were observed for all cases of overloads (OLR = 1.24 to 1.75) applied during R=0.7 CAL. Typically most crack growth models do not provide for a mechanism such as crack closure that would predict the observed load interaction effects at high R ratios. A mechanism based in the residual stress field ahead of the crack tip that provides for the observed effects is proposed.

8.1.1 Increase in Overload Ratio Increases Delay Effects

The first observation from the overload tests was that the overloads had a increasing delay response as the OLR increased and the effect was greater as the CAL R ratio increased. For single overloads during R=0.4 CAL the OLR of 1.75 gave a small crack growth rate retardation (N_{delay} = 22500) and the OLR of 2.0 gave a retardation of an order of magnitude greater (N_{delay} = 195000). During the R=0.7 test the effect was enhanced as an OLR of 1.24 gave a small transient effect yet for the OLR 1.35 test complete crack arrest occurred. The effect of overloads during R=0.1 CAL was the smallest. This has been observed by many in literature [25,29,59,96,97] and has been attributed to both an increase in the compressive residual stresses in the OLPZ with R ratios [33] and greater displacements in the wake of the crack tip which will enhance both plasticity and roughness induced closure [25,26,30].

To understand these observations the effect of ΔK firstly needs to be accounted for. In this series of tests the CAL crack growth rates decreased with increasing R ratio because the K_{max} level was kept constant and hence the cycle range reduced. Sensitivity to crack arrest or overload effects at higher R ratios primarily occurs due to the proximity of the test ΔK values to the ΔK_{th} values at each R ratio. Comparing the size of the test ΔK's with appropriate threshold range clarifies the interpretation of results:

Table 8.1 Comparison of test ΔK values with the fatigue threshold of Ti-1023

R ratio	Test ΔK	ΔK_{th} Ti1023	$\Delta K/\Delta K_{th}$
0.1	7.22	3.5	2.1
0.4	4.81	2.6	1.9
0.7	2.41	1.84	1.3

Tests performed at near-threshold conditions under R=0.7 CAL have shown that crack opening displacements are in the order of magnitude of the oxide layers and height of asperities [44]. A small disruption by an overload might easily increase the closure level so that ΔK_{eff} values which would be very close to threshold ΔK_{th} , enhancing the load interaction effects at high R ratio. The observation of crack arrest in the R=0.7 tests and the double overload OLR=2.0 for R=0.4 is likely due to ΔK_{eff} being reduced below the threshold range.

No general agreements exist in literature for the type of mechanism controlling the delay effects particularly at high R ratios where crack closure is supposedly minimal. Topper and Yu [42] found that delayed crack growth retardation in a steel increased significantly with OLR to a point where crack arrest occurred which is consistent with the test observations here. They proposed a residual stress field mechanism for the delay effects due to the overload creating a zone of compressive stresses at the crack tip. Others also found that delay distances are primarily attributed to the size of the plane stress OLPZ with increasing effects as OLR increases [97,98].The correlation of delay effects with OLPZ size, qualitatively agrees with other observations in literature. However, quantitative comparisons for each R ratio are clouded by the fact that delay distance were several times larger than the OLPZ. This is discussed and explained in the following section.

8.1.2 Delay Distance Greater than Overload Plastic Zone

A significant observation made during the SVAL tests was that the delay distances following an overload were much greater than the plane strain OLPZ. Typically the ratio of test delay distance to OLPZ size ranged from 3 to 22. This has been observed previously by Suresh [26] who introduced a roughness induced crack closure argument to explain the prolonged delay distance. However this does not offer a satisfactory mechanism because the fractography results did not give any evidence of fracture surface damage consistent with roughness induced closure either before or after the overloads. The fracture surface appearance remained virtually unchanged so that it is unlikely that this mechanism gave prolonged delay distances.

Delay distances longer than the overload plastic zone size have also been observed by Shuter and Geary [40] who found that delay distances were shorter in plane strain specimens than in plane stress specimens. This observation provides a plausible explanation of the larger than OLPZ size delay distance results which is that different growth rates occur between the surface and interior of the specimen. Turner et.al. [39] suggest that delay responses are different through the thickness because of a variation in constraint from the plane stress surface to the plane strain interior. They found that the post-overload crack front has greater curvature than pre-overload due to crack 'tunneling' in the plane strain interior [39].

FE work by Sun and Sehitoglu [36] found that under plane stress conditions the contribution to the K_{PR} parameter was dominated by residual stresses in the wake of the crack. Under plane strain conditions the contribution to K_{PR} was dominated by reversed deformations ahead of the crack. Even though the plane strain conditions are dominated by reversed deformation, the level of K_{PR} is still greatest at the plane stress edge of a specimen. They found that $K_{PR} = 0.65K_{max}$ under plane stress and $K_{PR} = 0.42K_{max}$ under plane strain providing a numerical simulation of the crack tunneling phenomena.

The observations of Turner et. al. and others [36,50,52,53] suggest that the surface plastic zone has a significant retarding effect on crack growth, due to greater extent of plasticity induced closure at the crack tip. This was not specifically observed in the current tests, because the specimens were not broken open after each overload (they were used for subsequent overload tests). The DCPD method measures changes in cross-sectional area of the specimen so the crack length would be an average of the through-thickness crack front length. If retardation is minimal in the specimen interior and grows a significant distance before the surface region grows through the plane stress OLPZ then the DCPD system would measure a change in length greater than the OLPZ. See Figure 8.1. The effect was likely to be present for all SVAL tests so that a good correlation of the OLPZ with OLR and R ratio can not be made.

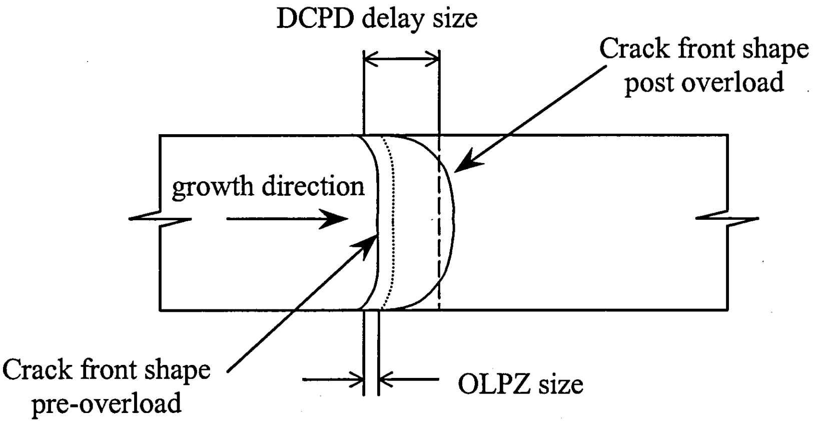

Figure 8.1 Explanation of large delay distances measured by DCPD system

8.1.3 Load Interaction Mechanisms at High R Ratio

The strain-load measurements made using the NTS gauges during the high R ratio overload test did not exhibit any deviations from linearity. These observations were supported by Shuter and Geary [40] and others [28,59] who did not measure any indications of closure with compliance gauge techniques but did observe transient crack growth behaviour following a single overload. In agreement with the SEM fracture surface examinations made here, they also found no factographic evidence of crack branching or roughness induced closure and so deduced that residual stresses ahead of the crack were responsible for retardation at high R ratio. Several other researchers [57] have also come to this conclusion only through elimination of other mechanisms but not by direct investigation of residual stresses. This general lack of direct evidence when using compliance measurements of closure does not necessarily mean that closure is absent at high R ratios nor that residual stresses are solely responsible.

Two explanations of the observations are now explored: (i) That compliance measurement techniques are not sensitive enough to detect closure and/or load-strain non-linearities, and (ii) That residual stresses ahead of the crack tip *and* crack closure on the fracture surfaces are responsible for load interaction effects

If a strain gauge is placed close to a crack tip and within the stress field of the crack tip singularity then by using LEFM the gauge sensitivity can be determined. The NTS gauge method measures strain on the surface of the specimen so the plane stress field around the crack tip is given by:

$$\sigma_y = K_I(2\pi r)^{-\frac{1}{2}}\cos(\theta/2)(1+\sin(\theta/2)\sin(3\theta/2)) \quad \text{(from Equation 3.3)}$$

For a gauge located 1 mm below the crack tip the strain range for CAL R=0.1, K_{max} = 20.4 MPa.m^{½} is 1290 με and 3680 με for titanium and aluminium respectively. The difference is due to the respective material Young's modulus. Now assuming that a crack will close over a length equal to the OLPZ [33] then the closed length will impart a change in stress intensity. This closed length is proportional to the material yield strength because $r_p \propto (K_{max}/\sigma_{YS})^2$ so will be greater for the 7010 specimen. The effective change in crack length will manifest itself as a change in stress intensity factor, say δK. This δK that will be detected as a strain non-linearity in the load-strain curve. A similar treatment of δK using Equation 3.3 results in strain changes, δε of 7 με and 120 με for titanium and aluminium respectively due to both Young's modulus and yield strength differences. Only the latter strain is able to be detected by the current equipment.

Interestingly the NTS gauge did measure significant non-linearities for both Ti1023 and 7010 R=0.1 SVAL tests. This indicates that crack closure does occur over the lower portion of the load-strain curve and must occur over a significant distance because it was detectable in Ti1023. Therefore crack closure does affect low R ratio cycles but it is currently undetermined here for high R ratios in Ti1023. This correlates with several FEM treatments [20, 61] of the problem which indicate that at higher R ratios the distance behind the crack tip which is closed is greatly reduced and the sensitivity of the NTS technique is diminished. During the R=0.1 overload tests no *changes* in this closure level that could produce the observed changes in growth rates were observed which is disagrees with a significant majority of the literature [53,75,99,100]. However, comparisons of the specimen thickness, applied stress intensity factors with literature reveals several differences, namely predominantly plane strain, high strength material and near-threshold ΔK values. The result of this combination of test parameters is that relatively small amounts of plasticity occur at the crack tip so the mechanism which controls the load interaction effect is not measurable using current compliance techniques. This is consistent with Fleck [101] who also states that crack closure is unable to account for transient crack growth rates.

Although it has been established that static levels of crack closure can be measured for low R ratios it is difficult to determine its contribution at high R ratios. Additionally, the lack of correlation of delay distances with the OLPZ because of crack tunneling does not provide a good basis for a residual stress field argument. So a firm conclusion on the load interaction mechanism at high R ratios cannot be made at this stage. However, other test observations can be used to rationalise the mechanism: double overloads and the overload-underload combination at R=0.7.

The crack growth response after first overload in the double overload tests during R=0.1 and 0.4 (see Figures 7.5 and 7.6) was similar to that of the a single OL test (acceleration followed by delayed retardation). Application of second overload tended to 'neutralise' the transient effect of the previous overload and the subsequent transient growth rate response was then similar to that of a single overload (in terms of delay distance and cycles). The elimination of the previous overload effects suggests that the overload mechanism is controlled by the residual stress field ahead of the crack due to the instantaneous nature of the response. If closure were responsible then the second overload would tend to enhance the first because of increased displacements in the wake of the crack. This was not observed in the crack growth rate curves which suggests that crack closure is not the controlling mechanism of the transient response.

The effect of applying a tensile underload immediately after a tensile overload at high R ratio CAL (R=0.7) is to dramatically reduce the effect of the overload load interaction and in the cases of the OLR = 1.47 and 1.75 to preclude crack arrest. These observations compare well with other work [33,41,42]. A FEM treatment of fatigue crack growth, following a overload-underload combination was made by Zhang et.al. [33] who found that upon application of the underload the crack tip plastic zone yielded in compression and then subsequent re-loading gave a cyclic residual tensile stress at the crack tip. These residual tensile stresses replaced the residual compressive stress field resulting from the overload. The net result was an increase in ΔK_{eff} and a reduction in transient delay effects as observed here. The size of the reversed plastic zone is dependent on the change in loading (Equation 3.9) and since $(K_{ol}-K_{ul}) \gg (K_{ol}-K_{min})$ then the extent of the underload induced residual tensile field would be more significant during high R ratio loading. Closure exists for the lower portion of the loading curve so the reversed plastic zone size comparison is actually dependent on $(K_{ol}-K_{cl}) \gg (K_{ol}-K_{min})$.

In summary, these observations now suggest that residual stress fields are responsible for controlling the load interaction mechanism and they are most significant at high R ratios. It is proposed that static levels of crack closure exists at low R ratios and which only serves modify the applied ΔK at the crack tip to ΔK_{tip} in the manner suggested by Lang and Huang [54] so that $\Delta K_{tip} = K_{max} - K_{cl}$.

8.2 Crack Growth Mechanisms under SVAL

The proposition that plasticity in the residual stress field ahead of the crack tip controls the load interaction effects and that closure modifies the crack tip load range and only acts over the lower part of the cycle means that we need to give up the notion that ΔK_{eff} (Equation 3.12) is primarily determined by some contact phenomena of the fracture surfaces. ΔK_{eff} is more effectively determined by the point at which the fatigue crack tip experiences tensile stresses [38,36,54 which is the point at which the crack starts to propagate given by K_{PR} – the crack propagation stress intensity factor described in Section 3.6.3. This is not necessarily the traditionally measured closure load

It is known from Sun and Sehitoglu [36] that the point at which the crack tip stress becomes tensile, constitutes contributions from both crack closure and residual stresses. The difficulty with this work is in separating the contribution of crack closure in the wake of the crack from the contribution of residual stress fields in the crack tip plastic zone. The non-linearities in the compliance measured load-strain curves are most likely an addition of both plasticity induced crack closure and residual stresses ahead of the crack tip. Additionally the method and location of measurement strongly influences the level measured so the measurements made here can only give some approximate indication of K_{PR} levels [47].

If these observed load interaction effects due to the residual stress field occur under SVAL then it is likely that similar effects would occur under CVAL and that similar mechanisms would be responsible for a similar material, constraint and load levels. The overload-underload tests indicated that the occasional underload applied during CAL would tend to reduce the effect of any overloads or possibly accelerate crack growth in the absence of prior overloads. This is due to increased levels of tensile residual stresses in the crack tip plastic zone due to underloads [33]. This will impact on the interpretation of the CVAL tests because there are numerous tensile underloads due to GAG cycles and autorotations. The consequences of these underloads are discussed in the following section.

8.3 Complex Variable Amplitude Loading

8.3.1 Omission of Small Load Cycles

The fatigue crack growth behaviour of the small vibratory cycles was investigated by sequentially omitting different cyclic ranges of fatigue cycles from the Rotorix sequence. This omission procedure gave a significant effect on specimen life to failure particularly for the omission of the L16 vibratory cycles. This resulted in an increase of flights to failure of 3.6 for 7010 and 5.2 for Ti1023 and gave corresponding increases in average crack growth rates. The increase in specimen life due to omission of small cycles has been observed by others [65,66] and is due to a removal of damaging load cycles.

8.3.2 Fatigue Damage due to Vibratory Load Cycles

The significance of the contribution of vibratory cycles to the overall crack growth length damage requires further analysis of the crack growth rate curves. Under a safe life design of helicopter these small cycles would normally be ignored because they are not considered to cause fatigue damage [102] so it is important for a damage tolerance approach to quantify their effects on growth rates.

From Figures 7.25 and 7.26 the average crack growth rate per loading sequence can be determined at different levels of K_{peak} and from these the crack growth increment per sequence can be calculated. Based on the assumption that each cycle range causes the same amount of crack growth increment in each omission level test the crack length damage contribution for each range during the L16 tests can be derived. Hence the sum of all cycle range crack growth increments is given by the L16 test growth increment at each K_{peak} level. The difference between the L16 and L20 test will be due to the range 16 cycles. The extent of the different cycle range contributions to fatigue crack growth damage is shown in Figures 8.2 and 8.3 where the growth increments are expressed as a percentage of the growth increment from the L16 test.

In both materials the range 16 cycles cause a large proportion of the damage over the entire test. On average, the damage for the level 16 cycles is about 85% for Ti1023 and 75% for 7010. The fractographic examination of the fracture surfaces confirmed that most of the crack length damage had been caused by the L16 cycles. Referring to Figures 7.35 and 7.39 shows that bands of crack growth results from the long periods of high R ratio L16 cycles but these are not present on the fracture surface of the L32 Ti1023 test. The bands of L16 cycle growth account for about 80% of the fracture surface area. The next largest contributor to crack growth damage are the level 32 and above cycles. The damage contributions are typically 15% for Ti-1023 and 20% for 7010. In both materials the level 20 cycles give negligible contributions to crack damage which is expected because they only constitute 0.1% of the loading sequence.

Even though the L16 cycles constitute 94% of the total number of cycles in the sequence, the significant contribution to crack growth damage by the vibratory L16 cycles is an unexpected result. This is because the ΔK values of the cycles are very close to the threshold stress intensity range at the start of the test yet they dominate most of the crack growth damage from this point. A linear summation of crack growth life by the conservative Esacrack model (Table 7.12) indicated that the L16 should only contribute 41% of the damage. Said another way, the L16 cycles had *greater* fatigue crack growth rates under helicopter spectrum test loading than under equivalent CAL conditions. This is a significant observation because most fatigue crack models would not predict that these smaller cycles grow faster under CVAL because the models are generally developed to predict crack growth rate retardation. Hence prediction of growth rates under helicopter CVAL could give misleading predictions. The results from the Esacrack analysis (Table 7.12) indicate this is the case and under-predict the Ti-1023 L16 test by a factor of three.

These analyses show that the small range cycles have accelerated growth rates under CVAL compared with the equivalent cycles under CAL. This suggests that the K_{PR} or K_{cl} of the cycles is lower giving an increased ΔK_{eff} when compared with constant amplitude loading. An explanation of this observation is proposed in the following sections.

8.3.3 Crack Closure under Helicopter CVAL

The attempt to correlate crack closure measurements under the selected rotorhead loading sequence in 7010 and Ti1023 gave different results for each material. The Ti1023 crack closure measurements gave no detectable change in the measured non-linearity level (K_{cl} = 4.6 MPa.m$^{1/2}$) throughout the sequence. This is consistent with various sources [23,68] that state that crack closure does not vary during complex load sequences for stationary cracks. However, the 7010 crack closure measurements for the same sequence gave significantly varying levels of closure throughout. The closure level measured varied from K_{cl} = 4.6 to 17

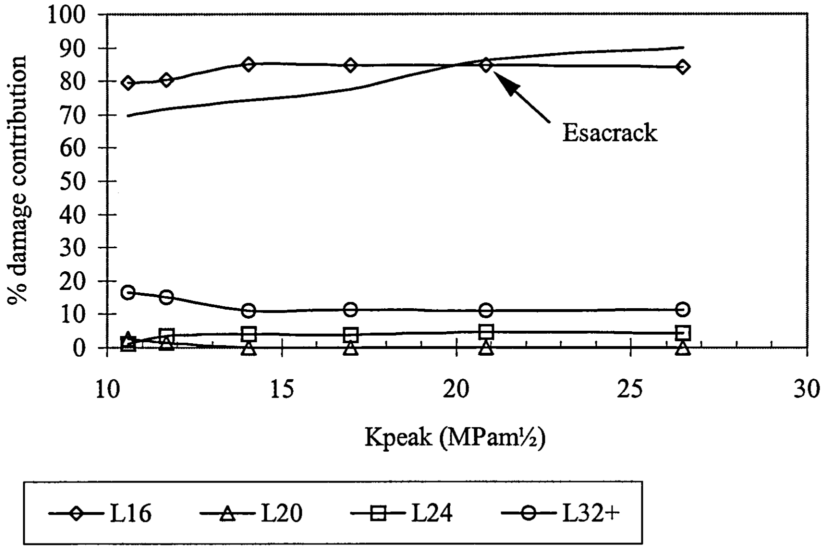

Figure 8.2 Percentage contribution to crack length damage for each omission range for Ti-1023 showing L16 results from Esacrack predictions.

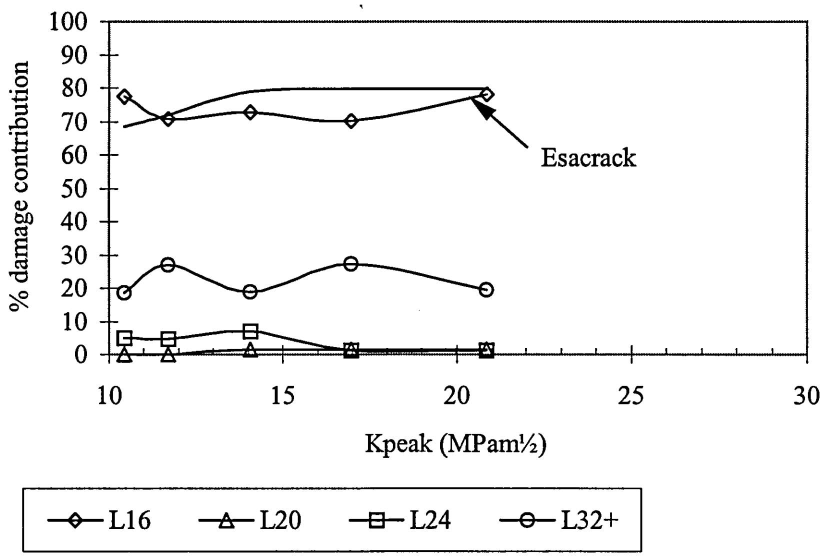

Figure 8.3 Percentage contribution to crack length damage for each omission range for 7010 showing L16 results from Esacrack predictions.

MPa.m$^{1/2}$. This difference with literature here is that the crack is not stationary because growth greater than the largest plastic zone size generated by the sequence. Change! The differences in closure observations between the materials are due to the relative compliance of the specimens and the sensitivity of the strain measurement equipment as discussed earlier.

Sun and Sehitoglu [36] state that K_{PR} is a resultant of both the crack closure in the wake of the crack and the residual stress fields ahead of the crack which is corroborated by Marci and Lang [32]. If this is true then the varying changes in gauge linearity (as opposed to conventional closure) are indications of residual stress field changes *plus* some contribution of closure at low R ratio. The changes in loads at the non-linearities that were observed during the 7010 selected rotorhead sequence would then coincide with instantaneous changes in residual stress fields in addition to a static level of crack closure.

In summary, the crack closure contributions defined at the point of non-linearity are confined to the low R ratio cycles and the fluctuations are due to changes in the residual stress field from load level changes. Hence, the crack propagation stress intensity factor K_{PR} could provide a suitable means to calculate ΔK_{eff} on a cycle-by-cycle or block-by-block basis. However, these tests only give a qualitative guide to what is happening to K_{PR} as compliance measurement techniques can not provide a definitive measurement of this. Further investigation of K_{PR} determination was not specifically designed for in these tests but the method suggested by Lang and Huang [54] would be suitable.

8.3.4 Model for Accelerated Growth Rates of Small Vibratory Load Cycles

The key to the accelerated growth rates is the 'form' of the loading sequence. Typically most cycles have similar K_{max} values there are no tensile overloads and periodic underloading occurs due to the GAG cycles and low R ratios manoeuvres. The underload tests in the SVAL section indicated that the underload can eliminate or reduce the effect of overloads during high R ratio loading so could cause acceleration during constant amplitude loading. However, the GAG underloads occur infrequently so it is most likely that underloading due to the occasional low R ratio manoeuvre is responsible for reducing K_{PR}. This effect of intermittent underloads causing acceleration of high R ratio CAL crack growth rates is consistent with observations by Fleck [101].

The residual stress model offered by Lang and Huang [54] and given in Section 3.6.3 provides the best clarification of these results. The following provides a factor for growth rate acceleration in high R ratio fatigue cycles with periodic block underloading using the equations of this model and the parameters of the selected loading sequence tests on Ti1023.

Consider typical constant amplitude loading at high R ratio cycles of R=0.8. (From CVAL Test 10: $K_{max} = 20.4$ MPa.m$^{1/2}$, $K_{min} = 16.32$ MPa.m$^{1/2}$, $\Delta K_{th} = 1.8$ MPa.m$^{1/2}$ and $K_{cl} = 4.6$ MPa.m$^{1/2}$). From Equation 3.16 and accounting for $K_{cl}<K_{min}$ gives:

$R_{tip} = K_{min}/K_{max} = 0.8$

Substituting into Equation 3.19 gives:

$K_{PR} = (0.455+0.321R_{tip}+0.208R^2_{tip}) \cdot K_{max} = 17.24$ MPa.m$^{1/2}$

Therefore $\Delta K_{eff,\,RCS} = (K_{max} - K_{PR}) - \Delta K_{th} = \underline{1.36 \text{ MPa.m}^{1/2}}$

Now consider a subsequent low R ratio manoeuvre to say R=0.5, CAL at $K_{max} = 10.2$ MPa.m$^{1/2}$, $K_{min} = 5.1$ MPa.m$^{1/2}$, $\Delta K_{th} = 1.8$ MPa.m$^{1/2}$ and $K_{cl} = 4.6$ MPa.m$^{1/2}$. Substituting into Equations 3.16 and 3.19:

$K_{PR} = (0.455+0.321R_{tip}+0.208R^2_{tip}) \cdot K_{max} = 6.81$ MPa.m$^{1/2}$

At this point it is assumed that K_{PR} remains at this level when the R=0.8 loading resumes with $K_{min} > K_{PR}$. The effect of the low R ratio manoeuvre has been to reduce the crack propagation stress intensity factor K_{PR} below K_{min} such that the subsequent high R ratio cycles now have increased effective stress intensity factor ranges. Now the effective stress intensity factor range will now be:

$\Delta K_{eff,\,RCS} = (K_{max} - K_{min}) - \Delta K_{th} = \underline{2.28 \text{ MPa.m}^{1/2}}$

The increased $\Delta K_{eff,\,RCS}$ will result in an increase in crack growth rates for these cycles. Hence the proportion of underload effected high R cycles ($\Delta K_{eff,\,RCS,UL}$) to constant amplitude load cycles ($\Delta K_{eff,\,RCS,CAL}$) is $\Delta K_{eff,\,RCS,UL} / \Delta K_{eff,\,RCS,CAL} = 2.28 / 1.36 = \underline{1.7}$.

Equation 4.1 can be reduced to:

$$\frac{\frac{da}{dN_{UL}}}{\frac{da}{dN_{CAL}}} \propto \left(\frac{\Delta K_{eff,RCS,UL}}{\Delta K_{eff,RCS,CAL}} \right)^n$$

so that the acceleration of growth rates for underload affected high R cycles to constant amplitude load cycles is given by a factor of $1.7^n = 1.7^{2.55} \approx \underline{3.7}$. This factor can be determined at each K_{peak} (10.4 to 45 MPa.m^{½}) value of the test during the test and is given in Figure 8.4.

The above calculation demonstrates that a physical phenomenon can cause acceleration of the high R ratio load cycles but it remains an idealised mechanism because of the much more complex nature of the rotorhead loading sequence. Nevertheless it is a useful approximation to show that the acceleration factors predicted do average out over the test duration to about a factor of three.

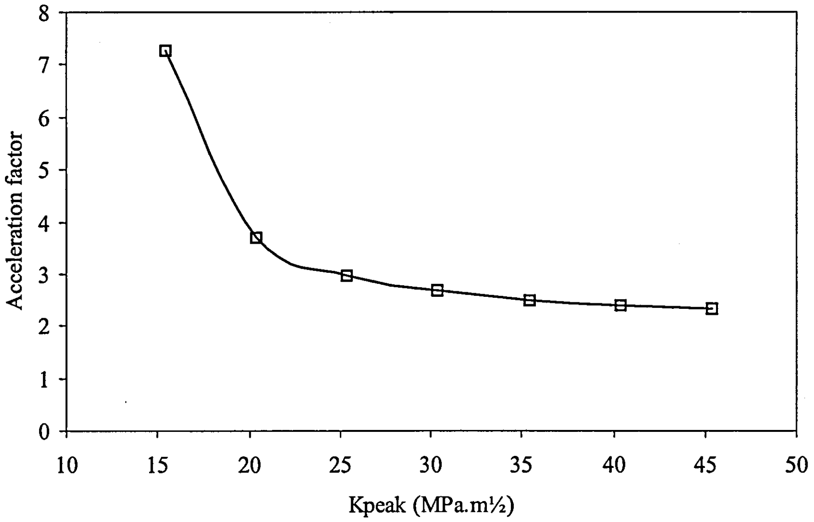

Figure 8.4 Acceleration factor for high R ratio, vibratory cycles as a result of reduced K_{PR} levels caused by intermittent low R ratio manoeuvres

Two crucial points remain to determine if K_{PR} does explain the vibratory load cycle crack growth rate acceleration: (i) Once K_{PR} is reduced by the low R ratio manoeuvres how does it change for subsequent high R ratio loading? and (ii) Are the low R ratio cycles also affected by increased K_{PR} levels due to the high R ratio cycles? The situation is illustrated in Figure 8.5.

The first point can be explained by a FE treatment of the overload-underload problem by Zhang et.al. [33]. They found that upon application of the underload the crack tip plastic zone yielded in compression and then subsequent re-loading gave a cyclic residual tensile stress at the crack tip as mentioned previously. The tensile residual stresses are then reduced in a transient manner under subsequent loading until the crack tip reached the boundary of the affected residual stress field. See Figure 8.6. The reversed plastic zone of the subsequent high R ratio cycles is fully enclosed in the underload affected zone. As long as the low R ratio manoeuvre is repeated within the affected zone then the K_{PR} level would be persistently reduced. This is consistent with the observed transient nature of the SVAL overload-underload test crack growth rates which suggests the effect is sustained for some number of cycles following the overload event. It is also indicated by the strain-load curves of the 7010 rotorhead loading sequence test. Referring to Figure 8.7 the point of non-linearity increases between curves 7 to 8 which are separated by a long section of high R ratio L16 cycles.

Secondly, the low R ratio manoeuvre cycles are not affected by the high R ratio cycle increasing K_{PR} because the underload reversed plastic size (given as $r_{p\text{-}UL} \propto (K_{max}-K_{cl})^2$) is larger than the reversed plastic zone size for the L16 cycle. The work of Marci and Lang [32] indicate this is the case because their measurements of K_{PR} were reduced instantaneously with the reduction in load level. Therefore, the low R ratio cycles behave as per normal. The analysis presented here is not done in a quantitative manner, but to do so would require some measurement of the K_{PR} level throughout the CVAL sequence.

The Esacrack prediction of the 7010 CVAL omission level tests was unconservative for all the tests. This could be attributed to the fact that material properties were taken from the model database and not the test material. There were some differences in the CAL test results and the model as indicated by Figure 6.9. Additionally the L16 test at 10kN had unexpectedly low crack growth rates as discussed in Section7.3.3. Higher crack growth rates would result in a lower crack growth life which may have shown an accelerated growth rate in a similar manner to the Ti1023 tests.

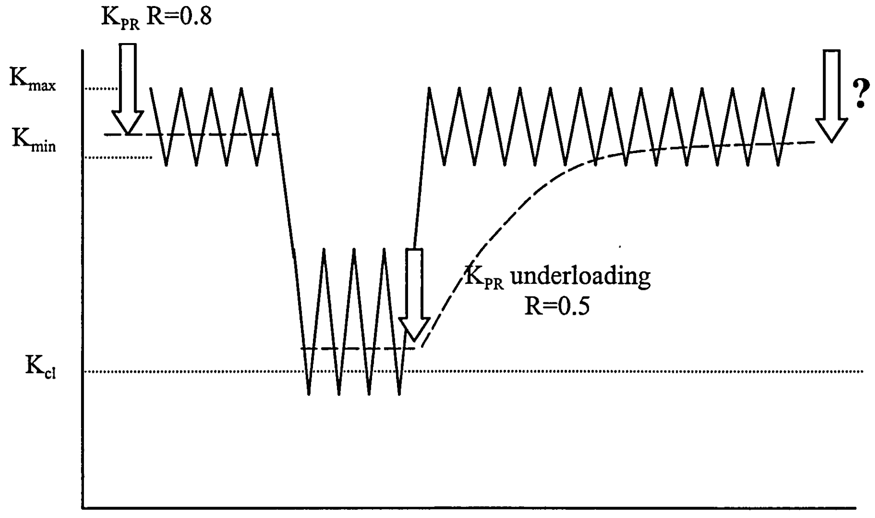

Figure 8.5 Schematic of changing K_{PR} levels due to periodic low R ratio block underloading.

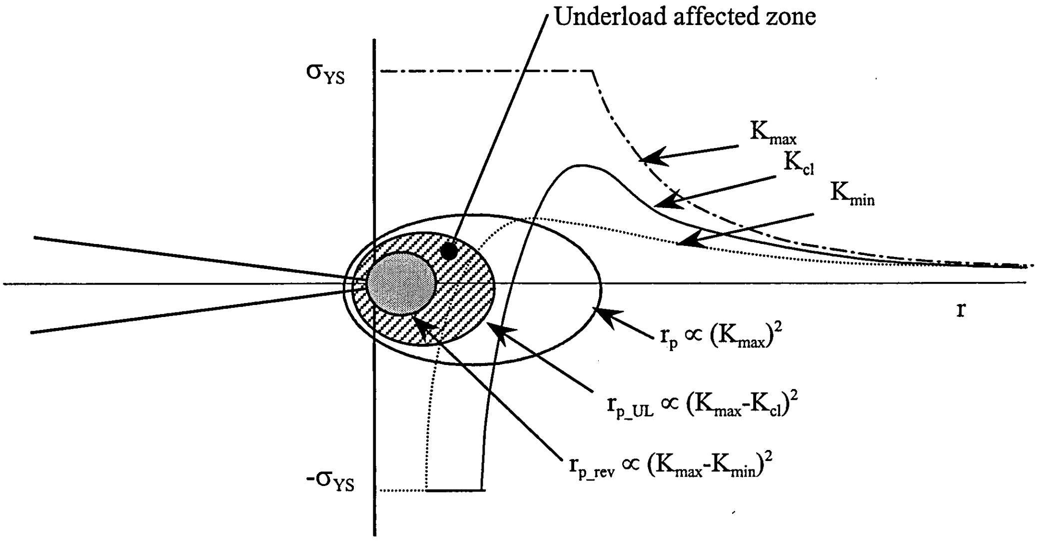

Figure 8.6 Schematic of crack tip plastic zone sizes and residual stress fields due to high R ratio loading and periodic low R ratio manoeuvre loading. Notation from Figure 8.5

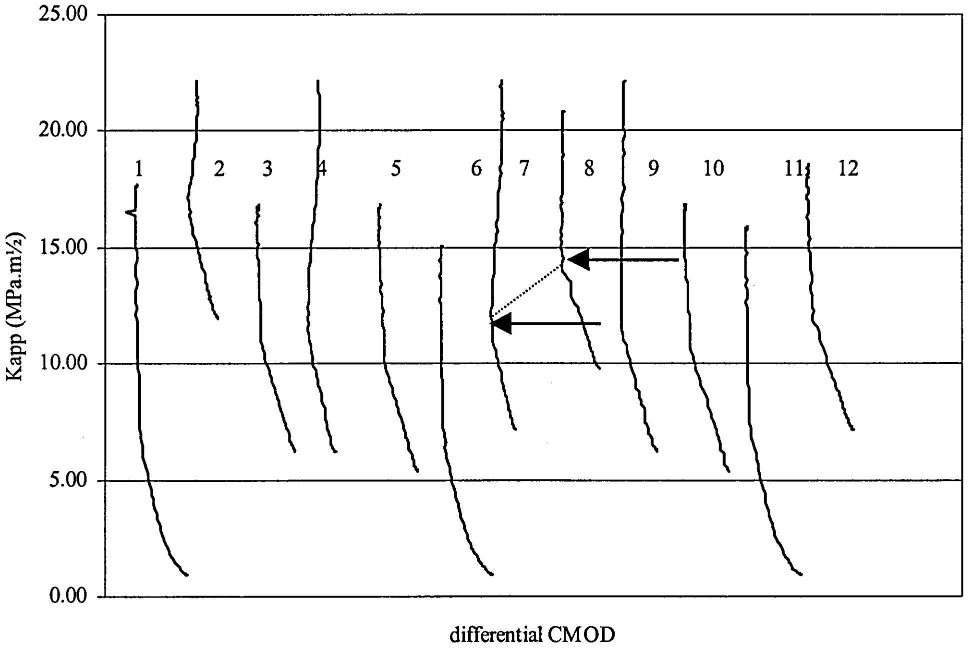

Figure 8.7 NTS gauge test on Ti1023 selected rotorhead sequence indicate change in non-linearity of curves 7 and 8 which were measured before and after a section of high R ratio vibratory loads.

8.4 Application to Helicopter Damage Tolerance Design

The omission and the accelerated growth rates of the high R ratio vibratory load cycles in the presence of periodic block underloading will impact on the damage tolerant design of helicopter structures in two ways:

(i) Design of fatigue loading sequences including omission techniques,
(ii) Selection of materials and component stress levels.

8.4.1 Design of Fatigue Loading Sequences

The development of the Rotorix loading sequence described in this thesis addressed some of the issues involved in the design of fatigue loading sequences. Namely, the representation of vibratory and manoeuvre loads and the simplification of the sequence for testing and analysis purposes.

The Helix/Felix methodology [5,6] used to develop the Rotorix loading sequence had two major shortcomings which arose from computer storage problems when the it was originally defined. These were the definition of a single mean load for each manoeuvre and the binning of load cycles into integer levels of 4. In reality, most manoeuvres performed during flight have a range of cycle means as the sequence will include entry into manoeuvre, steady state manoeuvre and then exit from the manoeuvre. The binning of cycle peaks and troughs into integer levels of 4 should also be avoided.

It is possible to describe a manoeuvre as a sequence of representative cycles by simply changing the sequence generation algorithm: A straightforward technique would be to identify actual strain gauge data representative of a typical manoeuvre, extract the data and gate it at an appropriate level. A fatigue loading sequence could then be made up of manoeuvre strain gauge data concatenated together into a sequence representing the service usage of the component. Realistic load changes would then be properly characterised and this would avoid binning and assigning a dominant mean

Differences exist between the Rotorix 16 and Felix28 [5,6] sequences which indicate that the sequence generation method is component and location dependent. The comparison with the Felix28 sequence which represents the rotorblade maximum bending moment location is shown below in Figure 8.8. The data shown is derived from a rainflow analysis of each sequence. The main difference is the larger cycle ranges in the Felix28 sequence which means that using the Felix28 sequence to perform rotorhead component testing would result in shorter crack growth lives. This demonstrates that each location has a unique loading sequence due to the complex nature of the loading paths from the main rotor to the rotorhead and into the fuselage of the helicopter.

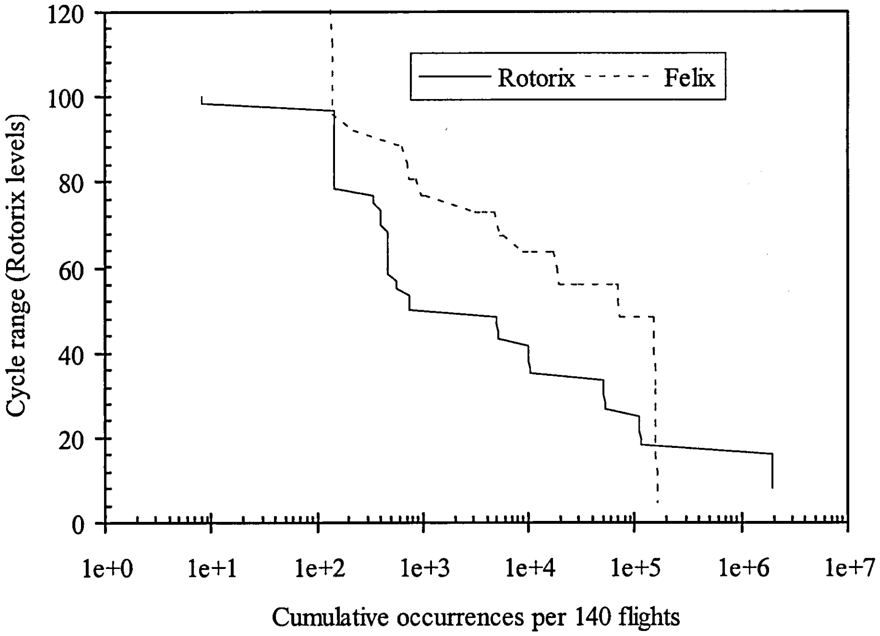

Figure 8.8 Comparison of cumulative occurrences between Felix 28 and Rotorix 16 helicopter loading sequences.

Simplification of a helicopter loading sequence for testing is best achieved by omission of the small vibratory load cycles which gives a significant reduction in sequence lengths. However, the main drawback demonstrated here is that these small cycles contribute to a significant amount of crack growth damage so test results can be misleading. A criteria for 'safe' omission of small load cycles could be based upon the mechanism of accelerated crack growth of these cycles as proposed earlier. This would be done by determining when a cycle range can be omitted from a sequence such that its omission will not result in changes in specimen life. This occurs when the $\Delta K_{eff,RCS}$ given by Equation 3.14 equals zero:

$$\Delta K_{eff,\,RCS} = (K_{max} - K_{PR}) - \Delta K_{th} = 0$$

$$\text{or } (K_{max} - K_{PR}) = \Delta K_{th} \qquad \textit{Eqn. 8.1}$$

The criterion needs to consider the range and mean of individual fatigue cycles because of the dependency of K_{PR} on these. A rainflow count of the Rotorix16 loading sequence indicates the L16 dominant cycle has maximum load level of 96 and minimum load level of 80 (R = 80/96 = 0.83). In this case $K_{PR} < K_{min}$ because of underloading manoeuvres so equation 8.1 can be written as:

$$K_{peak}\,(0.96 - 0.80) = 1.8\ \text{MPa.m}^{1/2}$$

Solving for the K_{peak} value at which the L16 cycles can be safely omitted gives $K_{peak} = 11.25$ MPa.m$^{1/2}$. Below this value the typical L16 cycles will not cause fatigue damage. This procedure can be applied to every high R ratio cycle in the loading sequence and used for both specimen and full-scale testing if stress intensity solutions are known beforehand. However, Figure 8.2 indicated that the L16 cycles were causing damage from at least $K_{peak} = 10.4$ MPa.m$^{1/2}$ at the start of the test. This discrepancy is due to the ΔK_{th} value used in the calculation which was taken from long crack threshold tests in Ref. [90]. The threshold value required by the Lang and Huang model is determined in a different way and would be smaller because it does not include K_{PR} which the long crack threshold test intrinsically does [54].

An interesting comparison can be made of a safe omission cycle range determined using a safe life based criteria with that determined by the above tests. Typically in the safe life design of a helicopter component, stresses are selected so that the main rotor vibratory loads are non-damaging. Heuler and Seeger [102] showed that a safe life, initiation based approach to omission of cycles would give a typical value for safe omission as 50% of the endurance limit of the material. This would give a safe omission level of 187.5 MPa for Ti1023 at typical stress levels under which the rotorhead operates [88]. This translates into a ΔK of 8.4 MPa.m$^{1/2}$ (for an arbitrary component) giving a K_{peak} of 52.5 MPa.m$^{1/2}$ for an R=0.83 cycle. This contrasts with the crack growth based analysis which gives a safe omission level of $K_{peak} = 11.25$ MPa.m$^{1/2}$. The 50% endurance limit criterion would result in misleading crack growth life predictions for a flawed structure. This results suggests it is unlikely to be possible to maintain safe life design stresses in damage tolerant helicopters. Lincoln [4] has stated that there is generally a lack of agreement in life prediction for a component designed under safe life and then subsequently analysed under damage tolerance. For example, parts with a long safe life have a short damage tolerance life and vice versa. The problem is associated with the initial design of the component which never considered crack growth propagation at the stress levels used in a safe life design.

8.4.2 Material Selection and Stress Levels in Design

The damage tolerance capability of a helicopter structure can be demonstrated by examining crack growth rates over a range of flaw sizes for an arbitrary edge cracked component. This example component is 'subjected' to the Rotorix 16 sequence with an operating peak tensile stress of 400 MPa (approximately one third of the σ_{UTS} for Ti1023) by converting the crack growth rate per sequence curve into crack lengths that will produce the same K_{peak}'s assuming similitude exists. This is shown in Figure 8.9. The experimental data can be applied to range of crack lengths from 0.35 to 4 mm.

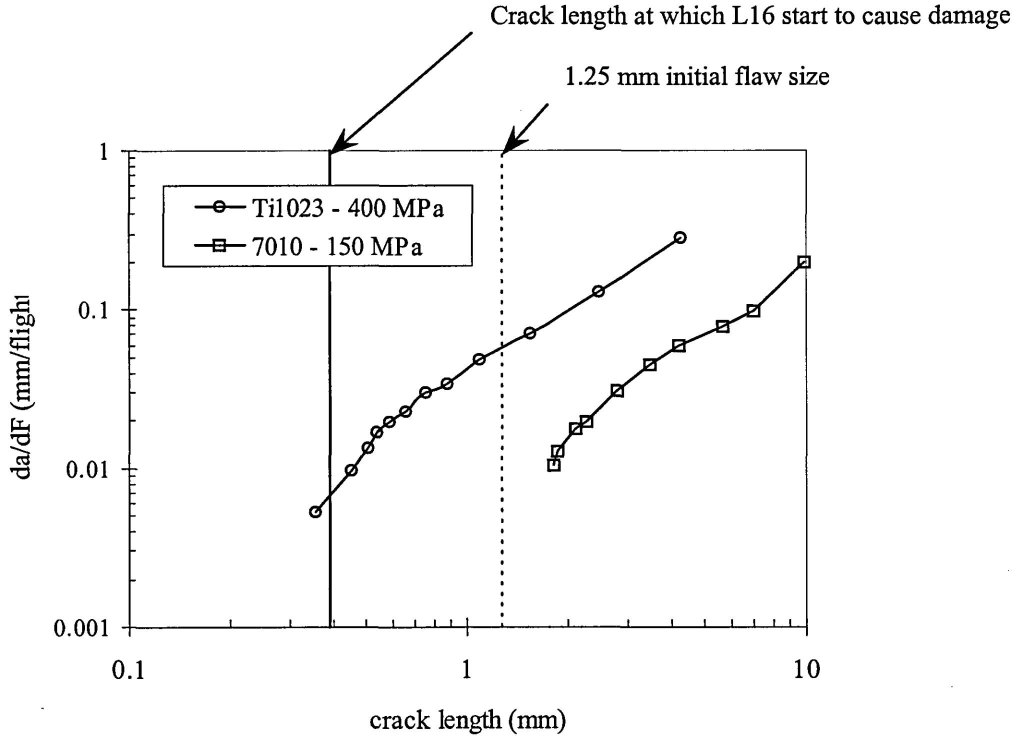

Figure 8.9 Average crack growth rates per flight against crack length for nominal edge cracked Ti1023 component at 400 MPa calculated through equivalence of K_{peak} values. The same procedure applied to the 7010 data but for a peak stress of 150 MPa is also shown.

Figure 8.9 indicates the crack length above which the vibratory load cycles will start to cause damage. At 0.39 mm this is will below the typical initial starting defect size of 1.25mm used in the aerospace industry [4]. Improving the damage tolerance capability of a helicopter structure would require the vibratory load cycles to be maintained below their fatigue threshold. Referring to Figure 8.9, an elimination of crack growth due to vibratory load cycles would require a shift of the curve to the left and/or reducing the size of the initial defect. This effectively requires a reduction in component peak stress level which usually translates into an increase in weight. A stress reduction approach similar to this was taken by Bell Helicopters in the damage tolerance design of a 6Al-4V titanium transmission adapter on the V-22 tiltrotor aircraft [103]. This component is subject to high-frequency rotor-induce vibratory loads during high speed, high load factor manoeuvres. A finite element model of the component indicated intrinsic flaws of 1.25 mm would not grow under service loading. The design had a 10% weight increase over the safe life designed adapter but this was offset by increased reliability and structural integrity maintained by the damage tolerance approach.

Yield strength and crack growth rate differences between 7010 and Ti1023 are also indicated in Figure 8.9. A typical maximum operating stress of 150 MPa was used for 7010. The graph shows that crack growth rates per flight are significantly less for 7010 even though overall growth rates for the same stress intensity (as in test) are higher. This example emphasises the differences between different parts of the helicopter structure because some materials will be more sensitive to crack growth under vibratory load cycles. This is mainly because of the lower operating stress that a safe life design gives for aluminium alloys and not necessarily due to material fatigue crack growth properties. Titanium or other high strength metals may have better fatigue crack growth properties but are subject to higher operating stresses. This indicates that aluminium fuselage structures would be amenable to damage tolerance design because vibratory load cycles will not grow from typical initial flaw sizes (1.25 mm). A reasonable inspection regime could be applied because crack growth will occur under manoeuvre load cycles in a similar manner to fixed wing transport aircraft.

9. CONCLUSIONS

The principal conclusions drawn from this work are summarised as follows:

(1) A fatigue loading sequence was developed for a location on the titanium rotorhead of a transport helicopter to represent the change in stress levels during simulated service usage. The sequence characterised a variety of loading cycles including ground-air-ground loads, manoeuvre loads and vibratory loads originating from the revolution of the main rotor.

(2) The significant feature of the rotorhead loading sequence was the large number of high mean stress vibratory cycles which constituted 94% of the entire sequence. These cycles typically had R ratios ranging from 0.7 to 0.9 and had cycles ranges of 16% of the peak load in the sequence.

(3) Simple variable amplitude loading tests using single and double overloads and overload-underload combinations were used to investigate the effect of these on the near-threshold fatigue crack growth rates in the Ti1023 titanium alloy. It was found that increasing the overload ratio increased the delay effect and this effect was increased as the baseline constant amplitude loading R ratio was increased. The effects were attributed to increased plasticity at the crack tip and proximity of the ΔK to the fatigue threshold respectively.

(4) It was found that the effect of the overload followed immediately by a tensile underload was to significantly reduce the delay effect and crack growth rate transient of the tensile overload.

(5) Measurements of strain-load curves near the crack tip were made to determine levels of crack closure occurring near the crack tip. Crack closure was measured for the lower portion of the loading curve and so affects low R ratio load cycles but was not measured for the high R ratio overload tests. Changes in the closure level before and after an applied overload did not occur. It was proposed that residual stress fields ahead of the crack tip resulting from the overload were responsible for the load interaction effects at high R ratios.

(6) Crack closure in high strength materials under plane strain, near-threshold conditions is confined very close to the crack tip and changes in closure are not detectable using traditional compliance techniques.

(7) The progressive omission of increasing load cycle ranges was used to investigate the effect of individual load cycle ranges in the rotorhead loading sequence.

(8) Small vibratory load cycles had the most significant effect on the overall growth rate of the variable amplitude loading sequence, causing up to 80% of the fatigue crack damage which was supported by fractographic examination. Comparison with a constant amplitude loading model, which predicted that the small cycles should contribute 41% of the damage, revealed that these small cycle were growing at an accelerated rate when applied in conjunction with periodic underloads due to low R ratio underloading.

(9) A residual stress field model was invoked to explain the accelerated growth rate behaviour of the vibratory load cycles. A new parameter was used to calculate ΔK_{eff} for the vibratory load cycles. This model showed that ΔK_{eff} is increased due to periodic underloads originating from the low R ratio manoeuvres in the loading sequence.

(10) Significant crack growth rates due to vibratory load cycles under helicopter loading conditions mean that the damage tolerant design of high strength (Ti1023) helicopter components will not be achieved using current stress levels given by a safe life analysis. A reduction in stress levels and initial flaw size is required but with increases in component weight and inspection length capability which are compromised against increased levels of maintainability and structural integrity.

(11) Lower strength aluminium alloy (7010) components are less sensitive to vibratory load cycles because of reduced operating stresses given by a safe life analysis. This indicates that aluminium fuselage structures would be amenable to damage tolerant design because vibratory load cycles will not grow from typical initial flaw sizes (1.25 mm). A reasonable inspection regime could be applied because crack growth will occur under manoeuvre load cycles in a similar manner to fixed wing transport aircraft.

9.1 Recommendations for future work

(1) Improvements of methods for generating fatigue loading sequences for helicopter components.

(2) Investigation of the transient nature of residual stress fields using techniques similar to Marci and Lang [32] model. SVAL and CVAL loading conditions relevant to helicopter components and loading conditions should be considered.

(3) Subsequent to (2) improvements of current cycle-by-cycle fatigue crack growth prediction models to incorporate the residual stress field approach which uses the point at which the crack tip stress field becomes positive to determine ΔK_{eff}.

(4) Investigation of fatigue crack growth from small or short fatigue cracks under helicopter loading spectra in high strength materials. This would aid damage tolerance design of components used in the construction of rotor and power transmission structures in helicopters.

10. REFERENCES

[1] FAA Airworthiness Regulations, Part 29, Transport Category Helicopters, Section 29.571, Fatigue Evaluation of Structure, Federal Aviation Administration, US Department of Transport.

[2] FAA Advisory Circular, AC 29.571-1, Fatigue Evaluation of Transport Category Rotorcraft Structure, Federal Aviation Administration, US Department of Transport.

[3] Robust Fatigue Crack Growth Model for Rotorcraft Metallic Structures, DTI Contract No. RA/6/30/06, June 1998.

[4] Lincoln, J.W., "Damage tolerance for helicopters," Aeronautical Fatigue in the Electronic Era, Proceedings of the 15th Symposium of International Committee on Aeronautical Fatigue, A. Berkovits Ed., 21-23 June, 1989, Jerusalem, Israel, pp. 263-290.

[5] Edwards, P.R., Darts, J., "Standardised fatigue loading sequences for helicopter rotors (Helix and Felix), Part 1: Background and fatigue evaluation," Technical Report 84084, Royal Aircraft Establishment, August 1984.

[6] Edwards, P.R., Darts, J., "Standardised fatigue loading sequences for helicopter rotors (Helix and Felix), Part 2: Final definition of Helix and Felix," Technical Report 84085, Royal Aircraft Establishment, August 1984.

[7] Noback, R., "State of the art and statistical aspects of helicopter fatigue substantiation procedures," Helicopter Fatigue Life Assessment, AGARD Conference Proceedings, AGARD-CP-297, September, 1980, pp.1-22.

[8] Gallagher, J.P., Giessler, F.J., Berens, A.P., " USAF Damage Design Handbook, Guidelines for the analysis and design of damage tolerant aircraft structures," Air Force Wright Aeronautical Laboratories, AFWAL-TR-82-3073, 1984.

[9] MIL-A-83444, USAF, Airplane Damage Tolerance Requirements, 1983.

[10] Tapavicza, M., "Damage tolerance concepts for modern helicopters," 12th European Rotorcraft Forum, Garmisch-Partenkirchen, West Germany, Sept. 22-25, 1986.

[11] Everett, Jr, R.A., "A comparison of fatigue life prediction methodologies for rotorcraft," NASA Technical Memorandum TM102759, December 1990.

[12] Schneider, G., Gunsallus, C., "Continuation of the AHS round robin on fatigue reliability," American Helicopter Society 47th Annual Forum, Phoenix, Arizona, May 6-8, 1991.

[13] Crawford, C.C., Carlson, R.L., Bates, P.R., " Damage tolerance analysis for rotorcraft: What the issues are," 17th European Rotorcraft Forum, Berlin, Germany, September 24-26, 1991.

[14] Schneider, G.J., "Application of damage tolerance to the H-53 Helicopter," ANSI/ENSIP Conference, AFWAL-TR-88-4128, June 1988.

[15] Tritsch, D.E., Schneider, G.J., Chamberlain, G., Lincoln, J.W., "Damage tolerance assessment of the HH-53 Helicopter," American Helicopter Society Annual 46th Forum, pp. 841-849, 1990.

[16] Van Etten, C.D., Keary, P.E., "Safe strength/damage tolerance assessment vs. a fail-safe approach in the design of the SH-2G engine mount structure," American Helicopter Society Annual 46th Forum, pp. 851-838, 1990.

[17] Boorla, R., "Damage tolerance analysis of dynamic components of rotary wing aircraft," Journal of the American Helicopter Society, Vol. 34, No. 4, October 1989, pp. 47-55.

[18] Spencer, C.W., Killian, S. L., "Structural analysis of large titanium castings in a high-cycle, rotor-induced vibratory load environment," American Helicopter Society Annual 51st Forum, Vol. 2, pp. 1615-1626, 1995

[19] Marquet, T., Struzik, A., "Damage tolerance applied to metallic components," 24th European Rotorcraft Forum, Marseilles, France September 1998.

[20] Broek, D., Elementary Engineering Fracture Mechanics, 4th Edition, Kluwer Academic Publishers, 1986.

[21] Rice, J.R., "Mechanics of crack tip deformation and extension by fatigue," Fatigue and Crack Propagation, ASTM STP 415, American Society of Testing and Materials, 1967, pp. 247-311.

[22] Dugdale, D.S., "Yielding of steel sheets containing slits," Mechanics and Physic of Solids, Vol. 8, pp. 100-104, 1960.

[23] Newman, J.C., "A crack closure model for predicting fatigue crack crowth under aircraft spectrum loading," Methods and Models for Predicting Fatigue Crack Growth under Random Loading, ASTM STP 748, J.B. Chang and C.M. Hudson, Eds., American Society for Testing and Materials, 1981, pp. 53-84.

[24] Paris, P.C., Erdogan, F., "A critical analysis of crack propagation laws," Transactions of ASME Journal of Basic Engineering, 1963, pp. 528-534.

[25] Ward-Close, C.M., Bolm, A.F., and Ritchie, R.O., "Mechanisms associated with Transient Fatigue Crack Growth under Variable-Amplitude Loading: an Experimental and Numerical Study," Engineering Fracture Mechanics, Vol. 32, No. 4, pp. 613-638, 1989.

[26] Suresh, S., "Micromechanisms of fatigue crack growth retardation following overloads," Engineering Fracture Mechanics, Vol. 18, No. 3, pp. 577-593, 1983.

[27] Davidson, D.L., "Determination of the local driving force for fatigue crack growth under variable amplitude loading," Proceedings of the Third International Spring Meeting of the French Metallurgical Society: Fatigue Crack Growth under Variable Amplitude Loading, J. Petit, D.L. Davidson, S. Suresh and P. Rabbe Eds., June 1988, pp. 1-11.

[28] Tsukuda, H., Ogiyama, H., Shiraishi, T., "Fatigue crack growth and closure at high stress ratios," Fatigue and Fracture of Engineering Materials and Structures, Vol. 18, No. 4, pp. 503-514, 1995.

[29] Geary, W., "A review of some aspects of fatigue crack growth under variable amplitude loading," International Journal of Fatigue, Vol. 14, No. 6, pp. 377-386, 1992.

[30] Damri, D., Knott, J.K., "Transient retardations in fatigue crack growth following a Single peak overload," Fatigue and Fracture of Engineering Materials and Structures, Vol. 14, No. 7, pp. 709-719, 1991.

[31] Elber, W., "The significance of fatigue crack closure," Damage Tolerance in Aircraft Structures, ASTM STP 486, American Society of Testing and Materials, 1971, pp. 230-242.

[32] Lang, M., Marci, G., "Reflecting on the mechanical driving force for fatigue crack propagation," Fatigue and Fracture Mechanics: 29th Volume, ASTM STP 1321, T.L. Panontin and S.D. Sheppard, Eds., American Society of Testing and Materials, 1997. To be published.

[33] Zhang, X., Chan, A.S.L., Davies, G.A.O., "Numerical simulation of fatigue crack growth under complex loading sequences," Engineering Fracture Mechanics, Vol. 42, No. 2, 1992, pp. 305-321.

[34] Kraken, Users Manual, nCode International Ltd., Sheffield, U.K., 1995.

[35] de Koning, A.U., Liefting, G., "Analysis of crack opening behaviour by application of a discretised Strip Yield model," Mechanics of Fatigue Crack Closure, ASTM STP 982, J.C. Newman, Jr. and W. Elber, Eds. American Society for Testing and Materials, Philadelphia, 1998, pp. 437-458.

[36] Sun, W., Sehitoglu, H., "Residual stress fields during fatigue crack growth," Fatigue and Fracture of Engineering Materials and Structures, Vol. 15 No., 2, pp. 115-128, 1992.

[37] Schijve, J., "Fatigue crack closure: observations and technical significance," Mechanics of Fatigue Crack Closure, ASTM STP 982, J.C. Newman, Jr. and W. Elber, Eds., American Society for Testing and Materials, pp. 5-34, 1988.

[38] Tsukuda, H., Ogiyama, H., Shiraishi, T., "Transient fatigue crack growth behaviour following single overloads at high stress ratios," Fatigue and Fracture of Engineering Materials and Structures, Vol. 19, No. 7, pp. 879-891, 1996.

[39] Turner C.C., Carmen, C.D., Hillberry, B.M., "Fatigue crack closure behaviour at high stress ratios," Mechanics of Fatigue Crack Closure, ASTM STP 982, J.C. Newman, Jr.

and W. Elber, Eds. American Society for Testing and Materials, Philadelphia, 1998, pp. 528-535.

[40] Shuter, D.M., Geary, W., “The influence of specimen thickness on fatigue crack growth retardation following an overload,” International Journal of Fatigue, Vol. 17, No. 2, pp.111-119, 1995.

[41] Carlson, R.L., Kardomateas, G.A., “Effects of compressive load excursions on fatigue crack growth,” International Journal of Fatigue, Vol. 16, pp. 141-146, 1994.

[42] Topper, T.H., Yu, M.T., “The effect of overloads on threshold and crack closure,” International Journal of Fatigue, Vol. 7, No. 3, 1985, pp. 159-164.

[43] Zuidema, J., Shen, W.Y., Janssen, M., “Retardation in fatigue crack growth in aluminium 2024 after blocks of underloading”, Fatigue and Fracture of Engineering Materials and Structures, Vol. 14, No. 10, 1991, pp. 991-1005.

[44] McClung, R.C., “The influence of applied stress, crack length and stress intensity factor on crack closure”, Metallurgical Transactions A, Vol. 22A, pp. 1559-1571, July , 1991.

[45] Liaw, P.K., Overview of crack closure at near-threshold fatigue crack growth levels,” Mechanics of Fatigue Crack Closure, ASTM STP 982, J.C. Newman, Jr. and W. Elber, Eds. American Society for Testing and Materials, Philadelphia, 1998, pp. 62-92.

[46] Ritchie R.O., Yu, W., Holm, D.K., Blom, A.F., “Development of fatigue crack closure with the extension of long and short cracks in aluminium alloy 2124: A comparison of experimental and numerical results,” Mechanics of Fatigue Crack Closure, ASTM STP 982, J.C. Newman, Jr. and W. Elber, Eds. American Society for Testing and Materials, Philadelphia, 1998, pp. 300-316.

[47] Abdel Mageed, A.M., Pandey, R.K., Chinadurai, R., “Effect of measurement location and fatigue loading parameters on crack closure behaviour,” Materials Science and Engineering, A150, pp.43-50, 1992.

[48] Fleck, N.A. “Influence of stress state on crack growth retardation. Basic questions in fatigue.” Vol. 1 ASTM STP 924, American Society for Testing and Materials, 1998, pp. 157-183.

[49] Cotterill, P.J., Knott, J.F., "Overload retardation of fatigue crack growth in a 9% Cr 1% Mo steel at high temperatures," Fatigue and Fracture of Engineering Materials and Structures, Vol. 16, No. 1, pp. 53, 1993.

[50] McEvily, A.J., Yang, Z., "Fatigue crack growth retardation mechanisms of single and multiple overloads," Proceedings of 4th International Conference on Fatigue and Fatigue Thresholds, H. Kitigawa and T. Tanaka (Eds.), Birmingham, U.K., 1990, 23-36.

[51] Newman J.C., Bigelow, C.A, Shivakumar, K.N., "Three dimensional elastic-plastic finite element analysis of constraint variation in cracked bodies," Engineering Fracture Mechanics, Vol. 46, No. 1, pp. 1-13, 1993.

[52] Dawicke, D.S., Grandt Jr A.F., Newman Jr J.C., "Three-dimensional crack closure behaviour," Engineering Fracture Mechanics, Vol. 36, No. 1, pp. 111-121, 1990.

[53] Shin, C.S., Fleck, N.A., "Overload retardation in a structural steel," Fatigue and Fracture of Engineering Materials and Structures, Vol. 9, No. 5, 1987, pp. 379-393.

[54] Lang, M., Huang, X., "The influence of compressive load on fatigue crack propagation in metals," Fatigue and Fracture of Engineering Materials and Structures, Vol. 21, 1998, pp. 65-83.

[55] Tong, F.C., Gray, T.G.F., "Fatigue crack closure study based on whole-field displacements," International Journal of Fatigue, Vol. 18, No. 8, 1996, pp. 593-601.

[56] Allison, J.E., Roland, C.K., Pompetzki, M.A., "A comparison of measurement methods and numerical procedures for the experimental characterisation of fatigue crack closure," Mechanics of Fatigue Crack Closure, ASTM STP 982, J.C. Newman, Jr. and W. Elber, Eds. American Society for Testing and Materials, Philadelphia, 1998, pp. 171-185.

[57] Carman, C.D., Turner, C.C., Hillberry, B.M., "A method for determining crack opening load from load-displacement data," Mechanics of Fatigue Crack Closure, ASTM STP 982, J.C. Newman, Jr. and W. Elber, Eds. American Society for Testing and Materials, Philadelphia, 1998, pp. 214-221.

[58] Donald, K.J., " A procedure for standardising crack closure levels," Mechanics of Fatigue Crack Closure, ASTM STP 982, J.C. Newman, Jr. and W. Elber, Eds. American Society for Testing and Materials, Philadelphia, 1998, pp. 222-229.

[59] Zhu, X.Y., Shaw, W.J.D., "Fatigue crack closure and its effect on life prediction in compact tension specimens," International Journal of Fatigue, Vol. 18, No. 7, 1996, pp. 499-505.

[60] Clerivet, A., Bathias, C., "Influence of some mechanical parameters on the crack closure effect in fatigue crack propagation in aluminium alloys," Fatigue Crack Closure, ASTM STP 982, J.C. Newman, Jr. and W. Elber, Eds. American Society for Testing and Materials, Philadelphia, 1998, pp. 583-597.

[61] Gray, I.G., "Fatigue crack propagation test programme for the A320 Wing," New Materials and Fatigue Resistant Aircraft Design, ICAF 14, Ottawa, 1987, pp. 297-335.

[62] Schijve, J., "The significance of flight-simulation fatigue tests," Report TU Delft LR466, Department of Aerospace Engineering, Delft University of Technology, Netherlands, June 1985.

[63] Sunder, R., "Contribution of individual load cycles to crack growth under aircraft spectrum loading," Advances in Fatigue Lifetime Predictive Techniques, ASTM STP 1122, M.R. Mitchell and R.W. Landgraf, Eds., American Society for Testing and Materials, pp. 176-190, 1992.

[64] Schijve, J., Vlutters, A.M., Ichsan, Provo Kluit, J.C., "Crack growth in aluminium alloy sheet material under flight-simulation loading", International Journal of Fatigue, No. 3, 1985, pp 127-136.

[65] Schra, L., Wanhill, R.J.H., "Influence of gust spectrum variations on fatigue crack growth behaviour of damage tolerant aluminium-lithium sheet materials," NLR TP 92445 U, National Aerospace Laboratory, Netherlands, 1992.

[66] Abelkis, P.R., "Effect of transport aircraft wing loads spectrum variation on crack growth," Effect of Load Spectrum Variables on Fatigue Crack Initiation and Propagation, ASTM STP 714, D.F. Bryan and J.M. Potter, Eds., American Society for Testing and Materials, 1980, pp. 143-169.

[67] Kim, C.Y., Song, J.H., "Fatigue crack closure and growth behaviour under random loading," Engineering Fracture Mechanics, Vol. 49, No. 1, pp. 105-120, 1994.

[68] Sunder, R., "Near-threshold fatigue crack growth prediction under spectrum loading," Advances in Fatigue Lifetime Predictive Techniques, ASTM STP 1122, M.R. Mitchell and R.W. Landgraf, Eds., American Society for Testing and Materials, 1992, pp. 161-175.

[69] Wanhill, R.J.H., "Flight simulation fatigue crack growth testing of aluminium alloys. Specific issues and guidelines" Fatigue, Vol. 16, 1994, pp. 99-110.

[70] Wheeler, O.E., "Spectrum loading and crack growth," American Society for Mechanical Engineers Transactions, Journal of Basic Engineering, Vol. 94 March 1972, pp. 181-186.

[71] Willenborg, J., Engle, R.M., Wood, H.A., "A crack growth retardation model using an effective stress concept," AFFDL-TR-71-1, Air Force Flight Dynamics Laboratory, Wright-Patterson Air Force Base, OH, Jan 1971.

[72] Dill, H.D., and Saff, C.R., "Spectrum crack growth prediction method based on crack surface displacement and contact analyses," Fatigue and Crack Growth under Spectrum Loads, ASTM STP 592, American Society for Testing and Materials, 1976, pp. 306-319.

[73] ten Hoeve, H.J., de Koning, A.U., "User manual for the crack opening models in the NASGRO-STRIPY-95 program," NLR CR 95399 L, National Aerospace Laboratory, Netherlands, 1995.

[74] Lazzeri, L., Pieracci, A., Salvetti, A., "An evaluation of fatigue crack growth prediction methods used in aircraft design," Proceedings of ICAF 95, Eds. J.M. Grandage and G.S. Jost, June 1995, Melbourne, Australia.

[75] Daniewicz, S.R., Bloom, J.M., " An assessment of geometry effects on plane stress fatigue crack closure using a modified strip-yield model," International Journal of Fatigue, Vol. 18, No. 7, pp. 483-490, 1996.

[76] Saff, C.R., "Crack growth retardation and acceleration models," Damage Tolerance of Metallic Structures: Analysis Methods and Application, ASTM STP 842, J.B. Chang and J.L. Rudd, Eds., American Society for Testing and Materials, 1984, pp. 36-49.

[77] Esacrack User's Manual, European Space Agency, ESA PSS-03-209, Issue 2, 1995.

[78] ten Hoeve, H.J., de Koning, A.U., "Implementation of the improved Strip-Yield Model into the NASGRO software - architecture and detailed design document," NLR CR 95312 L, National Aerospace Laboratory, Netherlands, 1995.

[79] de Koning, A.U., "Improvement and Verification of the Strip-Yield Model in the NASGRO Software for Damage Tolerance Analysis - Final Report," NLR CR 95663 L, National Aerospace Laboratory, Netherlands, 1995.

[80] Crack Growth Models, Final Report, Robust Crack Growth Model for Rotorcraft Metallic Structures, DTI Link Contract No. RA/6/30/06, Defence Evaluation and Research Agency, DERA/MSS2/WP9800180/1.0, 1998.

[81] Irving, P.E., Buller, R.G., "Prediction of Fatigue Life under Helicopter Loading Spectra for Safe Life and Damage Tolerant Design," Fatigue and Fracture Mechanics: 29th Volume, ASTM STP 1321, T.L. Panontin and D.S. Sheppard, Eds., American Society for Testing and Materials, 1998.

[82] Everett, R.A, Bartlett, Jr., F.D., Elber, W., "Probabilistic Fatigue Methodology for Six Nines Reliability," American Helicopter Society Annual 47st Forum, pp. 235-255, 1991.

[83] Buller, R.G., "A standardised fatigue loading sequence for helicopter main rotorhead structures (Rotorix)", DTI-LINK RA/6/30/06, Cranfield University Damage Tolerance Group Report CU/927/N/27, August 1996.

[84] ASTM E 647, Standard Test Method for Measurement of Fatigue Crack Growth Rates. American Society for Testing and Materials.

[85] Stress Intensity Factors Handbook, Vol. 1, Committee on Fracture Mechanics, The Society of Material Science, Japan, Y. Murakami Ed., Permagon Press, 1987.

[86] Sutton, G.R., "An improved electrical potential method for crack length measurement," Royal Aircraft Establishment, Technical Report 83063, August 1983.

[87] Donald, J.K., Bray, G.H., Bush, R.W., "An evaluation of the adjusted compliance ratio technique for determining the effective stress intensity ratio," 29th National Symposium on Fatigue and Fracture Mechanics, ASTM STP 1332, T.L. Panontin, S.D. Sheppard, Eds., American Society for Testing and Materials, 1997.

[88] Boyer, R.R., Rosenburg, H.W., "Ti-10V-2Fe-3Al Properties," in R.R. Boyer and H.W. Rosenburg (Eds.), Beta Titanium Alloys in the 1980's, Proceedings of a symposium sponsored by the Titanium Committee of AIME, The Metallurgical Society, Atlanta, Georgia, March 8, 1983, pp. 441-456.

[89] Haicheng, G., Shujuan, S., "Microstructural effect on fatigue thresholds in beta titanium alloy Ti-10V-2Fe-3Al," in H. Kitagawa and T. Tanaka (Eds.), Fatigue 90, Proceedings of the Fourth International Conference on Fatigue and Fatigue Thresholds, Vol. III, 15-20 July, 1990, pp. 1929-1934.

[90] Buller, R.G., Jenkins, S., "WP320 - Material data and component tests on WHMS 640 (Ti-10V-2Fe-3Al)", Final Report, DTI-LINK RA/6/30/06, GKN WHL LR-97182, 1998.

[91] Procurement of 10V-2Fe-3Al Titanium Alloy Forgings for Dynamically Critical Applications, Helicopter Material Specification, GKN Westland Helicopters, WHMS 640, Issue 1.

[92] Kuhlman, G.W., Chakrabarti, A.K., Yu, T.L., Pishko, R., Terlinde, G., "LCF, fracture toughness and fatigue/fatigue crack propagation resistance optimisation in Ti-10V-2Fe-3Al alloy through microstructural modification", Microstructure, Fracture Toughness and Fracture Crack Growth Rates in Titanium Alloys, Proceedings TMS-AIME Annual Symposium, Chakrabarti and Chesnutt (Eds.), 1987.

[93] Reynolds, M.A., Fitzsimmons, P.E., Harris, J.G., "Presentation of properties of a new High Strength Aluminium Alloy Designated 7010," Aluminium Alloys in the Aircraft Industry, Proceedings of Symposium, Turin, October, 1976.

[94] ASTM B577M, Standard Test Methods for Measurement of Mechanical Properties, American Society for Testing and Materials.

[95] Hudak and Clark, “Variability of fatigue crack growth rate testing,” Journal of Testing and Evaluation, Vol. 3, No. 6, 1975, pp. 454-476.

[96] Kumar, R., Garg, S.B.L., “Effect of yield strength and single tensile overload cycles on effective stress intensity range ratio in 6061-T6 alloy,” Engineering Fracture Mechanics, Vol. 34, No. 2, pp. 403-412, 1989.

[97] Kumar, R., “Prediction of delay cycles due to instance of single overload cycles,” Engineering Fracture Mechanics, Vol. 42, No. 3, 1992, pp. 563-571.

[98] Dexter, R.J., Hudak, S.J., Davidson, D.L., “Modelling and measurement of crack closure and crack growth following overload and underloads,” Engineering Fracture Mechanics, Vol. 33, No. 6, pp. 855-870, 1989.

[99] Wang, G.S., Blom, A.F., “A strip model for a fatigue crack growth predictions under general load conditions,” Engineering Fracture Mechanics, Vol. 40, No. 3, 1991, pp. 507-533.

[100] Dabayeh, A.A., Topper, T.H., “Changes in crack-opening stress after underloads and overload in 2024-T351 aluminium alloy,” International Journal of Fatigue, Vol. 17, No. 4, 1995, pp. 261-269.

[101] Fleck, N.A., “Fatigue crack growth due to periodic underloads and overloads,” Acta Metallurgica, Vol. 33, No. 7, pp. 1339-1354, 1985.

[102] Heuler, P., Seeger, T., “A criteria for omission of variable amplitude loading histories,” International Journal of Fatigue, Vol. 8, No. 4, pp. 225-230, 1986.

[103] Spencer, C.W., Killian, S. L., “Structural analysis of large titanium castings in a high-cycle, rotor-induced vibratory load environment,” American Helicopter Society Annual 51st Forum, Vol. 2, pp. 1615-1626, 1995.

APPENDIX A

COMPACT TENSION SPECIMEN MANUFACTURING DRAWING

TEST GRIP ASSEMBLY DRAWINGS

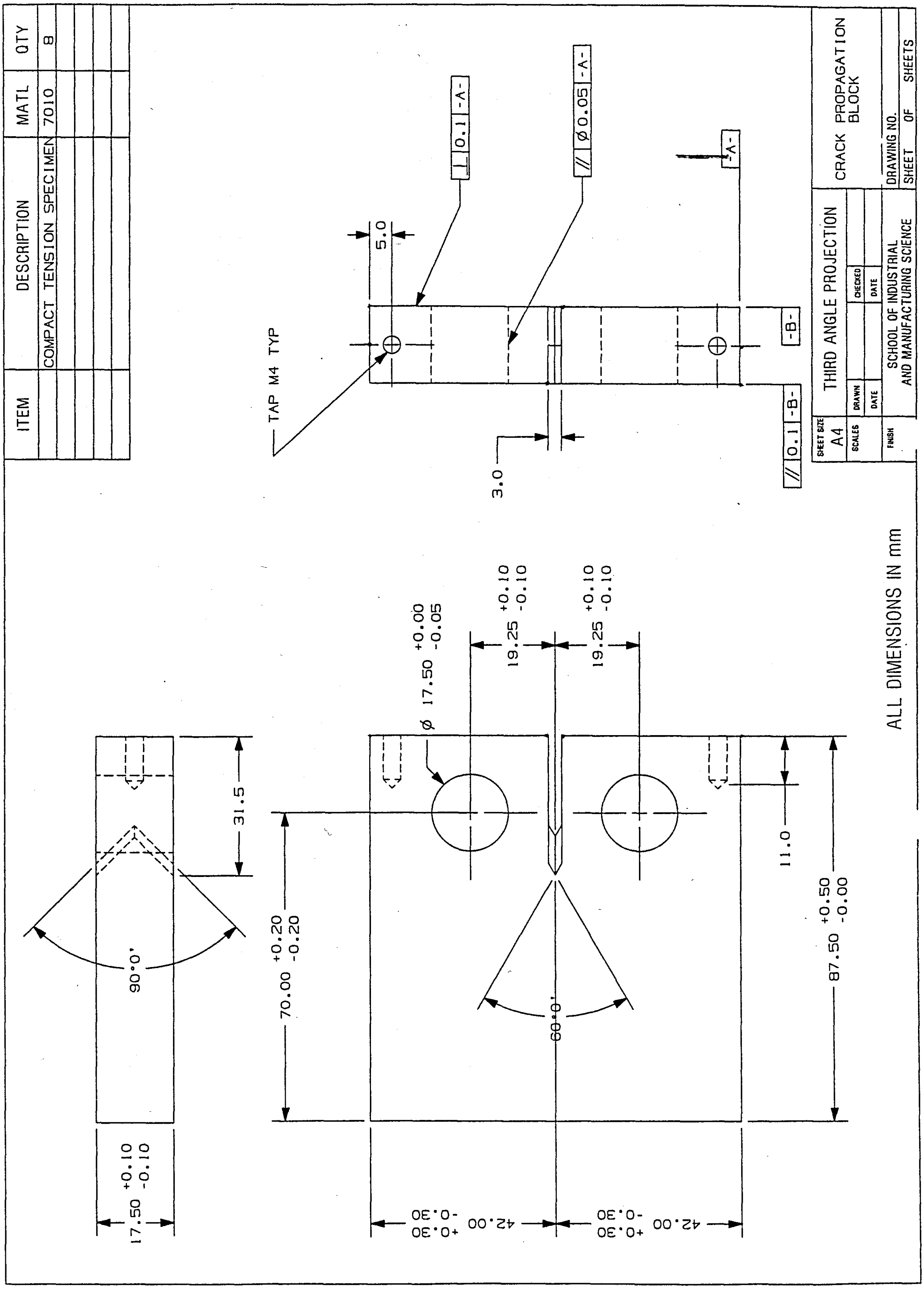
ITEM
DESCRIPTION
MATL
QTY
COMPACT TENSION SPECIMEN
7010
8
TAP M4 TYP
5.0
⊥ 0.1 -A-
// Ø 0.05 -A-
-A-
-B-
// 0.1 -B-
3.0
Ø 17.50 +0.00 -0.05
19.25 +0.10 -0.10
19.25 +0.10 -0.10
31.5
90.0°
70.00 +0.20 -0.20
60.0°
11.0
87.50 +0.50 -0.00
17.50 +0.10 -0.10
42.00 +0.30 -0.30
42.00 +0.30 -0.30
ALL DIMENSIONS IN mm
SHEET SIZE A4
SCALES
FINISH
THIRD ANGLE PROJECTION
DRAWN
DATE
CHECKED
DATE
SCHOOL OF INDUSTRIAL AND MANUFACTURING SCIENCE
CRACK PROPAGATION BLOCK
DRAWING NO.
SHEET OF SHEETS

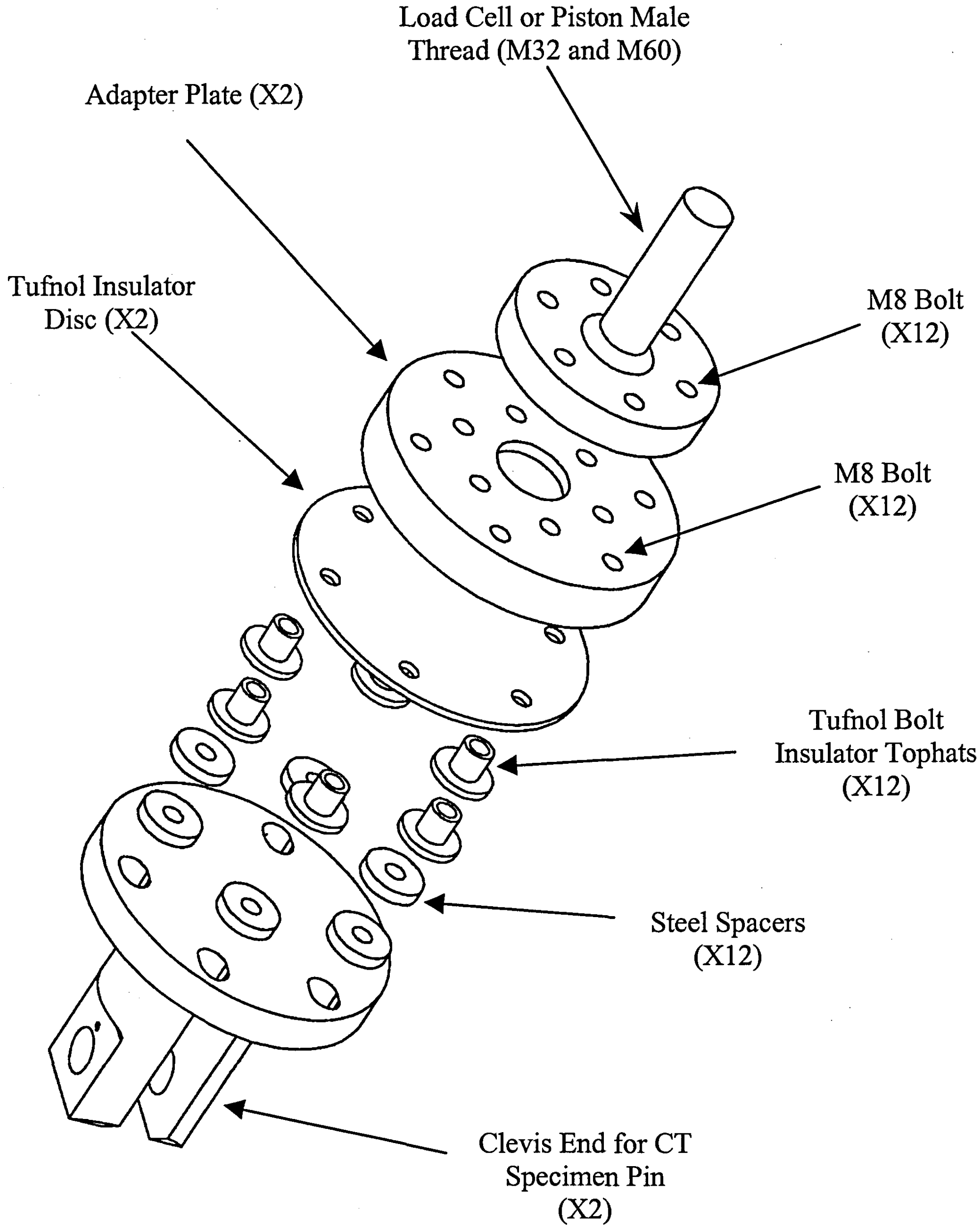

Figure B2 Assembly of compact tension specimen grips. Material: EN24T steel, Tufnol Insulators

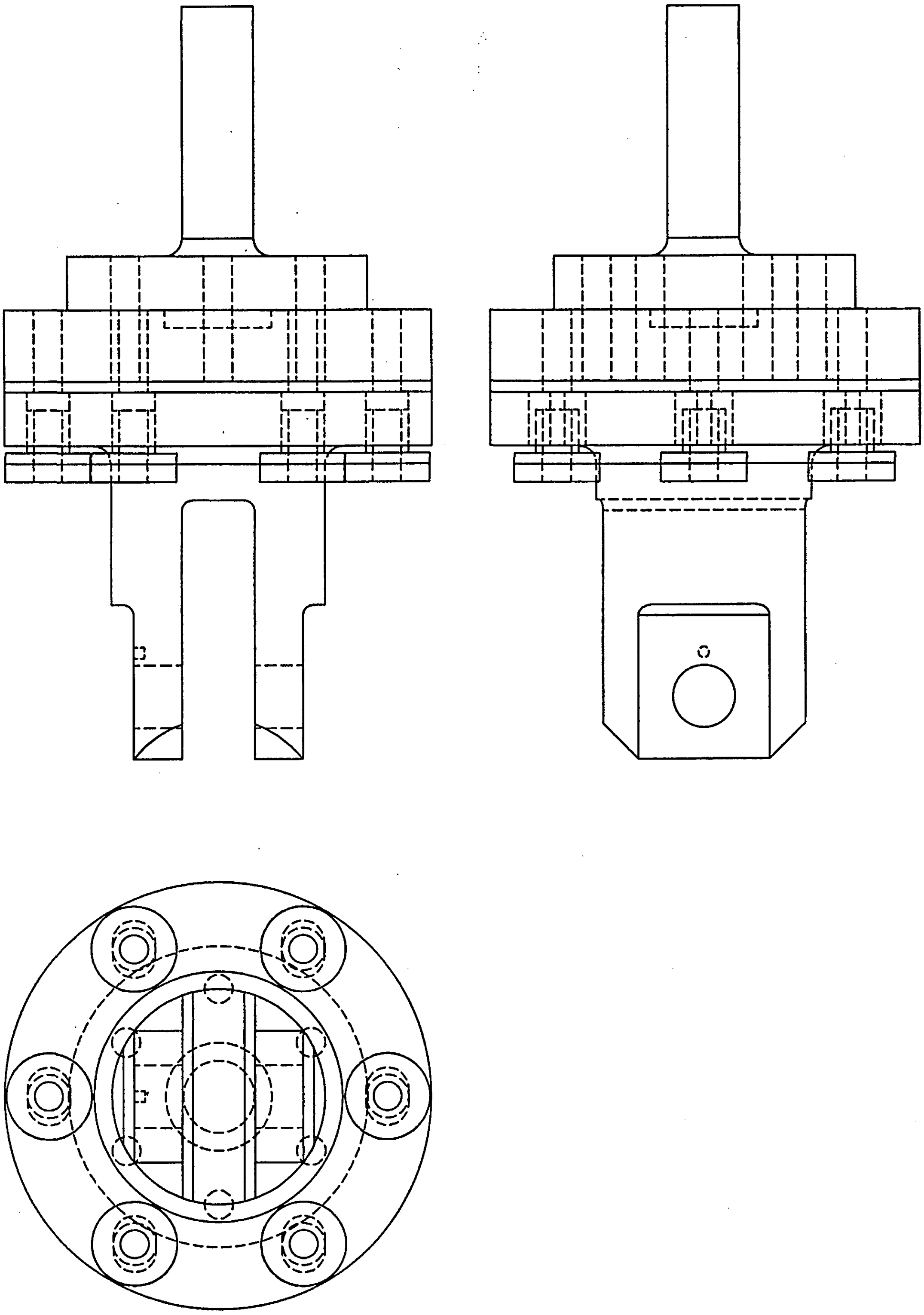

Figure B3 Assembled grips for compact tension specimen. Material: EN24T steel, Tufnol Insulators

APPENDIX B

DESIGN OF CRACK LENGTH AND CRACK CLOSURE MEASURMENT SYSTEM

B.1 Design of Direct Current Potential Drop Crack Length Measurement System

B.1.1 Requirements of System

The crack length measurement system was designed with accuracy and versatility in mind. The system needed to be accurate enough to measure the small increments of crack growth resulting from near-threshold growth rates and the small transient effects that would occur following a tensile overload. The system also needed to be versatile enough to be used on any specimen, 'communicate' with the digital fatigue loading machine and to incorporate measurement of crack closure at a later date. For these reasons a digitally based system relying on a PC computer control was chosen.

One of the main problems associated with crack length measurement using the DCPD method is electrical noise which reduces the accuracy of the system. It was decided early on in the design process that the use of high band width voltage amplifiers (which also amplify noise and hence would require a filter) could be eliminated by using a high-resolution digital voltmeter. To improve the low noise characteristics of the system a stable power supply also had to the selected and which preferably had a high current output so that the voltages generated (Ohm's law) across the specimen were as high as possible. That is, the greater the voltage generated, the greater the crack length resolution of the system.

B.1.2 System hardware

Both the power supply and digital voltmeter had to be programmable and controllable from the computer. A readily available programmable digital voltmeter (DVM) and a power supply (PS) were chosen so that the measurement system could be assembled together in a modular fashion and with minimal design of electrical circuitry. The basis of this modular system is the Model 488-PC2 IEEE 488.2 interface card [B1], more commonly referred to as a GPIB (General Purpose Interface Board). The GPIB allows communication between the controlling computer and the various pieces of equipment that constitute the DCPD system. The GPIB method was chosen primarily because the remote operation (from computer) of the Instron 8500 fatigue loading machine was based on the 488 GPIB so the system could be integrated with it and transportable between the fatigue machines.

The pieces of equipment chosen for the system were:

1. Viglen 386 personal computer,
2. Keithley Model 2000 Multimeter [B2] with ten channel scanner card,
3. Thurlby Thandar TSX 3510P DC Power Supply [B3],
4. Cambridge Electronic Design CED 1401, 16 Channel Analogue to Digital Converter [B4],
5. Instron 8500 digitally controlled fatigue loading machine [B5].

Figure B.1 shows the set-up of the equipment that constitutes the DCPD system. The timing and sequencing of voltage measurement and current pulsing is controlled from the CED 1401 which is a fully programmable analogue to digital (A-D) converter with its own processor. The significant feature of the CED 1401 is the 24 bits of digital input/output (I/O) that can be used for triggering events in external equipment. The 1401 processor has the ability to control each I/O so that precisely timed and sequenced events can be triggered. The PC is used to program the CED 1401 processor sequence set-up through its own data bus as shown in Figure B.1. This data bus is not only used for set-up but can also read back the digital 'word' generated at the I/O and can also download digitised analogue signals from the A-D converter.

The CED 1401 and the Instron 8500 are connected together through their respective digital I/O ports. This connection allows the cycle detector on the 8500 to trigger the sequenced events for voltage measurement and current pulsing once a pre-set cycle number is achieved.

The PC reads the digital 'word' generated by the CED 1401 processor and detects changes in this word to sequence the DVM scanner card measurements and to pulse the 20A current from the PS at the appropriate intervals via the GPIB. The voltage measurements at the DVM are taken at precise times to coincide with peaks loads using an external 'trigger link' as shown in Figure B.1. The trigger link is used because there are finite time elapses and variation in timing of events using the GPIB. The trigger link by-passes the GPIB and so the precisely timed sequences of the CED 1401 are used. There is also a finite time between the cycle detect on the 8500 and when the CED 1401 starts to sequence the I/O ports so an oscilloscope was used to measure the time between cycle detect and the first DVM measurement at peak load. The circuit connections between the DVM, 1401 and 8500 are shown in Figures B.2 and B.3.

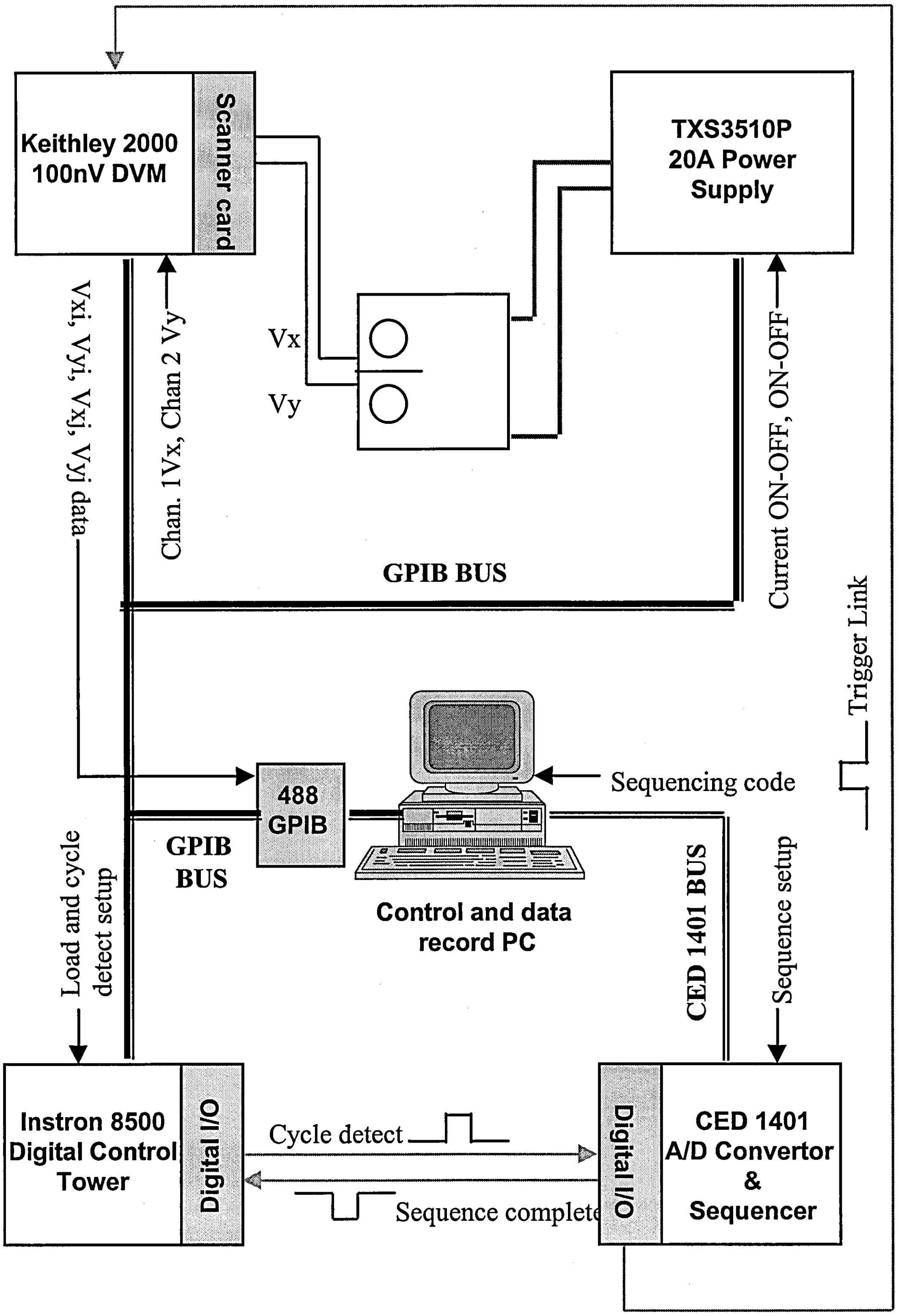

Figure B.1 Schematic of DCPD system

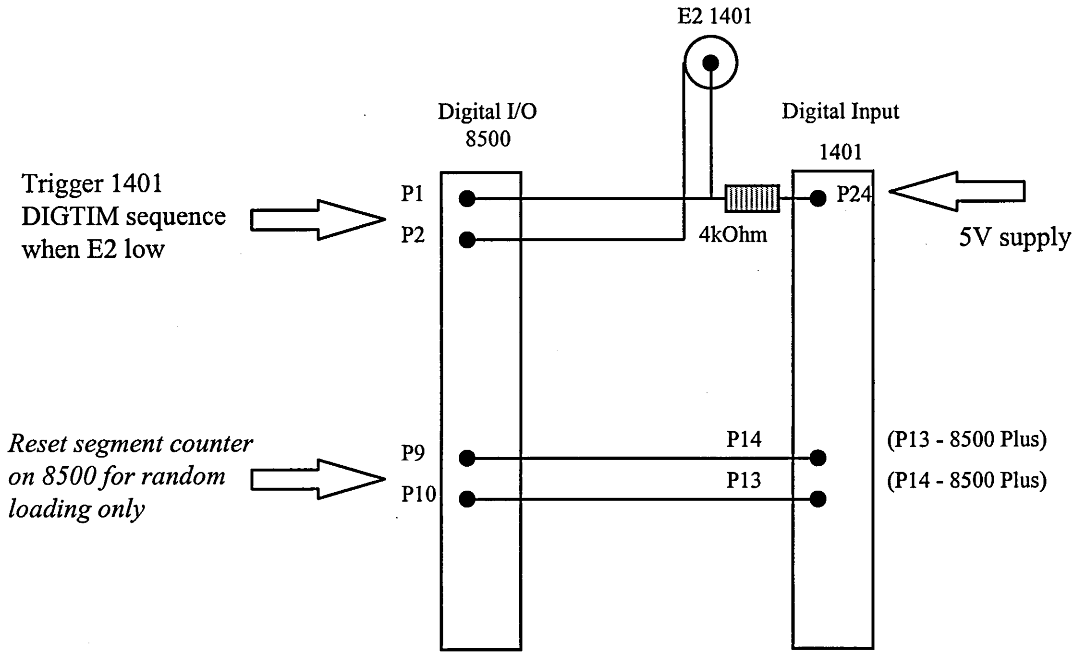

Figure B.2 Connection schematic between CED 1401 I/O and Instron 8500 I/O

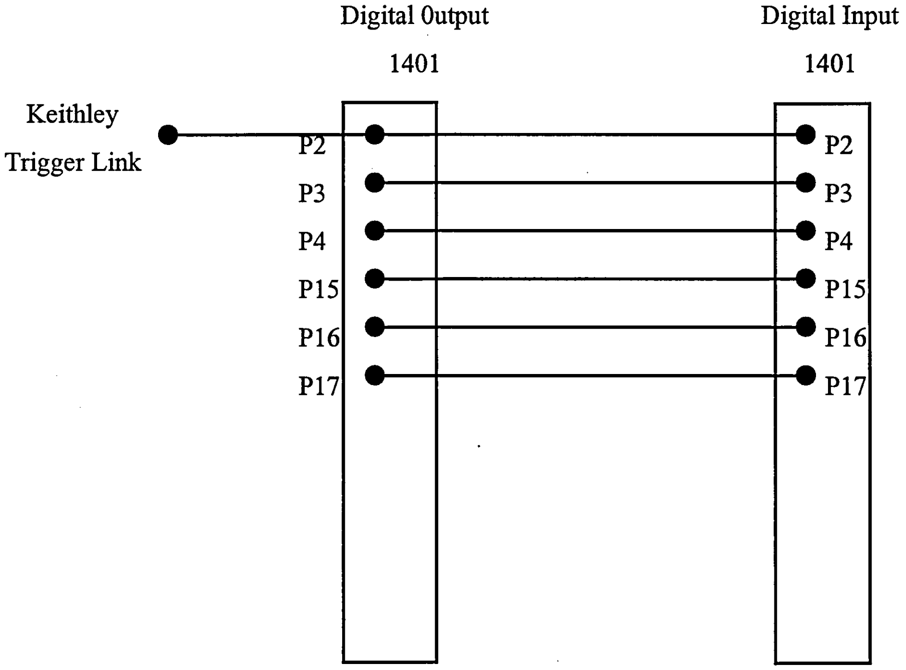

Figure B.3 Connection schematic between CED 1401 I/O's and Keithley Trigger Link

Each piece of equipment connected to the GPIB bus has its own address or identity so the software can send set-up information and/or request that data be downloaded to the PC. The CED 1401 has its own bus so it was not necessary for it to have its own address.

The DCPD does not employ any voltage amplifiers nor noise filters so a data averaging routine was employed to reduce the amount of natural electrical noise measured at the DVM. The leads for the voltage probes on the specimen are shielded using a braided screen wire. The current leads are twisted to reduce the electro-magnetic radiation from them. The power leads of all the equipment were plugged into the mains supply with a common earth to avoid ground loops in the system.

B.1.3 Software Design

The three main computer programs used to run the fatigue tests are described below.

B.1.3.1 Automated crack length and crack closure measurement

A computer program, written in the C language, was developed to perform automated crack length and crack closure measurement during the CAL and SVAL fatigue tests. The essential components of the program are described here and the sequence of events used to take a crack length measurement are explained in Figure B.4.

The program is used to initialise and configure each piece of equipment before the start of the test. Each component of the system is configured to respond to the GPIB interface (addressing, read-write format and response times) and to change any default settings that are used during test measurement. The CED 1401 was set up using manufacturer supplied software routines incorporated into the program.

The program prompts the user for test set up information which includes the cycle period for test measurement, starting voltage ratio $(V_x/V_y)_o$, current crack length, current cycle number and when to terminate the test. The rate at which data is stored to file can be selected as well. If crack closure measurements are to made then it prompts the user for the crack length at overload and displays post-overload crack closure measurement crack lengths. The program was written so that the crack closure measurement subroutine could be bypassed and only fatigue length measurements made.

The Instron 8500 is programmed with the CAL loads required for the test and is under remote control from the PC during the test. This locks out the front panel of the machine and control is only returned from the PC when the test finishes or the user interrupts the test by pressing F1 on the PC. The test is started from the program menu and crack length measurements are made at the pre-set cyclic intervals.

The 8500 has a cycle detect feature that is tripped when the pre-set cycle number at which DCPD measurements are to be made. This is achieved by loading a separate program in the 8500 memory as a string of cycle detect, trip and trip reset commands. When this trips, it triggers a digital I/O signal between the 8500 and the CED 1401. Referring to Figure B.4, this is a digital 'low' or '0' at the CED channel E2. The digital word sequence programmed into the CED 1401 only starts when E2 is low. Initially the digital word read by the CED (it outputs as well as inputs and reads the word) is set at '000000' and this is continually monitored by the PC until E2 goes low and the sequence starts. The program word sequence is shown in Figure B.4. The connections between the 1401 digital inputs and output pins which create the digital word are shown in Figure B.3. The PC reads each change and, depending on the word read, will configure the PS and DVM and take the appropriate voltage reading. The actual voltage reading is triggered directly from the CED 1401 to the DVM by the trigger link as explained earlier. Due to the random nature of electrical noise it is possible to reduce noise levels by averaging the data readings over a brief interval [B6]. Therefore the DVM takes 20 readings at 2000 Hz at the cycle peak and then averages these readings.

The terminology for the voltage readings is as follows:

V_{xi} - voltage across crack, with current on and includes emfs
V_{xj} - voltage across crack, without current and includes emfs
V_{yi} - voltage across reference location or specimen, with current on and includes emfs
V_{yj} - voltage across reference location or specimen, without current and includes emfs

Hence $V_x = V_{xi} - V_{xj}$ and $V_y = V_{yi} - V_{yj}$.

Once the sequence is complete the word is again read as '000000' and the PC downloads the four voltage readings from the DVM and performs the crack length calculation using the CT calibration equation given in Section 6.4. The data is stored to file as time, cycle number, V_x, V_y, V_x/V_x and crack length.

Once the crack length has been measured and stored it can be used to either:

(1) Stop the test if the required target length has been achieved by stopping load cycling on the 8500 and closing down the remote control of the DVM, PS, 8500 and the CED 1401.

or,

(2) Perform a programmed crack closure measurement as detailed in Section B.2.

When the calculation is complete and the cycle, voltage and crack length information is stored in a file, the computer clears the DVM buffer, resets the CED 1401 sequencer and cycle counter on the 8500. The cycle detector on the 8500 is reset using a GPIB command. The computer then goes back to monitoring the I/O word on the CED 1401 waiting for the next pre-set cycle detection.

B.1.3.2 Automated crack length measurement for sequence loading tests

The measurement of crack growth during complex loading sequences requires a modification of the DCPD system because the GPIB interface at the 8500 is now used by the Instron Random Loading Software (IRLS), version V21.44. Usually the cycle counter on the 8500 is pre-programmed and reset from the PC using a GPIB command. Pre-programming of the cycle counter is now performed using a different computer and GPIB interface which is also used for the IRLS. A separate program was written in C language and compiled to operate in a Microsoft Windows (IRLS operates under this) environment.

The program used to take crack length measurements is essentially the same as the program described above but with two differences: (1) It has no crack closure facility and (2) the reset of the cycle counter on the 8500 is triggered through a digital I/O connection from the CED.

To achieve the pre-programming and reset routine, the program sets up the 8500 to run the following sequence:

1. Pre-set the cycle detector on the 8500 to the desired measurement cycle increment using a separate program.
2. When pre-set cycle count reached first pre-programmed command set is tripped.
3. Pre-programmed commands set digital output to ‘low’ to the CED 1401 E2 as for existing system and arms digital input D1 on 8500 to detect ‘low’ input.
4. DCPD system runs through normal measurement sequence.

5. When measurement sequence is finished the DCPD sets the CED1401 DO 14 to low.
6. Digital input D1 detects low signal on the 8500 and trips second pre-programmed command set which resets the cycle detector and arms it.
7. Sequence complete. Return to 1.

This program is also used to set up the load and position safety limits on the 8500 for each particular test. The connections for the CVAL DCPD measurements are given in Figure B.2.

B.2 Design of Crack Closure Measurement System

B.2.1 Description of Hardware

The CED 1401 16 channel, 8 bit analogue to digital (A-D) converter was used to its full potential by taking measurements during cyclic loading of the specimens. A CED 1902 signal conditioner was coupled to the 1401 to amplify and filter the gauge signals. Refer to Figure B.5.

B.2.2 Crack Closure Measurement Procedure

Crack closure measurements were made by digitally recording the complete cyclic load-strain/CMOD curves at a frequency of 0.1 Hz at various crack lengths before, during and after particular loading events. Measurements were taken at different crack lengths and/or cycles - specific to each test case -before and after the overload event.

A loading frequency of 0.1 Hz was used because of the transient response time of the 1902 filter. The load and strain/displacement signals were sampled at a rate of 20Hz over five complete cycles (i.e. 1000 data sets). The data were then averaged over the five cycles to give a load-strain/displacement curve defined by 200 data points.

The measurement of load-strain curves for fatigue crack closure could be made either using CED supplied software or the CAL/SVAL program developed above. Both methods used exactly the same techniques for data acquisition. However, the custom designed software gave no interruption of the test apart from reduction in cyclic load frequency during the data acquisition process

Figure B.4 Flowchart of program used to set-up, configure, collect and store data in DCPD system.

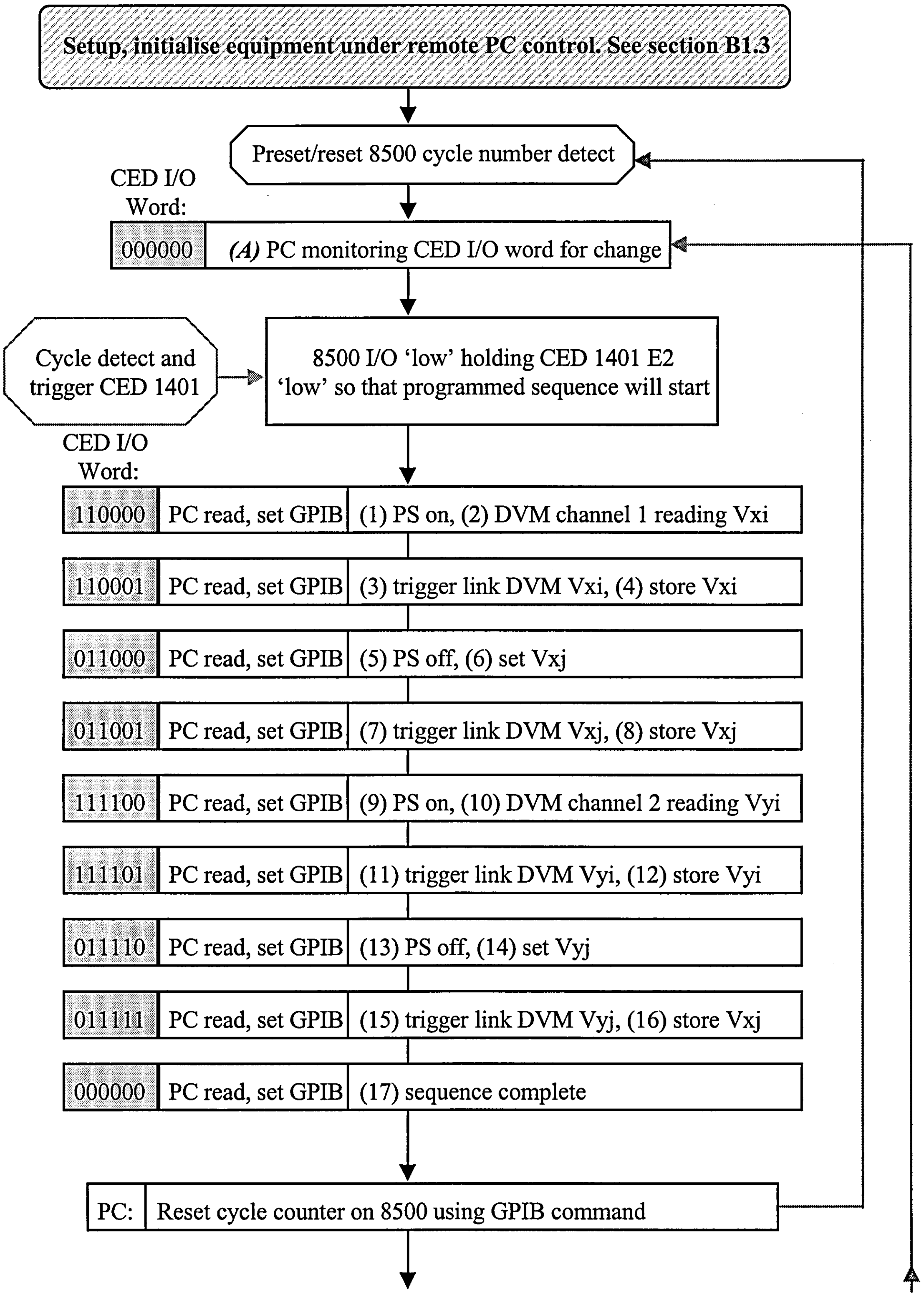

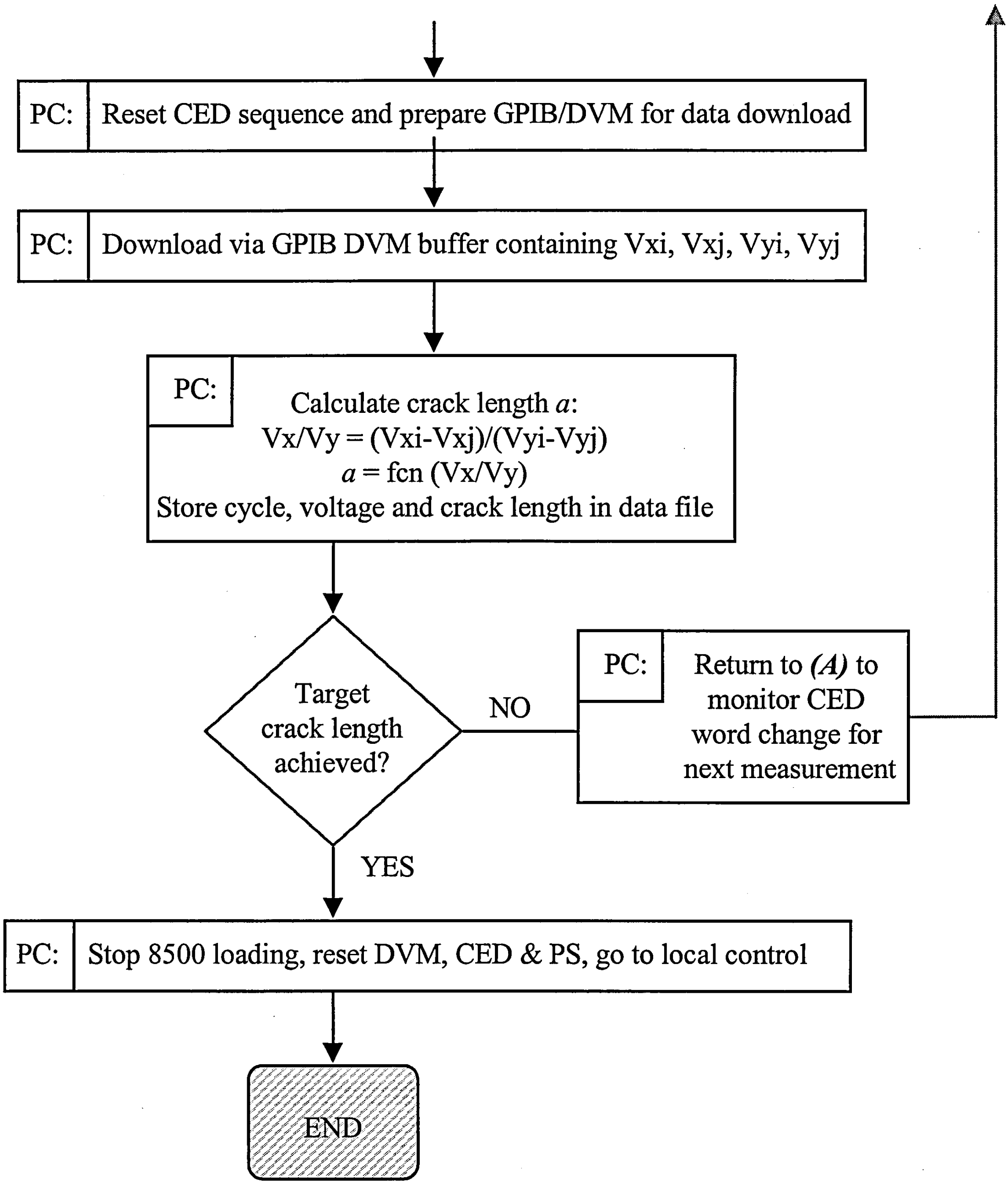
PC:
Reset CED sequence and prepare GPIB/DVM for data download
PC:
Download via GPIB DVM buffer containing Vxi, Vxj, Vyi, Vyj
PC:
Calculate crack length *a*:
Vx/Vy = (Vxi-Vxj)/(Vyi-Vyj)
a = fcn (Vx/Vy)
Store cycle, voltage and crack length in data file
Target crack length achieved?
NO
PC:
Return to *(A)* to monitor CED word change for next measurement
YES
PC:
Stop 8500 loading, reset DVM, CED & PS, go to local control
END

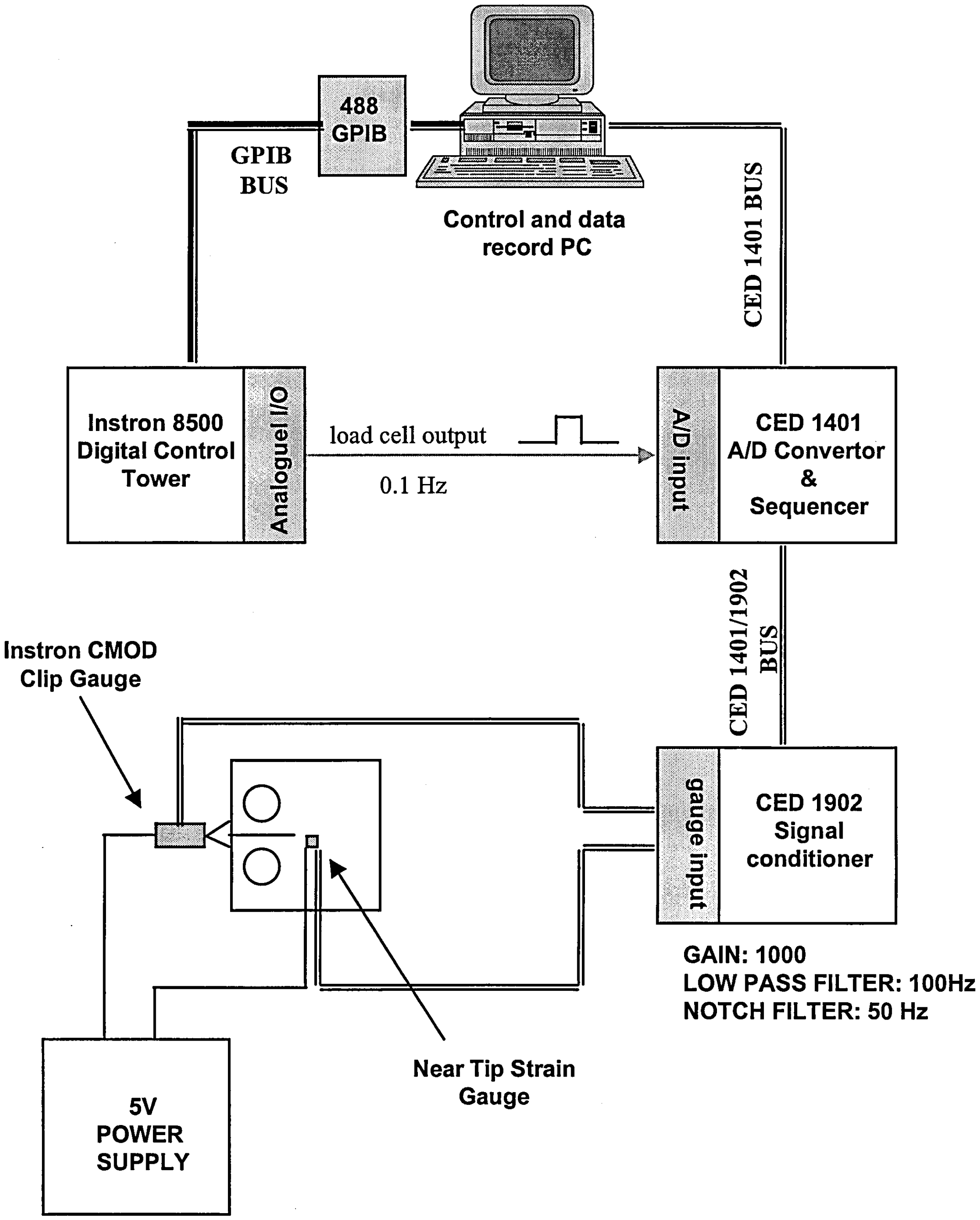

Figure B.5 Schematic of equipment used to measure crack closure.

B.3 References

[B1] Model 488-PC2 IEEE 488.2 Bus Interface Card User's Manual, ICS Electronics Corporation, USA, 1994.

[B2] Keithley Model 2000 Multimeter User's Manual, Test Instrumentation Group, Keithley Instruments Inc., USA, 1994.

[B3] Thurlby Thandar TSX3510P DC Power Supply User's Manual, Thurlby Thandar Instruments Ltd., UK, 1994.

[B4] The CED 1401 and 1401 Plus Owner's Handbook, V0.2, Cambridge Electronic Design Ltd, UK, 1992.

[B5] Instron 8500 User's Manual, Instron International Ltd, 1994.

[B6] Catlin, W.R., Lord, D.C., Prater, T.A., Coffin, L.F., "The Reversing D-C electrical potential method," Automated Test Methods for Fracture and Fatigue Crack Growth, ASTM STP 877, W.H. Cullen, R.W. Landgraf, L.R. Kaisand and J.H. Underwood, Eds., American Society for Testing and Materials, Philadelphia, 1985, pp. 67-85.